ULB UNIVERSITÉ LIBRE DE BRUXELLES

Année académique 2013–2014

UNIVERSITÉ PARIS SUD

Dynamical study of diatomics: Applications to astrochemistry, quantum control and quantum computing

Vranckx Stéphane

F.R.S. – FNRS Research Fellow

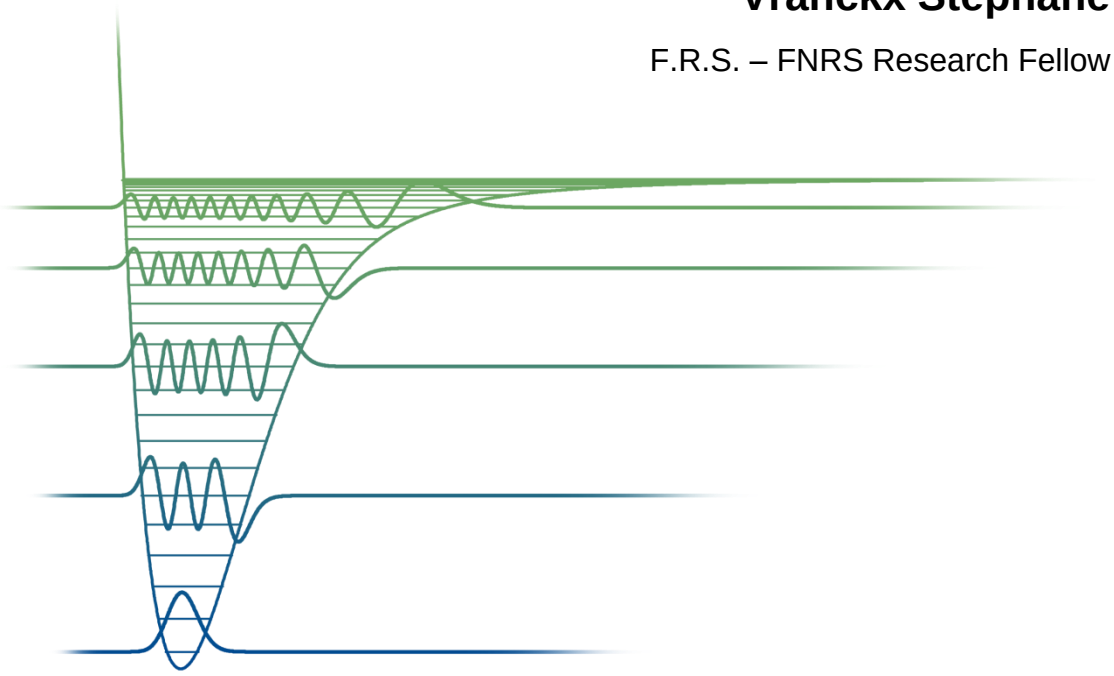

Thèse présentée en vue de l'obtention du grade de Docteur en Sciences, réalisée sous la direction de :

Nathalie Vaeck
Service de Chimie Quantique et Photophysique
Université Libre de Bruxelles

Michèle Desouter-Lecomte
Laboratoire de Chimie Physique
Université Paris-Sud

ABSTRACT

In this work, we theoretically study the properties of diatomic molecular systems, their dynamics, and the control thereof through the use of laser fields. We more specifically study three compounds:

- HeH^+, a species of great astrochemical importance which is thought to be the first molecular species to have formed in the universe;
- CO^{2+}, a metastable dication of particular interest in quantum control experiments due to its long-lived lowest vibrational level;
- $^{41}K^{87}Rb$, a polar molecule that can be formed at very low temperature and trapped, making it a good candidate for quantum computing schemes.

First, we use *ab initio* methods to compute accurate potential energy curves for the lowest singlet and triplet states of HeH^+ as well as the potential energy curves, transition dipole moments and nonadiabatic radial couplings of the ground $^3\Pi$ state of CO^{2+} and of its 11 lowest $^3\Sigma^-$ states.

In a second step, we use this *ab initio* data to compute the photodissociation and radiative association cross sections for the a and $b\,^3\Sigma^+$ states of HeH^+, as well as the values of the corresponding rate constants for astrophysical environments. The photodissociation cross sections from the lowest vibrational level of CO^{2+} are also determined.

Going one step further, we optimize laser control fields that drive the photodissociation dynamics of HeH^+ and CO^{2+} towards specific channels. We compare two field optimization methods: a Møller operator-based Local Control approach and Optimal Control Theory. In both cases, we add a constraint that minimizes the area of the optimized fields.

Finally, we focus on one of the potential applications of high-fidelity laser control: the use of small molecular systems as quantum computers. We more specifically study the potential

implementation of both *intra-* and *inter*molecular logic gates on data encoded in hyperfine states of trapped ultracold polar $^{41}K^{87}Rb$ molecules, opening interesting perspectives in terms of extensibility.

Keywords

Computational Chemistry ; *Ab initio* calculations ; Quantum Dynamics ; Photodissociation ; Radiative Association ; Cross section ; Quantum Control ; Local Control ; Optimal Control ; Quantum Computing.

ABSTRACT EN FRANÇAIS

Dans cette thèse, nous étudions théoriquement les propriétés de molécules diatomiques, leur dynamique de réaction ainsi que le contrôle de cette dynamique à l'aide de champs laser. Notre travail porte plus spécifiquement sur trois espèces :

– HeH^+, un composé-clé en astrochimie considéré comme la première espèce moléculaire qui s'est formée dans l'univers ;

– CO^{2+}, un dication métastable qui se prête bien à des expériences de contrôle quantique en raison du relativement long temps de vie de son état vibrationnel le plus bas ;

– $^{41}K^{87}Rb$, une molécule polaire qui présente la particularité de pouvoir être formée à très basse température et piégée, ce qui en fait un bon support physique potentiel pour la réalisation d'un ordinateur quantique moléculaire.

Nous utilisons tout d'abord des méthodes de calcul *ab initio* afin d'obtenir les courbes d'énergie potentielle des premiers états singulets et triplets de HeH^+ avec un haut de degré de précision, ainsi que les courbes d'énergie potentielle, les moments dipolaires de transition et les couplages non-adiabatiques radiaux de l'état fondamental $^3\Pi$ de CO^{2+} et de ses 11 premiers états $^3\Sigma^-$.

Ensuite, nous utilisons ces données *ab initio* pour calculer les sections efficaces de photodissociation et d'association radiative des états a et $b\,^3\Sigma^+$ de HeH^+, ainsi que les constantes cinétiques associées à ces processus dans les conditions rencontrées dans des environnements astrophysiques. Les sections efficaces de photodissociation du niveau vibrationnel le plus bas de CO^{2+} sont également calculées.

Nous allons ensuite un cran plus loin en optimisant des champs laser qui guident la dynamique de photodissociation de HeH^+ et CO^{2+} vers des canaux de dissociation spécifiques.

Nous comparons deux méthodes d'optimisation de ces champs: une approche de contrôle local basée sur les opérateurs de Møller et la théorie du contrôle optimal. Dans le deux cas, nous incluons une contrainte qui minimise l'aire des champs.

Enfin, nous nous concentrons sur l'une des applications possibles du contrôle laser à haute fidélité : l'utilisation de petits systèmes moléculaires comme ordinateurs quantiques. Nous étudions plus spécifiquement l'implémentation possible d'opérations logiques *intra-* et *inter*moléculaires sur des données encodées dans des états hyperfins de molécules de $^{41}K^{87}Rb$ piégées, ce qui ouvre des perspectives intéressantes en terme d'extensibilité.

Note : conformément à la loi française, un résumé en français plus détaillé de cette thèse est donné en annexe, page 195.

Mots-clés

Chimie computationnelle ; Calcul *ab initio* ; Dynamique quantique ; Photodissociation ; Association Radiative ; Section efficace ; Contrôle quantique ; Contrôle local ; Contrôle optimal ; Ordinateur quantique.

ACKNOWLEDGMENTS

During these last four years, I had the privilege of meeting and working alongside people of extraordinary qualities not only as scientists, but also as persons. Although writing a comprehensive list of all persons I am indebted to would probably prove impossible, I will at least attempt to acknowledge all of the groups of people who helped me, even if I cannot cite them all by name.

First of all, I wish to thank my two advisors, Nathalie Vaeck and Michèle Desouter-Lecomte, for their guidance and support throughout all my thesis. It is only thanks to their expertise and understanding that I was able to successfully complete this research.

I am also very grateful to all those who helped me during the realization of this work or who I collaborated with. In no particular order, I wish to thank: Jérôme Loreau, Sergey Ryabchenko, Jacques Liévin, Christoph Meier, Osman Atabek, Dominique Sugny, Alexander Dalgarno, Xavier Urbain, Philippe Pellegrini, Amine Jaouadi, Yves Justum, David Lauvergnat, Michel Godefroid, Daniel Hurtmans, Georges Destrée and Jean-Marie Teuler (as well as all those I may have forgotten).

More broadly, I would like to thank all members of the *Service de Chimie Quantique et Photophysique* and of the *ThéoSim* group I had the pleasure of working alongside with, for the convivial work atmosphere that exists in both laboratories thanks to them. I more particularly wish to thank all the people I have had the pleasure of sharing an office with, if even briefly: Ariane Razavi, Aurélie Chenel, Marcela Tudorie, Maxim Sanzharov, Mauro Tomasi, Guillaume Chaumont and of course Guillaume Jumet, Simon Verdebout, Cédric Nazé, Thomas Carette, Jérôme Loreau and Maxence Delsaut (who I must also thank for forcefully broadening my musical culture in unexpected and sometimes uncanny directions).

I also want to express gratitude to all my friends for their support, for their help, and simply for always being there through highs and lows. Extra special thanks is owed to the good souls who took the time of proofreading parts of this thesis: Sophie Bauduin, Florence Colliez,

Livio Filippin, Dariusz Golebiowski, Guillaume Jumet, Jérôme Loreau, Ludovic Santos and Ariane Razavi.

Finally, I cannot thank my family and Florence enough for their love and their support throughout the years. Since I could never have achieved this without their help, it is only justice that I dedicate this thesis to them.

On a less personal note, I also wish to acknowledge the financial support of the Belgian *Fonds de la Recherche Scientifique* (first through a *FRIA* grant then through my current position of *FNRS Research Fellow*), of the COST CUSPFEL Action for financing my short stay in the *Laboratoire Collisions, Agrégats, Réactivité IRSAMC* in Prof. Meier's group, as well as of the I.I.S.N. contract no. 4.4504.10 and of the *Tournesol* program for financing some of my trips between Brussels and Paris.

CONCERNING THE STRUCTURE OF THIS THESIS

With tens of thousands of PhD students graduating each year throughout the world[†], it should come as no surprise that there are many different ways of writing a PhD thesis, that vary from country to country, from university to university, from laboratory to laboratory – and even from one PhD advisor to the next within a given laboratory.

In the spirit of the earlier theses conducted at the *Service de Chimie Quantique et Photophysique* (CQP) of the *Université Libre de Bruxelles*, this thesis does not assume that its readers have extensive prior knowledge of physical chemistry and explains many notions that more knowledgeable readers are certainly familiar with.

Despite realizing my thesis under a joint supervision between two different countries, I chose to write my thesis in this way for several reasons. First of all, I see the task of explaining my research from the ground-up as an interesting writing exercise and as a fitting end to four years of research. Secondly, I remember feeling very thankful to earlier PhD students, back when I first started my Master Thesis, for having taken the time to write detailed and well-referenced introductions to their works. Additionally, I suspect such introductions may prove more useful than usual since this thesis contains contributions to different domains of physical chemistry: *ab initio* calculations, field-free molecular dynamics, laser control and quantum computing. Although readers familiar with computational chemistry will likely yawn at the perspective of reading about the Hartree-Fock method for the umpteenth time, I suspect many of them might appreciate a short introduction to quantum control and quantum computing if they have no prior experience in these fields.

However, I realize this way of writing may not be ideal for time-pressed readers, who might

[†]See for example: D. Cyranoski, N. Gilbert, H. Ledford, A. Nayar, and M. Yahia. Education: The PhD factory. *Nature*, 472:276–279, 2010. doi:10.1038/472276a.

want to skip straight to the parts presenting the original developments of this work and the results of our calculations. For their convenience, each chapter of this thesis starts with a short introduction detailing its structure and mentioning the number of the pages where the results sections begin.

Additionally, the PDF version of this thesis is hypertext-enabled: text written in blue may be clicked to reach the corresponding part of this work or the corresponding external webpage (as illustrated for example by the footnote on the previous page). A direct link to references through the DOI system is given whenever possible to facilitate the consultation of the works given in reference of this thesis.

Good reading to all!

Stéphane Vranckx

TABLE OF CONTENTS

LIST OF PUBLICATIONS

– D. Sugny, S. Vranckx, M. Ndong, O. Atabek and M. Desouter-Lecomte. External constraints on optimal control strategies in molecular orientation and photofragmentation: role of zero-area fields. *Journal of Modern Optics*, 2013. doi:10.1080/09500340.2013.844281

– S. Vranckx, J. Loreau, M. Desouter-Lecomte and N. Vaeck. Determination of photodissociation and radiative association cross sections from the same time-dependent calculation. *Journal of Physics B* 46:155201, 2013. doi:10.1088/0953-4075/46/15/155201

– J. Loreau, S. Vranckx, M. Desouter-Lecomte, N. Vaeck and A. Dalgarno. Photodissociation and radiative association of HeH^+ in the metastable triplet state, *Journal of Physical Chemistry A* 117:9846, 2013. doi:10.1021/jp312007q

– S. Vranckx, A. Jaouadi, P. Pellegrini, L. Bomble, N. Vaeck and M. Desouter-Lecomte. Implementing quantum gates and algorithms in ultracold polar molecules, *Advances in Atom and Single Molecule Machines* 279, 2013. doi:10.1007/978-3-642-33137-4_21

– E. Cauët, T. Carette, C. Lauzin, J. G. Li, J. Loreau, M. Delsaut, C. Nazé, S. Verdebout, S. Vranckx, M. Godefroid, J. Liévin and N. Vaeck. From atoms to biomolecules: a fruitful perspective. *Theoretical Chemistry Accounts*, 131:1254, 2012. doi:10.1007/s00214-012-1254-3

– P. Pellegrini, S. Vranckx and M. Desouter-Lecomte. Implementing quantum algorithms in hyperfine levels of ultracold polar molecules by optimal control. *Physical Chemistry Chemical Physics*, 13:18864, 2011. doi:10.1039/C1CP21184F

LIST OF TABLES

LIST OF FIGURES

UNITS USED IN THIS WORK

Unless otherwise explicitly noted, all results shown in this thesis are expressed in *atomic units* (a.u.):

Table 1: Conversion factors from atomic to S.I. units [1].

Dimension	Atomic unit definition	Value in S.I. units	
Mass	m_{e^-}	9.1096×10^{-31}	kg
Electrical Charge	e	1.6022×10^{-19}	C
Length	$a_0 = \dfrac{4\pi\epsilon_0\hbar^2}{m_{e^-}\, e^2}$	5.2918×10^{-11}	m
Energy	$E_h = \dfrac{m_{e^-}\, e^4}{(4\pi\epsilon_0\hbar)^2}$	4.3597×10^{-18}	J
Electric field	$\dfrac{m^2\, e^5}{\hbar^4}$	5.1422×10^{11}	V·m^{-1}
Time	$\dfrac{\hbar}{E_h}$	2.4189×10^{-17}	s
Dipole moment	$e\, a_0$	8.4784×10^{-30}	C·m

In this Table, m_{e^-} is the rest mass of the electron, e is its charge and $\hbar = h/2\pi$ is the reduced Planck constant. The atomic unit of energy is also called *hartree*, a term which we will use instead of "a.u." to avoid possible confusion with other dimensions. For the same reason, "a_0" will be used to refer to atomic units of length.

Since e, m_{e^-}, $\hbar$ and $4\pi\epsilon_0$ are all equal to 1 in atomic units, these factors will often be omitted in this work for the sake of readability.

Energies will occasionally be expressed in electronvolt (eV) or cm^{-1}:

Table 2: Energy conversion factors [1].

	hartree	eV	cm^{-1}	J
hartree	1	27.2114	219474.63	4.3597×10^{-18}
eV	3.6749×10^{-2}	1	8065.73	1.6021×10^{-19}
cm^{-1}	4.5563×10^{-6}	1.2398×10^{-4}	1	1.9863×10^{-23}
J	2.2937×10^{17}	6.2418×10^{18}	5.0344×10^{22}	1

CHAPTER

1

INTRODUCTION

1.1 Context of this work

In this thesis, we theoretically study the properties of small molecular systems and their control using laser fields.

This work stands at the crossroads of three scientific domains. The first is of course *Chemistry*, as we study the properties and dynamical behaviour of molecules. However, it could also be argued to belong to *Physics*, as we study very small molecular systems and their interaction with electromagnetic radiation: the fine line between physical chemistry and chemical physics tends to become blurred at this scale. Last but not least, our work also relates to *Computer science* as it not only uses computational techniques to describe the static and dynamic properties of small molecules but also explores the potential role of such systems in quantum computing.

Both computational chemistry and quantum computing are currently booming fields, as illustrated by the attribution of the 2012 Nobel Prize in Physics to Serge Haroche and David Wineland "*for ground-breaking experimental methods that enable measuring and manipulation of individual quantum systems*", as well as of the 2013 Nobel Prize in Chemistry to Martin Karplus, Michael Levitt and Arieh Warshell "*for the development of multiscale models for complex chemical systems*".

This thesis was realized under a joint supervision between the *Service de Chimie Quantique et Photophysique* (CQP) of the *Université Libre de Bruxelles* and the *Laboratoire de Chimie Physique* (LCP) of the *Université Paris-Sud*. It partly expands on previous works realized in both laboratories: the in-depth study of the hydrohelium cation started by Jérôme Loreau [2–5], as well as the dynamical and quantum control simulations of the LCP's *ThéoSim* group [6–10].

1.2 Structure of this work

This thesis is split into seven parts:

- The rest of this introductory chapter will be composed of a discussion of the reasons that led us to study certain diatomic molecules in particular, followed by a short introduction to the theoretical description of molecular systems.
- In the second chapter (p. 45), we will present some of the quantum chemical methods used to describe molecular properties for fixed geometries of the nuclei and the results we obtained therewith for the dications HeH^+ and CO^{2+}.
- The third chapter (p. 77) will be dedicated to the theoretical description of nuclear dynamics and its application to the computation of photodissociation and radiative association cross sections for these two molecules.
- In the fourth chapter (p. 113), we will go one step further in the description of the nuclear dynamics by not only including the effect of an external electric field on the nuclear dynamics, but also by showing how this field can be optimized to guide the dynamics towards a desired outcome. We more precisely optimize laser fields that guide the photodissociation of HeH^+ and CO^{2+} towards specific channels and introduce a constraint that minimizes the area of the fields.
- The fifth chapter (p. 157) will focus on one of the potential applications of these quantum control methods: the use of molecular systems as quantum computers. The results of our simulations of the implementation of the Grover quantum search algorithm on trapped $^{41}K^{87}Rb$ molecules will be detailed.
- Finally, the sixth and last chapter (p. 187) will expose the conclusions of our work and its perspectives.
- Additional details as well as a summary of this work in French are given in the appendix (p. 191).

1.3 Selection of the molecular systems

1.3.1 Why diatomic molecules?

Since its initial formulation in 1965, Moore's empirical law [11] describing the evolution as a function of time of the number of components per integrated circuit (at fixed cost) has thus far been relatively well verified: as it is often paraphrased, the computing power available for a given cost has been following an exponential augmentation since 1959 at least, roughly doubling every two year. This steady rise in computing power has progressively been opening new ventures of study for computational chemistry, allowing for an increasingly accurate description of bigger and bigger systems. However, although very impressive calculations have been

realized for large molecules, it is well-known that the complexity of such calculations and the computation time they require increase exponentially with the number of degrees of freedom of the considered system. Moreover, the accurate description of even small molecular systems remains challenging, depending on the level of accuracy one wishes to reach. Indeed, the accurate description of a system as small as a single, non-hydrogenoid isolated atom with spectroscopic accuracy is very far from trivial, as illustrated by the still ongoing efforts of the theoretical atomic physics community (see for example Refs. [12, 13] for recent works on atoms with few electrons or few valence electrons).

In this thesis, we work on the smallest possible molecular systems: diatomic molecules. The choice of such small molecular system allows us to push the accuracy of the theoretical description further than for larger systems, which is essential in quantum control using laser fields, as the properties of the optimized fields are highly sensitive to the *ab initio* data. In a recent review article, Brif, Chakrabarti and Rabitz go as far as stating that "*an objective assessment is that models used for polyatomic molecules in control computations are currently too simplified and computational techniques are inadequate for the true levels of complexity, resulting in theoretical designs that are not directly applicable to control experiments that work with real systems*" [14] (the current state of the art in quantum control and the experimental predictability of pulses optimized theoretically will be further discussed in the fourth chapter).

In this work, we more specifically study three diatomic molecules, chosen on the basis of their properties and of their importance in astrophysical environments, laboratory plasmas and quantum control experiments: the hydrohelium cation HeH^+, the carbon monoxide dication CO^{2+} and the polar alkali molecule $^{41}K^{87}Rb$.

1.3.2 The hydrohelium cation HeH^+

The hydrohelium cation HeH^+, also called *helium hydride ion* and *hydrohelium*(1+), is a species of interest because of its relative simplicity and its role in plasmas, both in the context of astrochemistry and of laboratory plasmas.

From a theoretical point of view, the simplicity of HeH^+ makes it attractive for accurate *ab initio* calculations: it is only constituted of two nuclei and two electrons and, in its ground state, it is the simplest closed-shell heteronuclear ion. This led to numerous computational chemistry studies of the properties of its ground state in the last decades, starting with the computation of its potential energy curve by Anex [15] in 1963, later expanded upon by Kołos and Peek [16] as well as Bishop and Cheung [17]. This culminated with the computation of its pure vibrational spectrum by Stanke *et al.* in 2006, which shows exceptional agreement with experimental measurements [18].

The excited states of HeH^+ have also been the subject of several publications. In the 1970s, Green *et al.* published an *ab initio* study of the singlet and triplet Σ, Π and Δ excited states of HeH^+ up to $n = 3$[†] [19–22]. Loreau *et al.* recently expanded this work by considering excited

[†]For convenience, we will often characterize the electronic states of HeH^+ by the highest value of the principal quantum number n of the corresponding atomic fragments.

states up to $n = 4$ and internuclear distances between the H and He nuclei up to $R = 200$ atomic units [2]. Unless otherwise noted, all *ab initio* data for HeH^+ used in this work comes from the calculations of Loreau *et al.*, as detailed in Chapter 2.

The theoretical study of HeH^+ by the *Service de Chimie Quantique et Photophysique* and the *Laboratoire de Chimie Physique* was in part motivated by its potential role in the diagnostic of laboratory plasmas, such as those that will be created in the ITER[†] nuclear fusion reactor. The spectroscopic study of the emission lines from impurity ions such as helium indeed allows insight into the properties of such plasmas, but the interpretation of this data requires a good understanding of the interactions between the impurities and the main constituents of the plasmas. Charge transfer reactions between H and He^+ are of particular interest in that respect [23, 24], leading to an in-depth dynamical study by Loreau *et al.* of the charge transfer between $He^+(1s)$ and H between 0.1 and 100 eV, using a quasimolecular approach based on the *ab initio* data calculated for HeH^+ [4].

HeH^+ is also a species of interest in astrochemistry: not only is it constituted of the two most abundant atoms in the universe, hydrogen and helium, it is also believed to be the first molecular ion to have formed in the universe, by radiative association of H^+ and He [25–27]:

$$He + H^+ \rightarrow HeH^+ + h\nu. \tag{1.1}$$

Moreover, HeH^+ is predicted to be formed in certain regions of space with high enough fractional abundances to be observable [28], for example in certain nebulæ [29] such as NGC7027 [25, 30], in supernovæ [31], and in metal-poor stars [32] (helium-rich white dwarfs in particular [33]). Every attempt of extra-terrestrial observation of this cation so far has however proven inconclusive at best [34, 35], which may in part be due to the fact that its $J = 1$–0 rotational line coincides with a rotational line of CH [36]. The recent announcement of the first detection of a noble gas molecular ion in space, $^{36}ArH^+$ [37], makes the apparent absence of HeH^+ all the more surprising.

Although HeH^+ has been observed in laboratory plasmas as early as 1925 [38] and has been the subject of numerous experimental studies [39–42], it continues to elude astronomical observations even today. Such experimental studies have however brought attention to the properties of its $a\,^3\Sigma^+$ state [39, 40], which is metastable as its radiative decay toward the ground $^1\Sigma^+$ state is spin-forbidden. Its radiative lifetime was computed by Loreau *et al.* and found to be as high as 149 s in its lowest rovibrational level, suggesting HeH^+ might be detectable in this state in astrophysical environments where the collision rate is low [3].

In this thesis, we first pursue the work started by Loreau *et al.* by investigating the astrochemistry of HeH^+ in its first two triplet states. We compute the cross sections characterizing their destruction by photodissociation and their formation by radiative association, with a particular focus on the methodological aspects of the extraction of both cross sections from a single dynamical calculation. We then theoretically optimize laser pulses that guide the photodissoci-

[†] *International Thermonuclear Experimental Reactor.*

ation of HeH^+ towards specific channels, expanding on the work started by Bomble *et al.* [43]: despite the deceptive apparent simplicity of HeH^+, its dynamics is nontrivial due to the large role played by nonadiabatic couplings, making it a good test case for quantum control. The fields are optimized using Local Control Theory and Optimal Control Theory, with a new constraint that minimizes the total field area.

1.3.3 The carbon monoxide dication CO^{2+}

The CO^{2+} dication, or CO_{III}, is another diatomic ion of interest in several fields of research. It also bears historical importance in the study of dication properties as it was the first molecular dication to ever be discovered, in 1930 [44][†].

At first glance, the metastability of diatomic dications AB^{2+} can seem surprising. Yet as early as 1933, a few years only after the first detection of CO^{2+}, quantum chemistry pioneer Linus Pauling published the first theoretical prediction of a metastable dication, He_2^{2+} [46], showing the characteristic potential energy curve that all "kinetically stable"[‡] dications share (1.1). At large internuclear distances, Coulombic repulsion dominates, but at short distances, chemical bonding actually occurs, stabilizing the doubly charged molecular species. The net result of the two phenomena is a (usually shallow) potential energy well situated above the dissociation limit into $A^+ + B^+$ [48].

Since the laws of quantum mechanics allow tunneling through potential energy barriers, such states are not stable and so-called "kinetically-stable" molecular dications spontaneously dissociate into their constitutive fragments. Their lifetime however strongly varies from one species to another and from one rovibrational level to another: the energy barrier is smaller for excited rovibrational levels, leading to shorter lifetimes. In the case of CO^{2+}, the lifetime of all vibrational levels of the ground $X\ ^3\Pi$ state was found to be shorter than a microsecond, except one: the $v = 0$ level, which has an estimated lifetime of several seconds at least [49]. This characteristic makes it a very interesting species for laser control experiments, as it means that CO^{2+} can be obtained in a vibrationally pure state instead of a mixture of several vibrational states at once.

This constitutes the main reason of our choice of CO^{2+} as a test system for our quantum control simulations, as the group of experimenters of X. Urbain at the *Université catholique de Louvain*, who previously studied the formation of CO^{2+} by electron impact on CO^+ [50], has expressed a strong interest in performing laser control experiments on CO^{2+} in the near future.

Moreover, dications are thought to play an important role in various astrochemical media. The carbon dioxide dication CO_2^{2+}, which has a measured lifetime of 4.2 seconds [51], has for example been predicted to be one of the constituents of the high atmosphere of Mars and

[†] J. J. Thomson's 1921 *Rays of Positive Electricity* is sometimes also cited as the first published detection of a dication. However, although Thomson does mention doubly charged compounds as a possible source of some of its experimental data, he does not appear to unequivocally detect and identify one [45].

[‡] Dications AB^{2+} can be divided in two categories: *kinetically stable* dications whose lowest state is metastable and dissociates into $A^+ + B^+$, as shown in Fig. 1.1, and *thermodynamically stable* dications, whose lowest state is bound and dissociates into $A^{2+} + B$ (see Ref. [47] for a comparison). CO^{2+} belongs to the former category.

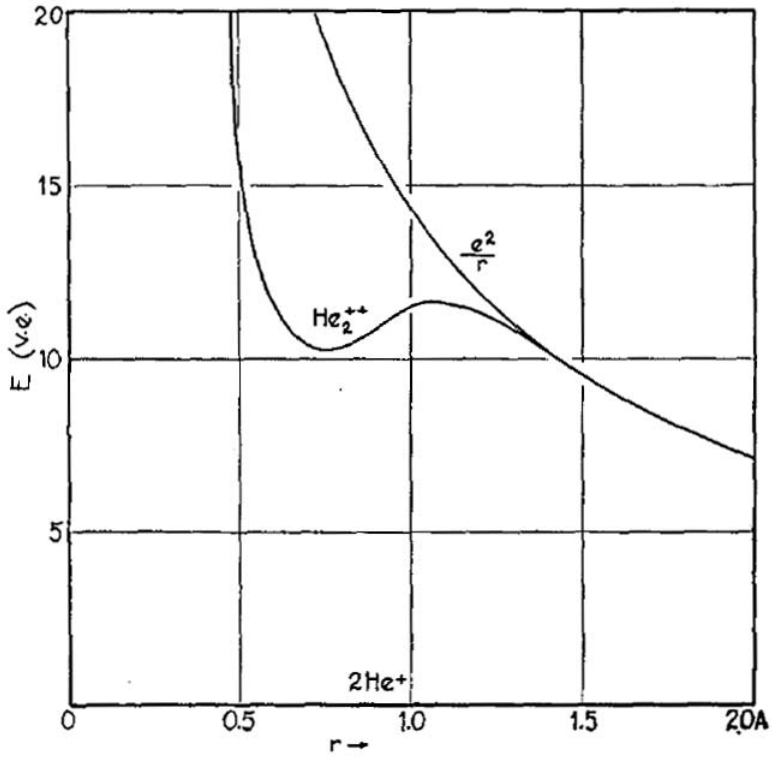

Figure 1.1: The potential energy curve of the He_2^{2+} dication as published in Pauling's 1933 paper [46]. He comments, "(...) *at large distances, the two He^+ ions repel each other with the force e^2/r^2; at about 1.3 Å, the resonance interaction of the electrons becomes important, causing the force to become attractive at about 1.1 Å, and leading to the formation of a molecule* (...)".

Venus [52, 53]. Other dications of carbon-containing species, such as fullerenes and polycyclic aromatic hydrocarbon [54], have been predicted to be present in the interstellar environment.

Additionally, neutral carbon monoxide CO is the most abundant interstellar molecule after H_2 [55]. It is often used as a reference to estimate H_2 abundances on the basis of presumed CO/H_2 abundance ratios: even at low temperature, it can be detected thanks to its $J = 1$–0 emission line, contrarily to molecules such as H_2 that have no permanent dipole moment and therefore no rotational spectrum. Its monocation CO^+ is also known to be present in planetary atmospheres (not only that of Earth's but also those of Mars, Venus, ...), stellar atmospheres, comet tails, planetary nebulæ (such as NGC 7027) and in interstellar space [56]. It is therefore thought that the dication CO^{2+} is very likely to be also present in space in sufficient quantities to allow its remote detection [57].

From a quantum chemist's point of view, diatomic dications in general are interesting due to their high density of electronic states dissociating into either two singly-charged ionic fragments or an atomic dication and a neutral atom, leading to many avoided and/or unavoided crossing [58]. Like HeH^+, CO^{2+} therefore features important nonadiabatic couplings, making its dynamic nontrivial – with the added peculiarity that its ground electronic state is metastable. The simulation of its photodissociation dynamics and of its control are therefore of interest.

Although several experimental [59–66] and theoretical [67–69] studies of CO^{2+} have been

realized, none have focused on its photodissociation in highly excited $^3\Sigma^-$ channels. In this work, we compute the potential energy curves, nonadiabatic couplings and permanent dipole moment of the $X\,^3\Pi$ and of the 11 first $^3\Sigma^-$ channel of CO^{2+}, as well as the corresponding transition dipole moments (the majority of these states had never been described theoretically before). This *ab initio* data is then used to compute the $X\,^3\Pi \rightarrow ^3\Sigma^-$ photodissociation cross sections of CO^{2+} for the first time as well as laser fields that enhance its dissociation in the C^{2+} + O fragments. As in the case of HeH^+, we use both Local Control and Optimal Control Theory to achieve this goal, with emphasis on the determination of fields that have an area equal to zero.

1.3.4 The diatomic polar molecule $^{41}K^{87}Rb$

Among the many molecular systems considered as potential candidates for quantum computing (see Chapter 5), trapped polar molecules stand among the most promising candidates [70] because of their long decoherence time and their strong dipole-dipole interaction. Moreover, ultracold $^{41}K^{87}Rb$ molecules can be obtained in their absolute lowest energy level and trapped [71–74].

The reasoning behind the choice of ultracold diatomic polar molecules and of KRb in particular as a support for quantum information will be further detailed in Chapter 5, after we have explained the basic principles of quantum computing and the essential properties a physical system has to possess to be used to encode and process quantum information.

The main properties of the three systems studied in this work are summarized in Table 1.1.

Table 1.1: Main properties of the systems studied in this work, with masses expressed in dalton (1 Da = 1.66×10^{-27} kg).

	Nuclei	Electrons	Mass	Reduced mass
$^4He^1H^+$	2	2	5	$\frac{4}{5}$
$^{12}C^{16}O^{2+}$	2	12	28	$\frac{192}{28}$
$^{41}K^{87}Rb$	2	56	128	$\frac{3567}{128}$

Note: The rest of this chapter is dedicated to a short introduction to the theoretical description of diatomic molecular systems. Readers already familiar with the subject may want to skip either to the beginning of Chapter 2 (p. 45) or straight to the results of our calculations, in Section 2.3 (p. 53).

1.4 Theoretical description of molecular systems

Because of their small size, molecules are quantum systems. Their behavior is therefore governed by the central equation of quantum mechanics, the *time-dependent Schrödinger equation*:

$$i\hbar\frac{\partial}{\partial t}\Psi(\mathbf{r},t) = H\Psi(\mathbf{r},t). \tag{1.2}$$

It contains the two physical quantities that are essential to the theoretical description of quantum systems:

1. the *wavefunction* $\Psi(\mathbf{r},t)$, a function from which properties of the system such as the electron probability density can be obtained;
2. the *Hamiltonian operator* H, the mathematical operator whose eigenvalue is the energy of the system.

It is worth remarking that the Schrödinger equation is an ordinary and linear first-order differential equation in t, which means that if the value of the wavefunction $\Psi(\mathbf{r},t_0)$ is known at some time t_0, its values at all other times can be determined [75]. Furthermore, if the Hamiltonian of the system is time-independent, the Schrödinger equation admits a series of solutions $\Psi_n(\mathbf{r},t)$ corresponding to *stationary states*, whose properties such as their energy E_n are independent of time. Since the spatial variables $\mathbf{r}$ and the time variable t are independent from each other, the wavefunction can be written as:

$$\Psi_n(\mathbf{r},t) = \phi_n(t)\psi_n(\mathbf{r}). \tag{1.3}$$

Inserting this in the time-independent Schrödinger equation (Eq. 1.2) leads to two very important results. The first is the *time-independent Schrödinger equation*:

$$H\psi_n(\mathbf{r}) = E_n\psi_n(\mathbf{r}). \tag{1.4}$$

The second is the differential equation:

$$i\hbar\frac{\partial}{\partial t}\phi_n(t) = E_n\phi_n(t), \tag{1.5}$$

whose solution gives the time-dependence of the stationary states:

$$\phi_n(t) = e^{-iE_nt/\hbar}. \tag{1.6}$$

The wavefunction of stationary states can thus be written as

$$\Psi_n(\mathbf{r},t) = e^{-iE_nt/\hbar}\psi_n(\mathbf{r}). \tag{1.7}$$

Although this wavefunction obviously depends on t, it is important to note that the properties that derive from it, such as the energy or the probability density, are independent of time.

1.4.1 Dynamics of molecular systems

How, then, can the time evolution of a quantum system be described? Let us now consider a wavefunction that is composed of a linear superposition of stationary states:

$$\Psi_n(\mathbf{r},t) = \sum_n c_n \, e^{-iE_n t/\hbar} \, \psi_n(\mathbf{r}). \tag{1.8}$$

This kind of wavefunction, called a *wavepacket*, has explicit time-dependence. The propagation of wavepackets in time and the extraction of chemically relevant data from their behaviour will be discussed in Chapter 3 (p. 77). Let us just state for now that studying the time evolution of wavepackets can give us a very intuitive view of the dynamics of quantum systems.

It is however important to note that the same information can be obtained from the evolution of the time-dependent wavepacket $\Psi_n(\mathbf{r},t)$ and from solving the time-independent Schrödinger equation, provided the Hamiltonian is independent of time. Two formalisms thus exist to describe dynamical processes: the *time-dependent formalism*, where the time evolution of the system is described explicitly by simulating the evolution of its wavepacket in time to obtain information about its dynamics; and the *time-independent* formalism, where the same information is obtained by solving the time-independent Schrödinger equation through coupled-channel or algebraic methods (see Ref. [76] for an overview of time-dependent and time-independent methods).

Historically, dynamical problems were first described using the time-independent formalism, as it tends to require less computational resources. However, both methods have advantages and drawbacks; the best method to use therefore depends on the kind of system studied. In this work, we use the time-dependent formalism as it allows an intuitive and detailed look into the dynamics and can be used even in cases where the Hamiltonian is time-dependent, such as when we consider molecules exposed to laser fields. It is therefore necessary to use a time-dependent approach when optimizing laser control fields to guide the dynamics of molecular systems, as discussed in Chapters 4 and 5.

1.4.2 Hamiltonian operator for molecular systems

The theoretical description of a molecule first requires finding the expression of its Hamiltonian H. Its general form is the sum of the kinetic and potential energy operators for the considered system:

$$H = T + V \tag{1.9}$$

Since a molecule is composed of electrons and nuclei, its Hamiltonian can be further decomposed into the following terms:

$$H = T^{\mathrm{N}} + T^{\mathrm{e}} + V^{\mathrm{NN}} + V^{\mathrm{eN}} + V^{\mathrm{ee}}, \tag{1.10}$$

where T^{N} and T^{e} are the kinetic energy of the nuclei (N) and electrons (e) while V^{NN}, V^{eN} and

V^{ee} represent the Coulomb interaction potential terms: the electronic repulsion between the nuclei, the attraction between the electrons and the nuclei, and the repulsion between the electrons, respectively.

For a molecule composed of N nuclei with coordinates $\mathbf{R}_1, \mathbf{R}_2, ...\mathbf{R}_N$ and masses $M_1, M_2, ...M_N$ as well as n electrons with coordinates $\mathbf{r}_1, \mathbf{r}_2, ...\mathbf{r}_n$, the general form of the Hamiltonian is thus:

$$\begin{aligned} H = &- \sum_{i=1}^{N} \frac{\hbar^2}{2M_i} \nabla^2_{\mathbf{R}_i} - \sum_{i=1} \frac{\hbar^2}{2m_{e^-}} \nabla^2_{\mathbf{r}_i} + \sum_{i=1}^{N} \sum_{j=i+1}^{n} \frac{Z_i Z_j e^2}{4\pi\epsilon_0 |\mathbf{R}_i - \mathbf{R}_j|} \\ &- \sum_{i=1}^{N} \sum_{j=1}^{n} \frac{Z_i e^2}{4\pi\epsilon_0 |\mathbf{R}_i - \mathbf{r}_j|} + \sum_{i=1}^{n} \sum_{j=i+1}^{n} \frac{e^2}{4\pi\epsilon_0 |\mathbf{r}_i - \mathbf{r}_j|}, \end{aligned} \tag{1.11}$$

where ∇^2 is the Laplacian $\nabla^2 = \frac{\partial}{\partial x^2} + \frac{\partial}{\partial y^2} + \frac{\partial}{\partial z^2}$ (with x, y and z being either the Cartesian coordinates $\mathbf{r}$ of the electrons or $\mathbf{R}$ of the nuclei). For convenience, we will use atomic units throughout this work (see page 23) so that $\hbar$, m_{e^-}, $4\pi\epsilon_0$ and e are all strictly equal to 1. Let us also introduce the variables r_{ij} to represent the distances between two particles i and j (be them electrons or nuclei):

$$\begin{aligned} H = &- \sum_{i=1}^{N} \frac{1}{2M_i} \nabla^2_{\mathbf{R}_i} - \sum_{i=1} \frac{1}{2} \nabla^2_{\mathbf{r}_i} + \sum_{i=1}^{N} \sum_{j=i+1}^{n} \frac{Z_i Z_j}{r_{ij}} \\ &- \sum_{i=1}^{N} \sum_{j=1}^{n} \frac{Z_i}{r_{ij}} + \sum_{i=1}^{n} \sum_{j=i+1}^{n} \frac{1}{r_{ij}}. \end{aligned} \tag{1.12}$$

The Schrödinger equation for molecules can thus be written as

$$(T^{\text{N}} + T^{\text{e}} + V^{\text{NN}} + V^{\text{eN}} + V^{\text{ee}})\Psi(\mathbf{r}, \mathbf{R}) = E\Psi(\mathbf{r}, \mathbf{R}), \tag{1.13}$$

where $\Psi(\mathbf{r}, \mathbf{R})$ is the total molecular wavefunction. Computational chemists usually split the molecular Hamiltonian into two parts: the nuclear kinetic energy T^{N} on one side and the *electronic Hamiltonian* H^{el} as well as the nuclear Coulombic repulsion V^{NN} on the other:

$$H = \underbrace{T^{\text{N}}}_{\text{Reaction dynamics}} + \underbrace{V^{\text{NN}} + H^{\text{el}}}_{\text{Electronic structure}}, \tag{1.14}$$

with

$$H^{\text{el}} = T^{\text{e}} + V^{\text{eN}} + V^{\text{ee}}. \tag{1.15}$$

Note that two conventions coexist in the definition of the electronic Hamiltonian H^{el}, with some authors choosing to include the nuclear repulsion potential V^{NN}, although it is a purely "nuclear" term that does not depend on the coordinates of the electrons (compare for example two widely-used reference books, *Physics of Atoms and Molecules* [75] by Bransden and Joachain with Jensen's *Introduction to Computational Chemistry* [77]). This is however a simple matter of convention and, as we will see in Section 2.1, it makes a lot of sense to regroup V^{NN} with the

electronic terms, as each electron can be thought of as evolving in an electric field generated by the other electrons *and* the nuclei.

1.4.3 The Born-Oppenheimer approximation

The first step in most theoretical descriptions of molecular systems is the *Born Oppenheimer-Approximation* [78, 79]. Since the electrons are thousands of times lighter than the nuclei ($m_{\mathrm{p}^+} \approx 1836\ m_{\mathrm{e}^-}$), it seems reasonable to assume that they move much faster than the nuclei and thus adjust *instantaneously* to any change in their positions.

Under this assumption, the theoretical description of a molecular system can be split into two successive steps:

1) the resolution of the electronic part of the problem for fixed geometries of the nuclei;

2) the description of the nuclear motion based on these results.

Let us first write the Schrödinger equation *for the electrons only*, by neglecting the kinetic energy of the nuclei, T^{N}:

$$\left(H^{\mathrm{el}} + V^{\mathrm{NN}}\right) \Psi_j^{\mathrm{el\ adia}}(\mathbf{r},\mathbf{R}) = E_j^{\mathrm{el\ adia}}(\mathbf{R})\ \Psi_j^{\mathrm{el\ adia}}(\mathbf{r},\mathbf{R}), \tag{1.16}$$

where $\Psi_j^{\mathrm{el\ adia}}$ is the *adiabatic electronic wavefunction* of the electronic state j and $E_j^{\mathrm{el\ adia}}(\mathbf{R})$ is its adiabatic potential energy. Note that the index j we use here is meant to designate each electronic state unequivocally, it can be seen as shorthand for a set of indexes characterizing the spatial symmetry and the spin of the state considered, as will be introduced in Section 1.6.

By solving Eq. 1.16 for different fixed geometries of the nuclei (*i.e.* different values of coordinates $\mathbf{R}$), the *potential energy (hyper)surfaces* of the considered electronic state are obtained[†]. In the case of diatomic molecules, only one coordinate needs to be considered: the internuclear distance R between the two nuclei, which means the electronic energy of each state is characterized by a one-dimensional *potential energy curve*. These energy (hyper)surfaces or curves can be seen as an effective potential created by both the electrons and the nuclei, in which the nuclei move according to the time-dependent nuclear Schrödinger equation.

E^{el} is however not the only energy term that must be taken into account: contributions arising from the nuclear part of the total Schrödinger equation must also be included:

$$E = E^{\mathrm{el}} + E^{\mathrm{N}}. \tag{1.17}$$

The adiabatic electronic wavefunctions $\Psi_j^{\mathrm{el\ adia}}(\mathbf{r},\mathbf{R})$ are orthonormal and form a complete set[‡]. We can thus express the total molecular wavefunction $\Psi(\mathbf{r},\mathbf{R})$ as:

[†] Note that in this context, $\mathbf{R}$ and $\mathbf{r}$ have very different status: the coordinates of the nuclei $\mathbf{R}$ are treated as parameters while the coordinates of the electrons $\mathbf{r}$ are treated as variables.

[‡] For the sake of readability, we will usually omit the "adia" index in the rest of this work.

$$\Psi(\mathbf{r},\mathbf{R}) = \sum_j \Psi_j^{\mathrm{N}}(\mathbf{R})\ \Psi_j^{\mathrm{el\ adia}}(\mathbf{r},\mathbf{R}), \tag{1.18}$$

where $\Psi_j^{\mathrm{N}}(\mathbf{R})$ are the nuclear wavefunctions and only depend on the coordinates $\mathbf{R}$ of the nuclei. This separation allows the resolution of the electronic and nuclear motions separately.

1.4.3.1 Nuclear motion

Let us focus for a moment on the motion of the nuclei and on the associated nuclear kinetic energy operator T^{N}. The nuclear motion of a molecule composed of N nuclei possesses $3N$ degrees of freedom, that can be divided in three categories:

- 3 translational degrees of freedom, which correspond to concerted translations of the nuclei in space along the x, y and z axes of the Cartesian laboratory-fixed frame.
- 2 or 3 rotational degrees of freedom (depending on whether the molecule is linear or not), which correspond to the rotation of the molecule around the x, y (and z for non-linear molecule) axes of the laboratory frame.
- $3N-5$ or $3N-6$ vibrational degrees of freedom, which correspond to variations of the internuclear distance(s), *i.e. internal* motions of the molecule.

Studying the translational motion of the nuclei is of little interest to quantum chemists, who therefore use a coordinate system centered on the center of mass of the molecule to separate the global movements of its nuclei from their relative motion[†].

Moreover, it is convenient to use internal coordinates such as bond lengths, angles between two bonds and torsion angles to describe the internal motions of the nuclei instead of the positions $\mathbf{R}_i$ of each individual nucleus. In the case of diatomic molecules, which are only composed of two nuclei, a single scalar coordinate $R = |\mathbf{R}_1 - \mathbf{R}_2|$ is sufficient to describe the molecular geometry unequivocally. The developments that follow are given for diatomic molecules, which have two rotational degrees of freedom and a single vibrational degree of freedom.

The nuclear kinetic energy operator itself can be rewritten as the sum of two contributions, by separating the Laplacian of the nuclear coordinates $\nabla^2_{\mathbf{R}_i}$ (expressed in spherical coordinates) into a term that only depends on the internuclear distance R and a term that contains the angular dependence:

$$\begin{aligned} T^{\mathrm{N}} &= T^{\mathrm{vib}} + T^{\mathrm{rot}} \\ &= -\frac{1}{2\mu}\frac{\partial^2}{\partial R^2} + \frac{1}{2\mu R^2}\mathbf{N}^2, \end{aligned} \tag{1.19}$$

[†]Note however that this leads to the appearance of a *mass polarization term* H^{mp} in the Hamiltonian, which arises from the fact that the internal motion and the center of mass motion of a system of more than two particles cannot be rigorously separated. As in most quantum chemistry calculations [77], this term is neglected in the present work.

where $\mu = (M_1\ M_2)/(M_1 + M_2)$ is the reduced mass of the molecule and $\mathbf{N}$ is its nuclear angular momentum. The first term corresponds to vibrational motions and depends on the internuclear distance R only, while the second corresponds to the rotation of the molecule (*i.e.* a rigid rotor, assuming the internuclear distance R is independent of the rotational motion) and contains the angular dependence of the nuclear motion.

Correspondingly, the nuclear wavefunction Ψ^{N} can also be split into a vibrational and a rotational part:

$$\Psi^{\mathrm{N}}(\mathbf{R}) = \Psi^{\mathrm{vib}}\ \Psi^{\mathrm{rot}}. \tag{1.20}$$

Note that Eq. 1.19 only shows the nuclear kinetic operator. To solve the vibrational and rotational Schödinger equations and obtain the energy E^{vib} and E^{rot} of the vibrational and rotational levels, the Hamiltonian operator must not only contain the corresponding kinetic operator but also the potential V, obtained by solving the electronic Schrödinger equation.

For example, assuming a harmonic potential, the vibrational equation leads to the following eigenvalues:

$$E^{\mathrm{vib}} = h\nu\left(v + \frac{1}{2}\right), \tag{1.21}$$

where v is the *vibrational quantum number*. We will discuss the resolution of the vibrational equation for more realistic potentials further in Section 2.2 (p. 53), after having solved the electronic Schrödinger equation to obtain the electronic potential as a function of R.

Similarly, the rotational part of the problem has very simple eigenvalues if a simplified model is used. If we assume that the molecule behaves as a rigid rotor, *i.e.* that the internuclear distance R is independent of the rotational motion, the rotational kinetic operator can be rewritten as [75]:

$$\begin{aligned} T^{\mathrm{rot}} &= \frac{1}{2\mu R^2}\mathbf{N}^2 \\ &= B(R)\ \mathbf{N}^2, \end{aligned} \tag{1.22}$$

where $B(R)$ is called the *rotational constant* of the diatomic molecule[†]. The eigenvalues of $H^{\mathrm{rot}} = T^{\mathrm{rot}} + V$ are the rotational energies E^{rot}. If the molecule behaves as a rigid rotor, they take the form:

$$E^{\mathrm{rot}} = B\ J(J+1), \tag{1.23}$$

where J is the rotational quantum number. If the molecule cannot be approximated by a rigid rotor, additional terms need to be added to take into account the centrifugal distortion.

[†]Note that spectroscopists usually use a slightly different definition of the rotational constant B, that is independent of the internuclear distance R: $B = 1/2\mu R_{\mathrm{e}}^2$, where R_{e} is the equilibrium distance.

In the end, the energy of a molecule in the Born-Oppenheimer approximation is therefore composed of the following sum of terms:

$$E = E^{\text{el}} + E^{\text{vib}} + E^{\text{rot}}, \tag{1.24}$$

to which additional terms linked to the nuclear spins may be added. Although they are often neglected in quantum chemistry because of their small magnitude compared to the others, we will look into them in Chapter 5, when implementing quantum algorithms in the hyperfine levels of molecules exposed to electric and magnetic fields.

1.4.3.2 Diabatic representation

The Born-Oppenheimer approximation led us to neglect the effect of the nuclear kinetic operator T^{N} on the electronic wavefunction $\Psi_j(\mathbf{r},\mathbf{R})$. Now that we have seen the expression of the operator, let us see what this approximation exactly entails.

Let us first insert the expression of the total wavefunction in terms of electronic and nuclear wavefunctions (Eq. 1.18) into the total Schrödinger equation (Eq. 1.13):

$$\left(T^{\text{N}} + H^{\text{el}} + V^{\text{NN}}\right) \sum_j \Psi_j^{\text{N}}(\mathbf{R})\ \Psi_j^{\text{el adia}}(\mathbf{r},\mathbf{R}) = E \sum_j \Psi_j^{\text{N}}(\mathbf{R})\ \Psi_j^{\text{el adia}}(\mathbf{r},\mathbf{R}). \tag{1.25}$$

Multiplying by $\Psi_k^{\text{el}}(\mathbf{r},\mathbf{R})$ on the left and integrating leads to:

$$\sum_j \left\langle \Psi_k^{\text{el}}(\mathbf{r},\mathbf{R}) \,\middle|\, T^{\text{N}} + H^{\text{el}} + V^{\text{NN}} \,\middle|\, \Psi_j^{\text{el}}(\mathbf{r},\mathbf{R}) \right\rangle \Psi_j^{\text{N}}(\mathbf{R}) = E \sum_j \Psi_j^{\text{N}}(\mathbf{R}) \left\langle \Psi_k^{\text{el}}(\mathbf{r},\mathbf{R}) \,\middle|\, \Psi_j^{\text{el}}(\mathbf{r},\mathbf{R}) \right\rangle. \tag{1.26}$$

Since the electronic wavefunctions Ψ_k^{el} are orthonormal and since $H^{\text{el}} + V^{\text{NN}}$ does not act on the nuclear wavefunction, this can be rewritten as:

$$\sum_j \left\langle \Psi_k^{\text{el}}(\mathbf{r},\mathbf{R}) \,\middle|\, T^{\text{N}} \,\middle|\, \Psi_j^{\text{el}}(\mathbf{r},\mathbf{R}) \right\rangle \Psi_j^{\text{N}}(\mathbf{R}) + E_k^{\text{el}} \Psi_k^{\text{N}}(\mathbf{R}) = E\ \Psi_k^{\text{N}}(\mathbf{R}). \tag{1.27}$$

We have seen in Eq. 1.19 that $T^{\text{N}} = -\frac{1}{2\mu}\left(\frac{\partial^2}{\partial R^2} - \frac{\mathbf{N}^2}{R^2}\right)$. Inserting this in Eq. 1.27, developing the second derivative in R then reuniting the terms in $\Psi_k^{\text{N}}(\mathbf{R})$ and $\Psi_j^{\text{N}}(\mathbf{R})$ leads to:

$$\left(-\frac{1}{2\mu}\frac{\partial^2}{\partial R^2} + E_k^{\text{el}} - E\right)\Psi_k^{\text{N}}(\mathbf{R}) - \sum_j \left(\frac{1}{\mu}F_{kj}\frac{\partial}{\partial R} + \frac{1}{\mu}G_{kj} - H_{kj}^{\text{rot}}\right)\Psi_j^{\text{N}}(\mathbf{R}) = 0, \tag{1.28}$$

where:

$$\begin{aligned} H_{kj}^{\text{rot}} &= \frac{1}{2\mu R^2}\left\langle \Psi_k^{\text{el}}(\mathbf{r},\mathbf{R}) \,\middle|\, \mathbf{N}^2 \,\middle|\, \Psi_j^{\text{el}}(\mathbf{r},\mathbf{R}) \right\rangle, \\ F_{kj} &= \left\langle \Psi_k^{\text{el}}(\mathbf{r},\mathbf{R}) \,\middle|\, \frac{\partial}{\partial R} \,\middle|\, \Psi_j^{\text{el}}(\mathbf{r},\mathbf{R}) \right\rangle, \\ G_{kj} &= \left\langle \Psi_k^{\text{el}}(\mathbf{r},\mathbf{R}) \,\middle|\, \frac{\partial^2}{\partial R^2} \,\middle|\, \Psi_j^{\text{el}}(\mathbf{r},\mathbf{R}) \right\rangle. \end{aligned} \tag{1.29}$$

These elements respectively constitute the *nonadiabatic rotational coupling matrix* $\mathcal{H}^{\text{rot}}$ (*i.e.* the matrix of the rotational Hamiltonian from Eq. 1.22), the *first-order nonadiabatic radial coupling matrix* $\mathcal{F}$ and the *second order nonadiabatic radial coupling matrix* $\mathcal{G}$. Some useful properties of the radial couplings are demonstrated in the Appendix on page 191, such as the fact that the matrices $\mathcal{F}$ and $\mathcal{G}$ are linked by the relation:

$$\mathcal{G} = \mathcal{F}^2 + \frac{\partial}{\partial R}\mathcal{F}. \tag{1.30}$$

The elements of matrix $\mathcal{G}$ can thus easily be deduced from those of matrix $\mathcal{F}$.

In the Born-Oppenheimer approximation, all the non-diagonal terms kj of the matrices $\mathcal{H}^{\text{rot}}$, $\mathcal{F}$ and $\mathcal{G}$ are neglected, leading to a set of uncoupled equations (one for each state). Similarly, their diagonal elements jj are usually neglected. This leads to the expression:

$$\left(-\frac{1}{2\mu}\frac{\partial^2}{\partial R^2} + E_k^{\text{el}}\right)\Psi_k^{\text{N}}(\mathbf{R}) = E\Psi_k^{\text{N}}(\mathbf{R}), \tag{1.31}$$

which, if the rotational part of the kinetic energy Hamiltonian T^{N} is neglected, can also be written as:

$$\left(T^{\text{N}} + E_k^{\text{el}}\right)\Psi_k^{\text{N}}(\mathbf{R}) = E\Psi_k^{\text{N}}(\mathbf{R}). \tag{1.32}$$

The Born-Oppenheimer approximation must however be used with caution: the neglect of the couplings can lead to significant errors in the theoretical description of molecules. It can be shown that the radial coupling between two states k and j is inversely proportional to the difference between their energies, as demonstrated in the Appendix on page 192:

$$F_{kj} = \frac{\left\langle \Psi_k^{\text{el}} \middle| \frac{\partial}{\partial R} H^{\text{el}} \middle| \Psi_j^{\text{el}} \right\rangle}{E_k^{\text{el}} - E_j^{\text{el}}}. \tag{1.33}$$

The Born-Oppenheimer approximation is therefore invalid in situations where states have similar energies. For a diatomic molecule, this corresponds to an *avoided crossing*: two states of the same symmetry cannot have the same energy simultaneously, which implies that their potential energy curves cannot cross each other. Note that, although avoided crossings lead to significant radial couplings, non-negligible coupling terms also arise in other situations.

It is therefore important to go beyond the Born-Oppenheimer approximation by taking the nonadiabatic couplings into account, as they significantly affect the behaviour of molecular systems [80]. However, the presence of intense and narrow nonadiabatic couplings such as those associated to nonadiabatic crossing poses difficulties in the numerical resolution of the coupled equations 1.28.

These difficulties can be circumvented by defining a *diabatic basis* of representation such that the nonadiabatic coupling elements $\mathcal{F}$ are strictly equal to zero, thus diagonalizing T^{N}. This is achieved by looking for a matrix $\mathcal{D}$ such that:

$$\frac{\partial}{\partial R}\mathcal{D} + \mathcal{F} \cdot D = 0. \tag{1.34}$$

This transformation matrix allows the re-expression of the adiabatic potential energy curves into the diabatic representation. They indeed correspond to the diagonal elements of the electronic Hamiltonian matrix $\mathcal{H}^{\text{el}}$:

$$E_k^{\text{el}} = V_{kk} = \left\langle \Psi_k^{\text{el}} \middle| \mathcal{H}^{\text{el}} \middle| \Psi_k^{\text{el}} \right\rangle. \tag{1.35}$$

Using the matrix $\mathcal{D}$ found in Eq. 1.34, $\mathcal{H}^{\text{el}}$ can be obtained in the diabatic basis through the following transformation:

$$\mathcal{H}^{\text{el dia}} = \mathcal{D}^{-1}\, \mathcal{H}^{\text{el adia}}\, \mathcal{D}. \tag{1.36}$$

While $\mathcal{H}^{\text{el}}$ was diagonal in the adiabatic picture, this transformation leads to the appearance of non-diagonal elements V_{jk}^{dia}, called the *diabatic couplings*. Choosing to work in a diabatic basis in order to diagonalize T^{N} thus comes at a price: the electronic Hamiltonian H^{el} ceases to be diagonal.

The rotational couplings $\mathcal{H}^{\text{rot dia}}$ can similarly be obtained in the diabatic basis through the relation:

$$\mathcal{H}^{\text{rot dia}} = \mathcal{D}^{-1}\, \mathcal{H}^{\text{rot}}\, \mathcal{D}. \tag{1.37}$$

The diabatic rotational couplings matrix $\mathcal{H}^{\text{rot dia}}$ is then added to the diabatic electronic Hamiltonian matrix $H^{\text{el dia}}$. A new adiabatic basis that takes the rotation couplings into account is then obtained by re-diagonalizing the H^{el}.

Note that Eq. 1.34 can admit multiple solutions. The standard diabatic representation is the one which coincides with the adiabatic representation for large internuclear distance [80], thus ensuring that the passage to the diabatic representation does not affect the energy of the atomic fragments. This is achieved by imposing the initial condition:

$$\lim_{R \to +\infty} \mathcal{D} = \mathcal{I}, \tag{1.38}$$

where $\mathcal{I}$ is the identity matrix, with elements $I_{ij} = \delta_{ij}$. Note that, once again, the development shown here is only valid for diatomic molecules and that more complex schemes are required for polyatomic molecules, as illustrated for example by the works of Prof. Baer on the subject [81–83].

1.5 Cross sections and rate constants

In Chapter 3 of this work, we use time-dependent calculations to compute two physical quantities that characterize the dynamics of chemical reactions: *rate constants* and *cross sections*.

In chemistry, reactions are usually characterized by *rate constants* $k(T)$, which provide a direct link between the rate of a reaction and the concentrations of the compounds it involves, as a function of temperature. Although rate constants are very useful, they only characterize reactions on a macroscopic scale: they result from a very large number of microscopic events with a wide distribution of parameters such as reactant collision geometry, initial internal excitation level and relative kinetic energy.

To describe how reactions occur at the scale of individual molecules, a microscopic parameter is required: the *reaction cross section* σ [75]. This physical quantity represents the reaction probability as a function of energy (typically, the relative kinetic energy between the two colliding reactants, or the energy of the incident photon in photoinitiated reactions) and as a function of other possible parameters, such as the collision angles θ and ϕ in the case of *differential cross sections*. The term "cross section" derives from the classical picture, where it represents the characteristic surface of the collision between two reactants in a hard sphere model. It is therefore expressed in units of area (typically cm^2 or Bohr radius squared a_0^2).

Knowing the value of the cross section for a given reaction as a function of the energy, as well as the energy distribution corresponding to the physical conditions in which the reaction occurs, the correspond rate constant can easily be determined, as will be shown in Section 3.2.1.2 and 3.2.2.2 for photodissociation and radiative association reactions (p. 85 and p. 90, respectively).

1.6 Symmetry properties of heteronuclear diatomic molecules

Group theory plays a crucial role in the theoretical description of molecules, as many of their properties are intrinsically linked to their symmetry. For example, whether an electronic dipole transition between two electronic states is permitted or forbidden depends on their spatial symmetry and their spin.

Heteronuclear diatomic molecules have a cylindrical symmetry and therefore belong to the $C_{\infty v}$ point group. Their symmetry operations include the identity, the rotation by any arbitrary angle around the internuclear axis z and the infinity of symmetry planes which include that axis. The corresponding character table is shown in Table 1.2.

Given the cylindrical symmetry of diatomic molecules (and linear molecules in general), their electronic Hamiltonian H^{el} commutes with the z-component of the orbital angular momentum operator, L_z, but not with L^2, L_x and L_y. The electronic wavefunctions Ψ^{el} are thus

Table 1.2: Character table of the $C_{\infty v}$ point group of symmetry.

$C_{\infty v}$	E	$2\,C_{\infty}(\phi)$	$\cdots$	$\infty\sigma_v$
$A_1 = \Sigma^+$	1	1	$\cdots$	1
$A_2 = \Sigma^-$	1	1	$\cdots$	-1
$E_1 = \Pi$	2	$2\cos(\phi)$	$\cdots$	0
$E_2 = \Delta$	2	$2\cos(2\phi)$	$\cdots$	0
$E_3 = \Phi$	2	$2\cos(3\phi)$	$\cdots$	0
$\vdots$	$\vdots$	$\vdots$	$\vdots$	$\vdots$

eigenfunctions of both H^{el} and L_z [75]:

$$\begin{aligned} L_z\Psi^{\text{el}} &= M_l\,\hbar\,\Psi^{\text{el}}, & m_l &= 0,\pm1,\pm2,\pm3,... \\ &= \pm\Lambda\,\hbar\,\Psi^{\text{el}}, & \Lambda &= 0,1,2,3,... \end{aligned} \tag{1.39}$$

The states can therefore be classified according to the corresponding value of $\Lambda = |m_l|$:

Λ value	0	1	2	3	...
	$\Updownarrow$	$\Updownarrow$	$\Updownarrow$	$\Updownarrow$	
State designation	Σ	Π	Δ	Φ	...

Since all reflections with respect to a plane containing the internuclear axis z are part of the symmetry operations of linear molecules, their Hamiltonian also commutes with the corresponding σ_v operators. For example, the reflexion σ_{xz} along the (xz) plane leaves the energy unchanged, but transforms L_z into $-L_z$, since its effect amounts to $y \to -y$ and since:

$$L_z = -i\hbar(x\frac{\partial}{\partial y} - y\frac{\partial}{\partial x}). \tag{1.40}$$

When applied to a wavefunction associated to an eigenvalue $\Lambda \neq 0$, the σ_{xz} operator therefore transforms it into a wavefunction with eigenvalue $-\Lambda$ *while leaving the energy unchanged*, meaning that all states with $\Lambda \geq 0$ are doubly degenerate[†].

[†]Strictly speaking, the interaction between the electronic and rotational motions lifts that degeneracy. This phenomenon, called Λ-*doubling*, will not be taken into account in this work [75].

Σ states, for which $\Lambda = 0$, are however not degenerate. Since a plane reflexion is an involution (*i.e.* an operation that is its own inverse), applying it twice in a row on a wavefunction must yield back the original wavefunction, meaning that the eigenvalue of σ_v^2 is 1 and that the eigenvalue of σ_v can only be either $+1$ or -1. In the first case, the reflexion leaves the wavefunction unchanged and the state is denoted Σ^+ while in the second case, the reflexion changes the sign of the wavefunction and the state is denoted Σ^-.

Note that the MOLPRO *ab initio* software package [84], which we use in this work to solve the time-independent Schrödinger equation, only works in Abelian point groups of symmetry, *i.e.* groups that respect the commutative law for all operations (such as $C_1, C_2, C_i, C_s, C_{2v}, C_{2h}, D_2$, and D_{2h}). For molecules belonging to point groups with degenerate symmetry, MOLPRO instead uses an Abelian subgroup, such as C_{2v} in the case of heteronuclear diatomic molecules. The character table of the C_{2v} point group is reproduced in Table 1.3 and the correlation between the $C_{\infty v}$ and the C_{2v} point groups is shown in Table 1.4.

Table 1.3: Character table of the C_{2v} point group of symmetry.

C_{2v}	E	C_2	$\sigma_v(xz)$	$\sigma_v(yz)$
A_1	1	1	1	1
A_2	1	1	-1	-1
B_1	1	-1	1	-1
B_2	1	-1	-1	1

Table 1.4: Correlation between the $C_{\infty v}$ and the C_{2v} point groups of symmetry.

$C_{\infty v}$		C_{2v}
$A_1 = \Sigma^+$	$\Longleftrightarrow$	A_1
$A_2 = \Sigma^-$	$\Longleftrightarrow$	A_2
$E_1 = \Pi$	$\Longleftrightarrow$	$B_1 + B_2$
$E_2 = \Delta$	$\Longleftrightarrow$	$A_1 + A_2$
$\vdots$		$\vdots$

In addition to their spatial symmetry, the electronic states of heteronuclear diatomic molecules (and of molecular systems in general) are also characterized by their spin. The electronic wavefunction indeed commutes with the spin operator S^2 and the operator S_z associated to its projection on the z axis, with eigenvalues $S(S+1)\hbar^2$ and $\hbar m_s$ respectively. If the spin-orbit coupling is neglected, each state has a spin degeneracy of $2S+1$, called the *spin multiplicity*, which is commonly used to characterize molecular states according to the following convention:

S value	0	1/2	1	3/2	...
m_s values	0	$\pm 1/2$	$0, \pm 1$	$\pm 1/2, \pm 3/2$	...
	⇕	⇕	⇕	⇕	
Spin multiplicity	1	2	3	4	...
State designation	Singlet	Doublet	Triplet	Quadruplet	...

The complete nomenclature of molecular electronic state is based on their spin and spatial symmetry according to the convention ${}^{2S+1}\Lambda$, which is usually combined with the spectroscopic notation for molecular states. This (originally empirical) approach to state designation assigns an additional letter to each state, with X being the ground state and $A, B, C, ...$ being the excited states of the same spin multiplicity, from lowest to highest energy. States with a different spin multiplicity than that of the ground state are denoted with lowercase letters $a, b, c, ...$ in order of ascending energy.

1.6.1 Selection rules for diatomic molecules

The spin multiplicity and spatial symmetry of electronic states lead to the existence of *selection rules*: transitions between electronic states may be "forbidden" due to their respective symmetry and that of the operator involved in the transition.

In this work, we will more precisely focus on the electric dipolar selection rules for diatomic molecules. Knowing the symmetry properties of the transition dipole moment operator, the following selection rules can be inferred [85]:

- $\Delta S = 0$, meaning for example that singlet ↔ singlet or triplet ↔ triplet transitions are permitted, but that singlet ↔ triplet transitions are forbidden. Note that this rule breaks down if spin-orbit interactions are non-negligible.

- Among Σ states, only $\Sigma^+ \leftrightarrow \Sigma^+$ and $\Sigma^- \leftrightarrow \Sigma^-$ transitions are allowed while $\Sigma^- \leftrightarrow \Sigma^+$ transitions are forbidden.

- $\Delta\Lambda = 0$ for transitions caused by μ_z (the component of μ along the internuclear axis z), while $\Delta\Lambda = \pm 1$ for μ_x and μ_y. $\Sigma \leftrightarrow \Sigma$ transitions are therefore permitted through the μ_z component ("parallel" transitions) and $\Sigma \leftrightarrow \Pi$ are permitted through μ_x, μ_y ("perpendicular" transitions), while transitions like $\Sigma \leftrightarrow \Delta$ are strictly forbidden under the dipolar selection rules.

CHAPTER

2

AB INITIO CALCULATIONS

We have seen in Section 1.4.3 (p. 35) that the first step in the theoretical description of molecular systems is the resolution of the electronic Schrödinger equation for fixed geometries of the nuclei. In this chapter, we will present some of the theoretical methods that have been developed in this aim and the results we obtained therewith for the molecular cations HeH^+ and CO^{2+}.

This chapter is organized as follows: we first give a general theoretical introduction on the *ab initio* methods used in this work. We then expose:

- A short overview of the results of the calculations of Loreau *et al.* for the $^1\Sigma^+$, $^3\Sigma^+$ and $^3\Pi$ states of HeH^+ (Section 2.3, p. 53), followed by the results of our additional calculations for its $X\,^1\Sigma^+$, $a\,^3\Sigma^+$ and $b\,^3\Sigma^+$ states (Section 2.3.2, p. 59).

- The result of our calculations for the $X\,^3\Pi$ state of CO^{2+} and for its thirteen first $^3\Sigma^-$ states, most of which had never been described in literature before (Section 2.4, p. 63).

All *ab initio* results presented in this work were obtained using the MOLPRO Quantum Chemistry Package designed and maintained by H.-J. Werner and P. J. Knowles [84], and were performed on the HYDRA ULB/VUB computing cluster [86].

2.1 *Ab initio* methods

Various methods have been developed throughout the years to solve the electronic Schrödinger equation. In this work, we focus on *ab initio* ("*from first principles*") methods, which only rely on the basic principles and laws of quantum mechanics to describe atoms and molecules, without requiring any empirical parameter. Given the history of chemistry as an

experimental and empirical science, the fact that many properties of molecules can be computed *without requiring any knowledge besides that of the laws of quantum mechanics* deserves recognition.

Of course, such computations are far from trivial. *Ab initio* approaches require more computational resources than semi-empirical approaches, which use parameters based on experimental data to speed up calculations. Since the Schrödinger equation cannot be solved exactly for most molecular systems, approximations have to be used even in *ab initio* methods, with high-level *ab initio* approaches requiring less approximations but more computational resources [87].

Note that unless otherwise explicitly specified, all wavefunctions Ψ shown in this chapter are electronic wavefunctions $\Psi^{\text{el}}(\mathbf{r},\mathbf{R})$ and that the $^{\text{el}}$ indices are omitted for the sake of readability.

2.1.1 Hartree-Fock

Historically, the first *ab initio* method used in computational chemistry is the *Hartree-Fock method*. Even today, it is often used as a starting point for more accurate calculations.

The Hartree-Fock approach is based on the *variational method*, which relies on the fact that, for a system described by a Hamiltonian H, the exact wavefunction Ψ yields the exact energy E_{exact}, while any other wavefunction $\tilde{\Psi}$ yields a higher energy $E_{\tilde{\Psi}}$:

$$E_{\tilde{\Psi}} = \frac{\left\langle \tilde{\Psi} \,\middle|\, H \,\middle|\, \tilde{\Psi} \right\rangle}{\left\langle \tilde{\Psi} \,\middle|\, \tilde{\Psi} \right\rangle} \geq E_{\text{exact}} = \frac{\langle \Psi \mid H \mid \Psi \rangle}{\langle \Psi \mid \Psi \rangle}. \tag{2.1}$$

This means that if we take a random trial wavefunction $\tilde{\Psi}$ which depends on a series of parameters $\alpha, \beta, \gamma, ...$, the correct wavefunction can be gradually approximated by adjusting these parameters so as to minimize $E_{\tilde{\Psi}}$. With the right choice of trial wavefunction and parameters, the exact wavefunction can be approached.

How should the wavefunction be defined to achieve this? First and foremost, in order to correctly describe the quantum nature of the electrons, the electronic wavefunction Ψ must respect Fermi-Dirac statistics, which entails it has to be antisymmetric under the exchange of two electrons (*i.e.* exchanging two electrons flips the sign of the wavefunction) and that two electrons must differ by at least one of their quantum number (*i.e.* respect the "Pauli exclusion principle").

These two conditions are conveniently met if the wavefunction is expressed as a *Slater determinant*:

$$\Psi(\mathbf{x}_1, \mathbf{x}_2, ...\mathbf{x}_n) = \frac{1}{\sqrt{n!}} \begin{vmatrix} \chi_a(\mathbf{x}_1) & \chi_b(\mathbf{x}_1) & \cdots & \chi_n(\mathbf{x}_1) \\ \chi_a(\mathbf{x}_2) & \chi_b(\mathbf{x}_2) & \cdots & \chi_n(\mathbf{x}_2) \\ \vdots & \vdots & \ddots & \vdots \\ \chi_a(\mathbf{x}_n) & \chi_b(\mathbf{x}_n) & \cdots & \chi_n(\mathbf{x}_n) \end{vmatrix}, \tag{2.2}$$

or if it is expressed as a linear combination of such determinants, called a *configuration state*

function (CSF). In this expression, the coordinate $\mathbf{x}_i$ represents the position $\mathbf{r}_i$ and the spin σ_i of electron i, and each function $\chi_k(\mathbf{r}_i,\sigma_i)$ or simply $\chi_k(i)$ is a spin-orbital, *i.e.* a one-electron wavefunction for electron i that not only characterizes its spatial distribution, but also whether its spin z-projection is up or down. Each spin-orbital $\chi_k(\mathbf{r}_i,\sigma_i)$ can thus be expressed as the product of a spatial orbital $\phi_k(\mathbf{r}_i)$ and of a spin function α (for $\sigma_i = 1/2$) or β (for $\sigma_i = -1/2$):

$$\begin{aligned}\chi_k(i) &= \phi_k(\mathbf{r}_i)\ \alpha, \text{ or} \\ &= \phi_k(\mathbf{r}_i)\ \beta.\end{aligned} \tag{2.3}$$

Both the spatial orbitals and the spin-orbitals form orthonormal sets:

$$\langle \chi_k \mid \chi_l \rangle = \delta_{kl}. \tag{2.4}$$

Let us now look at the electronic Hamiltonian. As we have seen in Eqs. 1.12 and 1.15, for a molecular system containing n electrons and N nuclei, H^{el} is composed of the following terms:

$$\begin{aligned}H^{\text{el}} &= T^{\text{e}} + V^{\text{eN}} + V^{\text{ee}} \\ &= -\sum_{i=1}\frac{1}{2}\nabla^2_{\mathbf{r}_i} - \sum_{i=1}^{N}\sum_{j=1}^{n}\frac{Z_i}{r_{ij}} + \sum_{i=1}^{n}\sum_{j=i+1}^{n}\frac{1}{r_{ij}}.\end{aligned} \tag{2.5}$$

The first two terms can easily be expressed as a sum of *monoelectronic Hamiltonians* $h(i)$, each composed of the kinetic energy of an individual electron and of the potential terms arising from its interaction with all N nuclei:

$$h(i) = -\frac{1}{2}\nabla^2_{\mathbf{r}_i} - \sum_{j=1}^{N}\frac{Z_j}{r_{ij}}, \tag{2.6}$$

Upon integration with the full wavefunction, each h_i term will yield the corresponding monoelectronic energy ϵ_i for electron i:

$$\begin{aligned}\epsilon_i &= \langle \chi_a(1)\chi_b(2)...\chi_k(i)...\chi_n(n) \mid h(i) \mid \chi_a(1)\chi_b(2)...\chi_k(i)...\chi_n(n)\rangle \\ &= \langle \chi_k(i) \mid h(i) \mid \chi_k(i)\rangle\ \langle \chi_1(1) \mid \chi_1(1)\rangle\ \langle \chi_2(2) \mid \chi_2(2)\rangle ... \langle \chi_n(n) \mid \chi_n(n)\rangle \\ &= \langle \chi_k(i) \mid h(i) \mid \chi_k(i)\rangle.\end{aligned} \tag{2.7}$$

Of course, most molecules contain more than one electron – which significantly complicates matters as the third term of Eq. 2.5, the electron-electron repulsion, explicitly involves the coordinates $\mathbf{r}_i$ and $\mathbf{r}_j$ of two electrons. The Hartree-Fock method relies on the *mean-field approximation*, in which each electron moves in an average field generated by all other electrons. For a given electron i, the operator $v(i)$ associated to this mean field takes the following form:

$$v(i) = \sum_{k}^{n}\left(J_k(i) - K_k(i)\right), \tag{2.8}$$

where $J_k(i)$ is the *Coulomb operator* and $K_k(i)$ is the *exchange operator*. The Coulomb operator

$J_k(i)$ represents the repulsion potential felt by the electron i due to an electron j in a spin-orbital χ_k:

$$J_k(i)\chi_l(i) = \int \chi_k^*(j)\frac{1}{r_{ij}}\chi_k(j)\, d\mathbf{x}_j \;\; \chi_l(i). \tag{2.9}$$

On the other hand, the exchange operator $K_k(i)$ represents the effect of the exchange of electron i with an electron j in a spin-orbital χ_k:

$$K_k(i)\chi_l(i) = \int \chi_k^*(j)\frac{1}{r_{ij}}\chi_l(j)\, d\mathbf{x}_j \;\; \chi_k(i). \tag{2.10}$$

The energy associated to the mean-field operator is thus:

$$E^v = \frac{1}{2}\sum_i^n\sum_k^n \langle \chi_i \mid J_k(i) \mid \chi_i \rangle - \langle \chi_i \mid K_k(i) \mid \chi_j \rangle, \tag{2.11}$$

where the terms $J_i(i)$ and $K_i(i)$ cancel each other out.

The sum of the monoelectronic Hamiltonian $h(i)$ and the mean-field operator constitutes the *Fock operator*:

$$f(i) = h(i) + \sum_k^n (J_k(i) - K_k(i)). \tag{2.12}$$

One last term must be included: the Coulombic potential V^{NN} due to the repulsion between the nuclei. Since it is not a function of the electron coordinates $\mathbf{r}_i$ but only of those of the nuclei $\mathbf{R}_i$, it is simply a constant (for a given geometry of the nuclei) that needs to be added to the potentials:

$$\langle \Psi \mid V^{\mathrm{NN}} \mid \Psi \rangle = V^{\mathrm{NN}} \langle \Psi \mid \Psi \rangle = V^{\mathrm{NN}}. \tag{2.13}$$

Putting Eqs. 2.7, 2.11 and 2.13 together, we obtain the Hartree-Fock energy for a fixed geometry of the nuclei:

$$E^{\mathrm{HF}} = \frac{1}{2}\sum_i^n\sum_k^n \langle \chi_i \mid J_k(i) \mid \chi_i \rangle - \langle \chi_i \mid K_k(i) \mid \chi_j \rangle + V^{\mathrm{NN}}. \tag{2.14}$$

Our aim is now to find the wavefunction that minimizes this energy while ensuring that the spin-orbitals stay orthonormal. This amounts to a problem of optimization under constraint, which can be solved with the method of Lagrange multipliers by defining the following Lagrange function $\mathcal{L}$:

$$\mathcal{L} = E - \sum_i^n\sum_j^n \lambda_{ij} \langle \chi_i \mid \chi_j \rangle, \tag{2.15}$$

where λ_{ij} are the Lagrange multipliers. Taking the derivative of these equations to impose $\delta\mathcal{L} = 0$ leads to the n Hartree-Fock equations:

$$f(i)\;\chi_k(i) = \lambda_{kk}\;\chi_k(i). \tag{2.16}$$

Being nonlinear, the Hartree-Fock equations need to be solved iteratively: starting from an "initial guess" of wavefunctions $\{\chi\}$, the corresponding mean field and Fock operators are calculated and used to compute a new set of wavefunctions. This new set then serves as the starting point of the next iteration of the algorithm, and so on, until a *self-consistent field* is reached, *i.e.* until the calculation has converged to a set of orbitals that respects Eq. 2.16 and that corresponds to a global minimum of the energy.

While this can be achieved using a purely numerical approach for atoms, the resolution of the Hartree-Fock for molecules is usually carried out using an analytical approach based on the expression of the molecular orbitals as a combination of m functions from a basis set:

$$\chi_i(\mathbf{r}) = \sum_{\alpha=1}^{m} c_{i\alpha}\, \zeta_\alpha(\mathbf{r}). \tag{2.17}$$

This approach is called *Linear Combination of Atomic Orbitals* (LCAO), as the basis functions $\zeta_\alpha(\mathbf{r})$ are usually modeled after atomic orbitals (although they are generally not solutions of the atomic Hartree-Fock equations: rather, they are "atomic orbitals" in the sense that they are each centered on a specific atom). The resolution of the Hartree-Fock equations now requires finding the values of the coefficients $\{c\}$ in order to obtain the best expression for the orbitals $\{\chi\}$. Using a matrix notation, the Hartree-Fock can be rewritten in terms of the coefficients $\{c\}$ as:

$$\mathcal{F}\mathcal{C} = \mathcal{S}\mathcal{C}\lambda, \tag{2.18}$$

where $\mathcal{F}$ is the matrix of the Fock operator in the basis of the atomic orbitals $\{\zeta\}$, $\mathcal{C}$ is the matrix of coefficients $\{c\}$, λ is the diagonal matrix of orbital energies and $\mathcal{S}$ contains the overlaps between the atomic orbitals, *i.e.* $S_{\alpha\beta} = \langle\zeta_\alpha|\zeta_\beta\rangle$. This form of the Hartree-Fock equations is called the *Roothan* (or *Roothan-Hall*) equation and is solved by diagonalizing $\mathcal{F}$:

$$|\mathcal{F} - \lambda\mathcal{S}| = 0. \tag{2.19}$$

This yields as many solutions as there are atomic orbitals in the chosen basis. n of these solutions correspond to occupied spin-orbitals while the remaining $(m-n)$ solutions correspond to unoccupied, so-called "virtual" spin-orbitals.

The higher the number m of basis functions ζ, the lower the energy and the better the result: increasing the size of the basis set increases the flexibility offered to the spin-orbitals χ and brings the electronic wavefunction Ψ closer to its exact form upon optimization. However, even with an infinite basis set, the Hartree-Fock method will never yield the exact result for systems with more than one electron: its biggest flaw is that it relies on the mean-field approximation and on the assumption that the molecular system can be accurately described by a single electronic configuration, which leads to the neglect of *electron correlation*.

To go beyond these approximations and take (part of) the electron correlation into account, more complex *ab initio* approaches called *post-Hartree-Fock methods* have been developed.

2.1.2 Configuration Interaction

While the Hartree-Fock method is very convenient, it is often used as a first step to more refined and more resource-intensive approaches that aim at taking the electron correlation into account.

As we have seen in Eq. 2.2 (p. 46), the Hartree-Fock approach expresses the electronic wavefunction as a Slater determinant (or a linear combination thereof, *i.e.* a CSF) that corresponds to a single electronic configuration. The *Configuration Interaction* (CI) method goes one step further by expressing the wavefunction as a linear superposition of CSF corresponding to several electronic configurations, by promoting one or more electrons to the unoccupied, "virtual" spin-orbitals.

The wavefunction is thus expressed as a linear combination of the Slater determinants representing not only the base configuration, but also the n_S possible "singly-excited" configurations corresponding to the promotion of one electron towards a virtual spin-orbital, the n_D possible "doubly-excited" configurations corresponding to the promotion of two electrons towards virtual spin-orbitals, and so on for triple, quadruple, ... excitations:

$$\Psi^{\mathrm{el\,CI}} = d_0 \Psi_0^{\mathrm{el}} + \sum_i^{n_\mathrm{S}} d_i^{\mathrm{S}} \Psi_i^{\mathrm{el\,S}} + \sum_i^{n_\mathrm{D}} d_i^{\mathrm{D}} \Psi_i^{\mathrm{el\,D}} + \sum_i^{n_\mathrm{T}} d_i^{\mathrm{T}} \Psi_i^{\mathrm{el\,T}} + \ldots \tag{2.20}$$

In this expression, the factors d are called the *CI coefficients* and are optimized variationally (while respecting the constraint that the total wavefunction $\Psi^{\mathrm{el\,CI}}$ remains normalized). A *Full CI* approach implies taking into account every possible excitation of each electron in the total wavefunction. For most systems, this would however require a prohibitive amount of resources, which is why a *SDCI* approach is often used by truncating the sum in equation 2.20 after the single and double excitations (hence the "SD" in "SDCI"). This is justified by the fact that the configurations corresponding to single and double excitations are those that contribute the most to the energy, with triple excitations and beyond requiring more computational resources while only yielding diminishing returns. Note that for a two-electron system such as HeH^+, a SDCI is equivalent to a full CI.

2.1.3 Multiconfigurational methods

A typical CI approach only takes into account excited variants of a single reference configuration, using orbitals optimized for this configuration only. Many molecular systems however cannot accurately be described by a single electronic configuration: *multiconfigurational methods* are therefore necessary.

The *Multiconfiguration Self-Consistent Field* (MCSCF) method expresses the wavefunction as a linear combination of several CSF at once, as in a truncated CI approach, and optimizes both the coefficients of the superposition and the molecular orbitals *simultaneously* in order to minimize energy. Such calculations however require a large amount of computational resources, which scale nonlinearly with the number of included configurations. It is therefore important to select which configurations need to be included in the optimization.

The *Complete Active Space Self-Consistent Field* (CASSCF) method uses configurations generated on the basis of the partitioning of the orbitals into three categories:

1) The inactive orbitals, which stay doubly occupied in all considered configurations.

2) The active orbitals, in which the electrons are distributed in all possible ways to form the CASSCF expansion.

3) The virtual orbitals, which stay unoccupied in all considered configurations.

CASSCF approaches thus require the definition of an appropriate *active space* of orbitals in which all possible distributions of the electrons will be considered.

Note that a MCSCF calculation can be followed by a CI computation using an approach called *Multireference Configuration Interaction* or MRCI, which uses the MCSCF configurations as reference and expands the wavefunction by adding their single, double, ... excitations.

2.1.4 Basis sets

The choice of an appropriate method of calculation is not the only factor that influences the accuracy of an *ab initio* calculation. As we have seen in Eq. 2.17, analytical *ab initio* calculations are based on the expansion of the molecular orbitals in a basis of functions $\{\zeta_\alpha(\mathbf{r})\}$, whose form and amount deeply affect the result of the calculations (and the computational resources they require).

Expanding the molecular orbitals in a basis set would not constitute an approximation if the basis set was complete. Using a complete basis set is however impossible in practice, as that would require an infinity of basis functions and thus infinite computational resources. As a general rule of thumb, increasing the number of function in the basis set allows a better description of the molecular orbitals and more accurate calculations. However, all basis functions do not contribute equally to the description of the molecular orbitals: a reasonably accurate depiction of the molecular orbitals can therefore be obtained if the functions included in the basis set are chosen wisely [77].

Although these basis functions could theoretically take many shapes, two kind of functions centered on the atomic nuclei are usually used as "atomic orbitals": Slater-Type Orbitals (STO), which are usually based on the spherical harmonic functions, and Gaussian-Type Orbitals (GTO), which are composed of Gaussian functions or contractions thereof that imitate Slater-Type functions.

In this work, we use Gaussian-Type Orbitals exclusively. The overlap between two Gaussian functions is indeed much easier and much faster to calculate than between two Slater-Type orbitals, leading to a significant computational speedup. To further speed calculations up, a lot of basis sets are *contracted, i.e.* they are composed of atomic orbitals that are expressed as pre-optimized combinations of Gaussian functions:

$$\zeta_\alpha(\mathbf{r}) = \sum_{i=1}^{j} c_{\alpha i}\, \zeta_{\alpha i}^{\text{primitive}}(\mathbf{r}), \tag{2.21}$$

where the coefficients $c_{\alpha i}$ are pre-optimized[†] and where $\zeta_{\alpha i}^{\text{primitive}}$ are the Gaussian functions, also called *primitive functions*. These functions take the form:

$$\zeta_{\alpha i}(\mathbf{r}) = N(\xi)\ e^{-\xi|\mathbf{r}-\mathbf{R}|^2}, \tag{2.22}$$

where $\mathbf{R}$ is the position of the atom on which the primitive is centered, ξ is a parameter called the *Slater orbital exponent* and $N(\xi)$ is a normalization factor.

The smallest possible basis sets include only one function per occupied atomic orbital and are called *minimal basis sets*. This is for example the case of the STO-3G basis set, which uses a single function composed of the contraction of three Gaussians to describe each atomic orbital.

For more accurate calculations, bigger basis sets are however necessary. *Double zeta* basis sets for example use two functions to describe each atomic orbital while *triple zeta* use three, and so on.

In this work, we use the aug-cc-pVmZ basis sets optimized by Dunning *et al.* [88, 89], commonly abbreviated as AVmZ. Explaining the meaning of their name amounts to explaining their content and properties:

- **aug**, meaning "augmented", denotes the fact that the basis set contains diffuse functions, *i.e.* functions with components at large $|\mathbf{r}-\mathbf{R}|$ distances, that increase the flexibility of the basis set.

- **cc-p**, standing for "correlation consistent polarized", means that they include increasingly larger shells of polarization functions (d, f, g, ...) with increasing values of m.

- **V** means "valence", indicating that the index m denotes the number of functions used to describe the valence orbitals, while the core orbitals are described by a single function each.

- ***m*** is the number of functions per atomic orbital, which takes values such as "D" ("double"-zeta, $m = 2$), "T" ("triple"-zeta, $m = 3$), "Q" ("quadruple"-zeta, $m = 4$), 5, 6, ...

One of the advantages of the Dunning bases is that they allow for *Complete Basis Set extrapolation* (CBS). As mentioned earlier, the basis set used to describe a molecular system should ideally contain an infinity of functions to allow for maximal flexibility in the optimization (and to therefore reach the lowest possible energy for the chosen method). Although this is impossible in practice, it is possible to estimate the result that would be obtained with an infinite basis set by performing computations with AVmZ bases of growing size, then extrapolating the results to $m = \infty$. This is achieved by fitting the results for different values of m with an appropriate function then extrapolating its value to $m = \infty$ [90, 91].

[†]Note however that MOLPRO allows "uncontracted" calculations, in the course of which the coefficients $c_{\alpha i}$ are optimized variationally. This leaves more freedom to the optimization procedure, leading to lower energies and increased accuracy, at the cost of additional computational efforts.

2.2 Resolution of the vibrational equation

As we have seen, the time-dependent Schrödinger equation (Eq. 1.2, p. 32) can be solved to obtain the wavefunction $\Psi(t)$ at any time t, provided it is known at a particular time t_0. Dynamical simulations therefore require an initial wavefunction $\Psi(t_0)$. For collisional problems, this wavefunction must be built from scratch, by constructing a superposition of plane waves with different energies to create a wavepacket (Gaussian wavepackets are for example commonly used).

In the case of photodissociation reactions, such as those studied in Chapters 3 and 4 of this work, the initial wavepacket is however based on the rovibrational wavefunction of the initial state: the system is assumed to undergo a Franck-Condon (*i.e.* vertical) transition upon absorption of the photon, which corresponds to a distribution of the initial rovibrational wavefunction on the different excited states based on the corresponding transition dipole moment (this will be further detailed in Section 3.2.1.1, p. 82). The theoretical description of the dynamics of a photodissociation reaction therefore requires the resolution of the nuclear equation for the initial state in order to obtain the corresponding rovibrational wavefunctions.

This can be achieved by expanding the vibrational wavefunction in a basis of M functions $B_i(R)$:

$$\Psi^{\text{vib}}(R) = \sum_{i}^{M} c_i \, B_i(R) \tag{2.23}$$

In this work, this was done in a basis of *B-spline* functions [92] for the $X\ ^1\Sigma^+$, $a\ ^3\Sigma^+$ and $b\ ^3\Sigma^+$ states of HeH^+ and in a basis of sines for the $X\ ^3\Pi$ state of CO^{2+}. The vibrational equation was solved for different values of the rotational quantum number J by adding the rotational energy term $E^{\text{rot}}(R) = B(R)\ J(J+1)$ to the potential energy curves.

2.3 *Ab initio* calculations for HeH^+

2.3.1 *Ab initio* data from Loreau *et al.*

All dynamical calculations presented in this work were performed using the potential energy curves, nonadiabatic radial couplings and dipole moments computed by Loreau *et al.* [2] at the CASSCF and CI level using the MOLPRO quantum chemistry package [84].

That work expanded and improved upon the previous series of studies of the excited states of HeH^+ performed by Green *et al.* [19–22] in several ways:

– A larger basis set was used. To ensure a correct description of the excited states, the calculations were performed using the aug-cc-pV5Z basis set supplemented with one contracted Gaussian function per orbital per atom optimized by Loreau *et al.* with the AUTOSTRUCTURE [93–95] program to accurately describe the dissociation into excited states of helium. In total, a $[8s, 7p, 5d, 3f, 1g]$ basis set was used for both atoms.

– The calculations included states up to $n = 4$, *i.e.* 19 $^1\Sigma^+$, 19 $^3\Sigma^+$, 12 $^1\Pi$, 9 $^3\Pi$, 4 $^1\Delta$ and 2 $^3\Delta$ states.

– Calculations were performed for much higher internuclear distances (up to R=200 a_0), as the description of the Franck-Condon region alone is insufficient to perform dynamical simulations.

In addition to their adiabatic potential energy curves, Loreau *et al.* computed the permanent and transition dipole moments of each state, as well as the radial and rotational coupling matrices, which were used to diabatize both the potentials and the dipole moments. Only the couplings between successive states $F_{m,m\pm1}$ were taken into account in the determination of the adiabatic-to-diabatic transformation matrix $\mathcal{D}(R)$. Further details about the calculations of Loreau *et al.* can be found in Ref. [2].

In this work, we focus on the $X\ ^1\Sigma^+ \rightarrow\ ^1\Sigma^+$ transitions as well as the $a,b\ ^3\Sigma^+ \rightarrow\ ^3\Sigma^+$, $^3\Pi$ transitions. The potential energy curves and dipole moments of the $^1\Sigma^+$ states included in our dynamical calculations are shown in Figs. 2.1 and 2.3 while those of the $^3\Sigma^+$ and $^3\Pi$ states are shown in Figs. 2.2 and 2.5. Tables 2.1 and 2.2 give the fragments corresponding to the dissociation of each molecular state as well as the symbol used to designate each state in this work. For convenience, the $^1\Sigma^+$ states are denoted by uppercase Roman letters according to spectroscopic conventions, while the $^3\Sigma^+$ states are denoted by lowercase Roman letters and the $^3\Pi$ states are denoted by lowercase Greek letters.

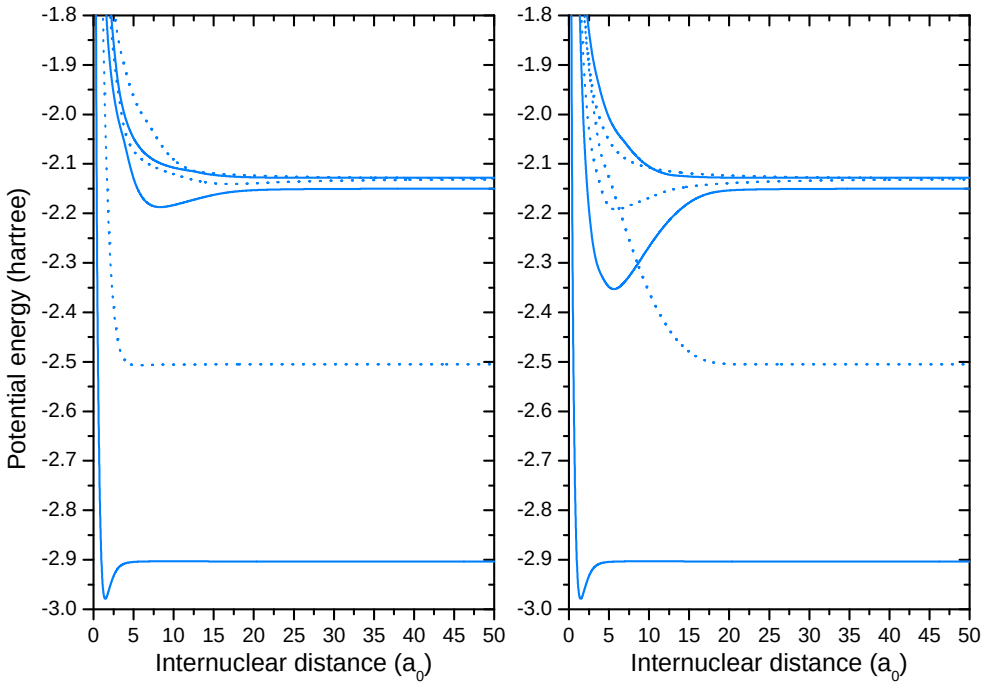

Figure 2.1: Adiabatic (left) and diabatic (right) potential energy curves of the n = 1–3 $^1\Sigma^+$ states of HeH^+. Full lines: states dissociating into He + H^+, dotted lines: states dissociating into He^+ + H.

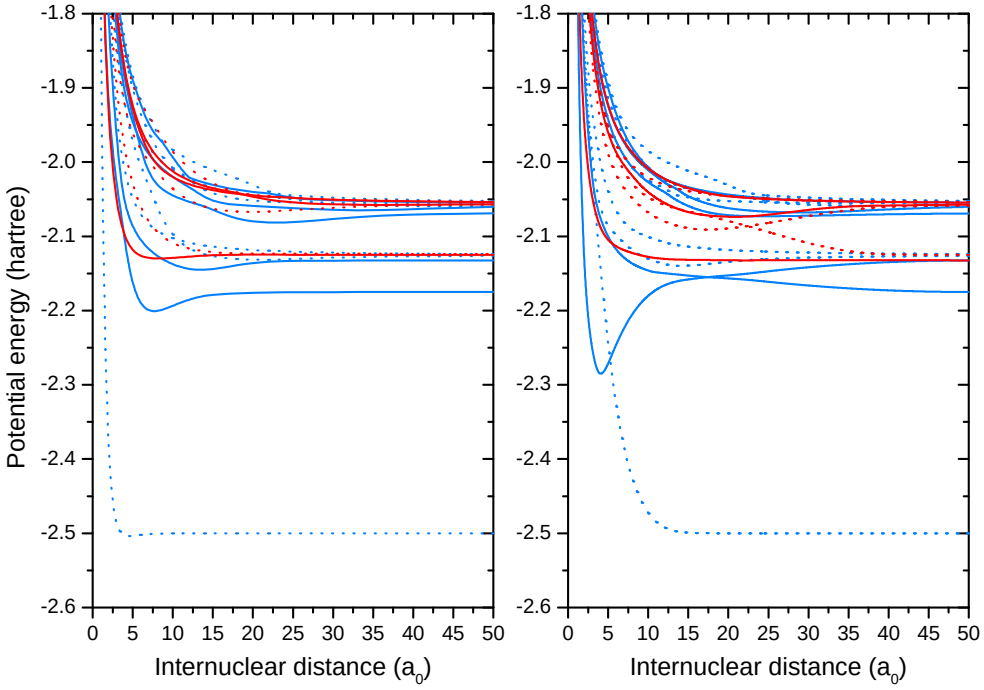

Figure 2.2: Adiabatic (left) and diabatic (right) potential energy curves of the $n = 1$–$3\ ^3\Sigma^+$ (blue) and $^3\Pi$ (red) states of HeH^+. Full lines: states dissociating into He + H^+, dotted lines: states dissociating into He^+ + H.

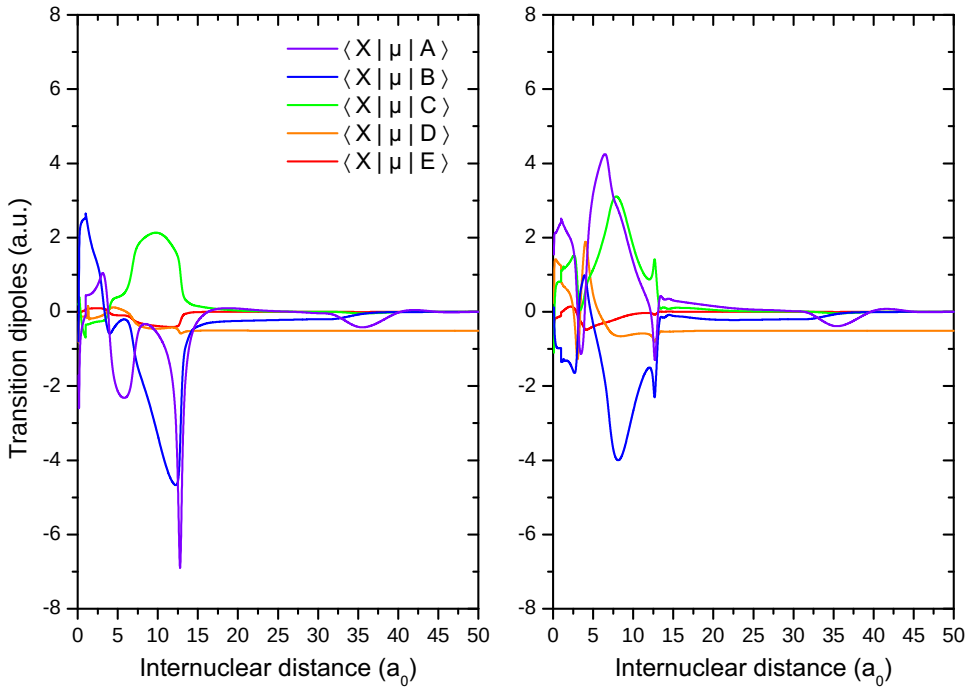

Figure 2.3: Adiabatic (left) and diabatic (right) transition dipole moments between the $X\ ^1\Sigma^+$ and the $n = 2$–$3\ ^1\Sigma^+$ states of HeH^+.

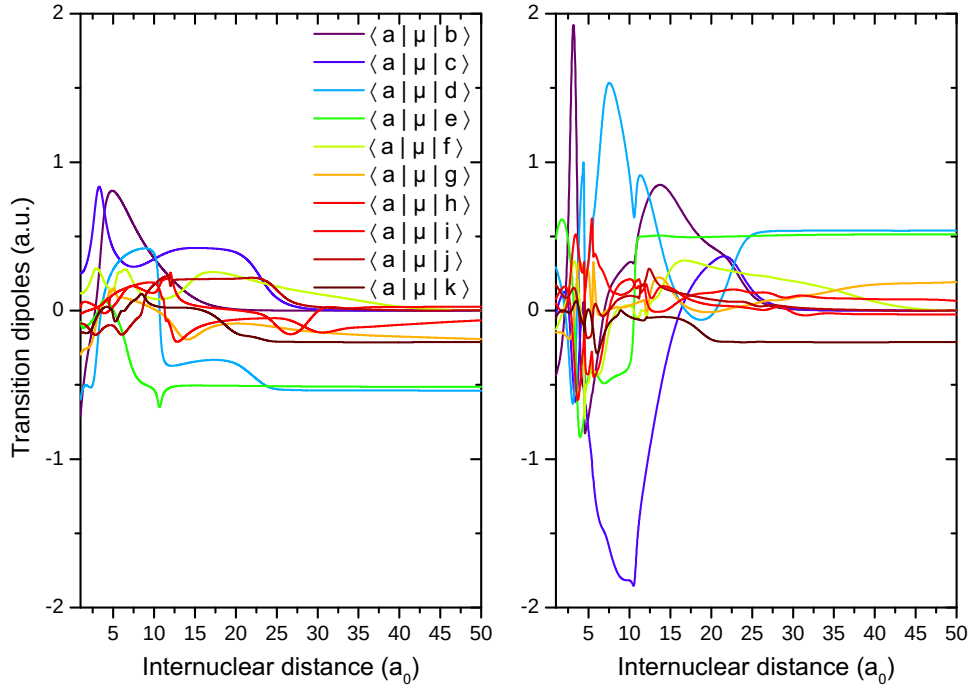

Figure 2.4: Adiabatic (left) and diabatic (right) transition dipole moments between the $a\,^3\Sigma^+$ and the other $n = 2$–$3\,^3\Sigma^+$ states of HeH^+.

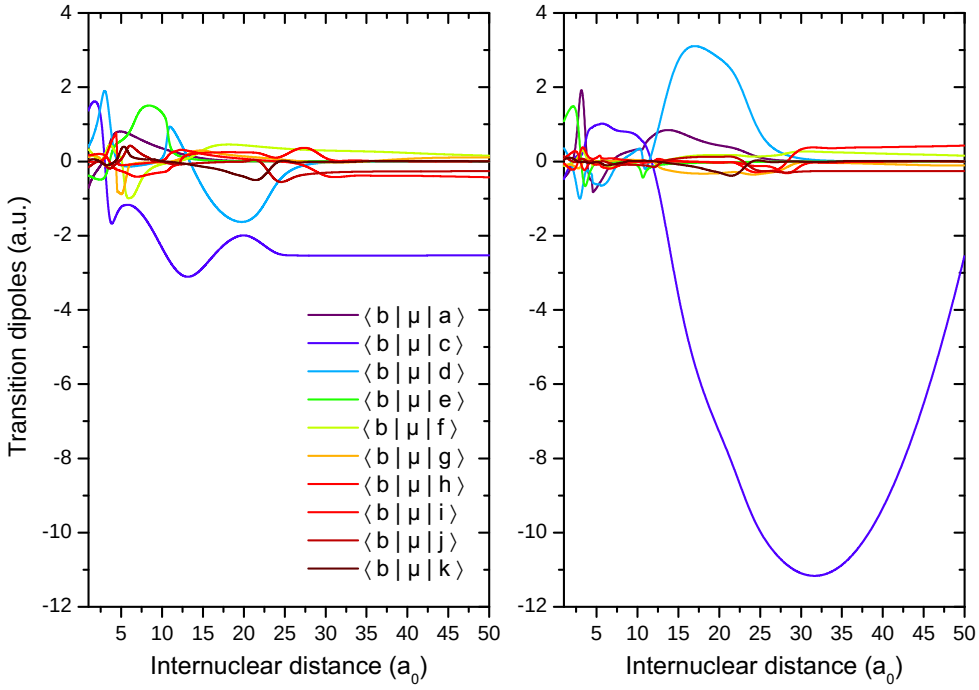

Figure 2.5: Adiabatic (left) and diabatic (right) transition dipole moments between the $b\,^3\Sigma^+$ and the other $n = 2$–$3\,^3\Sigma^+$ states of HeH^+.

Table 2.1: HeH^+ electronic states included in our dynamical simulations, ordered by symmetry and increasing dissociation energy. For convenience, $^1\Sigma^+$ states are denoted by uppercase Roman letters while $^3\Sigma^+$ states are denoted by lowercase Roman letters.

Designation	Symmetry	Corresponding fragments
X	$^1\Sigma^+$	$He(1s^2\,^1S) + H^+$
A	$^1\Sigma^+$	$He^+(1s\,^2S) + H(1s\,^2S)$
B	$^1\Sigma^+$	$He(1s2s\,^1S) + H^+$
C	$^1\Sigma^+$	$He^+(1s\,^2S) + H(2p\,^2P)$
D	$^1\Sigma^+$	$He^+(1s\,^2S) + H(2s\,^2S)$
E	$^1\Sigma^+$	$He(1s2p\,^1P) + H^+$
a	$^3\Sigma^+$	$He^+(1s\,^2S) + H(1s\,^2S)$
b	$^3\Sigma^+$	$He(1s2s\,^3S) + H^+$
c	$^3\Sigma^+$	$He(1s2p\,^3P) + H^+$
d	$^3\Sigma^+$	$He^+(1s\,^2S) + H(2p\,^2P)$
e	$^3\Sigma^+$	$He^+(1s\,^2S) + H(2s\,^2S)$
f	$^3\Sigma^+$	$He(1s3s\,^3S) + H^+$
g	$^3\Sigma^+$	$He(1s3p\,^3P) + H^+$
h	$^3\Sigma^+$	$He^+(1s\,^2S) + H(3d\,^2D)$
i	$^3\Sigma^+$	$He^+(1s\,^2S) + H(3p\,^2P)$
j	$^3\Sigma^+$	$He(1s3d\,^3D) + H^+$
k	$^3\Sigma^+$	$He^+(1s\,^2S) + H(3s\,^2S)$

Table 2.2: HeH^+ electronic states included in our dynamical simulations. For convenience, $^3\Pi$ states are denoted by lowercase Greek letters (continued from previous page).

Designation	Symmetry	Corresponding fragments
α	$^3\Pi$	$He(1s2p\,^3P) + H^+$
β	$^3\Pi$	$He^+(1s\,^2S) + H(2p\,^2P)$
γ	$^3\Pi$	$He(1s3p\,^3P) + H^+$
δ	$^3\Pi$	$He^+(1s\,^2S) + H(3d\,^2D)$
ϵ	$^3\Pi$	$He(1s3d\,^3D) + H^+$
ζ	$^3\Pi$	$He^+(1s\,^2S) + H(3p\,^2P)$

2.3.2 Rovibrational levels of the $X\,^1\Sigma^+$, $a\,^3\Sigma^+$ and $b\,^3\Sigma^+$ state of HeH^+

In this work, we study the dynamics of photodissociation and radiative association reactions involving the $X\,^1\Sigma^+$, $a\,^3\Sigma^+$ and $b\,^3\Sigma^+$ states of HeH^+, which requires computing their rovibrational wavefunction as accurately as possible. In this aim, we computed the potential energy curves of the $X, A, B\,^1\Sigma^+$ and $a,\ b\,^3\Sigma^+$ states during our master thesis using the same parameters as Loreau *et al.*, except for the basis set, which was varied from AVTZ to AV6Z (while still retaining the additional basis functions optimized by Loreau and coworkers [2]). These AVTZ, AVQZ, AV5Z and AV6Z series of results were then used to extrapolate the potential energy curves to Complete Basis Set, using a simple exponential function to fit the $m = 3$–6 results:

$$E_m = E_{m=\infty} + A\, e^{-Bm}. \tag{2.24}$$

An excellent agreement was found between our CBS-extrapolated results for the X, A, B, a, b states and the AV5Z results of Loreau *et al.* The latter were therefore used in all dynamical calculations presented here as they are far more extensive than our own calculations. The CBS-extrapolated data was however used to compute the energy and wavefunctions of all rovibrational levels of the $X\,^1\Sigma^+$ as well as of the a and $b\,^3\Sigma^+$ states, as molecular dynamics are known to be sensitive to the shape of the initial wavefunction.

In the case of the $X\,^1\Sigma^+$ state, only the photodissociation from the lowest $v = 0, J = 0$ rovibrational level was considered (see Chapter 3, p. 77 for more details). The wavefunction for this level and the energy of the other vibrational levels are shown on the potential curve of the state in Fig. 2.6, while their energy and the number of rotational levels situated below the dissociation limit for a given value of v are shown in Table 2.3.

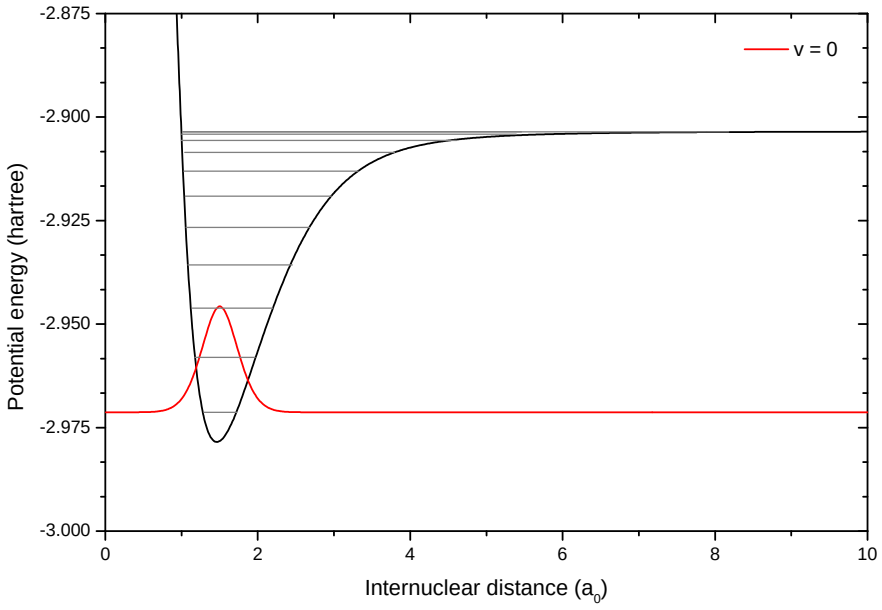

Figure 2.6: Potential energy curve, vibrational levels for $J = 0$, and $v, J = 0$ wavefunction of the $X\,^1\Sigma^+$ state of HeH^+.

Table 2.3: Properties of the vibrational levels of the $X\ ^1\Sigma^+$ state of HeH^+. "Rotational levels" denotes the number of rotational levels situated below the dissociation limit for a given v.

v	Energy (hartree)	Rotational levels
0	-2.97124353	24
1	-2.95798198	22
2	-2.94611664	21
3	-2.93565519	19
4	-2.92661993	17
5	-2.91904775	15
6	-2.91298791	13
7	-2.90848989	11
8	-2.90556267	8
9	-2.90405789	6
10	-2.90352197	4
11	-2.90340866	2

In the case of the a and $b\ ^3\Sigma^+$ states, we studied the photodissociation from the lowest rotational $J = 0$ level of every vibrational level (more details about this decision and the role of J are given in Chapter 3). Figures 2.7 and 2.8 show the potential energy curves, vibrational energies for $J = 0$ and some of the corresponding wavefunctions for states a and $b\ ^3\Sigma^+$, respectively. Their energies and number of rotational levels below the dissociation limit are given in Tables 2.4 and 2.5.

Table 2.4: Properties of the vibrational levels of the $a\ ^3\Sigma^+$ state of HeH^+. "Rotational levels" denotes the number of rotational levels situated below the dissociation limit for a given v.

v	Energy (hartree)	Rotational levels
0	-2.50129691	15
1	-2.50085152	12
2	-2.50044177	9
3	-2.50014388	7
4	-2.49999315	5
5	-2.49994062	3

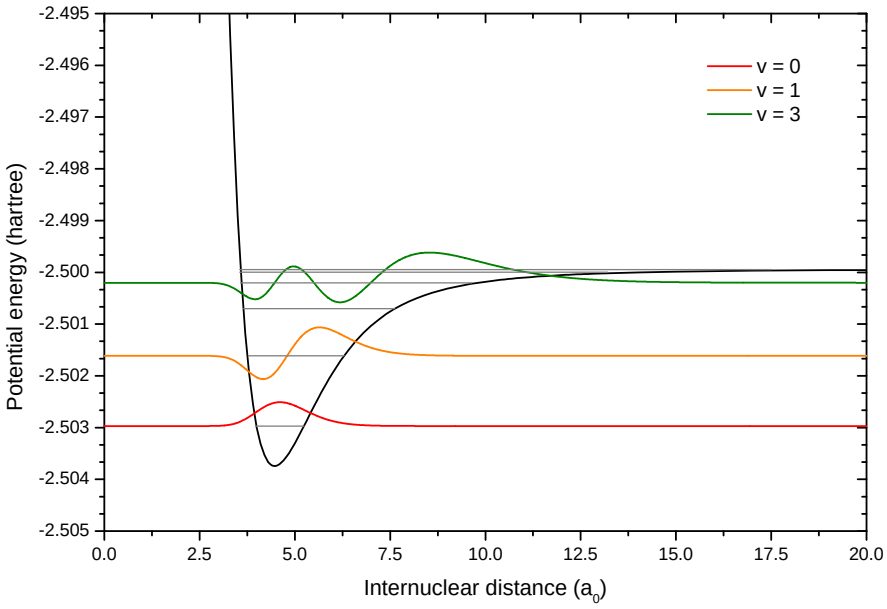

Figure 2.7: Potential energy curve, vibrational levels for $J = 0$ and a few vibrational wavefunctions of the $a\,^3\Sigma^+$ state of HeH^+.

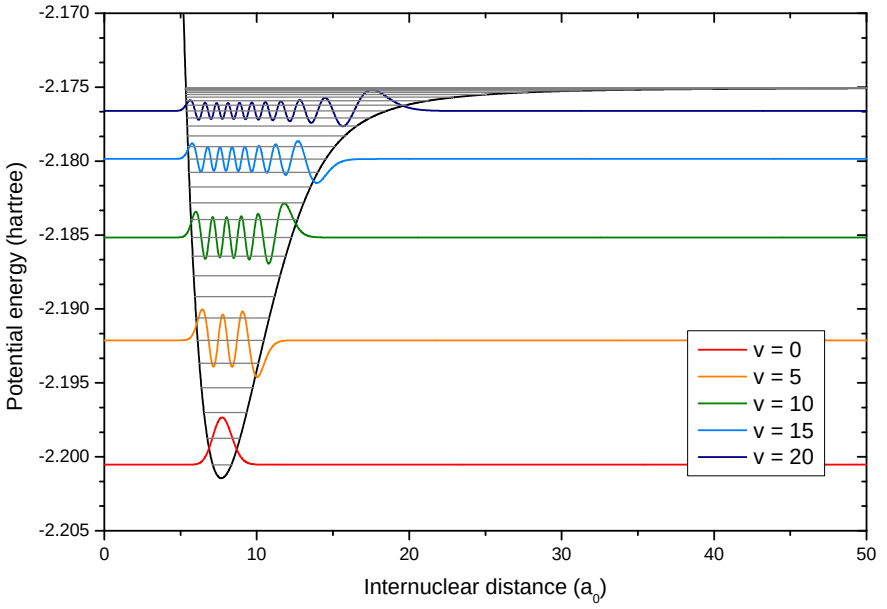

Figure 2.8: Potential energy curve, vibrational levels for $J = 0$ and a few vibrational wavefunctions of the $b\,^3\Sigma^+$ state of HeH^+.

Table 2.5: Properties of the vibrational levels of the $b\ ^3\Sigma^+$ state of HeH^+. "Rotational levels" denotes the number of rotational levels situated below the dissociation limit for a given v.

v	Energy (hartree)	Rotational levels
0	-2.20022691	74
1	-2.19844180	72
2	-2.19671292	70
3	-2.19504077	68
4	-2.19342593	66
5	-2.19186892	64
6	-2.19037024	62
7	-2.18893037	59
8	-2.18754997	57
9	-2.18622999	55
10	-2.18497185	53
11	-2.18377755	50
12	-2.18264974	48
13	-2.18159174	46
14	-2.18060751	44
15	-2.17970148	41
16	-2.17887834	39
17	-2.17814248	37
18	-2.17749725	35
19	-2.17694381	33
20	-2.17648011	30
21	-2.17610048	28
22	-2.17579624	26
23	-2.17555716	24
24	-2.17537269	22
25	-2.17523306	21
26	-2.17512983	19
27	-2.17505544	17
28	-2.17500330	15
29	-2.17496740	12
30	-2.17494373	10
31	-2.17492954	7
32	-2.17492279	3

2.4 *Ab initio* calculations for CO^{2+}

2.4.1 Earlier studies of CO^{2+}

As mentioned in the introduction, the molecular dication CO^{2+} has been the subject of a large number of studies, both experimental and theoretical.

Dozens of experimental studies on CO^{2+} have been realized since its first detection in 1930 [44], using techniques such as electron impact [96], Auger spectroscopy [59, 68], electron loss and double electron capture collisions [97], threshold photoelectrons coincidence spectroscopy [64, 98], translational energy spectroscopy [61], photoion-fluorescence photon coincidence [99], single-photon or multiphoton ionization of CO with ultrashort pulses [66], and many more.

In the last twenty years, many works have focused on the study of CO^{2+} in ion storage rings, allowing for more accurate measurements of its spontaneous dissociation [63, 100] (which was found to occur on a timescale of several seconds) and of its dissociative recombination [101].

The 2010 experimental closed-loop control of the vibrational population performed by Wells *et al.* [102] is of particular interest. A genetic algorithm was used to optimize a laser pulse which predominantly ionizes CO into either "non-dissociative" CO^{2+} (*i.e.* CO^{2+} in a metastable state) or dissociative CO^{2+}, leading to the detection of its fragments $C^+ + O^+$. This amounts to controlling the double ionization of CO to form CO^{2+} in either the $v = 0, 1$ levels of the $X\ ^3\Pi$ state and the $v = 0$ level of the lowest $^1\Sigma$ state, or in higher excited vibrational levels and dissociative electronic states. In Chapter 4 of this work, we theoretically explore another form of control: starting from CO^{2+} in the metastable $v = 0$ level of the $X\ ^3\Pi$ state, we optimize laser pulses that selectively photodissociate the molecule through its first $^3\Sigma^-$ channel correlating to the C^{2+} + O fragments. This scheme allows us to take advantage of the fact that vibrationally-pure CO^{2+} can be obtained experimentally, simplifying the control scheme and future experimental implementations: otherwise, cooling techniques would first have to be used to cool the molecule down vibrationally (see for example Ref. [103]).

Publications focusing on the theoretical description of CO^{2+} have been fraught with contradictions regarding both the symmetry of its lowest electronic state and the predissociation lifetimes of its metastable states.

Chronologically, the first attempt at a theoretical description of CO^{2+} appears to be the 1961 semi-empirical work of Hurley and Maslen, which relies on the virial theorem to derive an approximate expression of the potential energy curves of diatomic dications based on the corresponding curves of their neutral counterpart [104]. This approach however only yielded an estimation of the basic parameters characterizing the potential energy curves of the lowest states of such cations and was abandoned in favor of more accurate *ab initio* calculations in later works.

The first real *ab initio* study of CO^{2+} was performed by Wetmore *et al.* in 1984, who calculated the potential energy curves of the first few electronic states of each symmetry of CO^{2+} from $R = 1$ to 3 Å, using a Restricted Hartree-Fock SCF method with a $[3s, 2p, 1d]$ basis set followed by a CI calculation [67]. Although this work is notable for including 3–5 states of each

symmetry, it suffers from a low accuracy compared to more recent studies. It for examples incorrectly predicts the ground electronic state of CO^{2+} to be its lowest $^3\Sigma^-$ state, and describes it as having a small potential energy barrier instead of as being purely dissociative. Wetmore and his team attempted to explain the observed long lifetime of CO^{2+} in experiments and correctly attributed it to the $X\ ^3\Pi$ state, but erroneously concluded that its first lowest vibrational levels would quickly predissociate through the neighbouring $^3\Sigma^-$ channel and that the $v = 2$ level would have a longer lifetime.

The accuracy of Wetmore's original study was called into question in a 1985 study by Correia *et al.* using a CASSCF/MRCI approach with [5s, 3p, 1d], [7s, 6p, 1d] basis sets [68]. Their results partially contradict those obtained by Wetmore: notably, Correia *et al.* predict the ground state to be a $^1\Sigma$ state. Once again, this result was later contradicted by ulterior studies.

In 1989, Lablanquie *et al.* performed an experimental and theoretical study of the formation of CO^{2+} [62]. They computed the potential energy curves of the first states of the $^1\Pi$,$^3\Pi$,$^1\Sigma^+$,$^3\Sigma^+$ and $^3\Sigma^-$ symmetries using a SCF/CI approach in a [5s, 4p, 3d] basis set. Unlike Wetmore *et al.*, they correctly described the first $^3\Sigma^-$ as being dissociative, although they still predicted it to be the ground state.

This work was quickly followed by another 1989 study by Larsson *et al.*, who used a CASSCF/MRCCI approach with a [8s, 6p, 2d] basis to describe the first lowest state of the $^3\Pi$, $^3\Sigma^-$, $^3\Sigma^+$, $^1\Sigma^+$, $^1\Pi$ and $^1\Delta$ symmetries, as well as the second $^1\Sigma^+$ state of CO^{2+} [69]. This time, the ground state was correctly predicted to be the $^3\Pi$ state, as confirmed by subsequent studies.

Also notable is the 1993 publication of Andersen *et al.*, for two reasons [63]. It was the first experimental evidence that CO^{2+} can be stable on a timescale of several seconds, with a measured lifetime of 3.8 seconds at least. Moreover, Andersen and his coworkers used CASSCF/MRCI calculations with a [8s, 5p, 3d, 1f] basis set to compute not only the potential energy curves of the first lowest $^3\Pi$,$^3\Sigma^-$,$^1\Pi$ and $^1\Sigma^+$ states, but also the spin-orbit couplings between the $^3\Pi$,$^3\Sigma^-$ and $^1\Sigma^+$ states. Using these results, they estimated the predissociation lifetime of these electronic states and concluded that the $^3\Pi(v = 0)$ level is responsible for the long lifetime of the species, although their calculations yielded a much shorter lifetime than expected (20 ms instead of the observed > 3.8 s).

Another important study is that of Eland *et al.* in 2004 [57], who performed high level *ab initio* computations for the first $^3\Pi$,$^3\Sigma^+$,$^3\Sigma^-$,$^1\Pi$, $^1\Delta$ states as well as the two lowest $^1\Sigma^+$ states using a CASSCF/MRCI approach in the cc-pV5Z basis set. The tunneling widths of the vibrational levels of the metastable states were also computed and give an upper limit to their predissociation lifetime, as spin-orbit mediated predissociation through other electronic states is not taken into account in that work[†].

In 2006, Šedivcová *et al.* performed a CASSCF/icMRCI study of the nine lowest states of CO^{2+} using the cc-PV5Z and cc-PV6Z basis sets [105], and estimated the corresponding spin-

[†]For example, we obtain a lifetime of 10^{43} seconds for the $X\ ^3\Pi(v = 0)$ level, based on the $t = 1/2\pi c\Gamma$ formula and the tunneling width $\Gamma = 0.41669 \times 10^{-55}$ cm^{-1} given in the paper. The real lifetime is of course expected to be much shorter due to predissociation through the $^3\Sigma^-$ state, as later shown by Šedivcová *et al.* and Mrugała [49, 105].

orbit couplings. This data was additionally used to compute the predissociation lifetimes of the vibrational levels of the ground $X\ ^3\Pi$ state, leading to the conclusion that the lifetimes of the $v = 0, 1$ levels of the $X\ ^3\Pi$ state are much longer than 10 μs. Along with those of Eland *et al.*, the calculations of Šedivcová *et al.* remain the most accurate for CO^{2+} to this day.

Kumar *et al.* performed an additional study of the lowest states of CO^{n+} with $n = 0-6$ at the CASSCF/MRCI level using the AVQZ Dunning basis set [106]. Their work on CO^{2+} includes the first $^3\Pi$ and $^3\Sigma^+$ states computed with a (3 a_1, 2 b_1, 2 b_2) active space, and the lowest $^3\Sigma^-$ state computed with a (2 a_1, 2 b_1, 2 b_2) active space[†]. Although it is notable for studying the first electronic states of highly-charged carbon monoxide cations, this work brought little new to our knowledge of CO^{2+} as its lowest electronic states had already been described more accurately in earlier studies.

Finally, Mrugała further used the spin-orbit couplings computed by Šedivcová *et al.* [105], combined this time with the potential energy curves calculated by Eland *et al.* [57], to compute the predissociation lifetime of vibronic states of CO^{2+}, as this combination of *ab initio* data was found to best reproduce the experimental measurements [49]. More precisely, the repulsive potential of the lowest $^3\Sigma^-$ state as calculated by Šedivcová *et al.* was found to be insufficiently accurate in the medium-range internuclear distance, requiring the use of the potential energy curves of Eland *et al.* instead. Using this data, Mrugała obtained a lifetime of 3.6×10^{12} s for the $v = 0$ level of the $X\ ^3\Pi$ state and of 0.48 s for its $v = 1$ level. Based on Mrugała's conclusions, we use the *ab initio* results of Eland *et al.* as a point of comparison for ours.

To summarize, the current understanding of the lifetime of the vibrational levels of the $X\ ^3\Pi$ state CO^{2+} is the following: excited vibrational levels predissociate due to spin-orbit coupling to the repulsive lowest $^3\Sigma^-$ state, while the $v = 0$ and $v = 1$ vibrational levels, situated below the crossing between the two electronic states, have a much longer lifetime [102,105]. It is now well-established that the $v = 0$ level of the $X\ ^3\Pi$ state has a lifetime of several seconds [63], allowing for the experimental production of electronically and vibrationally pure CO^{2+} [107] and its use in quantum control experiments.

Note that all theoretical studies of CO^{2+} thus far have focused on the lowest states of each symmetry only. Moreover, all these calculations were performed (to the best of our knowledge) in a strict Born-Oppenheimer adiabatic picture, with a complete neglect of all nonadiabatic couplings (although spin-orbit couplings were taken into account in some of the most recent studies in order to properly describe the predissociation lifetime of the lowest electronic states). In this work, we describe the excited $^3\Sigma^-$ states of CO^{2+} for the first time, in the adiabatic and the diabatic representation.

2.4.2 *Ab initio* results for CO^{2+}

Our aim in this work was not to improve the accuracy of earlier adiabatic potential curves, but to compute the potential energy curves, nonadiabatic couplings as well as permanent and

[†]Their calculations were performed in MOLPRO, which only works in Abelian point group of symmetry, as explained in Section 1.6 (p. 41).

transition dipole moments for the ground $X\,^3\Pi$ state as well as for the first 11 $^3\Sigma^-$ states of CO^{2+}, most of which had never been described theoretically before.

More specifically, our aim was to compute the *ab initio* data required to describe the photodissociation of CO^{2+} through its $^3\Sigma^-$ states leading not only to fragments C^+ and O^+ but also to C^{2+} + O, as well as to compute laser control fields guiding the photodissociation process towards this second pair of fragments. This required computing a large number of $^3\Sigma^-$ states, as the first $^3\Sigma^-$ channel that dissociates into C^{2+} + O is the ninth one, in the Franck-Condon region. Moreover, we also included several higher-excited states to increase the accuracy of the highest-lying potential energy curves. In total, 13 $^3\Sigma^-$ states were included in our *ab initio* calculations, but only 11 were used in our dynamical simulations in an effort to reduce the duration of the computations (see Chapters 3 and 4).

We chose to focus on the $^3\Sigma^-$ states of CO^{2+} instead of the $^3\Pi$ states for two reasons. First and foremost, the photodissociation predominantly occurs through the $\Pi \rightarrow \Sigma$ perpendicular transition [107], making the Σ states a better target for laser control. Moreover, these transitions have been less studied than the parallel $\Pi \rightarrow \Pi$ and $\Sigma \rightarrow \Sigma$ transitions. Secondly, from a practical point of view, the lowest $^3\Sigma^-$ that dissociates into C^{2+} + O instead of C^+ + O^+ is the ninth one, while all $^3\Pi$ states up to the fourteenth dissociate into C^+ + O^+. Studying the photodissociation into C^{2+} + O through the $^3\Sigma^-$ channels thus required less computational effort than through the $^3\Pi$ channels as fewer electronic states needed to be included in the calculation.

Moreover, the computation of a large number of $^3\Sigma^-$ states is easier in MOLPRO than the computation of $^3\Pi$ states: being doubly degenerate, each $^3\Pi$ state counts as two states in the input of MOLPRO, which normally restricts the number of states that can be included in a calculation to 10. Thankfully, this number was increased to 20 by J. Liévin by modifying part of the MOLPRO 2006 source code during Jérôme Loreau's computations on HeH^+, a fact we took advantage of during our work on CO^{2+}.

Our calculations were however made difficult by severe convergence problems, that required the use of a very small spatial step ΔR between two computations (as small as 0.001 a_0 in some regions) to ensure convergence. Although this may seem excessive, the use of such small steps proved invaluable later on when correcting the signs of the radial nonadiabatic couplings and dipole moments, as discussed further in Section 2.4.4 (p. 71). Starting from computations at values of the internuclear distance R for which the algorithm converged well, several series of computations were performed in parallel towards lower and higher values of R in order to obtain a complete picture of the potential energy curves from $R = 1.5$ to 100 a_0.

Due to the large number of states included in our basis and the need for a very small spatial step between two calculations in some regions, our main series of calculation was performed in the AVTZ basis set to keep the computational time within reasonable limits. Additional calculations were however performed in the AVQZ, AV5Z and AV6Z basis set and compared to the AVTZ results. Although (as expected) the absolute energies of the states vary from one basis to another (up to ≈ 0.010 hartree), the difference of energy between the states varies comparatively little (≈ 0.003 hartree at most).

In the end, we had to choose between using a large basis and using a fine spatial grid to ensure convergence and a good description of the nonadiabatic couplings. Given the amount of avoided crossings between the considered states, the important role played by the couplings in the dynamics of species such as HeH^+ and the relatively small impact of the basis set on the relative energies, we chose to perform calculations in the AVTZ basis set and to use a very fine spatial grid (as small as $\Delta R = 0.001\ a_0$ in some regions). All calculations were performed with active space (6 a_1, 2 b_1, 2 b_2) as it was found to have good convergence properties.

The nonadiabatic $\partial/\partial R$ radial couplings were directly computed in MOLPRO using the 3-point finite difference method (*i.e.* by numerically computing the derivative of the wavefunction at a given distance R based on its value at two slightly displaced distances $R \pm \delta R$), while the rotational couplings were neglected in the present study.

2.4.3 Computation of the ground $X\,^3\Pi$ and of the first 13 $^3\Sigma^-$ states of CO^{2+}

Table 2.6 gives the fragments corresponding to the dissociation of the CO^{2+} electronic states included in our calculations. As previously reported in the most recent studies of CO^{2+}, we find the $^3\Pi$ state to be the ground state of CO^{2+} and to possess a potential energy barrier, with an equilibrium distance $R_e = 1.26$ Å, in agreement with the calculations of Larsson *et al.* [69]. Other values available in the literature range from 1.18 to 1.30 Å, as summarized in Table 2.7[†]. Note that, although the results of Šedivcová *et al.* could be expected to be the most accurate, Mrugała noted in her computational study of the lifetime of the metastable states of CO^{2+} that the best agreement with the experimental results were obtained when using the potential energy curves of Eland *et al.* [49].

Fig. 2.9 shows a comparison of the potential energy curve of the lowest $^3\Pi$ state of CO^{2+} as obtained in this work and as computed by Wetmore *et al.* [67] and Eland *et al.* [57]. To allow for easy comparison despite their use of different energy scales, the absolute energy of the curves of Wetmore *et al.* and Eland *et al.* was shifted so that they match ours at large internuclear distances.

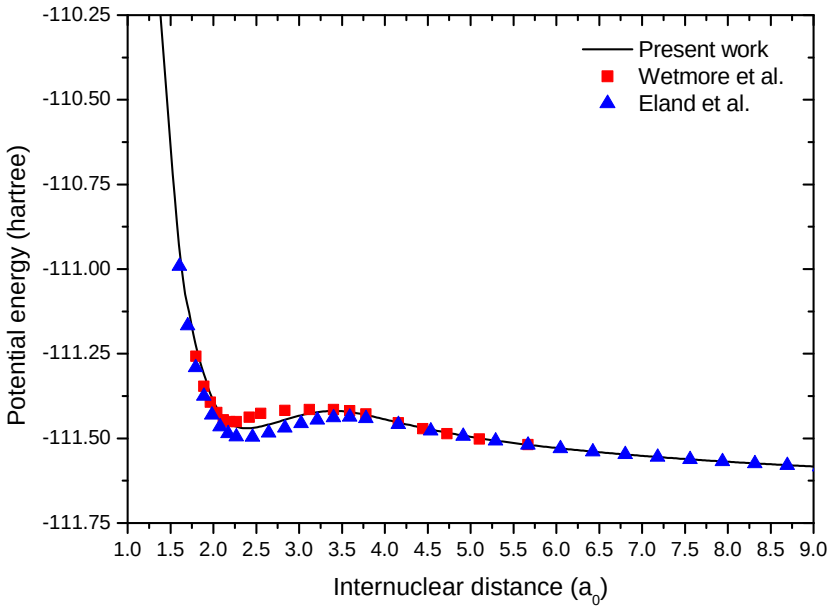

Figure 2.9: Comparison of our potential energy curve for the $X\,^3\Pi$ state of CO^{2+} (black line) with that of Wetmore *et al.* (red squares) and Eland *et al.* (blue triangles), adjusted to converge towards the same energy at large internuclear distances (the squares and triangles represent the only numerical values given explicitly in their papers).

[†]In addition to the values presented in Table 2.7, Kumar also incorrectly reported the equilibrium distance of Eland *et al.* [57] as being equal to 1.138 Å instead of 1.30 Å. The origin of that value is however unknown and may have been caused by a typographical error, as it does not appear to match with any other study.

Table 2.6: CO^{2+} electronic states included in our dynamical simulations. For convenience, $^3\Sigma^-$ states are numbered in ascending order of energy of their atomic fragments.

Designation	Symmetry	Corresponding fragments
X	$^3\Pi$	$C^+(2s^2 2p\ ^2P) + O^+(2s^2 2p^3\ ^4S)$
1	$^3\Sigma^-$	$C^+(2s^2 2p\ ^2P) + O^+(2s^2 2p^3\ ^4S)$
2	$^3\Sigma^-$	$C^+(2s^2 2p\ ^2P) + O^+(2s^2 2p^3\ ^2D)$
3	$^3\Sigma^-$	$C^+(2s^2 2p\ ^2P) + O^+(2s^2 2p^3\ ^2P)$
4	$^3\Sigma^-$	$C^+(2s^2 2p\ ^2P) + O^+(2s^2 2p^3\ ^2P)$
5	$^3\Sigma^-$	$C^+(2s2p^2\ ^4P) + O^+(2s^2 2p^3\ ^2D)$
6	$^3\Sigma^-$	$C^+(2s2p^2\ ^2D) + O^+(2s^2 2p^3\ ^4S)$
7	$^3\Sigma^-$	$C^+(2s2p^2\ ^4P) + O^+(2s^2 2p^3\ ^2P)$
8	$^3\Sigma^-$	$C^+(2s2p^2\ ^4P) + O^+(2s^2 2p^3\ ^2P)$
9	$^3\Sigma^-$	$C^{2+}(2s^2\ ^1S) + O(2s^2 2p^4\ ^4P)$
10	$^3\Sigma^-$	$C^+(2s2p^2\ ^2S) + O^+(2s^2 2p^3\ ^4S)$
11	$^3\Sigma^-$	$C^+(2s2p^2\ ^2D) + O^+(2s^2 2p^3\ ^2D)$

Table 2.7: Equilibrium distance R_e of the $X\ ^3\Pi$ state of CO^{2+} as reported in the literature and as computed in this work.

Study	R_e(Å)
Wetmore *et al.* [67]	1.18
Larsson *et al.* [69]	1.261
Lablanquie *et al.* [62]	1.28
Veseth [108]	1.238
Eland *et al.* [57]	1.30
Šedivcová *et al.* [105]	1.2392
Kumar *et al.* [106]	1.247
This work	1.26

The literature unfortunately contains very little data on the $^3\Sigma^-$ states of CO^{2+}. The 1989 study of Wetmore *et al.* included the five lowest $^3\Sigma^-$ states of CO^{2+}, however, its relatively low accuracy makes comparisons uneasy [67]. Moreover, their result for the lowest $^3\Sigma^-$ state are in disagreement with those of subsequent studies, as they predict the state to be quasibound instead of purely dissociative. Fig. 2.10 shows a comparison of the potential energy curve of the lowest $^3\Sigma^-$ state of CO^{2+} as obtained in this work and as computed by Wetmore *et al.* [67] and Eland *et al.* [57]. Again, to allow for easy comparison despite their use of different energy scales, the absolute energy of the curves of Wetmore *et al.* and Eland *et al.* was adjusted to match that of ours at large internuclear distances.

Fig. 2.11 shows the adiabatic potential energy curves of the $X\,^3\Pi$ state and of the 11 first $^3\Sigma^-$ states of CO^{2+} as computed in this work.

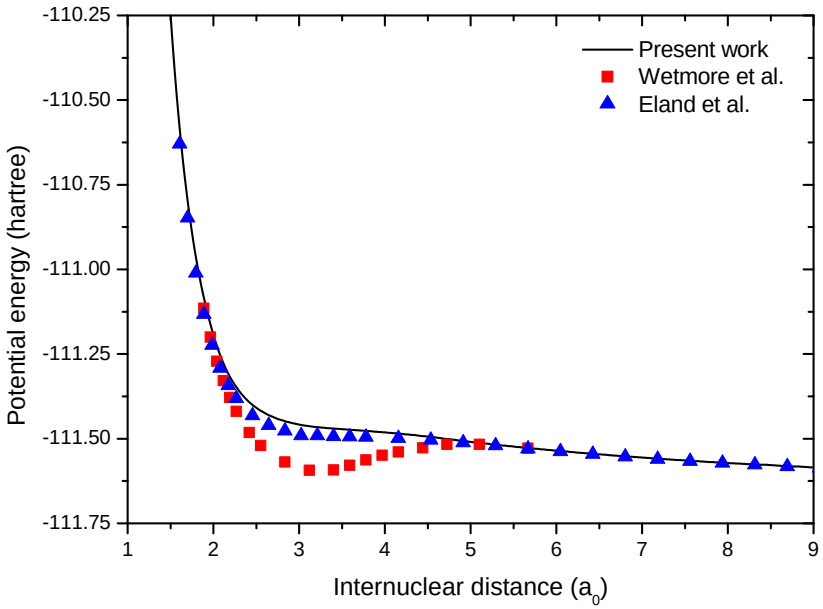

Figure 2.10: Comparison of our potential energy curve for the lowest $^3\Sigma^-$ state of CO^{2+} (black line) with that of Wetmore *et al.* (red squares) and Eland *et al.* (blue triangles), adjusted to converge towards the same energy at large internuclear distances (the squares and triangles represent the only numerical values given explicitly in their papers).

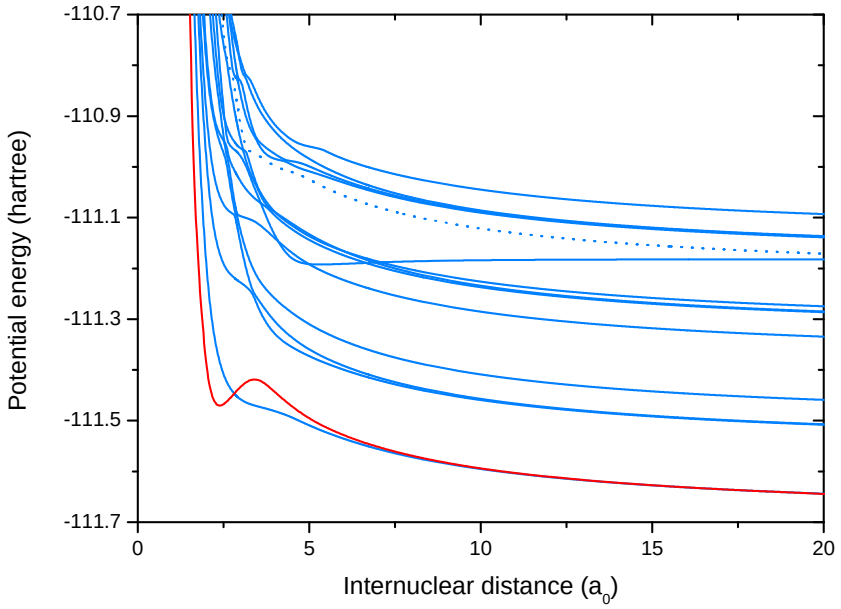

Figure 2.11: Adiabatic potential energy curves of the $X\ ^3\Pi$ (red curve) and of the 11 lowest $^3\Sigma^-$ states of CO^{2+} (blue curves). Full lines: states dissociating into $C^+ + O^+$, dotted line: state dissociating into $C^{2+} + O$.

2.4.4 Sign error corrections

Calculations of transition dipole moments and nonadiabatic couplings performed with MOLPRO suffer from an unfortunate problem: the results are obtained with an arbitrary sign, as MOLPRO computes the wavefunction with an arbitrary phase. This implies that, from one calculation to another, the signs of non-diagonal physical quantities which depend on the relative sign of two wavefunctions (such as transition dipole moments and radial nonadiabatic couplings) are susceptible to change. Fig. 2.12 shows two such "sign errors" in the nonadiabatic radial coupling between the second and third $^3\Sigma^-$ states of CO^{2+}.

Although this problem tends to be ignored or at least not mentioned in the vast majority of works[†], it is essential that these signs be coherent – especially if one wants to interpolate the data points to express them on a regular grid, as is for example done in order to use them in dynamical calculations. If not corrected beforehand, the values interpolated between points affected by a change of sign would be incorrect, potentially leading to significant errors even in situations where only the absolute value of the considered physical quantity is physically relevant.

We therefore attempted to develop a simple code which would read the uncorrected dipole moment and coupling values as a function of R, compare the value at each gridpoint with an

[†]With notable exceptions, such as the works of Errea *et al.* [109].

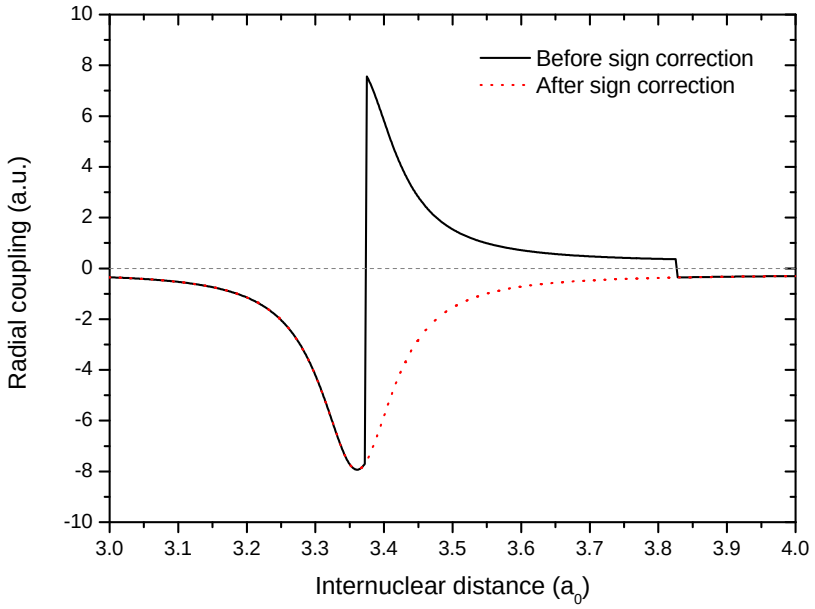

Figure 2.12: Nonadiabatic radial couplings between the second and third $^3\Sigma^-$ states of CO^{2+} before and after sign correction. Obvious sign errors can be seen at $R = 3.375$ and 3.828, leading to discontinuities devoid of physical meaning.

extrapolation based on the preceding points and flip the sign if it led to a smaller difference between the two. Upon closer inspection of the results, this code was however found to occasionally lead to errors in the regions where the distance between each data point was too big.

In the end, we found it faster (if somewhat fastidious) to use the usual sign correction method: by hand, as sign errors are usually obvious to the naked eye when the data is computed on a fine enough grid. The very fine spatial grid we used to compute the *ab initio* data proved invaluable in the correction of the signs, as it usually allowed us to plainly see where the transition dipole moments and radial couplings erroneously flipped signs, even in zones where they naturally varied strongly with R.

The signs of all 78 radial couplings and 91 transition dipole moments between the $X\,^3\Pi$ and the 13 first $^3\Sigma^-$ states were thus painstakingly corrected by hand, allowing for the diabatization of the potential energy curves and transition dipole moments.

2.4.5 Diabatization

As in the case of HeH^+, the excited potential energy curves of CO^{2+} possess large nonadiabatic radial couplings (as could be inferred from the shape of the adiabatic potential energy curves, which exhibit a very large number of avoided crossings). In addition to reasonably intense couplings, we found a series of very intense and narrow couplings that correspond to the C^{2+} + O potential energy curve crossing the C^+ + O^+ curves. Once again, our very fine spatial

grid turned out to be invaluable in localizing them precisely. However, they were found to lead to numerical problems in the diabatization algorithm due to their very high values. We thus performed the diabatization "manually" for these crossings by switching the corresponding potential energy curves and dipole moments at the precise position of the coupling peak, which amounts to assuming the non-radiative population transfers would be total in these regions. This procedure already had been used with success earlier, in the diabatization of HeH^+ [2].

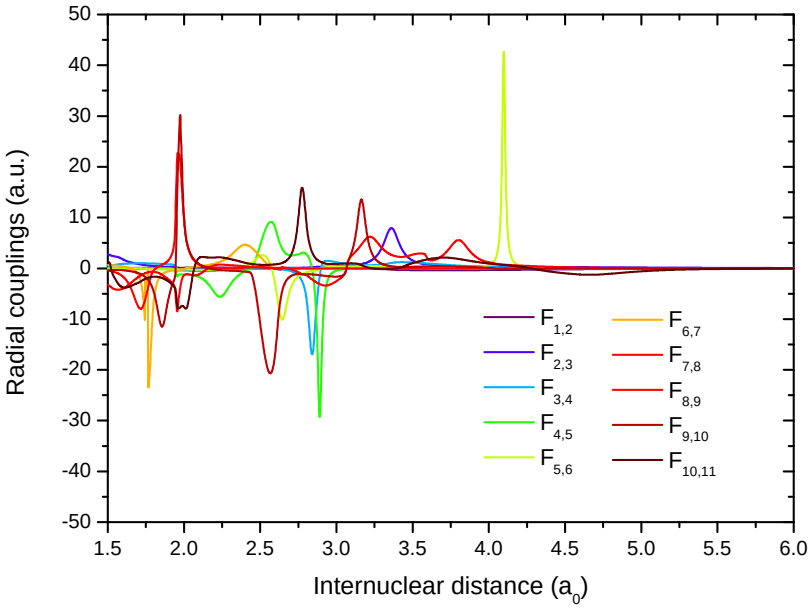

Figure 2.13: Nonadiabatic radial couplings between the 11 lowest $^3\Sigma^-$ states of CO^{2+}. For the sake of readability, only couplings between successive states $F_{m,m\pm1}$ are shown and the largest couplings ($\gg$ 100 a.u.), arising from the crossings between the C^{2+} + O potential energy curve with those of the C^+ + O^+ states, have been omitted.

As in the case of HeH^+, Eq. 1.34:

$$\frac{\partial}{\partial R}\mathcal{D} + \mathcal{F}\cdot D = 0, \tag{2.25}$$

was solved by continuity with the initial condition $\mathcal{D}(\infty) = I$, in order to ensure that the adiabatic and diabatic representations are identical at large internuclear distance. The adiabatic and diabatic potential energy curves are shown in Fig. 2.14 while the dipole moments are shown in Fig. 2.15. Note that the transition dipole moments are significantly smaller than those of HeH^+, indicating that higher electric field intensities will be required for efficient radiative population transfer.

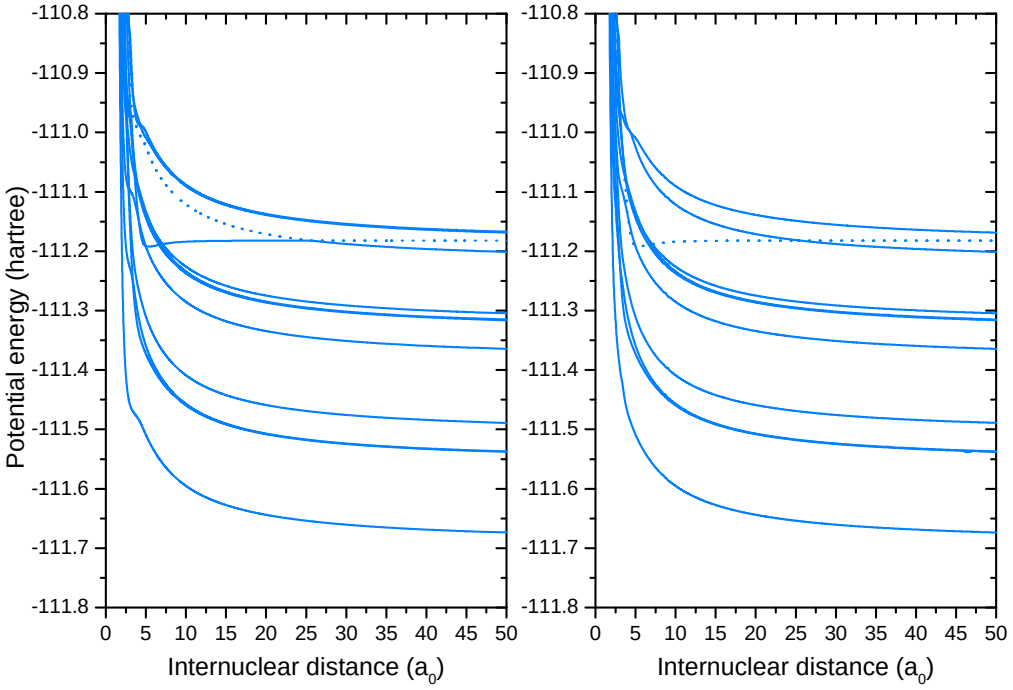

Figure 2.14: Adiabatic (left) and diabatic (right) potential energy curves of the first 11 $^3\Sigma^-$ states of CO^{2+}. Full lines: states dissociating into $C^+ + O^+$, dotted line: state dissociating into $C^{2+} + O$.

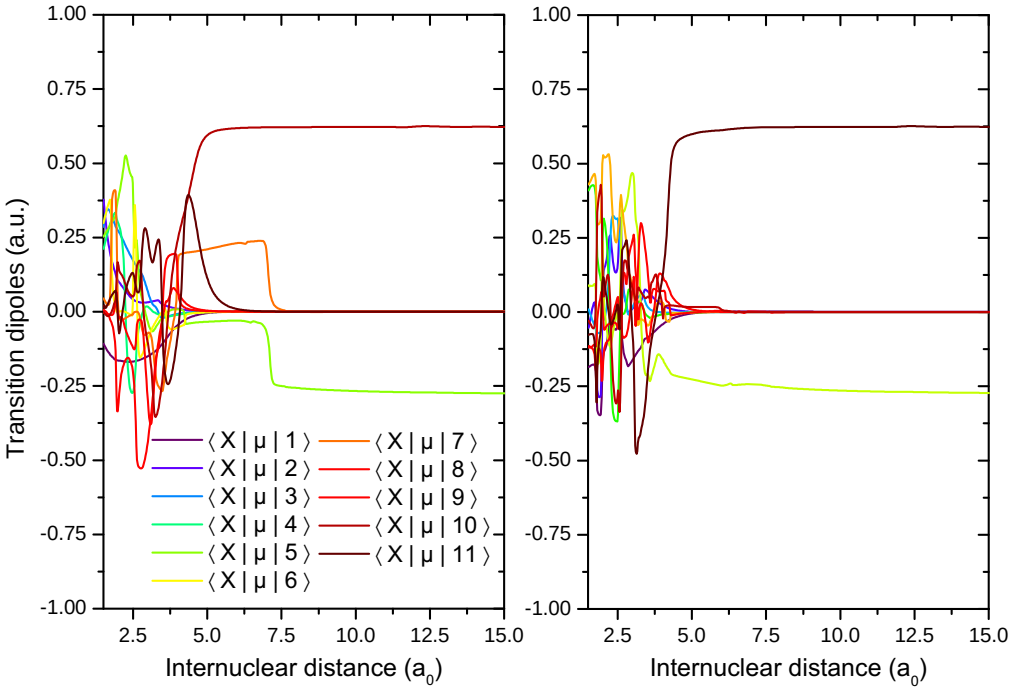

Figure 2.15: Adiabatic (left) and diabatic (right) transition dipole moment between the ground $X\ ^3\Pi$ state and the first 11 $^3\Sigma^-$ states of CO^{2+}.

2.4.6 Vibrational wavefunction

The energies and wavefunctions of the quasibound vibrational levels of the $X\ ^3\Pi$ state of CO^{2+} were computed by solving the nuclear Schrödinger equation in a basis of sines. In this work, our interest was limited to its lowest vibrational level, as the others are known to predissociate very quickly. All photodissociation calculations for CO^{2+} presented in Chapters 3 and 4 were thus performed with $v = 0$ as initial level.

The energy of the lowest vibrational level is in agreement with values available in the literature, as reported by Mrugała [49] and Šedivcová *et al.* [105], on the basis of their own *ab initio* calculations as well as on the experimental threshold photoelectrons coincidence data of Dawber *et al.* [98] and Hochlaf *et al.* [64] (Table 2.8). Fig. 2.16 shows our computed $v = 0$ wavefunction on the potential energy curve of the $X\ ^3\Pi$ state.

Table 2.8: Energy position in cm^{-1} of the $v = 0$ level of the $X\ ^3\Pi$ state of CO^{2+} with respect to the local minimum of its quasibound potential energy well, as reported in the literature and as computed in this work.

Study	$E(v = 0)(cm^{-1})$
Dawber *et al.* [98, 105]	806.7
Hochlaf *et al.* [64, 105]	677.1
Šedivcová *et al.* [105] (Stabilization method)	732.7
Šedivcová *et al.* [105] (Complex scaling method)	732.5
Mrugała [49]	732.2
This work	722.0

This *ab initio* data was used in two ways: first, to compute the cross sections for the photodissociation of the $X\ ^3\Pi$ state of CO^+ through the $^3\Sigma^-$ channels (Chapter 3) and secondly, to compute laser fields controlling this process to maximize the dissociation through the lowest $C^{2+} + O\ ^3\Sigma^-$ channel (Chapter 4).

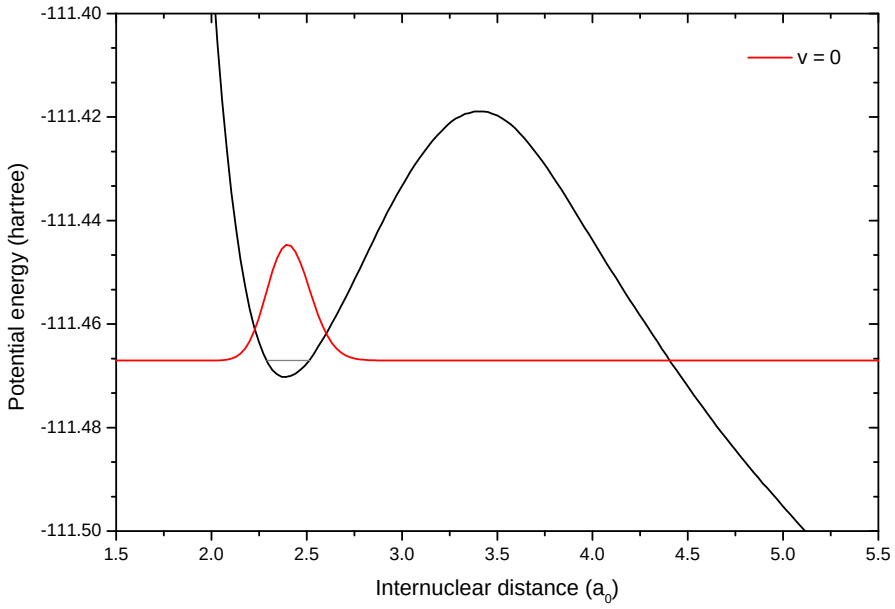

Figure 2.16: Computed potential energy curve of the $X\ ^3\Pi$ state of CO^{2+} and wavefunction of its $v = 0, J = 0$ level.

CHAPTER

3

FIELD-FREE DYNAMICS

Having solved the electronic part of the molecular problem and obtained physical quantities such as the potential, the nonadiabatic couplings and the dipole moments for a series of fixed geometries of the nuclei, one may solve the nuclear part of the problem in order to describe the dynamics of chemical reactions.

Several methods have been developed in this aim and can be split into three main categories:

- *Classical methods*, which treat both the electrons and nuclei as classical objects, significantly simplifying the calculations but leading to results which are often inaccurate for low energies (at which quantum effects play an important role) [110, 111].

- *Semi-classical methods*, which rely on the approximation that the nuclei behave classically, whereas the electrons are correctly described as behaving according to the law of quantum mechanics. Again, this approach simplifies the computations but may lead to inaccurate results [110–113].

- *Quantum methods*, which correctly treat both the electrons and the nuclei as quantum objects.

As mentioned in the introductory chapter, this last category of approaches is further split into time-independent and time-dependent methods. Although they both yield the same results, time-dependent approaches present the advantage of being appropriate even in cases where the Hamiltonian is time-dependent, such as when it includes a laser field (as studied in Chapters 4 and 5 of this thesis).

In the present chapter, we use a quantum, wavepacket-based time-dependent approach to study photodissociation and radiative association reactions at relatively low energy. All calculations presented in this chapter were performed on the HYDRA ULB/VUB computing cluster [86]. The wavepacket propagations and photodissociation cross sections calculations were realized using the code previously developed in the *ThéoSim* group of the *Laboratoire de Chimie Physique* (*Université Paris-Sud*), which we modified and adapted to suit our needs.

We start by giving a general introduction of time-dependent quantum dynamics for molecules, then present our results:

- For the $b\,^3\Sigma^+$ (Section 3.3.1, p. 92) and the $a\,^3\Sigma^+$ states of HeH^+ (Section 3.3.2, p. 105).
- For the $X\,^3\Pi$ state of CO^{2+} (Section 3.4, p. 109).

3.1 Theory of time-dependent quantum molecular dynamics

As we have seen in Chapter 1, the time evolution of any quantum system is governed by the time-dependent Schrödinger equation:

$$i\hbar\frac{\partial}{\partial t}\Psi(t) = H\Psi(t). \tag{3.1}$$

Knowing the wavefunction at a given time t_0 and assuming H is independent of time, the state of the system can be found at any other time t through the following equation:

$$\Psi(t) = e^{\frac{-iH(t-t_0)}{\hbar}}\Psi(t_0), \tag{3.2}$$

where $U(t_0,t) = e^{\frac{-iH(t-t_0)}{\hbar}}$ is the *time evolution operator* or simply *evolution operator*. The time-dependent description of the dynamics of molecular reactions can thus be split into three steps:

1. The definition of the initial wavefunction $\Psi(t_0)$ at time t_0.
2. The propagation of this wavepacket in time, from the initial time t_0 to the desired time t.
3. The extraction of the sought-after physical quantity, such as reaction cross sections, from the behaviour of the wavepacket.

While the definition of the initial wavefunction and the method of calculation of the cross sections may vary from one type of reaction to the next, the time propagation of the wavepacket is always realized through the same kind of methods, which we will now briefly explain (Section 3.1.1). We will then discuss the form of the initial wavepacket and the method of calculation of the cross section for the two kind of reactions we studied, photodissociation (Section 3.2.1, p. 81) and radiative association (Section 3.2.2, p. 86).

3.1.1 Time propagation

Different methods have been developed to solve the time-dependent Schrödinger equation by propagating the wavefunction in time, which differ by the expression of the time evolution operator. The *Chebyshev method* for example relies on the expansion of the operator as a sum of Chebyshev polynomials, but it is known to be very resource-intensive [114–116].

In this work, we use the *Split-Operator* method, so named because it is based on the approximation that the evolution operator $U(t_0, t) = e^{\frac{-iH(t-t_0)}{\hbar}}$ can be split into a product of several exponential operators [117, 118].

First of all, the propagation from the initial time t_0 to the target time t is divided into a series of n small timesteps $\delta t = \frac{t-t_0}{n}$, according to the following sampling criteria:

$$\delta t \leq \frac{\hbar}{\Delta V_{\max}}, \tag{3.3}$$

where $\Delta V_{\max}$ is the difference between the highest and lowest value of the potential, *i.e.* the "energy range" relevant to the calculation.

The propagation of the wavepacket from time t_0 to t is then achieved by applying n times in a row the evolution operator for the small timestep δt:

$$U(t_0, t) = \underbrace{e^{\frac{-iH\delta t}{\hbar}} e^{\frac{-iH\delta t}{\hbar}} \dots e^{\frac{-iH\delta t}{\hbar}}}_{n \text{ times}}. \tag{3.4}$$

Each of these time evolution operator for the short timestep δt are further split into a product of exponentials, on the basis of the Campbell-Baker-Hausdorff formula from Lie algebra (see for example Ref. [119], p. 137) and of the fact that H is the sum of T and V, two non-commuting operators:

$$\begin{aligned} U(\delta t) &= e^{\frac{-iH\delta t}{\hbar}} \\ &= e^{\frac{-i(T+V)\delta t}{\hbar}} \\ &\approx e^{\frac{-iV\delta t}{\hbar}} e^{\frac{-iT\delta t}{\hbar}} + O(\delta t^2). \end{aligned} \tag{3.5}$$

The error in δt can be pushed back to the third order by symmetrizing the product of the kinetic and potential factors [120]:

$$U(\delta t) \approx e^{\frac{-iV\delta t}{2\hbar}} e^{\frac{-iT\delta t}{\hbar}} e^{\frac{-iV\delta t}{2\hbar}} + O(\delta t^3). \tag{3.6}$$

In addition to the upper limit given in Eq. 3.3, the chosen timestep δt must therefore be small enough to prevent the error in $O(\delta t^3)$ inherent to the split-operator method from becoming significant.

For each timestep δt of the propagation, the three exponentials are applied on the wave-

function in succession. For each term, we adopt the representation where the corresponding operator is diagonal, using the adiabatic-to-diabatic $\mathcal{D}$ transformation matrix and its inverse $\mathcal{D}^{-1}$. The kinetic operator T is for example best applied in momentum space and the diabatic basis, where it simply takes the form:

$$e^{-i\frac{\delta t\, T}{\hbar}} = e^{-i\frac{\delta t\, \hbar\, k^2}{2m}}. \tag{3.7}$$

The transition from one space to the other is realized through the Fourier Transform $\mathcal{F}$ or the inverse Fourier Transform $\mathcal{F}^{-1}$. For each timestep δt, we thus apply the following operations in succession[†]:

$$\Psi(t+\delta t) = e^{-i\frac{\delta t V}{2\hbar}}\, \mathcal{D}^{-1}\, \mathcal{F}^{-1}\, e^{-i\frac{\delta t\, \hbar\, k^2}{2m}}\, \mathcal{F}\, \mathcal{D}\, e^{-i\frac{\delta t V}{2\hbar}}\, \Psi(t). \tag{3.8}$$

– Position space, adiabatic basis
– Momentum space, diabatic basis

The desired property can then be extracted from the behaviour of the wavepacket. In the present case, we computed the partial photodissociation and radiative association cross sections based on the behaviour of the wavepacket in the asymptotic region of the potential energy curves (*i.e.* at large values of the internuclear distance R).

3.1.1.1 Spatial grid and complex absorbing potential

This kind of numerical approach requires expressing all data, such as the potential energy curves, the wavefunctions, ... on a regularly-spaced spatial grid, whose spacing δx is also subject to a sampling criteria:

$$\delta x \leq \frac{\pi\hbar}{p_{\max}}, \tag{3.9}$$

where $p_{\max}$ is the highest wavepacket momentum considered in the calculation. The non-respect of this sampling criterion (which, as the criterion on δt given in Eq. 3.3, can be seen as direct consequence of the Shannon-Nyquist sampling theorem [121]) can lead to significant errors in the calculations [122].

The *ab initio* data is interpolated on this grid, whose length is typically equal to a few dozens or a hundred atomic units of length a_0. Care must however be taken to the fact that the fastest-moving components of the wavepacket can possibly reach the end of the grid before the end of the simulation and be reflected back towards the Franck-Condon region, causing interferences. Since using a very long spatial grid would be impractical and resource-consuming, it is common

[†]Note that this expression is only valid in cases where the Hamiltonian is time-independent. The evolution operator for a molecular system exposed to an external time-dependent electric field will be given in Eq. 4.55 (p. 132).

to avoid this problem by placing a *complex absorbing potential* at the end of the grid, which absorbs any wavepacket that nears the extremity of the spatial grid.

This is achieved by adding the following term to the Hamiltonian [123]:

$$H_{\text{abs}} = H - iW_{\text{abs}}(R), \tag{3.10}$$

where $W_{\text{abs}}(R)$ is a real function that is only non-negligible near the end of the spatial grid. In this work, it was defined as:

$$W_{\text{abs}}(R) = \begin{cases} 0 & \text{for} \quad R < R_{\text{abs}} \\ 0.01\dfrac{(R-R_{\text{abs}})^2}{(R_{\text{tot}}-R_{\text{abs}})} & \text{for} \quad R_{\text{abs}} \leq R \leq R_{\text{tot}}, \end{cases} \tag{3.11}$$

where R_{tot} is the value of R at the end of the grid and R_{abs} is the distance at which the complex absorbing potential starts. This expression is only valid for the region between R_{abs} and R_{tot}, as W_{abs} was defined as strictly equal to zero on the rest of the grid.

3.2 Reactions studied

This work focuses on the dynamics of two different (but intrinsically linked) processes: photodissociation and radiative association. In this section, we present these reactions and the methods we used to compute the cross sections and rate constants that characterize them.

3.2.1 Photodissociation reactions

Photodissociation, also called *photodecomposition*, *photofragmentation* and *photolysis*, is a chemical process in which the absorption of light by a molecule leads to its dissociation (Fig. 3.1). More precisely, the absorption of one (or more) photon and its conversion into internal energy places the molecule in the vibrational continuum of an excited state, leading to its decomposition into two fragments or more:

$$\text{AB} + N\ h\nu \longrightarrow (\text{AB})^* \longrightarrow \text{A}(\alpha) + \text{B}(\beta), \tag{3.12}$$

where AB is the parent molecule, N is the number of photons absorbed, $(\text{AB})^*$ is the excited molecule, and A and B are its fragments in internal states α and β.

Photodissociation plays an important role in many contexts, such as photosynthesis (where the photodissociation leads to the oxidation of the oxygen or sulfur of either H_2O or H_2S), atmospheric chemistry (where it notably serves as the driving force and energy source of the ozone cycle), laser conception (where it for example serves as the source of population inversion in iodine lasers [124]) and astrochemistry [125].

From an experimental point of view, photodissociation reactions are also of particular interest as they allow to probe phenomena such as bond breaking, internal energy transfer and radiationless transitions [111].

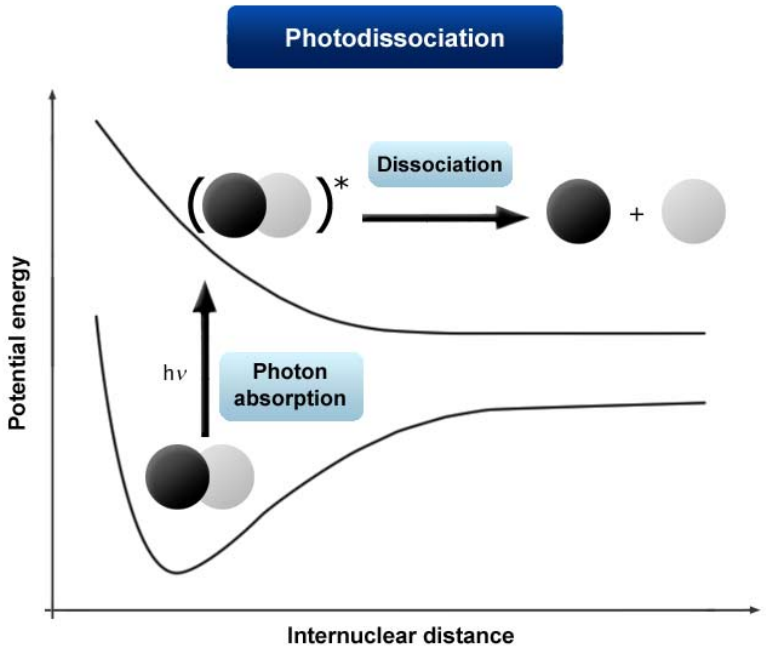

Figure 3.1: General diagram of a photodissociation process.

In this work, we study the photodissociation of the a and $b\ ^3\Sigma^+$ states of HeH^+ towards higher-lying n = 2–3 $^3\Sigma^+$ and $^3\Pi$ states, as well as the photodissociation of the $X\ ^3\Pi$ state of CO^{2+} towards its first 11 $^3\Sigma^-$ states.

3.2.1.1 Initial wavepacket and photodissociation cross sections

Photodissociation is initiated by the transition from an initial electronic state 0 to one or several excited states m[†]. This means the components of the initial wavepacket $\psi^{mJ'}_{0v''J''}(t=0)$ corresponding to the transition from the v'', J'' rovibrational level of the initial electronic state 0 towards the rotational level J' of the excited states m are obtained by multiplying the rovibrational wavefunction of the initial state, $\psi_{v''J''}(R)$, by the appropriate transition dipole moments $\mu_{0,m}(R)$:

$$\psi_{0v''J''\rightarrow mJ'}(R, t=0) = \mu_{0,m}(R)\ \psi_{v''J''}(R). \tag{3.13}$$

Several methods exist to compute the photodissociation cross sections on the basis of the behaviour of the wavepacket.

First of all, the *reflection principle* gives a simplified but intuitive picture of the relationship between the photodissociation cross section and the *ab initio* data it is computed with (*i.e.* the wavefunction of the initial rovibrational level, the potential energy curve of the excited state and

[†]For clarity, we use the following convention in this chapter: v'', J'' denote the rovibrational level of the lower electronic state (*i.e.* the *initial* state in photodissociation but the *final* state in radiative association), while J' denotes the rotational level of the upper state. The index v' is omitted because most of the dissociation channels we consider have no bound vibrational level.

the photodissociation cross section).

Let us consider the photodissociation of a diatomic molecule through a single excited dissociative channel, and let us approximate the shape of the rovibrational wavefunction of the initial state by a Gaussian function centered at the equilibrium distance R_e. In the classical approximation, the photodissociation cross section is then given by [111]:

$$\sigma(E) \approx e^{-2\alpha_R\left(R_t(E)-R_e\right)^2/\hbar} \left|\frac{dV}{dR}\right|^{-1}_{R=R_t(E)}, \tag{3.14}$$

where α_R is linked to the frequency ω of the harmonic oscillator associated to the initial electronic state by the relation $\alpha_R = \mu\omega$, R_e is the equilibrium internuclear distance, and where $R_t(E)$ is the classical turning point, defined by $H(R_t) = E$. Let us further assume that the excited potential energy curve is approximately linear around R_e:

$$\begin{aligned} & V(R) \approx V(R_e) - V_R\,(R - R_e), \\ \text{with} \qquad & V_R = -\left.\frac{dV}{dR}\right|_{R=R_e}. \end{aligned} \tag{3.15}$$

The photodissociation cross section is then given by:

$$\sigma(E) \approx \frac{e^{-\left[2\alpha_R(E-V_e)^2\right]\,/\,\left[\hbar\, V_R^2\right]}}{V_R}. \tag{3.16}$$

Although approximate, this development shows that the general shape of the cross section is linked to that of the initial wavepacket through a factor that depends on the slope of the potential of the dissociation channel in the Franck-Condon region. This allows us to get an intuitive (if somewhat simplified) picture of the relationship between the cross section, the rovibrational wavefunction of the initial state and the potential energy curve of the excited state, as illustrated in Fig. 3.2.

This classical and approximate method of computation of the photodissociation cross sections is however inappropriate for accurate calculations. In this work, we use two quantum methods of calculations of the photodissociation cross sections, which we show to be complementary.

The first method allows the computation of the *total* photodissociation cross section $\sigma^{\text{total}}_{0v''J''\to mJ'}(E)$, that is to say, the sum of the partial, channel-specific cross sections:

$$\sigma^{\text{total}}_{0v''J''\to J'}(E) = \sum_m \sigma^{\text{partial}}_{0v''J''\to mJ'}(E). \tag{3.17}$$

The total cross section is indeed linked to the behaviour of the wavepacket through the following relation [126]:

$$\sigma^{\text{total}}_{0v''J''\to J'}(E) = 4\pi\ \alpha\ a_0^2\ E\ \text{Re}\int_0^\infty C^{J'}_{0v''J''}(t)\ e^{i(E_{0v''J''}+E)t/\hbar}\ dt, \tag{3.18}$$

where E is the photon energy, $E_{0v''J''}$ is the energy of the rovibrational level of the initial state and

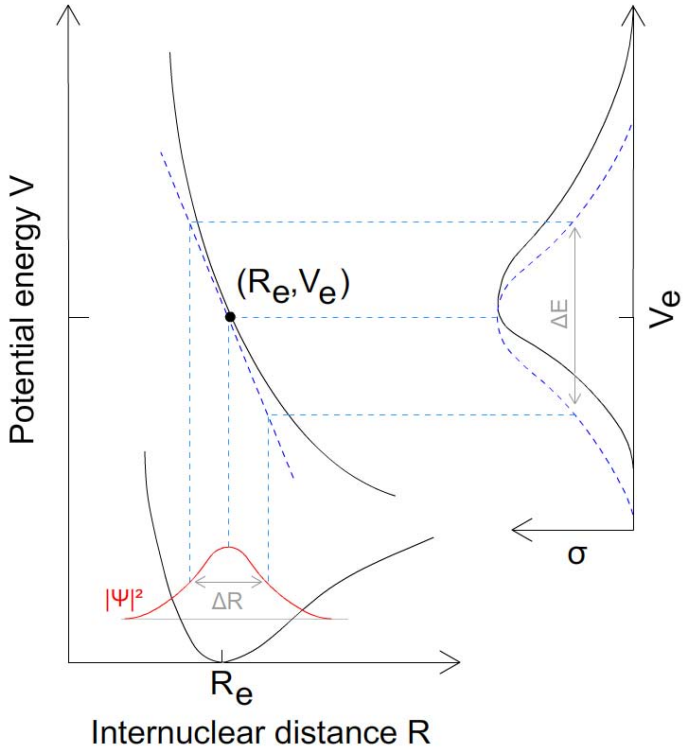

Figure 3.2: Illustration of the one-dimension reflection principle from a bound state to a purely dissociative channel (black curves). The cross section predicted through the reflection principle for a linear potential is represented by the blue dotted curve on the right, while the full black curve represents a more realistic case (Picture based on R. Schinke's *Photodissociation dynamics* [111]).

$C^{J'}_{0v''J''}(t)$ is the *autocorrelation function* of the wavepacket, *i.e.* the overlap between its shape at time t and at the initial time t_0:

$$C^{J'}_{0v''J''}(t) = \sum_m \left\langle \psi^{mJ'}_{0v''J''}(t=0) \,\middle|\, \psi^{mJ'}_{0v''J''}(t) \right\rangle . \tag{3.19}$$

The total cross section characterizes the depopulation of the initial state caused by the absorption of a photon, but it does not contain any channel-specific information: it for example does not tell us through which excited channels the dissociation preferentially occurs. It is therefore unsuitable if one wants to study the photodissociation of a molecule into specific fragments, compute photodissociation branching ratios or obtain radiative association cross sections from a specific excited channel towards the initial state (as will be exposed in Section 3.2.2.1, p. 87).

In order to do all of this, it is necessary to use a method that yields the *partial* (channel-specific) cross sections, such as the one introduced by Balint-Kurti *et al.* [127]. In this approach, the partial cross section characterizing the photodissociation from the initial state 0 through a specific channel m is given by:

$$\sigma^{\text{partial}}_{0v''J''\rightarrow mJ'}(E) = \frac{4\pi^2\ \alpha\ a_0^2\ k_m}{\mu}\ E\ \left|A^{0v''J''}_{mJ'}(E)\right|^2, \tag{3.20}$$

with

$$A^{0v''J''}_{mJ'}(E) = \frac{1}{\sqrt{2\pi}}\int_0^\infty \psi^{0v''J''}_{mJ'}(R_\infty, t)\ e^{i(E_{0v''J''}+E)\,t/\hbar}\ dt, \tag{3.21}$$

where μ is the reduced mass of the molecule, α is the fine structure constant, $k_m = \sqrt{2\mu(E_{0v''J''} + E - E^m_{\text{asymptotic}})}$ is the magnitude of the wave number in the considered channel m and R_∞ is a specific internuclear distance chosen for the computation of the Fourier transform $A^{0v''J''}_{mJ'}$. Ideally, this distance should correspond to the asymptotic region of the potential energy curves, *i.e.* to a large internuclear distance far from the interaction region, where the molecule can be considered as completely dissociated.

In this work, we use both the autocorrelation method (that yields the total cross section) and the method of Balint-Kurti *et al.* (that yields the partial cross sections). Although these two methods must in principle yield the same result (the sum of the partial cross sections obtained with the latter method must be equal to the total cross sections computed with the former), they attain this goal through different means, sometimes leading to discrepancies, as will be shown in the results of our computations.

Let us simply note for now that the autocorrelation method yields the total photodissociation cross section on the basis of what happens to the wavepacket in the Franck-Condon region, as it is based on the overlap of the wavepacket with its form at $t = 0$ (*i.e.* immediately after the excitation). On the other hand, the method developed by Balint-Kurti *et al.* [127] extracts the photodissociation cross sections from the behaviour of the wavepacket in the asymptotic region, at a large value R_∞ of the internuclear distance R).

3.2.1.2 Photodissociation rate constants

As we have seen in Section 1.5 of the introduction (p. 41), whereas cross sections represent the reaction probability as a function of energy for a single molecule, *rate constants* are macroscopic quantities that are more easily related to the amount of molecules formed or destroyed in a given set of physical conditions. Knowing the cross sections and the energy distribution for the physical conditions considered, the corresponding rate constants can easily be calculated.

In the case of photodissociation, one simply needs to know the photodissociation cross sections and the energy distribution of the incoming photons to compute the corresponding photodissociation rate constants. For example, the rate constants for the photodissociation reactions initiated by photons emitted by a blackbody of temperature $T_\star$ and of radius $R_\star$, situated at a distance R, are given by [25]:

$$k_0^{\text{Phot.}}(T) = \frac{4\pi}{h^3c^2}\left(\frac{R_\star}{R}\right)^2 \int \frac{\sigma_0^{\text{Phot.,tot}}(E_{h\nu}, T_{\text{M-B}})\ E_{h\nu}^2}{e^{E_{h\nu}/k_B T_\star} - 1}\ dE_{h\nu}, \tag{3.22}$$

where $\sigma_0^{\text{Phot.,tot}}(E_{h\nu}, T_{\text{M-B}})$ is the total photodissociation cross section characterizing the de-

struction of the initial electronic state 0, assuming a Maxwell-Boltzmann distribution of population in its rovibrational levels:

$$\sigma_0^{\text{Phot.,tot}}(E_{h\nu}, T_{\text{M-B}}) = \frac{\sum_{v'',J''}(2J''+1)\, e^{-E_{v'',J''}/k_B T_{\text{M-B}}}\, \sigma_{0v''J''}^{\text{Phot.,tot}}(E_{h\nu})}{\sum_{v'',J''}(2J''+1)\, e^{-E_{v'',J''}/k_B T_{\text{M-B}}}}. \tag{3.23}$$

Note that $T_{\text{M-B}}$ represents the temperature of the Maxwell-Boltzmann distribution of population in the initial state, while $T_\star$ denotes the temperature of the blackbody emitting the photons responsible for the photodissociation process. As in Roberge and Dalgarno's study of the photodissociation of the $X\,^1\Sigma^+$ state of HeH^+, we chose a ratio $(R_\star/R)^2$ of 10^{-13}, which corresponds to the physical conditions met in planetary nebulæ such as NGC7027, one of the best candidate for the detection of HeH^+ in space.

3.2.2 Radiative association

Radiative association can be seen as the inverse process of photodissociation: two molecular fragments collide and stabilize towards a bound state of the corresponding molecule by emitting the excess energy in the form of a photon (Fig. 3.3).

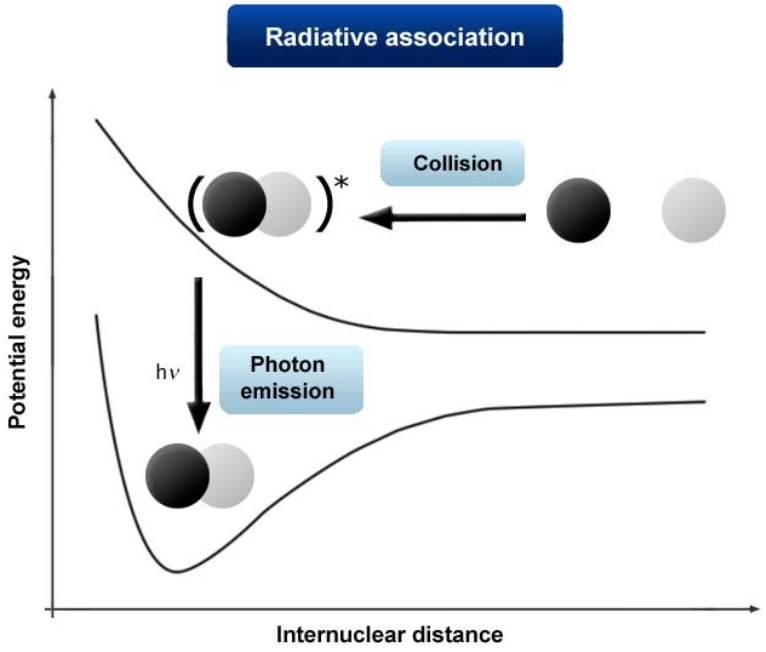

Figure 3.3: General diagram of a radiative association process.

Radiative association is known to play a key role in the formation of molecules in space: at low gas densities, it is the main process by which molecules are formed. In particular, ion gas phase radiative association reactions are known to play a dominant role in the low density, low temperature conditions of the interstellar medium, and ion-molecule radiative association is thought to play an important role in the synthesis of polyatomic species in interstellar clouds [128–130]. It is by radiative association that HeH^+ was first formed in the universe and it

is thought to remain one of its main mechanisms of formation even today [26].

In this work, we more specifically focus on the formation of HeH^+ in its a and $b\,^3\Sigma^+$ states by radiative association of either He^+ and H or He and H^+ through the corresponding $n = 2$ and 3 molecular states (previously listed in Tables 2.1 and 2.2, p. 57–58).

3.2.2.1 Radiative association initial wavepacket and cross sections

Radiative association cross sections are most commonly obtained through time-independent calculations, which require the discretization of the energy continuum and separate calculations for each collisional channel. By contrast, Martinazzo and Tantardini proposed a wavepacket-based method of computation of the radiative association cross sections, arguing that time-dependent methods often have better scaling properties than time-independent methods: in their approach, a single time-dependent calculation yields the radiative association cross section towards all lower channels and for several energies at once [131].

Being a collisional process, radiative association wavepacket-based time-dependent calculations would in principle require the definition of an initial wavepacket that would be propagated from the asymptotic region of a specific excited channel to the interaction region. Typically, this wavepacket would be defined as a Gaussian wave packet with a certain initial momentum, allowing it to cover a particular range of collision energy. Obtaining the cross section on the whole relevant energy range would thus often require several calculations, each covering part of the range of relevant collision energy.

In this work, we however use another time-dependent approach to compute the radiative association cross sections at the same time as the photodissociation cross sections. Since radiative association is the inverse process of photodissociation, the transition dipole matrix elements $M^2_{0v''J'',mJ'}(E) = |\langle\Psi_{0v''J''}|\mu|\Psi_{mJ'}(E)\rangle|^2$ involved in both processes are the same, with the photodissociation cross section from an initial rovibrational level v'', J'' of the 0 state being given by [132]:

$$\sigma^{\text{Phot.,partial}}_{0v''J''\to m}(E_{h\nu}) = \frac{8}{3}\frac{\pi^3}{c\,\hbar\,(4\pi\epsilon_0)}\sum_{J'=J''-1}^{J''+1}\nu\; S_{J'',J'}\; M^2_{0v''J'',mJ'}(E), \tag{3.24}$$

and the corresponding radiative association cross section through the channel m towards all v'', J'' levels of the 0 state being given by [132]:

$$\sigma^{\text{Rad.Ass.}}_{m\to 0}(E_k) = \frac{64}{3}\frac{\pi^5}{c^3\hbar\,(4\pi\epsilon_0)}\sum_{v'',J''}\sum_{J'=J''-1}^{J''+1}\frac{\nu^3_{v''J''}}{k^2_m}S_{J'',J'}\; M^2_{0v''J'',mJ'}(E), \tag{3.25}$$

where $S_{J'',J'}$ are the Hönl-London factors [133].

The radiative association cross section can therefore directly be computed on the basis of the same wavepacket propagation as the corresponding photodissociation cross section (or on the basis of the photodissociation cross section itself). By comparing Eq. 3.24 and 3.25, it is indeed seen that the radiative association cross section $\sigma^{\text{Rad.Ass.}}_{mJ'\to 0v'',J''}$ from an excited channel m towards the v'', J'' level of a lower state is related to the cross section characterizing the photodis-

sociation from that v'', J'' level of the lower state through the channel m by the relation [134]:

$$\sigma^{\text{Rad.Ass.}}_{mJ'\rightarrow 0v''J''} = \frac{E^2_{h\nu}}{\mu\, c^2\, E_k}\sigma^{\text{Phot.,partial}}_{0v''J''\rightarrow mJ'}. \tag{3.26}$$

While the photodissociation cross sections are expressed as a function of the incident photon energy $E_{h\nu}$, the radiative association cross sections are a function of the relative kinetic energy E_k of the two colliding fragments. The two energy scales differ simply by the photodissociation threshold energy $E_{\text{thresh},v''J''\rightarrow m}$, *i.e.* the energy difference between the initial level $v''J''$ and the asymptotic energy of a given dissociation channel m (Fig. 3.4):

$$E_{k,v''J''\rightarrow m} = E_{h\nu} - E_{\text{thresh},v''J''\rightarrow m}. \tag{3.27}$$

The presence of the collision energy E_k in the denominator of Eq. 3.26 implies that radiative association cross sections at low energy (and therefore the corresponding radiative association rate constants at low temperature) are highly sensitive to the value of the corresponding photodissociation cross sections near the threshold energy. Particular care must thus be taken to the accurate determination of photodissociation cross sections near the threshold energy if one wants to compute the corresponding radiative association cross sections, as further discussed in Section 3.3.1.1 (p. 92).

Although computing a radiative association cross section through the propagation of a *dissociative* wavepacket may seem counterintuitive, it presents some advantages: it circumvents the problem of the choice of the initial wavepacket shape in collisional problems and it allows the determination of the cross section on the whole Franck-Condon energy range through a single propagation, whereas several propagations are usually necessary to cover a wide range of energy in a time-dependent collisional approach [131]. Note, however, that the "dissociation" approach used here describes the radiative association from *several* collision channels towards a *single* bound state, whereas the usual collisional approach describes the radiative association from a *single* collision channel towards *several* lower states at once. Our approach is therefore more time-efficient if one wants to study the formation of a molecule in a specific state by radiative association from several collision channels at once, as is the case here. The usual collisional approach is however preferable if one wants to study the different bound electronic states that can be formed by radiative association through a specific initial collision channel.

Since radiative association can occur towards any of the rovibrational levels of the inferior state, its cross section $\sigma^{\text{Rad.Ass.}}_{m\rightarrow 0}$ is obtained by summing the contributions of all the rovibrational levels $\sigma^{\text{Rad.Ass.}}_{mJ'\rightarrow 0v''J''}$. However, since the rotational dependence of the cross sections was neglected in the present study, we approximated the radiative association cross sections by summing the cross sections for all vibrational levels multiplied by the corresponding number of rotational levels. We compared our results with those obtained by neglecting the vibrational dependence of the cross sections as well, which were obtained by multiplying the cross section for $J'' = 0$, $v'' = 0$ by the total number of rovibrational levels of the initial state.

We tested this method on a previously-studied case: the formation of HeH^+ in its ground X

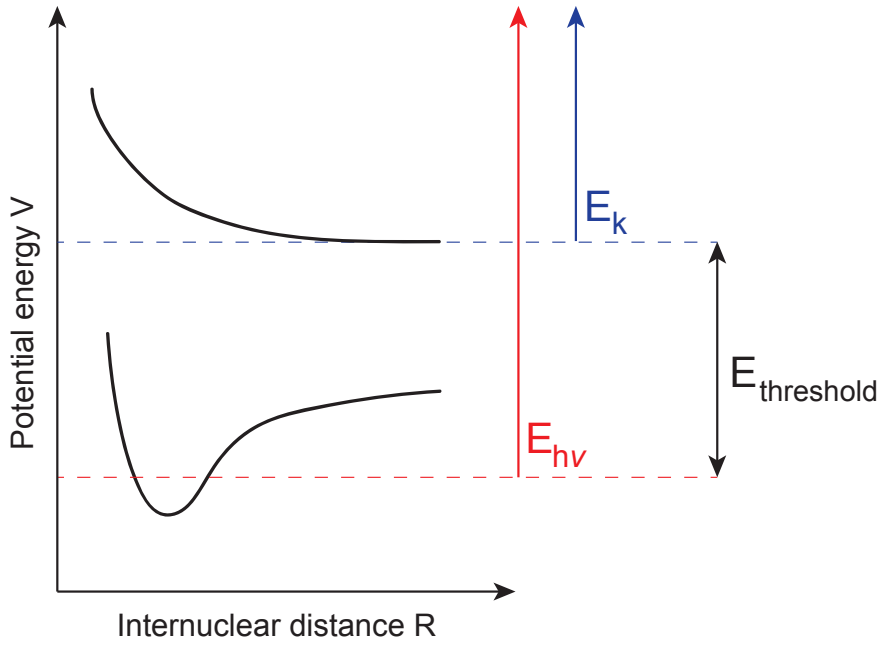

Figure 3.4: General diagram showing the photon energy $E_{h\nu}$ (red arrow) for a photodissociation process from the lowest electronic state (lower black curve), the relative kinetic energy E_k (blue arrow) for a collision process through the lowest excited channel (highest black curve), and the corresponding photodissociation threshold energy (black arrow). The dotted lines denote the zero of the two energy scales.

$^1\Sigma^+$ state by radiative association of He^+ ($1s$) and H($1s$), *i.e.* through the $A\,^1\Sigma^+$ channel [135]. In order to do this, we first computed the partial photodissociation cross sections from each bound vibrational level v'' of the $X\,^1\Sigma^+$ state through the $A\,^1\Sigma^+$ channel, then determined the corresponding radiative association cross section by using Eq. 3.26.

Fig. 3.5 shows the results of these calculations. The dotted black curve represents the radiative association cross section we obtained by neglecting the vibrational dependence of the photodissociation cross sections, *i.e.* by assuming that the cross section obtained for the photodissociation from the $v'' = 0$ level is valid for the photodissociation from all excited vibrational levels $v'' \neq 0$. This is to be compared with the full black curve, which represents the radiative association cross section we obtained by taking the vibrational dependence of the photodissociation cross section into account. That result is in good agreement with that of the earlier study by Kraemer *et al.* [135] (red dashed line). This demonstrates the important impact that the vibrational dependence of the photodissociation cross sections has on the final result, especially at low collision energies. Additional tests for different values of J'' found the rotational dependence of the cross section to be very small in this case.

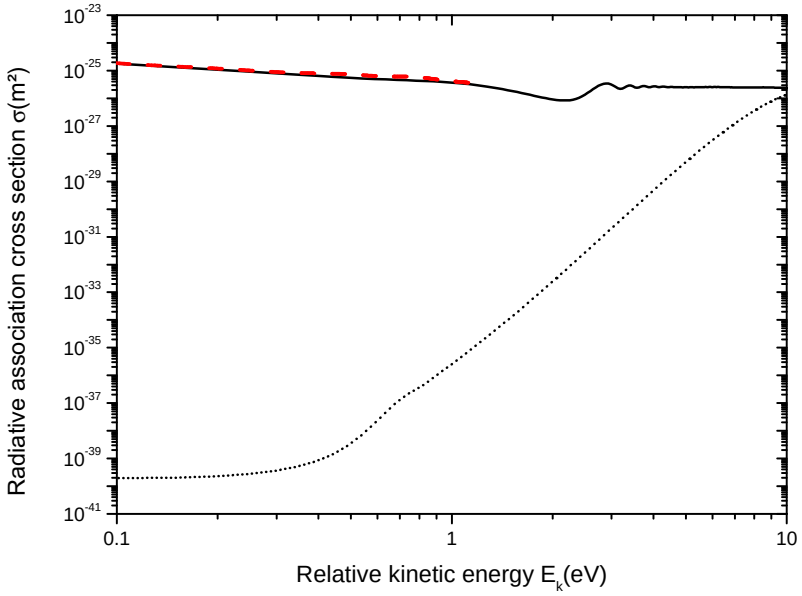

Figure 3.5: Cross section for the radiative association of $He^+(1s)$ and $H(1s)$ towards the ground $X\ ^1\Sigma^+$ state through the $A\ ^1\Sigma^+$ channel, with (black full line) and without (black dotted line) taking its vibrational dependence into account. The results are compared with those of Kraemer *et al.* (1995) (red dashed line).

3.2.2.2 Radiative association rate constants

Knowing the radiative association cross sections, the corresponding rate constants can easily be determined. For a given relative velocity v, the velocity-specific rate constant is simply given by the product of the velocity and of the corresponding radiative association rate constant [136]:

$$k(v) = v\,\sigma(v). \tag{3.28}$$

Of course, outside of specific experiments where the speed of incoming reactants is carefully selected, reactions usually occur between a large number of reactants whose velocities follow a statistical distribution. For the Maxwell-Boltzmann distribution, valid at thermal equilibrium, the rate constant at a given temperature T is given by:

$$k_{m\to 0}^{\text{Rad.Ass.}}(T) = \sqrt{\frac{8}{\pi\,\mu\,k_B^3\,T^3}} \int \sigma_{m\to 0}^{\text{Rad.Ass.}}(E_k)\,E_k\,e^{-E_k/k_B T}\,dE_k. \tag{3.29}$$

The following sections present the results we obtained for the a and $b\ ^3\Sigma^+$ states of HeH^+ (Section 3.3.1 and 3.3.2, p. 92 and p. 105 respectively) as well as the $X\ ^3\Pi$ state of CO^{2+} (Section 3.4, p. 109).

3.3 Photodissociation and radiative association of the triplet states of HeH^+

In this section, we discuss the computation of the photodissociation cross sections from the a and $b\,^3\Sigma^+$ states of HeH^+, as well as of the radiative association cross sections towards these two states. Although HeH^+ is one of the simplest closed-shell diatomic ions in its ground state, its nuclear dynamics in its excited states is far from trivial as they are strongly coupled by nonadiabatic interactions.

Until Loreau *et al.* started studying the triplet states of HeH^+ [2–6], only its formation in its singlet states had been considered in astrophysical contexts. Here, we study the possible formation of HeH^+ in its two lowest $^3\Sigma^+$ states by radiative association (as well as its destruction by photodissociation), as first started by Jérôme Loreau during his Ph.D. thesis. We expand his work in two directions, first by taking into account the full vibrational dependence of the photodissociation cross sections of the $a\,^3\Sigma^+$ state, and secondly by studying the photodissociation and radiative association of the $b\,^3\Sigma^+$ state for all vibrational levels.

The $b\,^3\Sigma^+$ channel of HeH^+ indeed corresponds to an interesting couple of molecular fragments: a proton H^+, and a helium atom He in its metastable $1s2s\,^3S$ state, which has a lifetime of about 8000 s. The $b\,^3\Sigma^+$ state is therefore a very good candidate for the formation of HeH^+ in a triplet state but, due to its very short radiative lifetime ($\tau \approx 10^{-8}$ s [137]), it is expected to quickly deexcitate towards the metastable $a\,^3\Sigma^+$ state.

Thanks to its very long radiative lifetime ($\tau = 149$ s for its lowest rovibrational level [3, 138]), the $a\,^3\Sigma^+$ state is expected to play an important role in the astrochemistry of HeH^+. Computing the rates of formation and destruction of both the a and $b\,^3\Sigma^+$ states is therefore crucial to the comprehension of the astrochemistry of HeH^+ in its triplet states.

While the computation of the photodissociation cross section from the lowest rovibrational level of the initial state is usually straightforward, the computation of individual cross sections for each initial rovibrational level tends not only to be time-consuming (as a full propagation is necessary for each $v'', J'' \rightarrow v', J'$ transition) but also to suffer from additional difficulties, mostly stemming from the wider spatial distribution of the initial wavepacket and from the appearance of centrifugal barriers in the excited states potentials for high values of J'. In the present work, we neglect the rotational dependence of the photodissociation cross sections, as calculations for large values of J''[†] found its impact to be much smaller than that of v'' and since its correct description would require an impractically high number of wavepacket propagations[‡].

All calculations were performed using the potential energy curves, nonadiabatic radial couplings and dipole moments computed by Loreau *et al.* [2] as well as the vibrational wavefunctions corresponding to the CBS-extrapolated potential energy curves we computed, as pre-

[†] Up to the largest values of J'' corresponding to levels below the dissociation limit.

[‡] For example, since the $b\,^3\Sigma^+$ state of HeH^+ supports a total of 1307 rovibrational levels, at least ≈ 3900 individual wavepacket propagation would be necessary to describe each possible $v'', J'' \rightarrow v', J'$ transition due to the $J' = J'' \pm 1, 0$ selection rule.

sented in Chapter 2, p. 59. All Σ and Π triplet states up to $n = 3$ were included in our dynamical calculations, *i.e.* 11 $^3\Sigma^+$ and 6 $^3\Pi$ states (shown on Fig. 2.2 on p. 55), as photodissociation perpendicular to the laser polarization was shown to play an important role in the case of the ground state [6].

We start by discussing the approach we used and the results we obtained for the $b\,^3\Sigma^+$ state, as its peculiarities make it a good example of the difficulties that may arise when computing photodissociation cross sections from excited vibrational levels of an excited electronic state, as well as of the need of combining two computation methods to obtain accurate results.

3.3.1 Results for the $b\,^3\Sigma^+$ state

All wavepacket propagations for the calculation of the photodissociation of the $b\,^3\Sigma^+$ were performed on a spatial grid of 2^{13} points that spans from an internuclear distance $R_{\text{min}} = 0.5\ a_0$ up to $R_{\text{max}} = 200\ a_0$. The use of a long spatial grid was made necessary by the wide spatial spread of the wavefunction of the highest initial vibrational levels. The Fourier transform for the computation of the partial cross sections was performed at $R_\infty = 175\ a_0$, and we placed a quadratic optical potential starting at $R_{\text{abs}} = 180\ a_0$ in order to avoid reflections of the wavepacket at the edge of the grid. Propagations up to 5×10^7 atomic units of time (1.2 ns) were performed, with a timestep δt of 1 a.u. for all 33 initial vibrational levels. Additional tests with shorter timesteps were carried out to ensure accuracy.

The $b\,^3\Sigma^+$ state exhibits properties which complicate the dynamics of its photodissociation: it is close in energy to a large number of other electronic states, both bound and dissociative, which are strongly coupled by nonadiabatic interactions. Moreover, its large number of vibrational levels (33) also make it a good example of the importance of taking the vibrational dependence of the photodissociation cross sections into account.

We ran into two difficulties in the course of our calculations: first, the presence of Gibbs oscillations in some of our cross sections and secondly, the presence of resonances which we could not adequately describe with the present approach.

3.3.1.1 Gibbs oscillations

Although it presents the advantage of yielding state-specific information, the method of calculation of the partial cross sections developed by Balint-Kurti *et al.* suffers from an important drawback: unlike the autocorrelation-based method, it only takes into account the parts of the wavepacket that reach the asymptotic region of the dissociation channels and ignores its trapped fractions as long as they stay in the potential energy wells. This should in principle be a good thing, but it has an unfortunate consequence: the partial cross sections obtained with this method often start abruptly at the threshold photodissociation energy and are thus affected by the Gibbs phenomenon [139], which causes ringing artifacts around jump discontinuities in Fourier transforms, as illustrated in Fig. 3.6.

Such Gibbs oscillations only appear if the cross section is non-negligible at the threshold energy. The reflection principle allows for an intuitive understanding of the conditions under

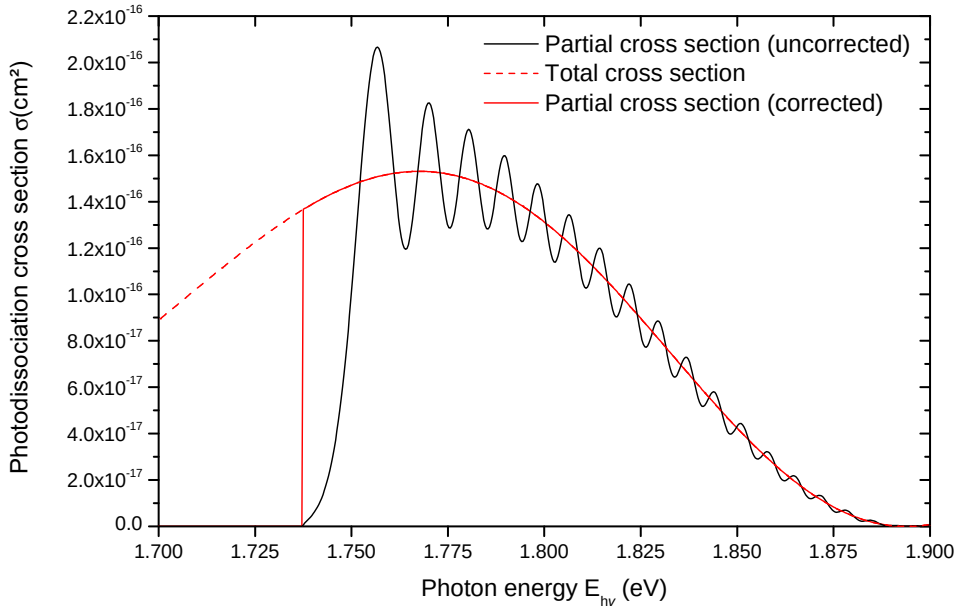

Figure 3.6: The Gibbs phenomenon leads to the appearance of discontinuities near the threshold energy in the partial photodissociation cross section from the $v'' = 2$ level of the $b\ ^3\Sigma^+$ state towards the $H^+ + He(1s2p\ ^3P)$ fragments (full line, black), while the total cross section as obtained through the Fourier transform of the autocorrelation function for short propagation times is perfectly smooth (dashed line). Thanks to this, the correct form of the partial cross section can be deduced (full line, red).

which this will happen: the dissociation channel has to support a bound vibrational level, which needs to be in a region where the wavefunction of the initial rovibrational level is non-negligible (Fig. 3.7, cases (c) and (d)). This is more likely to be the case for excited vibrational levels because of the wider spread of the wavefunction (Fig. 3.7, compare cases (b) and (d)). Despite this, the cross section may not start abruptly at the threshold energy for certain specific values of v'' as one of the nodes of the wavefunction may coincide, through the reflection principle, with the asymptotic energy of the dissociation channel (Fig. 3.7, case (e)). Whether or not Gibbs oscillations appear thus depends on several factors: the topology of the potential energy curves, their relative positions and the initial vibrational level.

The presence of such unphysical artifacts in the cross sections is particularly problematic in our case: as mentioned in Section 3.2.2.1, the radiative association cross sections at low energy are very sensitive to the value of the corresponding photodissociation cross sections near the threshold energy, potentially leading to severely inaccurate radiative association rate constants at low temperature if the ringing artifacts are not suppressed.

Although various filtering methods may be used to reduce these ringing artifacts [139], it is generally impossible to suppress them completely. It is however possible to do so in the present case using the total photodissociation cross section calculated from the autocorrelation func-

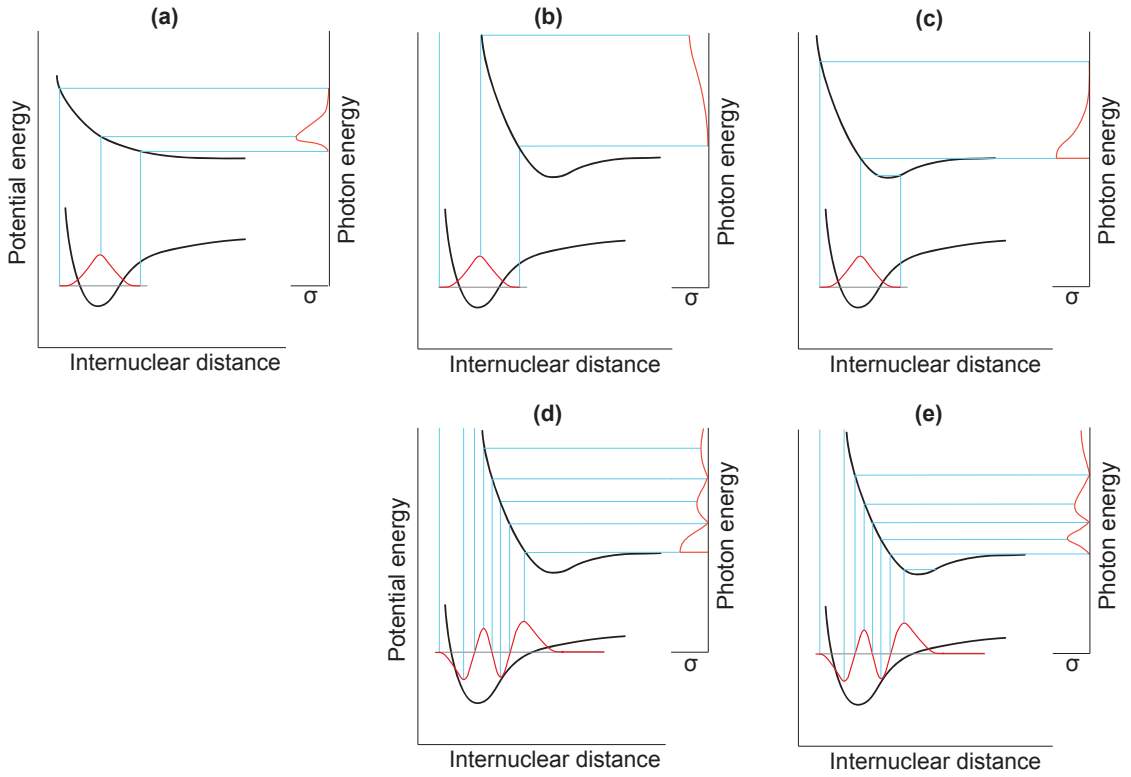

Figure 3.7: Schematic illustration of various cases where the partial photodissociation cross section σ does not start abruptly at the threshold energy (a, b, e) and where it does (c, d), depending on the shapes and relative position of the potential energy curves and on the initial rovibrational level.

tion for short propagation times (Fig. 3.8): since it (incorrectly) describes predissociation as a smooth envelope, no jump discontinuity occurs at the photodissociation threshold energy. It is therefore unaffected by the Gibbs phenomenon (Fig. 3.6). As the sum of the partial cross sections must be equal to the total cross section in the energy ranges where it contains no contribution from the incorrectly-described predissociation, the total cross section obtained for short propagation times can thus be used as a reference to suppress the ringing artifacts in a given partial cross section for a channel m_f:

$$\sigma^{\text{partial}}_{0v''J''\to m_f J'}(E) = \sigma^{\text{total}}_{0v''J''\to J'}(E) - \sum_{m\neq m_f} \sigma^{\text{partial}}_{0v''J''\to mJ'}(E) \tag{3.30}$$

However, this is only possible if the ringing artifacts do not occur in the same range of energy for two different exit channels, as their respective contributions to the total cross sections cannot be separated in that case. By combining the results of our computations of the partial and total photodissociation cross sections, we were able to reduce or suppress the ringing artifacts near the threshold energy and to obtain the partial photodissociation cross sections from the 33 vibrational levels of the $b\,^3\Sigma^+$ state through the 15 other $n = 2$–$3\,^3\Sigma^+$ and $^3\Pi$ dissociation channels.

At least two calculations were therefore performed for each initial vibrational level v'': one

with relatively long propagation times to obtain the partial cross sections through the method of Balint-Kurti *et al.*, and a shorter one to obtain the total cross section through the Fourier transform of the autocorrelation function.

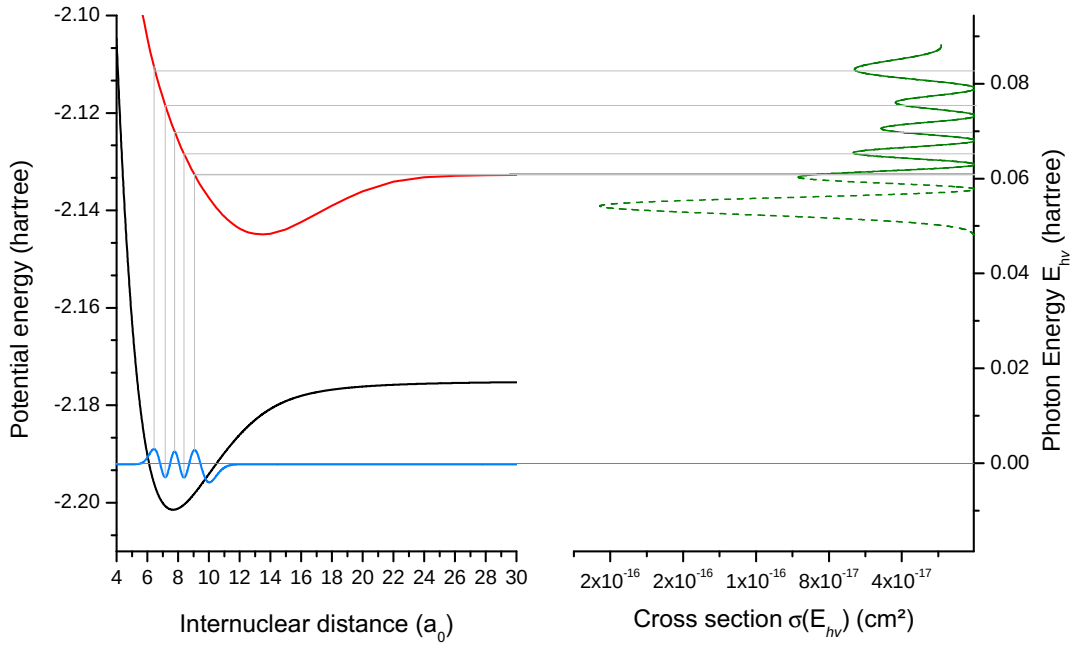

Figure 3.8: Computed photodissociation cross section of the $v'' = 5$ level of the $b\,^3\Sigma^+$ state of HeH^+ (black) through the $H^+ + He(1s2p\,^3P^o)$ channel (red). The Fourier transform of the autocorrelation not only yields the direct photodissociation cross section (green, full line), but also a contribution from predissociation (green, dotted line) which incorrectly appears as uninterrupted at the threshold energy for short propagation times.

3.3.1.2 Resonances

Two types of resonances are encountered in the photodissociation cross sections of the $b\,^3\Sigma^+$ state of HeH^+: *Feshbach* resonances and *Shape* resonances (Fig. 3.9)[†]. Unfortunately, our present method of calculation makes their accurate calculation impossible, or at least unreasonably time-consuming.

The Feshbach resonances are caused by the nonadiabatic crossing between a bound excited state and a lower dissociation channel: trapped parts of the wavepacket move back and forth in the potential energy well of the bound state until they nonadiabatically cross to the dissociative channel, leading to the appearance of resonances in its cross section [141]. We chose to neglect this kind of resonance completely in the present calculations: their exact determination would have required impractically long propagation times in our approach, as a non-negligible

[†]Another good example of a study where the two kind of resonances arise in the photodissociation cross sections of a diatomic cation can be found in Ref. [140], for example.

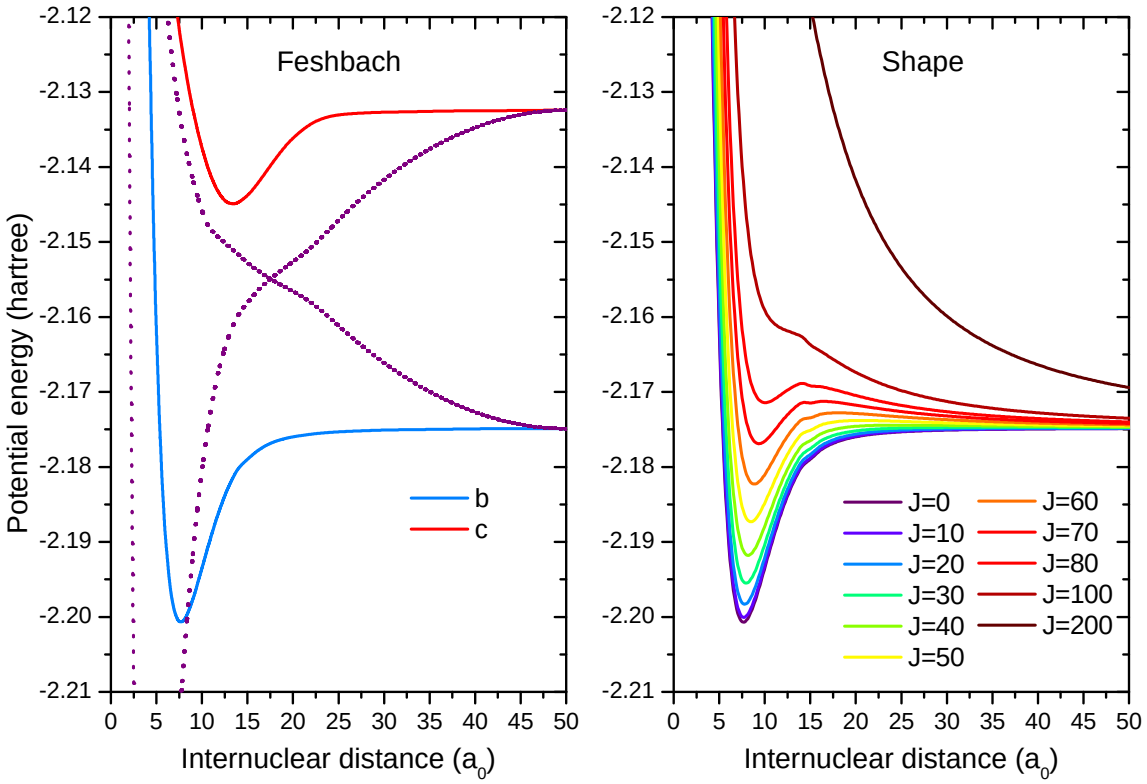

Figure 3.9: Example of situations leading to the appearance of resonances in the photodissociation cross sections. Left: the bound $c\,^3\Sigma^+$ state (red) is nonadiabatically coupled to the lower $b\,^3\Sigma^+$ state (blue), leading to the appearance of *Feshbach resonances* (dotted lines: corresponding diabatic curves). Right: for certain values of J such as $J = 80$, the potential energy curve of the $b\,^3\Sigma^+$ state exhibits a centrifugal barrier through which tunneling may occur, leading to *Shape resonances*.

fraction of the initial wavepacket was still found in bound potential energy wells after propagation times as high as 50×10^6 a.u. of time (1.2 ns). Their computation using other approaches would likewise have been very time-consuming due to the very large number of initial levels to consider (1307). Moreover, their impact on the photodissociation rate constants is expected to be small, as their asymmetric Fano profile would likely limit their net result upon integration of the cross sections to obtain the rate constants (Eq. 3.22). Since such resonances may be more adequately described using partitioning techniques [142] or the time-independent formalism [143, 144], we chose to neglect them completely in our calculations.

The oscillations of the wavepacket in the potential energy well can easily be suppressed when computing the total photodissociation cross section through the autocorrelation method (for low values of v'' at least): their appearance occurs on a longer timescale than direct photodissociation, as illustrated by the autocorrelation function in the case of the photodissociation of the $v'' = 5$ level (Fig. 3.10, black curve). The departure of the wavepackets from the Franck-Condon region and the return of their trapped fractions occur on two distinct timescales and, if the propagation is stopped before their return, the computed cross section shows no sign of resonances [126] and exhibits instead a smooth continuation of the cross section below the thresh-

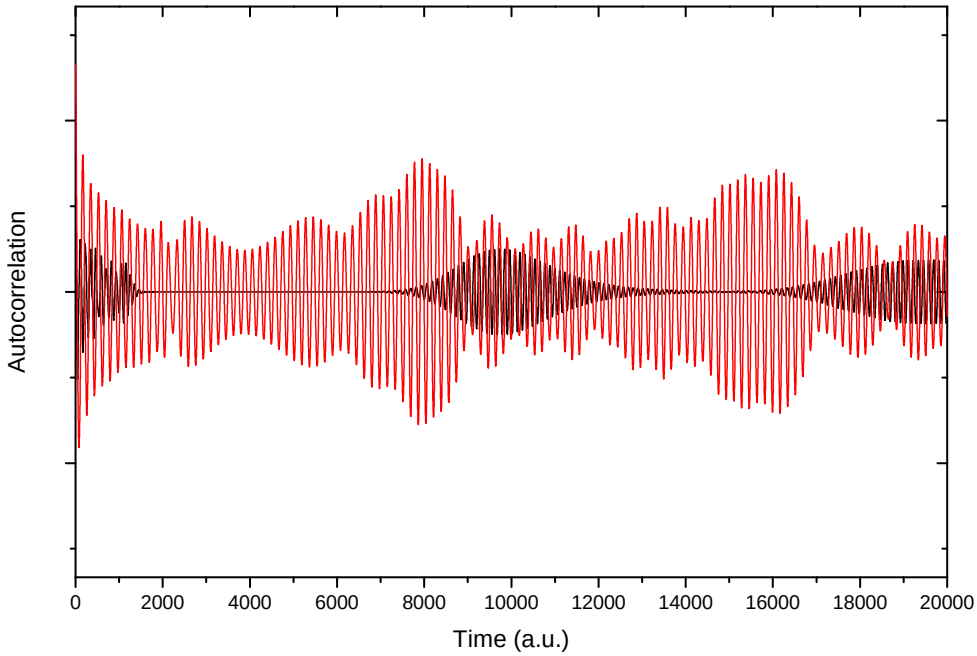

Figure 3.10: Autocorrelation function (arbitrary units) for the photodissociation of the $v'' = 5$ (black) and $v'' = 15$ (red) levels of the $b\,^3\Sigma^+$ state through higher excited $^3\Sigma^+$ channels. In the case of $v'' = 5$, two different time scales can clearly be observed: direct photodissociation occurs during the first 2000 a.u. of time, whereas the trapped fraction of the wavepacket comes back to the Franck-Condon region after about 7000 a.u. of time. This is however not the case for $v'' = 15$.

old energy. This can be understood intuitively as the autocorrelation function then contains no information about the trapped fraction of the wavepacket and behaves as if the complete wavepacket could directly reach the asymptotic region [141]. This smooth envelope gradually disappears for longer propagation times as the Feshbach resonances appear in its stead. While a resonance-free total cross section can easily be obtained for the first few vibrational levels by using short propagation times, this is often not possible for higher vibrational levels as the Franck-Condon region becomes wider, keeping the autocorrelation function from ever falling to zero (Fig. 3.10, red curve).

Partial photodissociation cross sections free from Feshbach resonances can however often be obtained by stopping the time propagation early enough, since the fraction of the wavepackets that dissociates directly usually reaches the asymptotic region on a much shorter timescale than the fraction that stays momentarily trapped in potential energy wells: the direct dissociation process and the nonadiabatic predissociation occur on two distinct timescales.

Shape resonances caused by tunneling through the centrifugal barriers are also expected to appear for high values of J', but the very large number (1307) of rovibrational levels of the $b\,^3\Sigma^+$ state precluded us from computing individual cross sections for each of them as a full wavepacket propagation would be necessary for each possible $J'' \rightarrow J' = J'' \pm 1$ transition towards other $^3\Sigma^+$ states, as well as for each possible $J'' \rightarrow J' = J'', J'' \pm 1$ transition towards $^3\Pi$

states. We therefore chose to completely neglect the rotational dependence of the cross sections, as its impact on the cross sections was shown to be smaller than that of the vibrational dependence in the case of the $X\ ^1\Sigma^+$ state [6, 145]. However, although the envelopes of the cross sections may not vary as significantly with J'' as with v'', shape resonances have been shown to significantly augment photodissociation and radiative association rate constants in some systems, especially at low temperature [146, 147]. It is therefore common to compute the envelope of the cross section through time-dependent methods without regards to shape resonances as their exact determination would require an impractically fine energy grid and long propagation times. They can indeed be computed separately, *e.g.* through the Breit-Wigner formalism [148, 149].

3.3.1.3 Photodissociation cross sections

As in the case of the photodissociation of the $X\ ^1\Sigma^+$ state, we found the initial vibrational level v'' to have a very large impact on the resulting photodissociation cross sections, whereas the impact of the initial rotational level J'' was found to be much smaller. This is illustrated by Fig. 3.11 and 3.12, which show the photodissociation cross sections from two of the lowest vibrational levels of HeH^+, and from the lowest and highest rotational levels of the lowest vibrational level of HeH^+, respectively.

As can be readily seen from Fig. 3.11, the initial vibrational level v'' dramatically affects the photodissociation cross section: the $v''=3$ result is significantly different from the $v''=0$ result. The impact of the vibrational excitation of the initial state on the photodissociation cross sections is indeed twofold:

1. The nodal structure of the wavefunction directly affects the photodissociation cross sections (see for example Fig. 3.13 or compare panels (b) and (d) in Fig. 3.7, p. 94).

2. Moreover, the spread of the wavefunction towards high values of R tends to favor transitions towards different excited channels.

Although not negligible, the influence of the initial rotational level J'' is comparatively much smaller, as shown in Fig. 3.12, which compares the results for $J''=0$, 15 and 73 within the $v''=0$ vibrational level. Moreover, the variation of the cross sections with increasing J'' is very progressive, unlike the dramatic changes observed whenever the initial vibrational level v'' is modified. This can be attributed to the fact that the nodal structure of the wavefunction stays unchanged when the value of J'' is modified, within a given vibrational level v''.

To give a broader overview of our results, Figures 3.13 and 3.14 show our total photodissociation cross sections from several vibrational levels of the $b\ ^3\Sigma^+$ state towards the 9 higher $n=2$–3 $^3\Sigma^+$ states and towards the 6 $n=2$–3 $^3\Pi$ states, respectively. The corresponding partial photodissociation cross sections were subsequently used to determine the radiative association cross sections towards the $b\ ^3\Sigma^+$ state for each excited channel. It is worth noting that the cross sections for the photodissociation through the $^3\Pi$ channels are much larger than for the photodissociation through the $^3\Sigma^+$ channels, confirming the large role played by perpendicular transitions in the destruction of HeH^+ by photodissociation, as previously reported for the

ground $X\,^1\Sigma^+$ state [6].

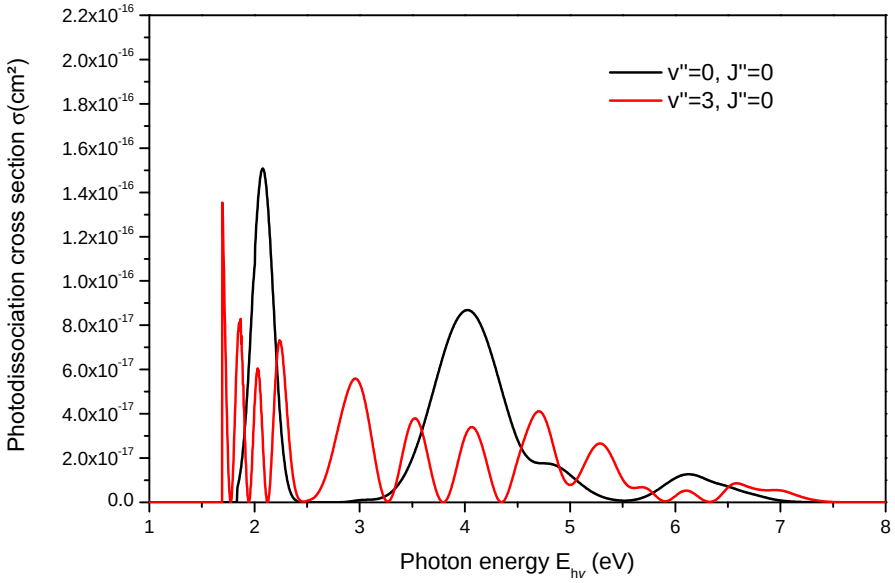

Figure 3.11: Comparison between the total photodissociation cross sections from the $v'' = 0, J'' = 0$ and $v'' = 3, J'' = 0$ rovibrational levels of the $b\,^3\Sigma^+$ state through the higher $n = 2$–3 $^3\Sigma^+$ channels.

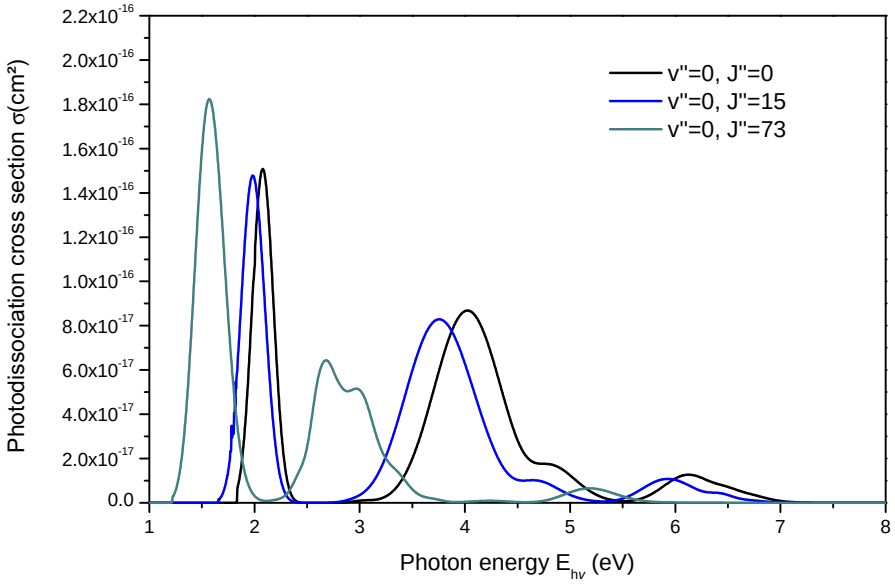

Figure 3.12: Comparison between the total photodissociation cross sections from the $v'' = 0, J'' = 0$; $v'' = 0, J'' = 15$ and $v'' = 0, J'' = 73$ rovibrational levels of the $b\,^3\Sigma^+$ state through the higher $n = 2$–3 $^3\Sigma^+$ channels.

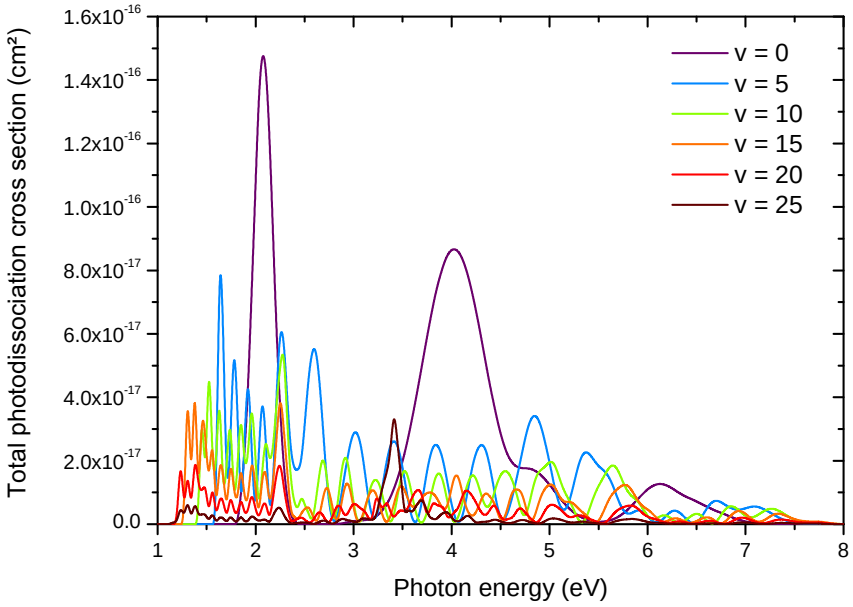

Figure 3.13: Total photodissociation cross sections from several vibrational levels of the $b\,^3\Sigma^+$ state through the higher $n = 2$–$3\,^3\Sigma^+$ channels.

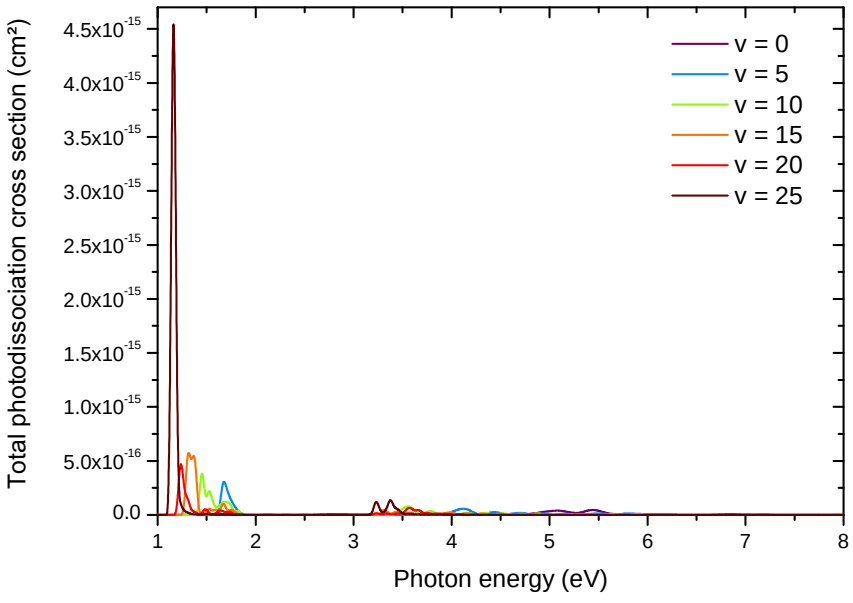

Figure 3.14: Total photodissociation cross sections from several vibrational levels of the $b\,^3\Sigma^+$ state through the $n = 2$–$3\,^3\Pi$ channels.

3.3.1.4 Radiative association cross sections

Like the corresponding photodissociation cross sections, the radiative association cross sections towards the $b\,^3\Sigma^+$ state of HeH^+ are found to change by several orders of magnitude when their vibrational dependence is taken into account, as shown in Fig. 3.15 for three of the excited channels. It is important to note that the radiative association cross sections at low energies are highly sensitive to the corresponding photodissociation results near the threshold energy, often requiring very long propagation time and correction of the Gibbs oscillations to properly describe the low-energy components.

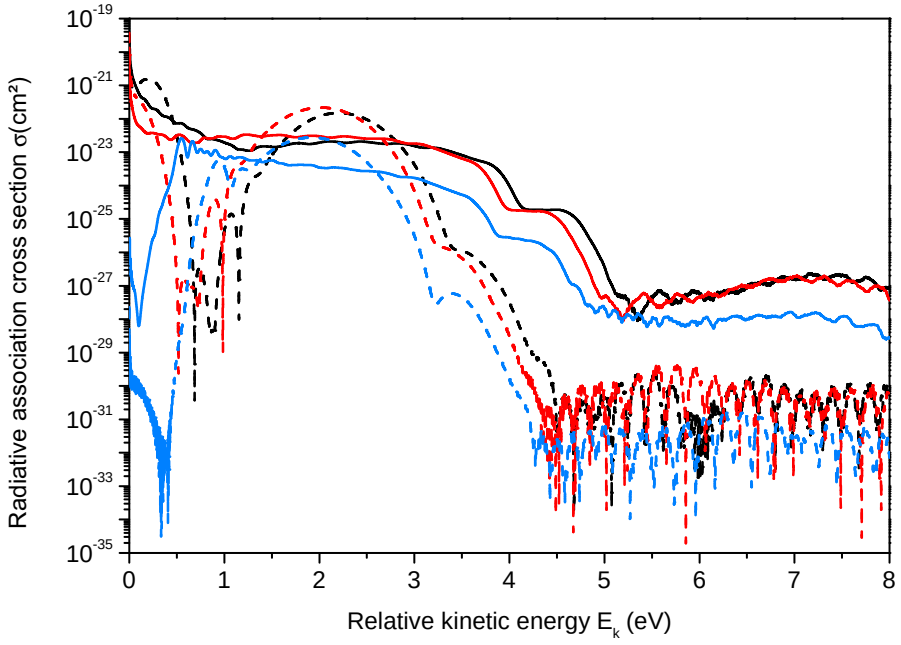

Figure 3.15: Cross sections for the radiative association of $He(1s3p\ ^3P)$ + H^+ (black curves), $He^+(1s\ ^2S)$ + $H(2p\ ^2P)$ (red curves), and $He^+(1s\ ^2S)$ + $H(2s\ ^2S)$ (blue curves) towards the $b\,^3\Sigma^+$ state of HeH^+ with (full lines) and without (dashed lines) taking the vibrational dependence of the cross sections into account. Note that the oscillations observed below 10^{-29} cm^2 are caused by numerical inaccuracies and have no physical sense.

3.3.1.5 Rate constants

Like in Roberge and Dalgarno's study of the photodissociation of the $X\,^1\Sigma^+$ state of HeH^+, we chose a ratio $(R_\star/R)^2$ of 10^{-13} (which corresponds to the physical conditions met in planetary nebulæ such as NGC7027) to compute our photodissociation rate constants [25]. As previously mentioned, the cross sections were assumed to be independent of J'' (*i.e.* $\sigma_{v'',J''} = \sigma_{v'',J''=0}$ for all J''). Fig. 3.16 shows our results as a function of the temperature of the central star $T_\star$ for different values of the temperature $T_{\text{M-B}}$ of the Maxwell-Boltzmann population distribution in the rovibrational levels of the initial state. Like in all calculations of this kind, it should be noted that

the photodissociation rate constants are likely to be underestimated at high blackbody temperature due to the absence of excited states beyond $n = 3$ in our computational basis.

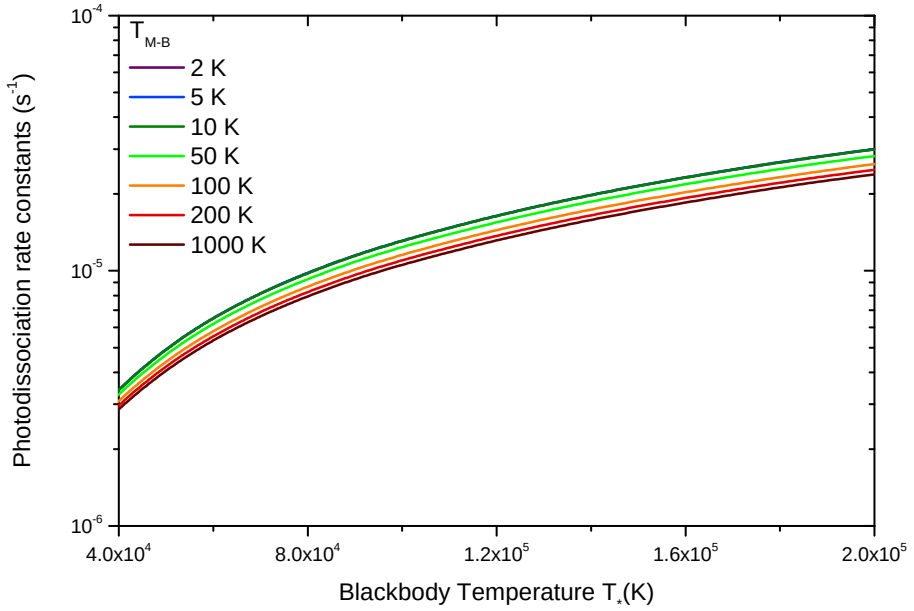

Figure 3.16: Rate constants for the photodissociation of the $b\,^3\Sigma^+$ state of HeH^+ through the $n = 2$–$3\,^3\Sigma^+$ and $^3\Pi$ states as a function of the temperature $T_\star$ of the blackbody, for the Maxwell-Boltzmann distribution corresponding to different temperatures $T_{\text{M-B}}$. The $T_{\text{M-B}} = 2$ K result, for which only the $v'' = 0, J'' = 0$ level is populated, is obtained for all Maxwell-Boltzmann distribution temperatures if the vibrational dependence of the cross section is neglected, as the photodissociation cross sections for all v'', J'' levels are then assumed to be equal to the cross section for the $v'' = 0, J'' = 0''$ level.

Both photodissociation and radiative association rate constants are found to vary strongly with the initial/final vibrational level v'' considered. Qualitatively similar results are to be expected for other systems in which the photodissociation cross sections of the first vibrational levels differ significantly near the threshold energy, which depends both on the shapes and on the relative positions of the potential energy curves.

Our results indicate that the formation of HeH^+ in its $b\,^3\Sigma^+$ state by radiative association is most likely to occur through the $c\,^3\Sigma^+$ (He($1s2p\,^3P$) + H^+) channel or through the α (He($1s2s\,^3P$) + H^+) and $\gamma\,^3\Pi$ (He($1s3p\,^3P$) + H^+) channels.

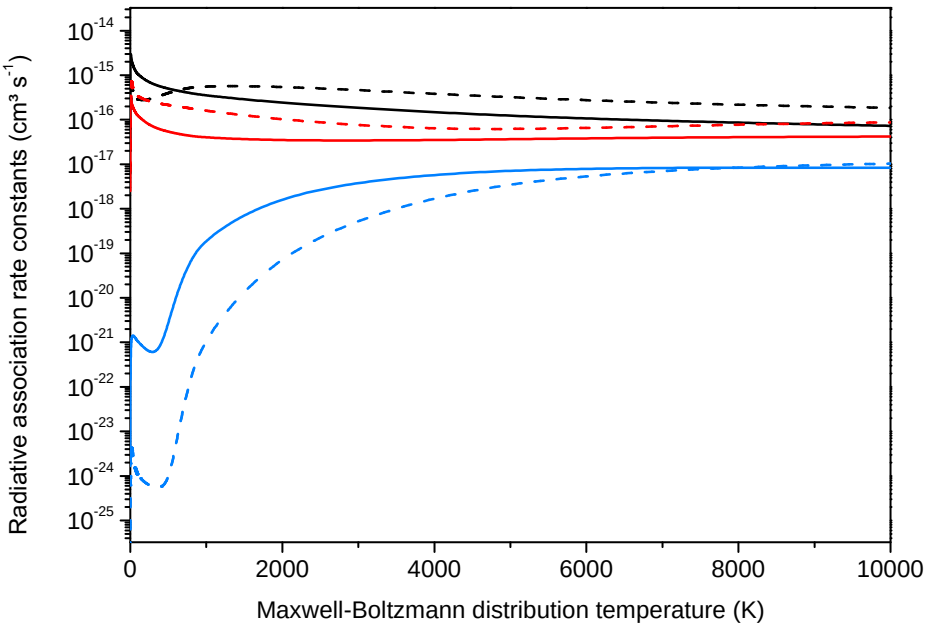

Figure 3.17: Rate constants for the radiative association of $He(1s3p\ ^3P)$ + H^+ (black curves), $He^+(1s\ ^2S)$ + $H(2p\ ^2P)$ (red curves), and $He^+(1s\ ^2S)$ + $H(2s\ ^2S)$ (blue curves) towards the $b\ ^3\Sigma^+$ state of HeH^+ through the $^3\Sigma^+$ channels with (full lines) and without (dashed lines) taking the vibrational dependence of the cross sections into account.

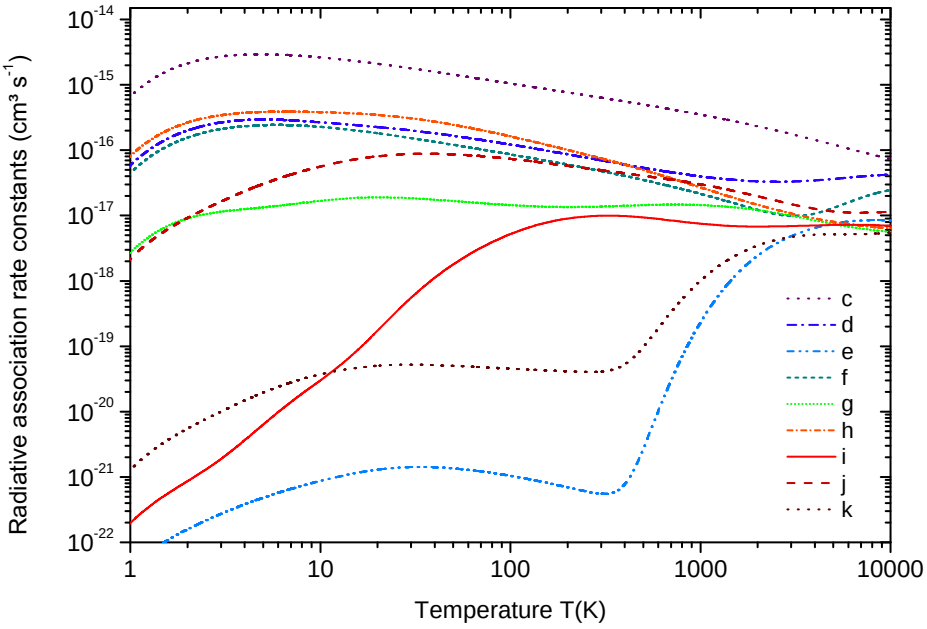

Figure 3.18: Rate constants for the formation of HeH^+ in its $b\ ^3\Sigma^+$ state by radiative association through the n = 2–3 $^3\Sigma^+$ channels. State designation follows the convention given in Table 2.1 (p. 57).

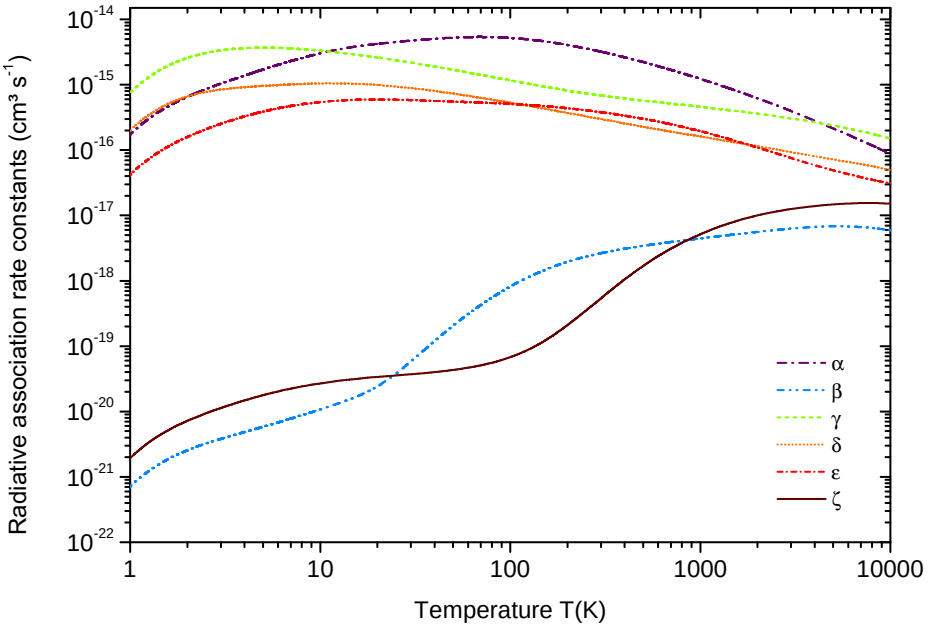

Figure 3.19: Rate constants for the formation of HeH^+ in its $b\,^3\Sigma^+$ state by radiative association through the $n = 2$–$3\ ^3\Pi$ channels. State designation follows the convention given in Table 2.2 (p. 58)

3.3.2 Results for the $a\,^3\Sigma^+$ state

By comparison to the $b\,^3\Sigma^+$ state, calculations for the $a\,^3\Sigma^+$ are relatively simple and straightforward. The $a\,^3\Sigma^+$ only possesses 6 bound vibrational levels for $J'' = 0$, significantly reducing the number of required wavepacket propagations.

Most calculations were performed on a spatial grid of 2^{13} points spanning from an internuclear distance $R_{\text{min}} = 0.5\ a_0$ up to $R_{\text{max}} = 100\ a_0$. The partial cross sections were calculated at $R_\infty = 75\ a_0$ and a complex absorbing potential starting at $R_{\text{abs}} = 80\ a_0$ was used. These parameters were however modified for the highest vibrational level, $v'' = 5$, due to the wider spatial spread of its wavefunction: the partial cross sections were calculated at $R_\infty = 100\ a_0$ and we used a quadratic optical potential ranging from $R_{\text{abs}} = 120\ a_0$ to the end of the grid, at $R_{\text{max}} = 150\ a_0$.

As in the case of the $b\,^3\Sigma^+$ state, propagations up to 5×10^7 atomic units of time (1.2 ns) were performed, with a timestep δt of 1 a.u. Tests with shorter timesteps were carried out to ensure accuracy. The same approach as before was used to suppress the Gibbs oscillations and to obtain resonance-free partial cross sections.

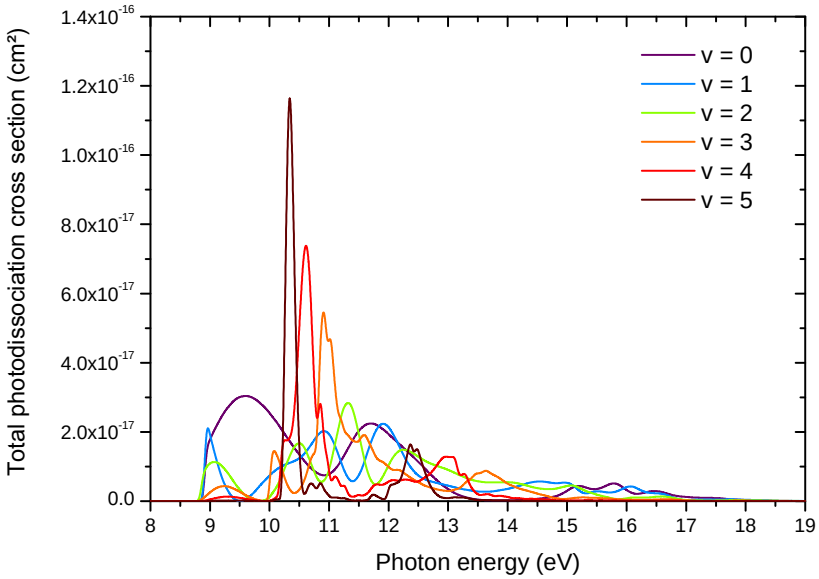

Figure 3.20: Total photodissociation cross sections from several vibrational levels of the $a\,^3\Sigma^+$ state through the higher $n = 2$–$3\ ^3\Sigma^+$ channels.

Figures 3.20 and 3.21 show the photodissociation cross sections from the $a\,^3\Sigma^+$ towards the $n = 2$–$3\ ^3\Sigma^+$ and $^3\Pi$ states, respectively. Even though the $a\,^3\Sigma^+$ state of HeH^+ has significantly less bound vibrational levels than the $b\,^3\Sigma^+$ state for $J'' = 0$ (6 instead of 33), the impact of the vibrational dependence of the photodissociation cross sections on the corresponding radiative association cross sections and on the rate constants is far from negligible, although it is comparatively small for the $b\,^3\Sigma^+$ ($He(1s2s\ ^3S) + H^+$) channel. Figure 3.22 shows the radiative association cross sections towards the $a\,^3\Sigma^+$ states from the first three higher $^3\Sigma^+$ channels, with

and without taking the vibrational dependence into account.

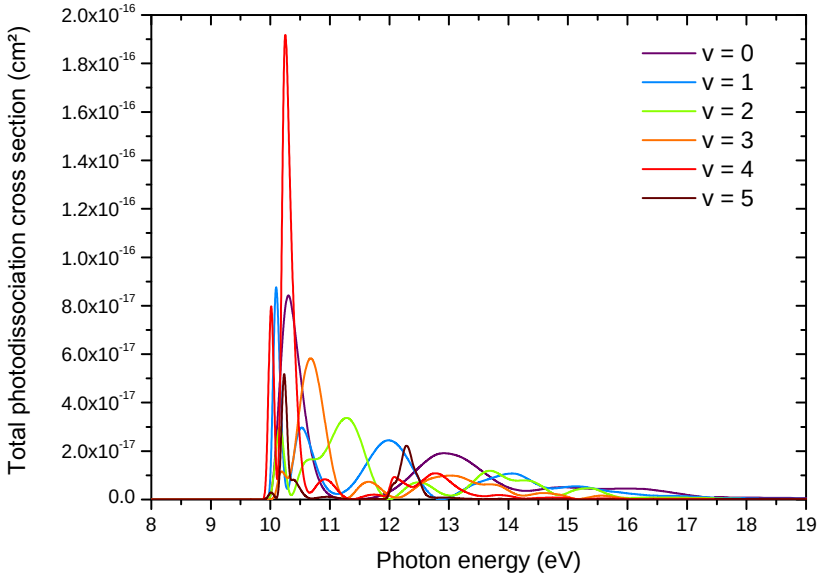

Figure 3.21: Total photodissociation cross sections from several vibrational levels of the $a\,^3\Sigma^+$ state through the $n = 2$–$3\,^3\Pi$ channels.

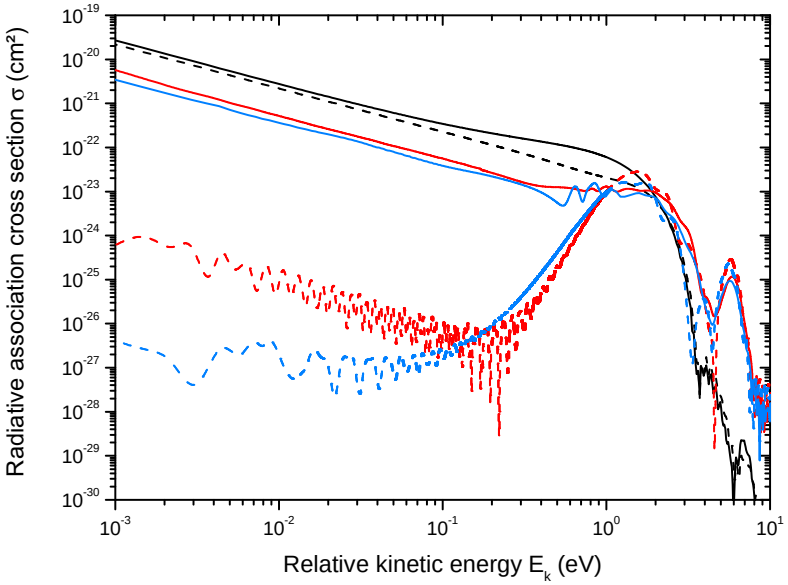

Figure 3.22: Cross sections for the radiative association of $\mathrm{He}(1s2s\,^3S) + \mathrm{H}^+$, $\mathrm{He}(1s2p\,^3P) + \mathrm{H}^+$ (red curves), and $\mathrm{He}^+(1s\,^2S) + \mathrm{H}(2p\,^2P)$ (blue curves) towards the $a\,^3\Sigma^+$ state of HeH^+ with (full lines) and without (dashed lines) taking the vibrational dependence of the cross sections into account.

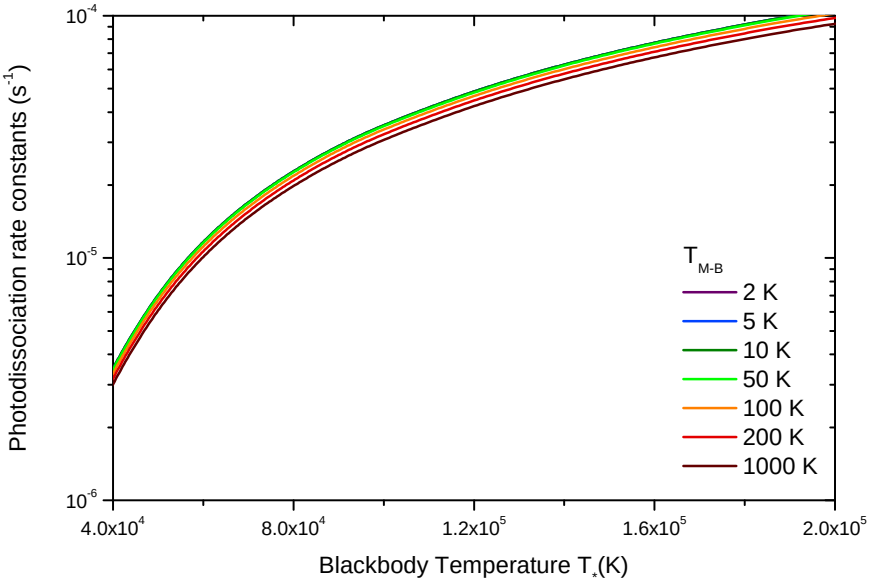

Figure 3.23: Rate constants for the photodissociation of the $a\,^3\Sigma^+$ state of HeH^+ through the $n = 2$–$3\,^3\Sigma^+$ and $^3\Pi$ states as a function of the temperature $T_\star$ of the blackbody, for the Maxwell-Boltzmann distribution corresponding to different temperatures $T_{\text{M-B}}$. The $T_{\text{M-B}} = 2$ K result, for which only the $v'' = 0, J'' = 0$ level is populated, is obtained for all Maxwell-Boltzmann distribution temperatures if the vibrational dependence of the cross section is neglected, as the photodissociation cross sections for all v'', J'' levels are then assumed to be equal to the cross section for the $v'' = 0, J'' = 0''$ level.

Figures 3.24 and 3.25 respectively show our computed rate constants for the radiative association from the $n = 2$–$3\,^3\Sigma^+$ and $^3\Pi$ states of HeH^+ towards its $a\,^3\Sigma^+$ state. In the $^3\Sigma^+$ symmetry, the highest rate constant at all temperature is that of the formation through the $b\,^3\Sigma^+$ channel, *i.e.* the collision of H^+ and metastable helium $He(1s2s\,^3S)$. Even higher rate coefficients have however been obtained for the radiative association through the two lowest $^3\Pi$ channels, α and β, which correspond to the collisions $He(1s2s\,^3P) + H^+$ and $He^+(1s\,^2S) + H(2p\,^2P)$, respectively.

On the basis of these results, J. Loreau proposed a rough estimate of the abundances of HeH^+ in planetary nebulæ. Despite the higher rate constants observed for some of the Π channels, the formation of HeH^+ in its $a\,^3\Sigma^+$ state is more likely to occur through the $b\,^3\Sigma^+$ by radiative association of metastable helium $He(1s2s\,^3S)$ and a proton H^+, due to the high abundances of these species in nebulæ. In this context, the quantity of HeH^+ in its $a\,^3\Sigma^+$ state assuming equilibrium between its formation by radiative association and its destruction by photodissociation is given by the relation:

$$n_{HeH^+(a\,^3\Sigma^+)}\; k^{\text{Phot.}}_{a\,^3\Sigma^+ \rightarrow\, ^3\Sigma^+,^3\Pi} = n_{He(1s2s\,^3S)}\; n_{H^+}\; k^{\text{Rad. Ass.}}_{b\,^3\Sigma^+ \rightarrow\, a\,^3\Sigma^+}, \tag{3.31}$$

where:

– $n_{HeH^+(a\,^3\Sigma^+)}$, $n_{He(1s2s\,^3S)}$ and n_{H^+} are the densities of HeH^+ in its $a\,^3\Sigma^+$ state, of helium in

its $1s2s\,^3S$ metastable state and of protons, respectively.

- $k^{\text{Phot.}}_{a\,^3\Sigma^+ \rightarrow\, ^3\Sigma^+,^3\Pi}$ is the photodissociation rate constant of the $a\,^3\Sigma^+$ state.
- $k^{\text{Rad. Ass.}}_{b\,^3\Sigma^+ \rightarrow\, a\,^3\Sigma^+}$ is the radiative association rate constant for the formation of HeH^+ in its $a\,^3\Sigma^+$ through the $b\,^3\Sigma^+$ channel.

In order to compute $n_{HeH^+(a\,^3\Sigma^+)}$, we use values of these parameters corresponding to the conditions encountered in a typical planetary nebula: $n_{H^+} = 10^{-4}$ cm^4, $n_{He^+} = 10^3$ cm^{-3}, $T_\star = 5\times10^4$ K and $T_{\text{M-B}} = 10^4$ K [150]. To compute the density of metastable helium $n_{He(1s2s\,^3S)}$, we use a formula derived by Clegg which depends on the ionized helium density n_{He^+}, the electron density and the temperature [151]. With our chosen set of parameters, this leads to an approximate value of $n_{He(1s2s\,^3S)} \approx 4\times10^{-3}$ cm^{-3}.

Using our computed rate constants, we obtain an estimated density of HeH^+ in its lowest triplet state of $n_{HeH^+(a\,^3\Sigma^+)}$ of approximately 3×10^{-10} cm^{-3}, which is much lower than the estimated density of HeH^+ in its ground $X\,^1\Sigma^+$ state [30]. The presence of a non-negligible quantity of helium in its triplet states in planetary nebulæ can nonetheless influence the abundances of neutral and ionized hydrogen and helium. Moreover, the formation of HeH^+ in its $a\,^3\Sigma^+$ state may have occurred in the early universe, since neutral helium was first formed by the recombination of He^+ with an electron, populating its metastable $1s2s\,^3S$ state among others [27, 138].

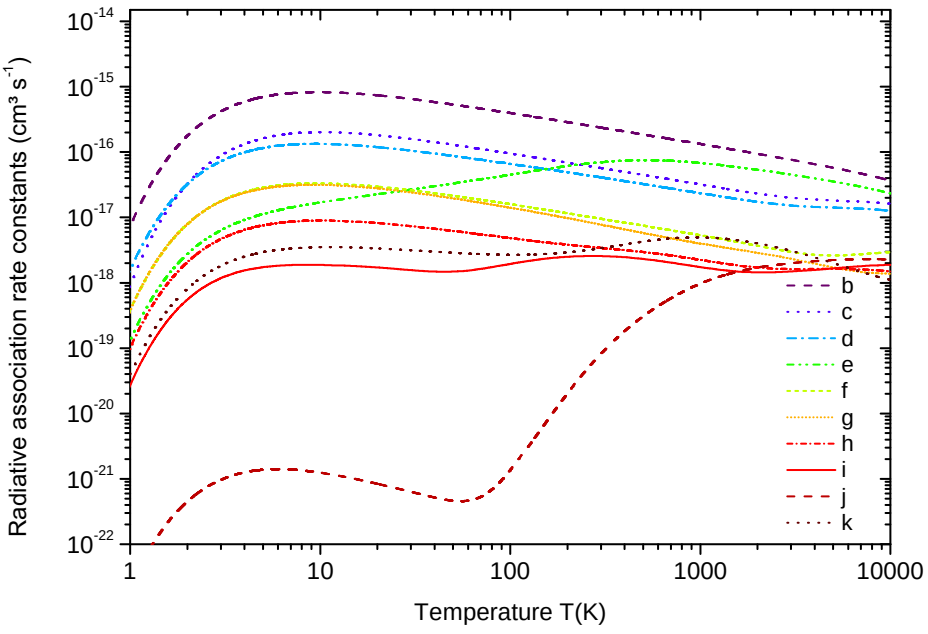

Figure 3.24: Rate constants for the formation of HeH^+ in its $a\,^3\Sigma^+$ state by radiative association through the $n = 2$–$3\,^3\Sigma^+$ channels. State designation follows the convention given in Table 2.1 (p. 57).

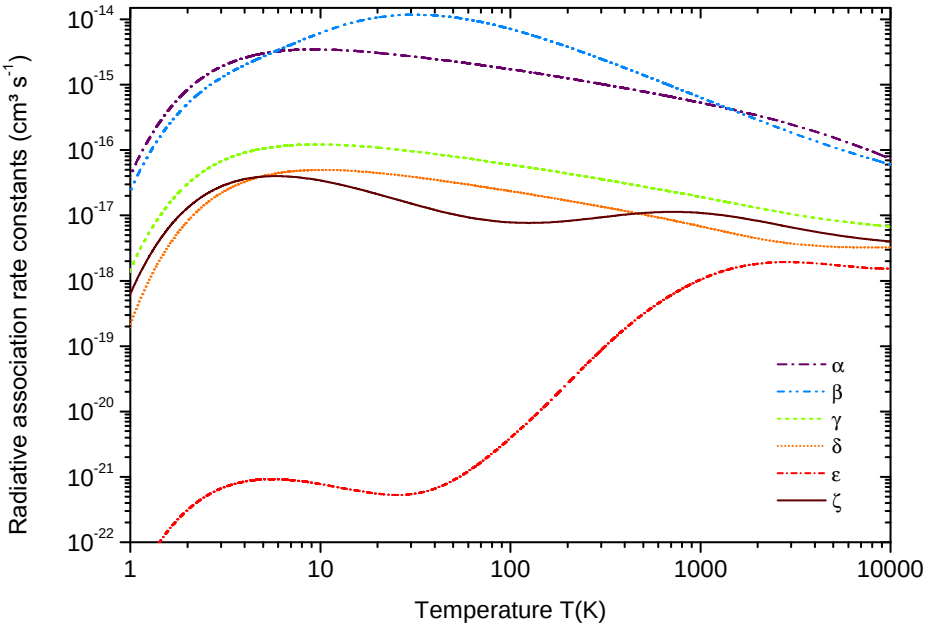

Figure 3.25: Rate constants for the formation of HeH^+ in its $a\,^3\Sigma^+$ state by radiative association through the n = 2–3 $^3\Pi$ channels. State designation follows the convention given in Table 2.1 (p. 57).

3.4 Photodissociation cross sections of CO^{2+}

Unlike HeH^+, CO^{2+} only has one long-lived vibrational level in its ground $X\,^3\Pi$ state. Only one set of partial photodissociation cross sections was thus calculated, that characterizes the photodissociation from the $v'' = 0$ level of the $X\,^3\Pi$ state towards the first eleven $^3\Sigma^-$ states. This makes the computation very straightforward compared to the case of HeH^+, especially since no bound excited electronic state is involved here.

The propagations were performed on a spatial grid of 2^{12} points spanning from an internuclear distance $R_{\mathrm{min}} = 1.5\ a_0$ up to $R_{\mathrm{max}} = 100\ a_0$. The computation of the partial cross sections was based on the value of the wavepacket at $R_\infty = 50\ a_0$ and the start of the complex absorbing potential was chosen as $R = 80\ a_0$. Propagations up to 10^5 atomic units of time (2.42×10^{-4} ns) were performed, with a timestep δt of 1 a.u. Propagations with shorter timesteps were also carried out to ensure accuracy.

Fig. 3.26 shows our computed partial cross sections. The respect of the reflection principle is much less obvious here than in the case of HeH^+, most likely due to the very sharp slope and somewhat "bumpy" shape of the potential energy curves of the excited states in the Franck-Condon region.

As in the case of HeH^+, the sum of the partial cross sections obtained with the method of Balint-Kurti *et al.* was compared with the total cross section as computed through the autocorrelation method, with a timestep $\delta t = 0.1$ a.u. and a total propagation time of 1000 a.u. Fig. 3.28

shows the resulting autocorrelation function. The total cross section as computed through the autocorrelation function and the sum of the partial cross sections as computed through the method of Balint-Kurti *et al.* were found to be in perfect agreement.

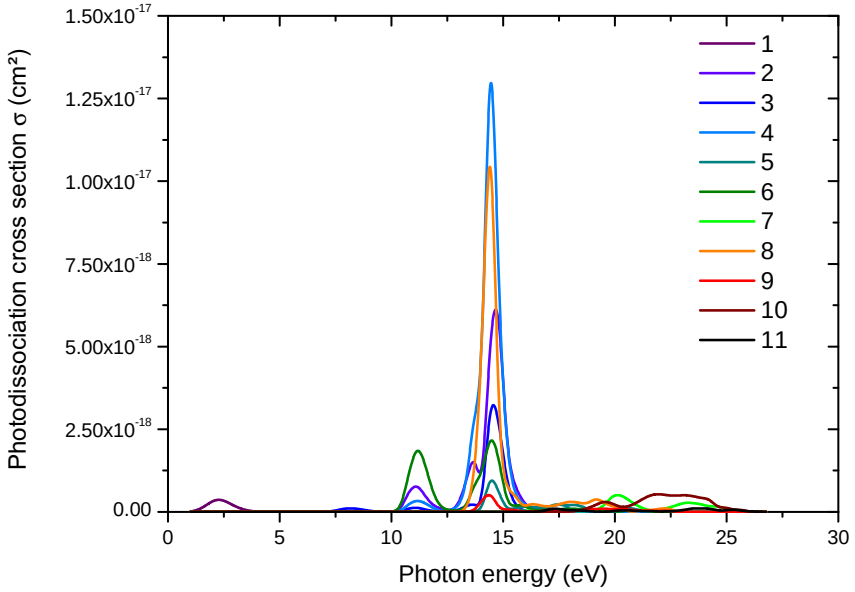

Figure 3.26: Partial photodissociation cross sections from the $v'' = 0$ level of the $X\ ^3\Pi$ state of CO^{2+} through its 11 lowest $^3\Sigma^-$ channels. State designation follows the convention given in Table 2.6 (p. 69).

The comparison with our $v'', J'' = 0$ results for the a and b states of HeH^+ is however interesting. Since the $^3\Pi \rightarrow ^3\Sigma^-$ transition dipole moments of CO^{2+} are much smaller than the $^3\Sigma^+ \rightarrow ^3\Sigma^+$ transition dipole moments of HeH^+, the associated photodissociation cross sections are much smaller too. The photodissociation process is also found to occur on a much shorter timescale than for HeH^+: the wavepacket leaves the Franck-Condon region in less than 10^3 a.u. of time and reaches $R = 50\ a_0$ in less than 10^4 a.u.). This quick dissociation can be attributed to the absence of bound or quasibound excited states, as well as to the fact that the potential energy curves of the excited states of CO^{2+} have much sharper slopes in the Franck-Condon region than those of HeH^+, leading to higher momenta for the excited wavepacket (as seen in Fig. 3.28, the wavepacket completely leaves the Franck-Condon region in about 1000 a.u. of time).

Of particular interest to us is the photodissociation cross section towards the ninth $^3\Sigma^-$ state, which dissociates into $C^{2+} + O$ instead of $C^+ + O^+$, as it is the target of our laser control simulations presented in Chapter 4. Our computed cross section for that channel is very small (see the red curve on Figs. 3.26 and 3.27) and several other channels have a higher cross section in that energy range. This is both due to the fact that the potential energy curves of the excited states are very close to each other in the Franck-Condon region (as seen earlier in Fig. 2.12, p. 72) and to the fact that the nonadiabatic couplings cause numerous nonradiative transition between

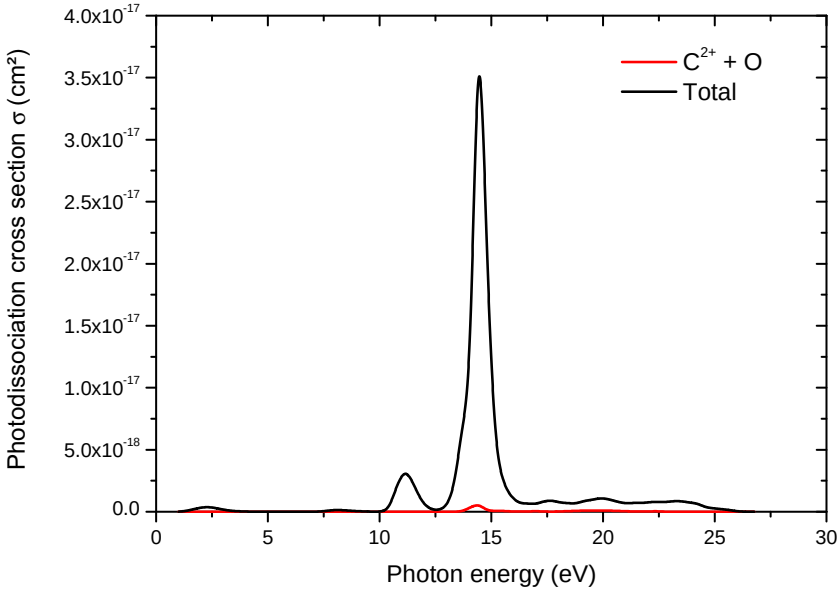

Figure 3.27: Total photodissociation cross section from the $v'' = 0$ level of the $X\,^3\Pi$ state of CO^{2+} through its 11 lowest $^3\Sigma^-$ channels (black curve), and partial photodissociation cross section through the $9^{th}\,^3\Sigma^-$ state (red curve), which is the first to dissociate into C^{2+} + O instead of C^+ + O^+.

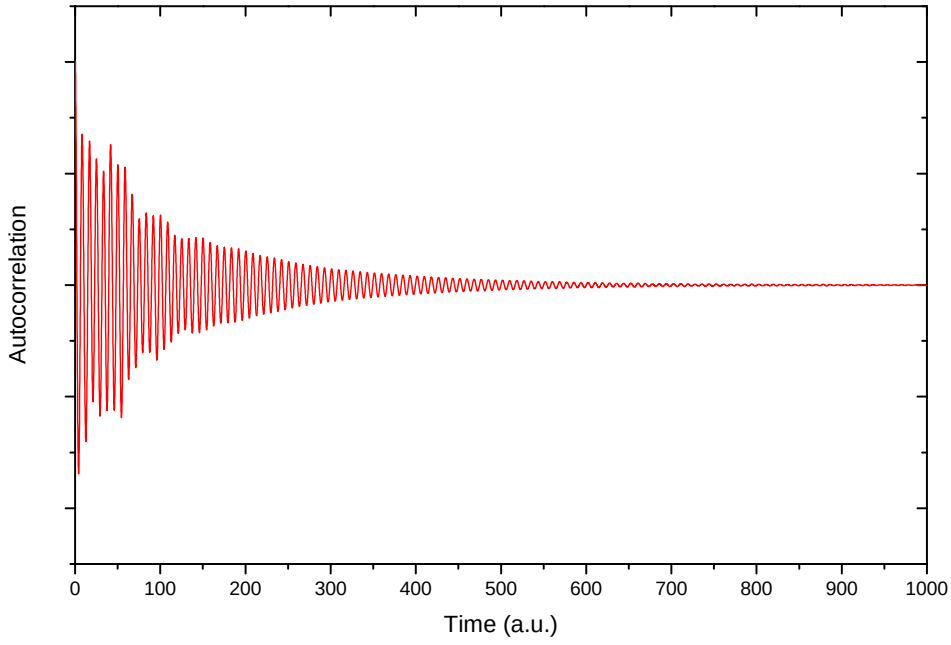

Figure 3.28: Autocorrelation function (arbitrary units) for the photodissociation of the $v'' = 0$ level of the $X\,^3\Pi$ state of CO^{2+} through the first 11 excited $^3\Sigma^-$ channels.

the different channels in the course of the photodissociation process.

As a consequence, a laser with a wavelength corresponding to that energy range would therefore mainly lead to dissociation through the $C^+ + O^+$ channels. In order to significantly dissociate CO^{2+} through the $C^{2+} + O$ channel instead, a more refined approach is therefore necessary: in the following chapter of this work, we theoretically optimize laser fields that guide the photodissociation dynamics of CO^{2+} and HeH^+ towards specific selected channels.

CHAPTER

4

LASER CONTROL OF PHOTODISSOCIATION REACTIONS

In this chapter, we take the study of the dynamics of photodissociation reactions one step further by actively controlling these processes through the use of laser fields. We start by a general introduction on the laser control of chemical processes (Section 4.1, p. 114) before presenting the two methodologies we used to theoretically optimize efficient laser pulses:

- **Local Control Theory** (Section 4.1.2, p. 116), and more specifically a recently-developed Local Control approach based on the use of Møller operators (as detailed on p. 118).
- **Optimal Control Theory** (Section 4.1.3 , p. 122).

In both approaches, we take a step towards the theoretical determination of "realistic", experimentally-feasible pulses by including additional constraints in the optimization process. We more specifically introduce a new kind of constraint that minimizes the total *area* of the electric field, whose implementation is detailed on p. 120 for Local Control and on p. 131 for Optimal Control. We then expose the results we obtained for our two test systems:

- The control of the photodissociation of the $X\ ^1\Sigma^+$ state of HeH^+ through its higher-excited $^1\Sigma^+$ channels (Section 4.3, p. 133).
- The control of the photodissociation of the $X\ ^3\Pi$ state of CO^{2+} through its $^3\Sigma^-$ channels (Section 4.4, p. 147).

All calculations presented in this chapter and the following were performed on the computing cluster of the *ThéoSim* group (*Laboratoire de Chimie Physique, Université Paris-Sud*), using

codes previously developed by members of that research group which we modified and adapted to suit our needs.

Note: in this work, expressions such as "control field", "control pulse", "optimized field", *etc.* will often be used to refer to the electric part of the electromagnetic field used to control the reaction dynamics.

4.1 Introduction to the laser control of chemical processes

Controlling the behaviour of chemical compounds has been one of the cornerstones of chemistry since its inception, be it through the choice of appropriate reactants, solvents and catalysts, or through the choice of appropriate physical conditions, such as pressure and temperature. Laser control goes beyond these traditional and macroscopic means of influencing the course of chemical reactions by allowing direct, microscopic control of molecular energy level populations through the use of a laser field.

Lasers indeed produce coherent light whose intensity and spectral range can be fine-tuned, making them ideal tools not only to measure the properties of molecules and to probe their dynamical behaviour, but also to influence the course of their dynamics, allowing for the quantum control of chemical processes. Thanks to the development of ultrashort laser sources and of the associated pulse shaping technologies, lasers can now be used not only to populate non-thermal states of a molecule (*i.e.* states which are inaccessible when energy is supplied to molecules in the form of heat), but also to influence the populations of the energy levels of a molecule throughout the course of a chemical reaction, thus influencing its final product(s) and yield.

Controlling the behaviour of molecules through the use of lasers is not a trivial task, but it is usually motivated by several factors. First and foremost, looking for the best ways to control chemical processes often leads to new insights into their dynamics and into the underlying physical phenomena. Secondly, laser control has many potential applications in various fields, such as quantum information (and in particular the use of trapped atoms and molecules as "quantum computers", which will be detailed in Chapter 5), microscopy [152, 153], biomedical functional imaging [154] and the highly-selective detection of chemical compounds [155, 156], to name only a few.

4.1.1 Control strategies: overview

The general strategy of laser control is straightforward: its aim is to tailor an external electric field $E(t)$ in order to guide the evolution of the system from an initial state $|\Psi_i\rangle$ to a final state $|\Psi_f\rangle$. Both theoretical and experimental approaches have been developed in order to achieve this goal.

Experimentally, the control of chemical reactions can be implemented using *Adaptive Feedback Control* (AFC), an empirical approach to the optimization of the control field that relies on

a feedback loop [157]. The effect of a trial laser pulse on the system is first assessed, then fed into a genetic algorithm that slightly modifies the pulse shape in an attempt to maximize the desired physical quantity. Through repeated experiments, the pulse is progressively optimized on the basis of the measured results, until the desired objective is satisfactorily reached [158].

This kind of approach is very efficient as it allows the quick optimization of experimentally-efficient laser pulses without requiring accurate computations of the properties of the molecule. However, in order to understand the underlying mechanism and gain insight into the subtleties of the dynamics, *ab initio* calculations are often required (as illustrated for example by the 2003 study of Daniel *et al.* [159, 160]). Moreover, this approach requires easy measurement of the physical quantity one wants to optimize, which is not always possible: we will for example see in Chapter 5 (p. 157) that molecular quantum computing relies on laser pulses which place molecules in specific superpositions of states – superpositions which cannot easily be measured, as direct measurement would lead to the collapse of the wavefunction[†].

In this kind of case, a theoretical determination of the control pulse is necessary. Although fields optimized theoretically are often not experimentally feasible today or as efficient in practice as in the simulations (*e.g.* because of inaccuracies in the *ab initio* data), theoretical simulations have played and still play an important role in the development of quantum control [162]. As noted by Brif *et al.*, "*the practical laboratory relevance of theoretical designs depends on the complexity of the system of interest, with simpler cases yielding theoretical models closer to reality*": since quantum control strategies are usually very sensitive to the properties of the system, such as the shape of the potential energy curves of surfaces, theoretical results obtained for complex polyatomic molecules are likely to be further from reality than those obtained for diatomic systems [14].

In cases where one only wants to transfer population from one molecular state to another, very simple pulses can be used. The simplest approach is probably the use of π-pulses, *i.e.* laser pulses that have a total area of π under their envelope and whose frequency correspond to a resonant transition between the initial state and the target state. Regardless of their shape, pulses that meet these two conditions indeed lead to a total population transfer from one state to another [163].

Another relatively simple and efficient approach is *Stimulated Raman Adiabatic Passage*, or STIRAP, which allows for efficient population transfer towards states that are not accessible by one-photon transitions. It consists in transferring population from the initial state to the desired state through an intermediary state by using two off-resonance laser pulses: a "Stokes" laser is first used to couple the intermediary state and the target state, then a "pump" laser transfers population from the initial to the target state [164, 165].

However, the aim of quantum control is often more complex than simply ensuring a population transfer from a single state to another. Moreover, unwanted transitions towards other states may occur and significantly decrease the efficiency of such simple approaches.

[†]Note however that indirect measurement of quantum systems that preserve state superpositions is not physically impossible, as illustrated for example by Ref. [161].

To determine control fields in those cases, two main theoretical approaches coexist: *Local Control*, in which the field is optimized at each timestep based on the instantaneous dynamics of the system, and *Optimal Control*, in which the field is optimized iteratively based on the entire dynamics from its start t_i to a final time t_f. Both approaches were used in this work and are detailed and compared in the following pages[†].

4.1.2 Local Control Theory

Local Control Theory (LCT) was first formulated in 1992 as a way to determine control fields which would excite molecular systems into specific states while preventing population transfers to other states [166,167]. Its philosophy is simple: for each timestep t of the dynamics, the value that the control field $E(t)$ should take in order to maximize (or minimize) the expectation value $\langle O \rangle$ of an observable O is computed [168].

Let us briefly derivate the expression of the Local Control field. First, the Hamiltonian $H(t)$ of the system is defined as:

$$H(t) = H_0 + W(t), \tag{4.1}$$

where H_0 is the Hamiltonian of the field-free system and $W(t)$ is the time-dependent perturbation which will influence its dynamics. In the cases studied here, we will guide the dynamics of molecular systems through their electric dipole interaction with the electric field $E(t)$ of a laser pulse:

$$W(t) = -\mu E(t), \tag{4.2}$$

where μ is the projection of the dipole operator on the polarization vector of the laser field.

As always, the time-dependent Schrödinger equation for our system is:

$$i\hbar \frac{\partial}{\partial t} |\Psi(t)\rangle = H(t) |\Psi(t)\rangle . \tag{4.3}$$

Our aim in controlling the system can be broadly defined as maximizing (or minimizing) the expectation value of a particular operator O. To achieve this, Local Control will endeavor to maximize or minimize its time derivative [169]:

$$\frac{d\langle O \rangle}{dt} = \frac{d}{dt} \langle \Psi(t)| O |\Psi(t)\rangle . \tag{4.4}$$

By applying the Ehrenfest theorem (*i.e.* replacing the time derivative of Ψ with its expression from the time-dependent Schrödinger equation (Eq. 4.3)), we obtain:

$$\frac{d\langle O \rangle}{dt} = \frac{i}{\hbar} \langle \Psi(t)| [H, O] |\Psi(t)\rangle + \langle \Psi(t)| \frac{\partial O}{\partial t} |\Psi(t)\rangle . \tag{4.5}$$

[†]For further details, the 2010 review of the state of the art in quantum control by Brif *et al.* provides an interesting overview of the history of laser control and of its applications [14].

Replacing the Hamiltonian by its expression given in Eq. 4.1 allows the dependence of $\langle O \rangle$ with the electric field $E(t)$ to become more apparent:

$$\frac{d\langle O \rangle}{dt} = \frac{i}{\hbar} \langle \Psi(t) | [H_0, O] | \Psi(t) \rangle - \frac{i}{\hbar} E(t) \langle \Psi(t) | [\mu, O] | \Psi(t) \rangle + \langle \Psi(t) | \frac{\partial O}{\partial t} | \Psi(t) \rangle . \tag{4.6}$$

If $i\frac{\partial}{\partial t}O = [H_0, O]$ (which is the case if O does not depend explicitly on time) and if H_0 and O commute[†], the first and last terms disappear and we obtain the general equation on which Local Control strategies are based:

$$\frac{d\langle O \rangle}{dt} = -\frac{i}{\hbar} E(t) \langle \Psi(t) | [\mu, O] | \Psi(t) \rangle . \tag{4.7}$$

We see indeed in this expression that, provided the operators μ and O do not commute, the electric field $E(t)$ can be used to influence the time evolution of $\langle O \rangle$, *e.g.* to gradually minimize or maximize its value.

Let us now derive the appropriate form of $E(t)$ for a concrete case. If the aim of the control is to populate a specific molecular energy state ϕ_i, O could be defined as the corresponding projector:

$$\begin{aligned} O &= P_i \\ &= |\phi_i\rangle \langle \phi_i| , \end{aligned} \tag{4.8}$$

or as a sum of such projectors if the aim is to maximize the populations of several states at once. By replacing O by this expression in Eq. 4.7 and developing the commutator, we obtain:

$$\begin{aligned} \frac{d\langle O \rangle}{dt} &= -\frac{i}{\hbar} E(t) \langle \Psi(t) | [\mu, O] | \Psi(t) \rangle \\ &= -\frac{i}{\hbar} E(t) \Big(\langle \Psi(t) | \mu O | \Psi(t) \rangle - \langle \Psi(t) | O \mu | \Psi(t) \rangle \Big) \\ &= -\frac{i}{\hbar} E(t) \Big(\langle \Psi(t) | \mu | \phi_i \rangle \langle \phi_i | \Psi(t) \rangle - \langle \Psi(t) | \phi_i \rangle \langle \phi_i | \mu | \Psi(t) \rangle \Big) \\ &= -\frac{i}{\hbar} E(t) \Big(\langle \Psi(t) | \mu | \phi_i \rangle \langle \phi_i | \Psi(t) \rangle - \Big(\langle \phi_i | \Psi(t) \rangle \langle \Psi(t) | \mu | \phi_i \rangle \Big)^* \Big). \end{aligned} \tag{4.9}$$

Since the difference between a complex number z and its complex conjugate z^* yields $2\,i\,\mathcal{I}(z)$ (where $\mathcal{I}(z)$ is the imaginary part of z), Eq. 4.9 can be rewritten as:

$$\begin{aligned} \frac{d\langle O \rangle}{dt} &= -\frac{2}{\hbar} E(t)\, \mathcal{I}\Big(\langle \Psi(t) | \mu | \phi(t) \rangle \langle \phi(t) | \Psi(t) \rangle \Big) \\ &= -\frac{2}{\hbar} E(t)\, \mathcal{I}\Big(\langle \Psi(t) | \mu O | \Psi(t) \rangle \Big). \end{aligned} \tag{4.10}$$

It is thus possible to ensure a monotonous increase (or decrease) of $\langle O \rangle$ by defining the field $E(t)$ as [166, 169]:

[†]That is to say, if the expectation value of O is a constant of motion.

$$E(t) = \pm\lambda\,\mathcal{I}\Big(\langle\Psi(t)|\,\mu O|\Psi(t)\rangle\Big), \tag{4.11}$$

where λ is a positive constant or a positive function of time which scales the intensity of the control field $E(t)$.

Local Control Theory usually yields control fields that are relatively simple and easy to interpret in terms of the successive state transitions they cause. While this simplicity implies they may be easier to implement experimentally than more complex fields such as those obtained using Optimal Control Theory, they are also often much less efficient.

4.1.2.1 Local Control Theory using Møller Operators

The main drawback of Local Control is a direct consequence of its philosophy: since the control field is determined for each timestep based on the *instantaneous* dynamic of the system, it does not take into account phenomena which may occur later in the dynamics. Nonadiabatic interactions may for example populate or depopulate the target state non-radiatively in the course of the dynamics. Attempts at maximizing the population of either adiabatic or diabatic states with Local Control in systems where nonadiabatic couplings strongly influence the dynamics are therefore unlikely to be very successful.

Moreover, the field-free molecular Hamiltonian H_0 does not commute with projectors on adiabatic or diabatic states $P_j = |\phi_j\rangle\langle\phi_j|$ in the presence of nonadiabatic couplings: as a result, the first term of Eq. 4.7 is not equal to zero. While its neglect was found to still lead to meaningful results in two-state systems with a well-localized coupling [170, 171], this was found not to be the case in a strongly-coupled system such as HeH^+ [43].

In order to solve this problem and go one step further than conventional Local Control Theory, Prof. Meier (LCAR-IRSAMC, *Université Paul Sabatier*) developed, in collaboration with *Université Paris-Sud*'s LCP, a variant of Local Control based on Møller Operators which takes the full dynamics into account to determine the control field [43]. Its basic idea is simple: in the context of photodissociation, the aim is not to maximize the population of specific *electronic states* throughout the whole dissociation process but to maximize the formation of specific *fragments*. It therefore makes more sense to define the target operator O as a *scattering projector* P_j^{sc} (or as a sum of scattering projectors) correlated with the desired exit channel(s):

$$P_j^{sc} = \int |\phi_j^-(p)\rangle\langle\phi_j^-(p)|\;dp, \tag{4.12}$$

where $|\phi_j^-\rangle$ is an outgoing scattering state with momentum p which correlates with the fragments associated to the dissociation of electronic state j. Unlike projectors on adiabatic or diabatic states, scattering projectors commute with the field-free Hamiltonian, allowing for the LCT approach to be used to maximize their expectation value even in cases with strong nonadiabatic couplings. However, the calculation of the scattering states usually is a very difficult task as it requires solving the multi-channel problem for all scattering energies. In a time-dependent approach, this can however be circumvented by computing them through the use of *Møller op-*

erators $\Omega_{\mp}$ [172–174], which are defined as:

$$\Omega_{\mp} = \lim_{t \to \pm\infty} e^{iHt/\hbar} e^{-iH_{frag}t/\hbar}, \tag{4.13}$$

where H is the full molecular Hamiltonian and H_{frag} is the Hamiltonian of the fragments for very large internuclear distances $R = \infty$, where all nonadiabatic couplings have vanished. Using the appropriate Møller operator, a scattering state $|\phi_j^-(p)\rangle$ can be written as:

$$\begin{aligned} |\phi_j^-(p)\rangle &= \Omega_- \, |j,p\rangle \\ &= \lim_{t \to \infty} e^{iHt/\hbar} e^{-iH_{frag}t/\hbar} \, |j,p\rangle \, . \end{aligned} \tag{4.14}$$

where $|j,p\rangle = e^{ipR/\sqrt{2\pi}}$ is an outgoing plane wave in channel j with energy $p^2/2m$.

By following the same reasoning as in Eqs. 4.9 to 4.11, we obtain the expression of the Local Control field which ensures a monotonous increase of the population of the selected scattering states:

$$E(t) = \pm\lambda \, \mathcal{I}\Big(\int \lim_{t' \to \infty} \langle \Psi(t)| \, e^{iHt'} \, |j,p\rangle \times \langle j,p| \, e^{-iHt'} \, \mu |\Psi(t)\rangle \; dp \Big). \tag{4.15}$$

In order to compute it, we proceed in the following way:

1. At each timestep t for which we want to determine the control field $E(t)$, the wavepacket $|\Psi(t)\rangle$ and the promoted wavepacket $\mu|\Psi(t)\rangle$ are propagated from time t to time t', up to the asymptotic region ("$R = \infty$", *i.e.* beyond the interaction region).

2. Their Fourier Transform is computed in order to obtain the momentum distribution in every dissociation channel j, which is then used to determine the control field through Equation 4.15.

This approach was shown to go beyond conventional Local Control strategies by taking into account the effect of nonadiabatic transitions as they occur later in the dynamics [43]. Concretely, this leads for example to control fields that can temporarily transfer population out of a target state and into an unwanted state (which would be impossible in a conventional Local Control approach), provided this leads to a higher final population in the desired dissociation channel at the end of the dynamics. The original study by Bomble *et al.* for example features a control field that transfers population from a target state to an unwanted one, to take advantage of the effect of a nonadiabatic transition that transfers population back to the desired dissociation channel later in the dynamics [43].

However, this Møller operator-based approach is slower than conventional Local Control, as full propagations of the wavepackets up to the asymptotic region are required for each timestep t. Indeed, for each step t for which we want to determine our control field $E(t)$, a full propagation is necessary from time t to time t' so that the asymptotic wavepackets $|\Psi(t)\rangle$ and $\mu|\Psi(t)\rangle$ can be found and used to determine the value of $E(t)$ at time t. These propagations thankfully become shorter and shorter throughout the calculation, as t gradually increases and becomes closer to t'. Additionally, these field-free propagations from t to t' can be realized with a longer

timestep δt_{free} than the one used for the determination of the field $E(t)$, which needs to be very small to ensure accuracy.

4.1.2.2 Zero-area constraint in Local Control

Bomble *et al.* first applied the Møller-operator based Local Control approach to the photodissociation of HeH^+ [43], using the *ab initio* data previously computed by Loreau *et al.* [2]: the large role that the nonadiabatic couplings play in the photodissociation dynamics of HeH^+ make it an ideal test case for this method.

However, one of the fields Bomble *et al.* optimized suffers from a common but often-ignored problem: its time-integrated area is not equal to zero, as can be seen in Fig. 4.1. This is experimentally unrealistic for a laser pulse, since Maxwell's equations require the time-integrated area of a freely propagating electromagnetic pulse to be strictly equal to zero (a problem which was first raised in the context of control using "half-cycle pulses" [175–177]). A short demonstration of where this stems from is given in the Appendix on page 193, which can intuitively be summed up as such: a laser pulse can be thought of as a superposition of monochromatic sine waves, whose individual time-integrated areas are all strictly equal to zero. Its area should therefore be equal to zero too.

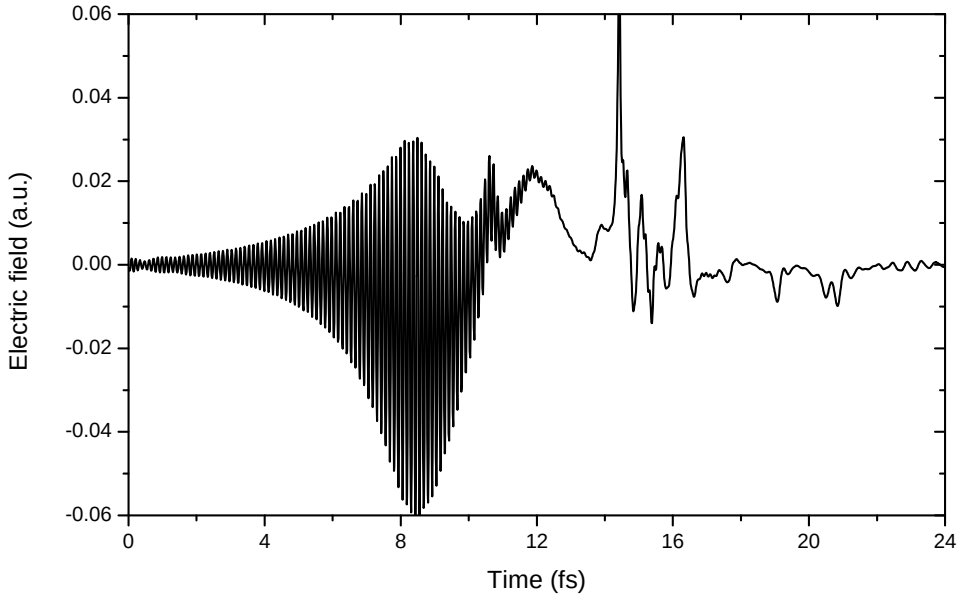

Figure 4.1: Local Control field guiding the photodissociation of HeH^+ towards the $He + H^+$ fragments through its $^1\Sigma^+$ channels, recomputed using the same *ab initio* data and parameters as Bomble *et al.* [43]. The time-integrated area of the field is visibly not equal to zero due to a non-oscillating, "Stark" contribution (that can most easily be seen after 12 fs). This case will be studied in detail in Section 4.3.1 (p. 135).

Although this is not always so obvious to the naked eye, many other theoretically-optimized

fields published in the literature have a non-zero area, with only few authors acknowledging this problem[†].

The case of the control of the photodissociation of HeH^+ led us to consider these optimized electric fields as being composed of two contributions: an oscillating part with zero area associated to an electromagnetic pulse, and a non-oscillating part caused by a non-periodical electric field, as can for example be created by applying an electric tension between two conducting plates. We dubbed this part of our electric fields the "Stark contribution" due to its presumed effect on the energies of the eigenstates of the molecular systems we consider. Although the control of reactions using both laser pulses and static electric fields could constitute an interesting area of research, we chose to focus here on the electromagnetic part of our optimized pulses and to suppress the "Stark" contribution as much as possible.

In order to do so, we worked in collaboration with the group of Prof. Sugny (*Laboratoire Interdisciplinaire Carnot de Bourgogne* of the *Université de Bourgogne*) in order to implement constraints that minimize the area of the field in both Local Control and Optimal Control Theory. As a general rule of thumb, optimizing a control field with additional constraints is indeed generally more efficient than applying the constraints on the field after its optimization [179]: it seems therefore preferable to optimize a field with the area constraint than trying to modify it, post-optimization, to bring its area as close to zero as possible. In order to implement the zero-area constraint in Local Control, Prof. Sugny proposed to add a term penalizing the area of the field to the cost functional $V(t)$ [180]:

$$V(t) = \langle\Psi(t)|\,O\,|\Psi(t)\rangle - \nu A(t)^2, \tag{4.16}$$

where ν is a positive parameter that weighs the area constraint and where $A(t)$ is the area of the electric field $E(t)$ at a given time t, e.g.:

$$A(t) = \int_0^t E(t)\,dt. \tag{4.17}$$

In other words, instead of simply maximizing $\langle\Psi(t)|\,O\,|\Psi(t)\rangle$, the aim of this method is to both maximize $\langle\Psi(t)|\,O\,|\Psi(t)\rangle$ and minimize $\nu A(t)^2$ in order to obtain the highest value of $V(t)$ possible. Note that $A(t)$ is squared to avoid favouring negative values of the area and in order to lead to a simple expression of the electric field $E(t)$. To find that expression, we indeed write the time derivative of $V(t)$, which yields a result very similar to Eq. 4.4, differing only by the appearance of the area penalty term:

$$\frac{dV(t)}{dt} = -\frac{i}{\hbar}E(t)\,\langle\Psi(t)|\,[\mu, O]\,|\Psi(t)\rangle - 2\nu A(t)E(t). \tag{4.18}$$

This thus leads to the presence of an additional $-2\nu A(t)E(t)$ term in the expression of the control field $E(t)$, which we can generally express as:

[†]See for example Ref. [178], whose authors write: "*we note that the electric field in Fig. 8 does not strictly fulfill the condition of a time integral which is equal to zero. This might be fixed by introducing a new constraint on the electric field, at the risk of making the calculation unfeasible due to slow convergence*".

$$E(t) = \lambda(t)\Big(\langle\Psi(t)|\, i[\mu, O]\,|\Psi(t)\rangle - 2\nu A(t)\Big). \tag{4.19}$$

Note however that, in this formulation, the constraint does not minimize the *global* area of the field $A(t_f)$ but minimizes, at each timestep t, its area *up to that particular time* $A(t)$.

Using this strategy, we present in Section 4.3.1 (p. 135) the first fields optimized in Local Control with a constraint on the area [180].

4.1.3 Optimal Control Theory

Optimal Control Theory (OCT) is a general method to optimize the value of a given "performance index" while respecting a set of constraints, with very wide-ranging applications in various fields of science and engineering. Although it finds its root in the calculus of variation, the paternity of Optimal Control as it is used today is generally attributed to Soviet mathematician Lev Pontryagin [181][†].

The basic philosophy of Optimal Control is to optimize the value of a functional $J(t)$ that can broadly be defined as [162]:

$$J(t) = \text{Objective} - \text{Constraints}. \tag{4.20}$$

The first step is thus the mathematical definition of what constitutes our "objective" and of the constraints that need to be respected. Once this is done, solving the control problem amounts to finding a way to maximize the functional $J(t)$ – but instead of achieving this by imposing the sign of its time derivative $\partial J/\partial t$, like in Local Control, Optimal Control will focus on maximizing its final value at a given time t_f.

In this work, we focus on the application of Optimal Control Theory to the optimization of laser control fields that guide the dynamics of molecular processes towards specific goals while respecting predefined constraints [183]. Our work is based on the form of the functional first defined by Zhu *et al.* [184]:

$$J = \text{Objective} - \text{C}_{\text{Intensity}} - \text{C}_{\text{Schröd.}}, \tag{4.21}$$

or, more accurately,

$$\begin{aligned} J = &\left|\langle\Psi(t_f)|\,\phi_f\rangle\right|^2 - \int_0^{t_f} \alpha(t)\,|E(t)|^2\,dt \\ &- 2\mathcal{R}\left(\langle\Psi(t_f)|\,\phi_f\rangle \int_0^{t_f} \langle\lambda(t)|\,\frac{\partial}{\partial t} + i\hbar(H_0 - \mu E(t))\,|\Psi(t)\rangle\;dt\right), \end{aligned} \tag{4.22}$$

where the first term is the objective, the second is a constraint on the intensity of the field and the third is a constraint imposing the respect of the time-dependent Schrödinger equation at each timestep. Let us look at these terms one at a time.

[†] For the curious, a 1996 article attempts at tracing back the roots of Optimal Control Theory and shows that things are not so clear-cut [182].

4.1.3.1 Objective

As in Local Control, our aim can be generalized as the maximization of the expectation value of an operator O. However, this time, our aim is not to maximize its value at each timestep t but only its final value at time t_f:

$$\langle O \rangle_{t_f} = \langle \Psi(t_f) | O | \Psi(t_f) \rangle \tag{4.23}$$

If our aim is to maximize the final population of a given state ϕ_f, the appropriate operator O is the corresponding projection operator $|\phi_f\rangle \langle \phi_f|$:

$$\begin{aligned} \text{Objective} &= \langle \Psi(t_f) | \phi_f \rangle \langle \phi_f | \Psi(t_f) \rangle \\ &= \left| \langle \Psi(t_f) | \phi_f \rangle \right|^2, \end{aligned} \tag{4.24}$$

which is the expression used by Zhu *et al.* [184], among many others. In this case, the functional J will be maximal when the wavefunction $\Psi(t)$ at time t_f is strictly equal to the target wavefunction ϕ_f, *i.e.* when the system has reached the desired state.

Note that the way the objective is defined is very important, as the form of the control field depends on it.

4.1.3.2 Constraint on the intensity

Special care must be taken to prevent the control field $E(t)$ from reaching exceedingly high values at any point t in time: the higher limit is usually fixed at 0.05 a.u., *i.e.* around 2.57×10^{10} V·m^{-1} [7][†]. This is achieved through the second term of Eq. 4.22, the constraint on the field intensity, whose expression is rather straightforward:

$$C_{\text{Intensity}} = -\int_0^{t_f} \alpha(t) \, |E(t)|^2 \, dt, \tag{4.25}$$

where $\alpha(t)$ is a parameter that modulates the intensity of the control field. It is usually defined as a constant α_0 or as a constant multiplied by an envelope $s(t)$, that ensures a smooth beginning and ending of the field:

$$\alpha(t) = \frac{\alpha_0}{s(t)}. \tag{4.26}$$

The envelope $s(t)$ is equal to 0 for $t = 0$ and $t = t_f$, and smoothly raises up to 1 in the interval, so that the constraint $\alpha(t)$ on the intensity is maximal at the beginning and the end of the pulse to ensure that $E(t = 0) = E(t_f) = 0$. Its most widely-used form is that of a sine-squared envelope:

$$s(t) = \sin^2\left(\pi \frac{t}{t_f}\right). \tag{4.27}$$

[†]Note that tests with stricter constraints indicate that the results presented in this work should stay qualitatively correct for much lower field intensities, albeit with reduced values of the objectives.

However, although such an envelope guarantees a very smooth start and end of the pulse, it is known to limit the window during which the field can reach reasonably high amplitudes, as shown in Fig. 4.2. This has a similar effect to limiting the duration of the pulse and can lead to very high field amplitudes at $t = t_f/2$, as this is the only time where the envelope is equal to unity [185]. To get around this, we occasionally use in this work a modified envelope that begins and ends smoothly like a sine-squared envelope in a certain amount of time t_{sine}, but that is strictly equal to 1 in-between:

$$s(t) = \begin{cases} \sin^2\left(\pi \dfrac{t}{2\ t_{\text{sine}}}\right) & \text{for} \quad 0 \leq t < t_{\text{sine}}, \\ 1 & \text{for} \quad t_{\text{sine}} \leq t \leq t_f - t_{\text{sine}}, \\ \sin^2\left(\pi \dfrac{t_f - t}{2\ t_f - t_{\text{sine}}}\right) & \text{for} \quad t_f - t_{\text{sine}} < t \leq t_f. \end{cases} \tag{4.28}$$

A comparison between the two envelopes for $t_f = 2000$, $t_{\text{sine}} = 400$ a.u. of time is given in Fig. 4.2.

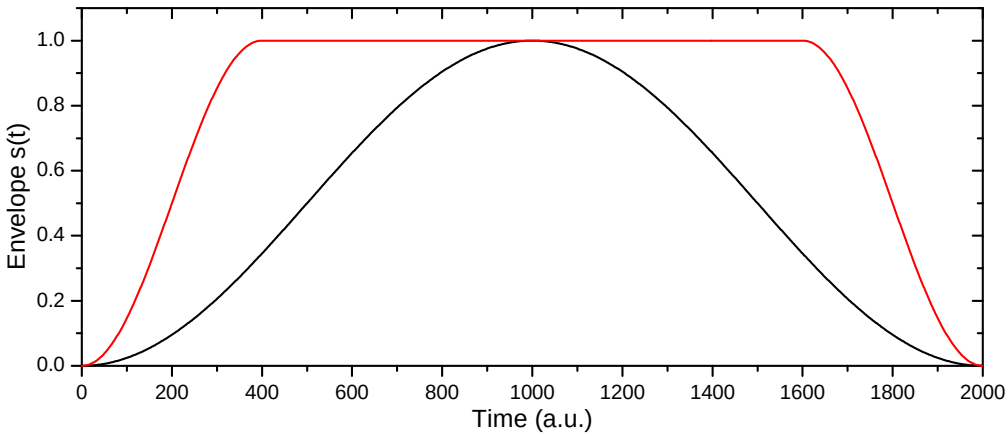

Figure 4.2: Sine-squared (black) and modified sine-squared (red) envelopes $s(t)$ that ensure a smooth start and end of the optimized pulses.

4.1.3.3 Constraint on the respect of the Schrödinger equation

Finally, the third and last term of Eq. 4.22 ensures that the time-dependent Schödinger equation is verified throughout the dynamics:

$$C_{\text{Schröd.}} = -2\mathcal{R}\left(\langle\Psi(t_f)|\phi_f\rangle \int_0^{t_f} \langle\lambda(t)| \frac{\partial}{\partial t} + i\hbar(H_0 - \mu E(t))\,|\Psi(t)\rangle\ dt\right), \tag{4.29}$$

where $\lambda(t)$ can be regarded as a Lagrange multiplier ensuring the respect of the Schrödinger equation, and where the term $\langle\Psi(t_f)|\phi_f\rangle$ in front of the integral was introduced by Zhu *et al.* to decouple the boundary conditions of the equations obtained in the subsequent development (Eqs. 4.31 and 4.33) [184]. $\mathcal{R}$ denotes the real part of the expression that follows between brackets.

Note that, as in the case of Local Control, the Hamiltonian H has been expressed as the sum of the field-free Hamiltonian H_0 of the molecular system and of its electric dipole interaction $-\mu E(t)$ with the electric component of the laser field (Eqs. 4.1 and 4.2, p. 116).

4.1.3.4 Derivation of the coupled equations

Now that each term of Eq. 4.22 has been examined, we can look for the expression of $E(t)$ that will maximize the functional J. That functional depends on three functions: $\lambda(t)$, $\Psi(t)$ and $E(t)$. To find the optima of J, let us thus write the derivatives $\delta J_\lambda, \delta J_\Psi$ and δJ_E, and impose that they must be equal to zero [186]:

$$\begin{aligned}\delta J_\lambda &= J[\lambda(t)+\delta\lambda(t),\Psi(t),E(t)] - J[\lambda(t),\Psi(t),E(t)] \\ &= -2\mathcal{R}\left(\langle\Psi(t_f)|\phi_f\rangle \int_0^{t_f} \langle\delta\lambda(t)|\left(\frac{\partial}{\partial t} + i\hbar(H_0-\mu E(t))\right)|\Psi(t)\rangle\, dt\right).\end{aligned} \tag{4.30}$$

Since $\delta\lambda(t)$ is arbitrary, δJ_λ will be equal to zero if:

$$i\hbar\frac{\partial}{\partial t}|\Psi(t)\rangle = (H_0-\mu E(t))\,|\Psi(t)\rangle\,. \tag{4.31}$$

In other words, the wavefunction $\Psi(t)$ of the system must respect the time-dependent Schrödinger equation for all times t. The boundary condition is given by the initial state ϕ_i of the system: $\Psi(t=0)=\phi_i$.

Similarly, writing δJ_Ψ and injecting Eq. 4.31 in the resulting expression yields:

$$\begin{aligned}\delta J_\Psi &= J[\lambda(t),\Psi(t)+\delta\Psi,E(t)] - J[\lambda(t),\Psi(t),E(t)] \\ &= 2\mathcal{R}\left[\langle\Psi(t_f)|\phi_f\rangle\left(\langle\phi_f|\delta\Psi\rangle - \int_0^{t_f}\langle\lambda(t)|\,i\hbar(H_0-\mu E(t))\,|\delta\Psi\rangle\, dt\right)\right],\end{aligned} \tag{4.32}$$

which leads to the following condition[†]:

$$i\hbar\frac{\partial}{\partial t}|\lambda(t)\rangle = (H_0-\mu E(t))\,|\lambda(t)\rangle\,, \tag{4.33}$$

i.e. $\lambda(t)$ must respect the Schrödinger equation, with the boundary condition $\lambda(T)=\phi_f$.

Finally, imposing $\delta J_E = 0$ leads to the third condition:

$$\begin{aligned}\delta J_E &= J[\lambda(t),\Psi(t),E(t)+\delta E] - J[\lambda(t),\Psi(t),E(t)] \\ &= -2\int_0^{t_f}\left[\alpha(t)E(t) + 2\mathcal{I}\left(\langle\Psi(t)|\phi_f\rangle\langle\lambda(t)|\mu|\Psi(t)\rangle\right)\right]\delta E\, dt.\end{aligned} \tag{4.34}$$

This leads to the expression of the control field $E(t)$:

$$E(t) = -\frac{1}{\alpha(t)}\mathcal{I}\left(\langle\Psi(t)|\lambda(t)\rangle\langle\lambda(t)|\mu|\Psi(t)\rangle\right). \tag{4.35}$$

[†]The detailed development can for example be found in Ref. [186].

Any control field $E(t)$ that satisfies Eqs. 4.31, 4.33 and 4.35 at once is a locally optimal solution to the control problem [184].

4.1.3.5 Optimization of the control field

Two algorithms are commonly used to solve this set of coupled nonlinear equations: the *Krotov algorithm* [187, 188] and the *Rabitz* (or *Zhu-Rabitz*) *algorithm* [184]. In this work, we use the latter, which ensures a monotonic increase[†] of the objective as a function of the number of iterations. In addition to the obvious (such as the relevant *ab initio* data, a value for parameters such as a_0, ...), the algorithm requires the following physical quantities to be known:

- The total duration of the pulse t_f.
- The initial wavefunction $\Psi(t=0)$.
- The desired final wavefunction ϕ_f at time t_f.
- A trial control field $E^{(0)}(t)$, that serves as an "initial guess" for the algorithm to start with.

The algorithm begins by a preparation phase, that is followed by the repetition of two steps at each iteration:

Preparation phase: backward propagation with the trial field

- Using the trial field $E^{(0)}(t)$, the wavepacket $\lambda^{(1)}(t)$ is propagated *backward* in time using Eq. 4.33, starting from the boundary condition $\lambda^{(1)}(t_f) = \phi_f$:

$$i\hbar\frac{\partial}{\partial t}|\lambda^{(1)}(t)\rangle = (H_0 - \mu E^{(0)}(t))\,|\lambda^{(1)}(t)\rangle\,. \tag{4.36}$$

First phase of each iteration: forward propagations

- Since $\lambda^{(1)}(t=0)$ and $\Psi^{(1)}(t=0) = \phi_i$ are now both known, they can be used to determine a new control field $E^{(1)}(t=0)$ using Eq. 4.35:

$$E^{(1)}(t) = -\frac{1}{\alpha(t)}\mathcal{I}\Big(\langle\Psi^{(1)}(t)|\,\lambda^{(1)}(t)\rangle\,\langle\lambda^{(1)}(t)|\,\mu\,|\Psi^{(1)}(t)\rangle\Big). \tag{4.37}$$

- Using this new control field $E^{(1)}(t)$, the wavefunction $\Psi^{(1)}(t)$ can be propagated forward in time from the boundary condition $\Psi^{(1)}(t=0) = \phi_i$ up to t_f using Eq. 4.31:

$$i\hbar\frac{\partial}{\partial t}|\Psi^{(1)}(t)\rangle = (H_0 - \mu E^{(1)}(t))\,|\Psi^{(1)}(t)\rangle\,. \tag{4.38}$$

- Step by step, both $E^{(1)}(t)$ and $\Psi^{(1)}(t)$ are thus determined from time $t=0$ to t_f.

[†] *i.e.* for each iteration, the objective increases or, at worst, stays constant.

Second phase of each iteration: backward propagations

- Since we now know $\Psi^{(1)}(t)$ from time $t = 0$ to t_f, we can use it with $\lambda^{(2)}(t_f) = \phi_f$ to determine a new field $E^{(2)}(t)$ using Eq. 4.35:

$$E^{(2)}(t) = -\frac{1}{\alpha(t)}\mathcal{I}\Big(\langle\Psi^{(1)}(t)|\,\lambda^{(2)}(t)\rangle\,\langle\lambda^{(2)}(t)|\,\mu\,|\Psi^{(1)}(t)\rangle \Big). \tag{4.39}$$

- Using this new control field $E^{(2)}(t)$, the wavefunction $\Psi^{(1)}(t)$ can be propagated backward in time from the boundary condition $\lambda^{(2)}(t = t_f) = \phi_f$ up to $t = 0$ using Eq. 4.31:

$$i\hbar\frac{\partial}{\partial t}|\lambda^{(2)}(t)\rangle = (H_0 - \mu E^{(2)}(t))\,|\lambda^{(2)}(t)\rangle\,, \tag{4.40}$$

- Step by step, both $E^{(2)}(t)$ and $\lambda^{(2)}(t)$ are thus determined from time $t = t_f$ to t_0.

Repeated iterations and convergence

- Once the second phase of an iteration is complete, the first phase of the next iteration begins with the indices of the wavefunctions $\lambda(t), \Psi(t)$ and of the control field $E(t)$ incremented respectively by 1 and by 2: for the second iteration, $\lambda(t)^{(2)}$ replaces $\lambda(t)^{(1)}$, $\Psi(t)^{(1)}$ is renamed $\Psi(t)^{(2)}$ and $E^{(2)}(t)$ replaces $E^{(0)}(t)$ in the above summary.

- The efficiency of the optimized pulse is assessed by computing the objective, as previously shown in Eq. 4.24:

$$\text{Objective} = \left|\langle\Psi^{(n)}(t_f)|\phi_f\rangle\right|^2, \tag{4.41}$$

  where the index n is the number of the most recent iteration. The iterative optimization is performed until the desired value of the objective is reached (which may be higher than 99% for applications in quantum computing, as will be discussed in Chapter 5).

- Instead of computing a completely new control field $E^{(n)}(t)$ at each step of each iteration, we use a method first proposed by Palao *et al.* in which the field as given in Eq. 4.37 and 4.39 is treated as a correction $\Delta E^{(n)}(t)$ to its value at the previous step $E^{(n-1)}(t)$ [189]:

$$E^{(n)}(t) = E^{(n-1)}(t) + \Delta E^{(n)}(t). \tag{4.42}$$

  This method allows the control field to keep a "memory" of its earlier values (and in particular of the trial field $E^{(0)}$) and can prevent it from becoming too intense [189].

4.1.3.6 Multi-target Optimal Control Theory

The development we have shown so far is valid if our aim is simply to maximize a transfer of population from an initial state ϕ_i towards a final state ϕ_f at time $t = t_f$. However, if our aim

to optimize transitions from N initial states ϕ_i^k towards N final states ϕ_f^k at once, a *multi-target* approach is necessary. This will be of particular importance in Chapter 5, where the aim is to implement quantum logic gates that can operate on any initial state or any initial state superposition, which requires simultaneously controlling the transitions from several initial states to several final states.

In this aim, a form of the functional J generalized to the multi-target case has been developed, with Eq. 4.22 taking the following generalized form [190]:

$$J = \frac{1}{N}\sum_{k=1}^{N}\left|\langle\Psi_k(t_f)|\phi_f^k\rangle\right|^2 - \int_0^{t_f}\alpha(t)\,|E(t)|^2\,dt \\ -2\sum_{k=1}^{N}\mathcal{R}\left(\langle\Psi_k(t_f)|\phi_f^k\rangle\int_0^{t_f}\langle\lambda_k(t)|\,\frac{\partial}{\partial t} + i\hbar(H_0-\mu E(t))\,|\Psi_k(t)\rangle\,dt\right). \tag{4.43}$$

Using the same kind of development as in Section 4.1.3.4 leads to $2N+1$ coupled equations instead of just three. The first $2N$ equations impose the respect of the time-dependent Schrödinger equation for the wavefunctions $\Psi(t)$ and $\lambda(t)$ of all N states:

$$i\hbar\frac{\partial}{\partial t}|\Psi_k(t)\rangle = (H_0-\mu E(t))\,|\Psi_k(t)\rangle\,, \tag{4.44}$$

$$i\hbar\frac{\partial}{\partial t}|\lambda_k(t)\rangle = (H_0-\mu E(t))\,|\lambda_k(t)\rangle\,, \tag{4.45}$$

with $k = 1,2,...,N$, and with the boundary conditions $\Psi_k(t=0) = \phi_i^k$ and $\lambda_k(t_f) = \phi_f^k$. Finally, the $(2N+1)^{\text{th}}$ equation gives the generalized form of the control field [191]:

$$E(t) = -\frac{1}{\alpha(t)}\sum_{k}^{N}\mathcal{I}\Big(\langle\Psi_k(t)|\,\lambda_k(t)\rangle\,\langle\lambda_k(t)|\,\mu\,|\Psi_k(t)\rangle\Big). \tag{4.46}$$

The performance of the optimized control field can be assessed at each iteration by computing the corresponding objective as shown in the first term of Eq. 4.43:

$$\text{Objective} = \frac{1}{N}\sum_{k=1}^{N}\left|\langle\Psi_k(t_f)|\phi_f^k\rangle\right|^2. \tag{4.47}$$

Note however that in the case of quantum computation, simply optimizing a series of transitions from initial to final states is often not sufficient: the relative phases of the states have to be controlled too, as will be discussed in Section 5.2.1.3, p. 177. Let us simply state for now that in such cases, another form of the objective, which takes the phase into account, may be used [189, 192, 193]:

$$\text{Objective} = \frac{1}{N}\left|\sum_{k=1}^{N}\langle\Psi_k(t_f)|\phi_f^k\rangle\right|^2. \tag{4.48}$$

This, in turn, modifies the expression of the control field $E(t)$:

$$E(t) = -\frac{1}{\alpha(t)}\mathcal{I}\left(\sum_k^N \langle\Psi_k(t)|\,\lambda_k(t)\rangle \sum_k^N \langle\lambda_k(t)|\,\mu\,|\Psi_k(t)\rangle\right). \tag{4.49}$$

4.1.3.7 Comparison with Local Control Theory

Since both Local Control and Optimal Control Theory are used in this work, let us briefly highlight the main differences between the two approaches:

- Whereas Local Control approaches compute the value of the control field $E(t)$ that maximizes the value of an observable O *at each timestep* t based on the *instantaneous* dynamic of the system, Optimal Control Theory looks at the dynamics *as a whole* in order to maximize the value of O *at the final time* t_f.

- Another difference between Local Control and Optimal Control is that the former approach yields a control field from $t = 0$ up to potentially very long times, as long as transitions that increase the objective can still occur (in our case, until the wavepacket has completely left the initial state), while the latter is an iterative procedure which requires the choice of a final time t_f prior to the start of the calculation. In this context, having performed a field-free propagation is very useful as it gives an estimate of the relevant timespan for the control field.

- Unlike Local Control schemes, Optimal Control requires an initial "guess" pulse[†]. Better results (or at least faster convergence towards a high-fidelity pulse) are of course obtained if the guess pulse is chosen in a physically sensible way: its spectrum should ideally already contain the frequencies corresponding to the desired transitions. In this work, two kind of initial guess pulses are tested and compared: Gaussian pulses with carrier frequencies corresponding to the desired transition(s), and pulses optimized by Local Control Theory.

One of the reasons why Optimal Control Theory leads to better results than Local Control Theory is quite intuitive. The best way to maximize a given observable at a time t_f is not necessarily to try to maximize its value at each intermediary timestep: it is instead preferable to take a look at the bigger picture and to maximize its final value only, even if it means allowing temporary diminutions of the observable.

For example, in the case of systems where nonadiabatic couplings play an important role in the dynamics, trying to maximize the population of the target state at each timestep is not

[†]Note however that, to provide a starting point to the Local Control algorithm as presented here, we promote a very small fraction of the vibrational wavefunction of the initial state to the excited channels. This is a purely numerical "trick" to get the algorithm started that does not modify the final result, as was verified by simulating the photodissociation dynamics in presence of our optimized fields with the photodissociation code used in Chapter 3.

the best way to go, since non-radiative transitions are likely to depopulate it later in the dynamics. However, by considering the dynamics as a whole, such nonadiabatic interactions may be taken advantage of, by temporarily populating state whose population is later transferred nonadiabatically to the target state, for example. As noted in Section 4.1.2.1, Møller operator-based Local Control already takes one step in that direction, but Optimal Control is more flexible as it allows the inclusion of constraints on the properties of the field as defined *on the chosen time interval as a whole*. Depending on the nature of the problem and on the exact definition of the objective, it may indeed be necessary to include additional constraints in the cost functional.

In this work, we use two additional constraints: a constraint that limits the fluence of the optimized pulses (Section 4.1.3.8) and a new constraint that minimizes their total area (Section 4.1.3.9, p. 131).

4.1.3.8 Constraint on the fluence

Unlike Local Control Theory, Optimal Control Theory optimizes the field as a whole, from the beginning to the end of its duration. This allows the minimization of the *fluence* of the control field, defined as[†]:

$$F = \int_{t_0}^{t_f} |E(t)|^2 \, dt. \tag{4.50}$$

Instead of adding a new constraint term to the functional J, the fluence of the control field can simply be adjusted to a given value F_0 at each iteration by defining the parameter α_0 in Eq. 4.26 (p. 123) not as a constant, but as a variable factor that gets recalculated at each step n of each iteration so that the fluence of the field always stays equal to F_0 [194, 195]:

$$\begin{aligned} \alpha_0^n &= \sqrt{\frac{\int_{t_0}^{t_f} |E^n(t)|^2}{F_0}} \\ &= \sqrt{\frac{F^n}{F_0}}, \end{aligned} \tag{4.51}$$

where $E^n(t)$ and F^n are the control field at step n and its fluence, respectively.

Note that setting a fixed value for the fluence does not necessarily prevent the electric field from punctually reaching high values: since the fluence is the result of a time integration of $|E(t)|^2$ from $t = 0$ to t_f, high values of $E(t)$ can still be attained for certain times t, provided they are compensated by lower values on the rest of the time interval t_f. However, comparing different fields with the same fluence can be useful to assert their "efficiency" for a given amount of energy, even if their peak intensity and their duration are different.

[†]Note that this definition of the fluence is the one that is commonly used in quantum control ("*the time-integrated intensity*", as put by Werschnik and Gross [194]), but that experimentalists may be more used to defining the "fluence" of a laser pulse as its amount of energy per unit of surface area.

4.1.3.9 Zero-area constraint in Optimal Control

Similarly to what we showed in Section 4.1.2.2 (p. 120) for Local Control theory, a constraint on the total (time-integrated) area of the field can be added in the field optimization through Optimal Control Theory. As in Local Control Theory, this constraint was first formulated by Prof. Sugny, who presented the first implementation of this constraint in Optimal Control Theory in our 2013 paper [180] (in which we presented its first implementation in Local Control Theory).

The approach is similar to that used in Local Control Theory. First, the area of the field is defined as:

$$A = \int_0^{t_f} E(t)\, dt. \tag{4.52}$$

Note that, unlike in the case of Local Control Theory, the area A of the field is now computed for the *whole* duration of the field, from $t = 0$ to $t = t_f$ (compare with Eq. 4.17, p. 121). Using this definition of the area, an additional constraint term penalizing high field areas, C_{Area}, is added to the cost functional J:

$$C_{\text{Area}} = -\nu A^2, \tag{4.53}$$

where ν is a parameter that modulates the weight of the area constraint. The fact that A is squared in this expression ensures that both positive and negative field areas are penalized and leads to the appearance of a simple term in the new expression of the control field [180]:

$$E(t) = -\frac{1}{\alpha(t)}\mathcal{I}\Big(\langle\Psi(t)|\,\lambda(t)\rangle\,\langle\lambda(t)|\,\mu\,|\Psi(t)\rangle\Big) - 2\nu A. \tag{4.54}$$

Unlike in the Local Control approach, where only the area of the field *up to the considered timestep* is taken into account, this constraint takes into account the area of the field as a whole. This makes the constraint a bit less strict than in Local Control, where we will see that it tends to "stifle" the field intensity by trying to minimize its area at each timestep t.

Note however that, unlike in Local Control theory, this approach might not necessarily suppress Stark contributions to the trial field: it might instead lead to the appearance of additional Stark contributions of opposite sign, thus ensuring that the global area is equal to zero while still failing to make the pulse physically realistic. It therefore seems preferable to suppress low-frequency contributions in the trial field before optimizing it with Optimal Control Theory.

4.2 Model used in our control simulations

These calculations presented in this work were performed under the following assumptions:

– Due to the short duration of the pulses (compared to the rotational period), the frozen rotation approximation is used [179]. The molecules are assumed to be pre-aligned with respect to the laser pulse so that the desired kind of transitions occur: for HeH^+, we optimize

parallel, $^1\Sigma^+ \rightarrow {}^1\Sigma^+$ transitions while for CO^{2+}, we optimize perpendicular, $^3\Pi \rightarrow {}^3\Sigma^-$ transitions.

- The electric field is defined as real, which corresponds to a fixed polarization.
- The molecules we study, HeH^+ and CO^{2+}, are assumed to initially be in their lowest possible energy state: the $v'', J'' = 0$ level of their ground adiabatic electronic state.
- Like our field-free calculations in Chapter 3, the dynamics are performed in the diabatic representation.

The time propagation were carried out using the Split-Operator method, previously described for time-independent Hamiltonians in Section 3.1.1, p. 79. However, since the Hamiltonian is now time-dependent due to the inclusion of the interaction with the electric field $-\mu E(t)$, the time-evolution operator for a small step δt given in Eq. 3.6 (p. 79) becomes [6]:

$$U(t, t+\delta t) = e^{\frac{-iV\delta t}{4\hbar}} e^{\frac{i\mu E(t)\delta t}{2\hbar}} e^{\frac{-iV\delta t}{4\hbar}} e^{\frac{-iT\delta t}{\hbar}} e^{\frac{-iV\delta t}{4\hbar}} e^{\frac{i\mu E(t)\delta t}{2\hbar}} e^{\frac{-iV\delta t}{4\hbar}}, \tag{4.55}$$

where the term $e^{\frac{i\mu E(t)\delta t}{2\hbar}}$ is built by diagonalizing the transition moment matrix μ one time for the whole calculation, then by multiplying its eigenvalues by the appropriate value of the electric field $E(t)$ at each timestep t. Note that $E(t)$ is assumed to be constant on each small time interval δt. The timestep δt therefore needs to be even smaller than for field-free propagations to ensure good accuracy. Its value was fixed to 0.05 a.u. ($\approx 1.21 \times 10^{-3}$ fs) for all time-dependent calculations presented in this chapter.

As in most quantum control studies, the efficiency of our optimized pulses is assessed by measuring the objective or *fidelity, i.e.* the final population in the target channels. For convenience, we will express it in % (that is to say, the percentage of the total population that has been transferred to the desired channels).

However, another interesting criterion to assess the quality of our optimized pulses is that of *selectivity*, as the objective alone does not tell the full picture. Compare for example two situations:

1. A pulse which leads to very high populations not only in the target channels, but also in the other, unwanted channels.
2. A pulse which leads to low populations in the target channels and to very low populations in unwanted channels, while leaving most of the population in the initial state.

The objective will be much higher in the former case than in the latter, as it is defined as the sum of the populations in the target channels at the final time t_f. However, if one wants to photodissociate the molecule into particular channels preferentially, the latter situation seems preferable as it strongly favors the dissociation in the desired channels: even if a large fraction

of the population is left in the initial state, repetition of the optimized pulse may lead to total dissociation if necessary.

To assess the selectivity of our pulse, we simply compute the ratio between the final populations in the target channels and in the other dissociation channels:

$$\text{Selectivity} = \sum_{i=1}^{n_{\text{target}}} p_{i\ \text{target}} \Bigg/ \sum_{i=1}^{n_{\text{others}}} p_{i\ \text{others}}, \tag{4.56}$$

where $p_{i\ \text{target}}$ and $p_{i\ \text{others}}$ are the populations at time t_f in the target channels and in the other dissociation channels, respectively, and where n_{target} and n_{others} are the corresponding number of dissociation channels. Note that the final population of the initial state is not taken into account in that calculation.

In addition, we use two physical quantities that were first proposed by Sugny *et al.* to assess the effect of the area constraint on the optimized fields [180]:

$$\begin{aligned} A_{\text{norm}} &= \frac{\int_0^{t_f} E(t)\ dt}{\int_0^{t_f} |E(t)|\ dt}, \\ B_{\text{norm}} &= \frac{\int_0^{t_f} E_{\text{wc}}(t)\ dt}{\int_0^{t_f} E_{\text{woc}}(t)\ dt}, \end{aligned} \tag{4.57}$$

where $E_{\text{wc}}(t)$ is the field optimized with a constraint on the area ($\nu \neq 0$) and $E_{\text{woc}}(t)$ is the field optimized without constraint on the area ($\nu = 0$). A_{norm} can be seen as the "normalized" area of a given pulse, while B_{norm} is the ratio between the areas of two pulses obtained with and without constraint on the area (all other parameters being kept equal). Appropriate choices of the area constraint ν are expected to lead to low values of both A_{norm} and B_{norm}.

4.3 Laser control of the photodissociation of HeH^+

Building on the work started by Bomble *et al.* [43], we focused on one of the specific cases presented in their seminal paper[†]: the photodissociation of the $X\ ^1\Sigma^+$ state of HeH^+ into the fragments $H^+ + He(1s2s\ ^1S)$ or $H^+ + He(1s2p\ ^1P)$, which corresponds to its third and sixth $^1\Sigma^+$ channels respectively (states B and E in the notation used in Table 2.1, p. 57).

We used the same *ab initio* data as Bomble *et al.* in all calculations [43]: the potential energy curves, transition dipole moments and nonadiabatic couplings of the six lowest $^1\Sigma^+$ states of HeH^+ computed by Loreau *et al.* [2], expressed on a spatial grid of 2^{13} points ranging from $R_{\text{min}} = 0.1\ a_0$ to $R_{\text{max}} = 100.0\ a_0$.

The scattering projector (Eq. 4.12) was defined as a projector on the scattering states correlating with the dissociation of the third and sixth $^1\Sigma^+$ electronic states of the molecule:

$$P^{sc}_{j=3,6} = \sum_{j=3,6} \int |\phi_j^-(p)\rangle \langle \phi_j^-(p)|\ dp. \tag{4.58}$$

[†]Case B of the original article.

Accordingly, the selectivity was defined as:

$$\begin{aligned} \text{Selectivity} &= p_{\mathrm{H^+ + He}} \Big/ p_{\mathrm{H + He^+}} \\ &= \sum_{i=3,6} p_i^{\,^1\Sigma^+} \Bigg/ \sum_{i=2,4,5} p_i^{\,^1\Sigma^+}, \end{aligned} \tag{4.59}$$

where $p_{\mathrm{H^+ + He}}$ and $p_{\mathrm{H + He^+}}$ are the populations in the dissociating channels leading to fragments H^+ + He and H + He^+, respectively, and where $p_i^{\,^1\Sigma^+}$ is the population in the i^{th} $^1\Sigma^+$ channel at time t_f.

As in that earlier study, HeH^+ is initially assumed to be in the $v'', J'' = 0$ level of its $X\ ^1\Sigma^+$ state. The partial cross sections for the $X\ ^1\Sigma^+ \rightarrow\ ^1\Sigma^+$ photodissociation of HeH^+ computed by Sodoga *et al.* [6] were reproduced in this work in order to determine the corresponding radiative association and rate constants (Fig. 3.5, p. 90). We show in Fig. 4.3 the partial photodissociation cross sections from the $v'', J'' = 0$ level of the $X\ ^1\Sigma^+$ towards the higher $^1\Sigma^+$ channels, as they will help in the interpretation of our control fields.

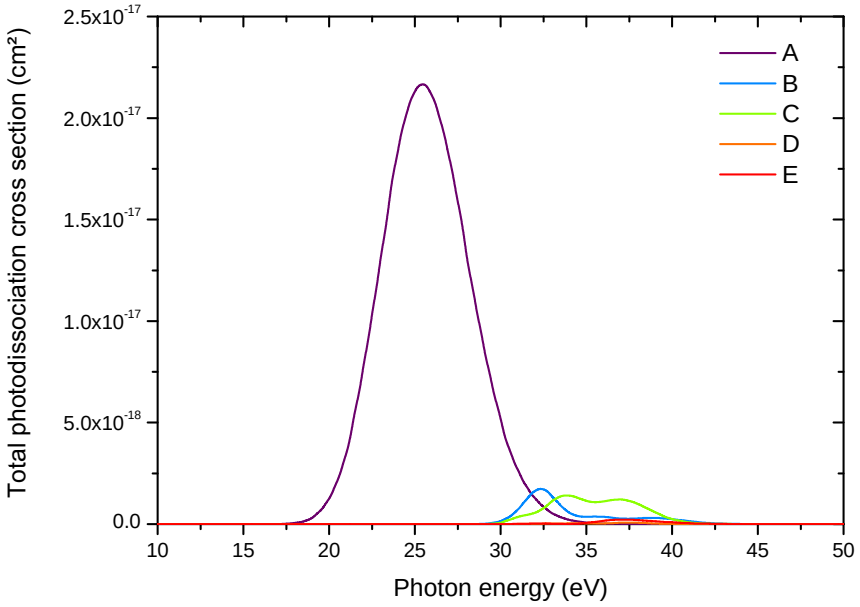

Figure 4.3: Partial photodissociation cross sections from the $v'' = 0$ level of the $X\ ^1\Sigma^+$ state of HeH^+ through its 5 lowest $^1\Sigma^+$ excited channels. State designation follows the convention given in Table 2.1 (p. 57). In this chapter, our aim will be to enhance the photodissociation in the *B* and *E* channels (blue and red curves, respectively).

To facilitate the comparison between our different results, a summary of the properties of our most efficient optimized pulses will be given in Table 4.3, p. 146.

4.3.1 Local Control of HeH^+

Our Local Control calculations were performed with the same parameters as Bomble *et al.* [43]: a short timestep $\delta t = 0.05$ a.u. of time for the determination of the laser field, a longer timestep $\delta t_{\text{free}} = 0.2$ a.u. for the field-free propagations, and an intensity parameter $\lambda = 4.2$. Only the value of the constraint ν on the area of the field was modified from one calculation to the next.

We first reproduced the field obtained by Bomble *et al.* [43] by using the exact same parameters, with $\nu = 0$ (*i.e.* no constraint on the area). The resulting field has already been shown in Fig. 4.1 (p. 120). As we have seen, although this control field leads to a reasonable objective (given the low values of the transition dipole moments and the complexity of the dynamics), it suffers from a fundamental flaw: its total area is not equal to zero, spurring our search for zero-area fields.

In a first step, we tried to suppress the non-oscillating "Stark" part of the field to measure its impact on the objective. We then computed new fields by adding a constraint on both its area (to ensure it is as close to zero as possible) and its fluence (to prevent the field from becoming too intense).

4.3.1.1 Suppression of "Stark" contributions

In a first attempt to get rid of the Stark contribution, we tried computing local averages of the field intensity and substracting them from the field itself in the hope of averaging out the oscillations and finding the Stark contribution as a baseline. Since this led to a mitigated result and to a sharp drop in the field's efficiency, we however looked for more efficient alternatives.

We realized it was much simpler to compute the Fourier Transform of the control field and to remove its "low"-frequency components[†], as the "Stark" contributions correspond to frequencies much lower than the oscillating, "electromagnetic" part of the control field.

By separating the "low-" and "high-"frequency components in Fourier space then performing an inverse Fourier transform on the resulting two pulses, we were able to perfectly split the original computed field into a purely "Stark" field and a purely "oscillating" laser field (Fig. 4.5).

The objective corresponding to the version of the field without Stark component was however found to have fallen from 8.55 % to 4.48 %, while its normalized area A_{norm} went from 6.39×10^{-4} to -3.59×10^{-4}. However, interestingly, the final population diminishes even more in the unwanted dissociation channels than in the target $H^+ + He$ channels, leading to an augmentation of the selectivity $p_{H^+ + He} / p_{H + He^+}$ from 1.07 to 1.24.

[†]The use of the words "low-" and "high-"frequency is purely relative.

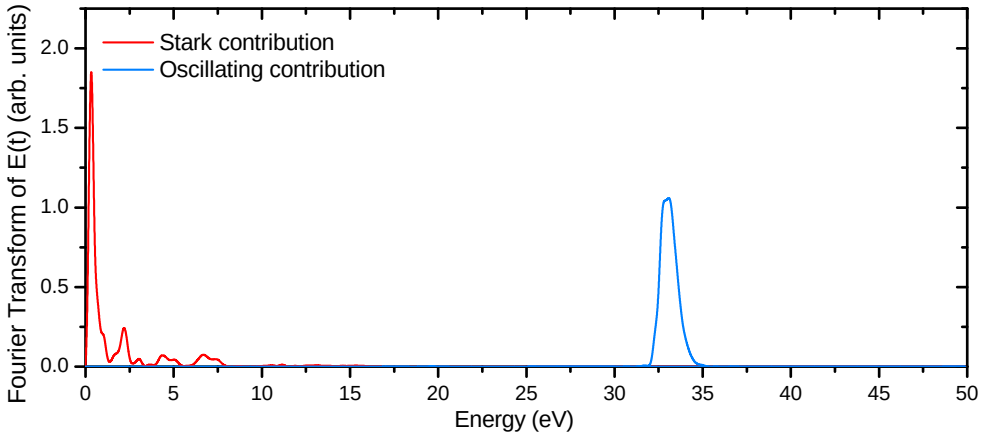

Figure 4.4: Fourier Transform of the LCT pulse optimized by Bomble *et al.* We split it into two components: the low-frequency, Stark contribution (red curve) and the high-frequency, oscillating contribution (blue curve).

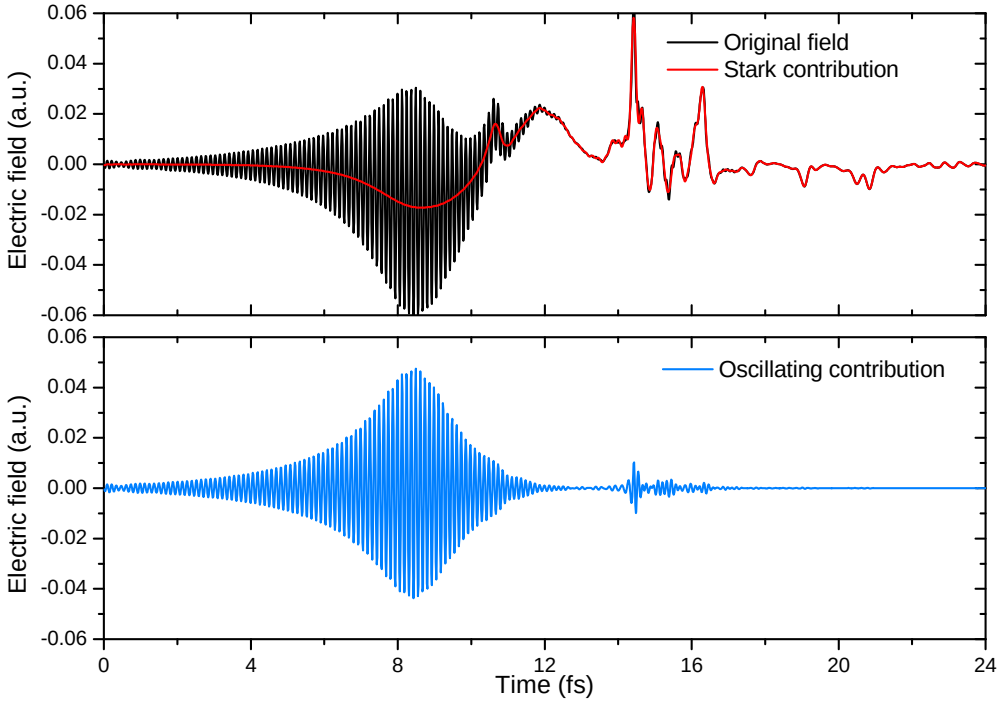

Figure 4.5: The local Control Field optimized by Bomble *et al.* with parameters $\lambda = 4.2$, $\nu = 0$ (upper panel, black curve) can be separated into a low frequency "Stark" contribution (upper panel, red curve) and an oscillating part (lower panel, blue curve) by filtering its Fourier transform.

4.3.1.2 Effect of the area constraint

While simply removing the "Stark" contribution to the control field led to a very sharp drop in its total area, it left room for improvement. Even fields which do not contain a low-frequency contribution obvious to the naked eye indeed often have a non-zero area.

We computed the Local Control field for several values of the area constraint parameter ν in

order to assess its effect both on the fidelity and on the appearance of the Stark contributions. The intensity parameter λ was kept constant for all computations and equal to 4.2, as in the original calculation of Bomble *et al.*

Fig. 4.6 shows the fields obtained for $\nu = 0, \nu = 0.05$ and $\nu = 0.10$ as well as the corresponding objectives. As can be seen to the naked eye, augmenting the value of the area constraint ν leads to a progressive diminution of the "Stark" contribution to the field and to a diminution of its total area.

However, high values of ν also diminish the field intensity and lead to very reduced values of the objective (from 8.55% for $\nu = 0$ to 4.75% for $\nu = 0.10$). This diminution of the intensity can be attributed to the fact that the area constraint minimizes the area $A(t)$ for each timestep t as the field is being constructed, preventing its value $E(t)$ from becoming too high at any point in time. The diminution of the objective with increasing ν is both a consequence of the lower field intensities and of the progressive disappearance of the "Stark" component.

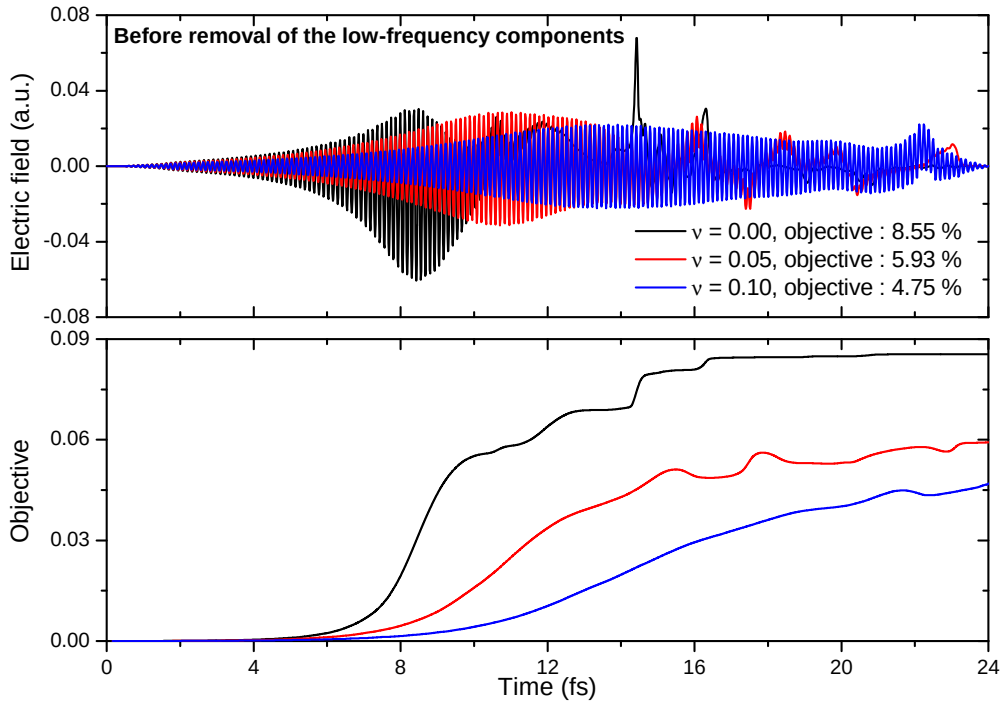

Figure 4.6: Upper panel: LCT-optimized fields for the control of the photodissociation of HeH^+, obtained with parameters $\lambda = 4.2$ and $\nu = 0$ (black curve), $\nu = 0.05$ (red curve) and $\nu = 0.10$ (blue curve). Lower panel: Corresponding objectives as a function of time.

Unfortunately, even for high values of ν, the "Stark" component does not disappear completely. In order to completely remove it from our optimized fields, we filtered their low-frequency contributions, as previously done for the $\nu = 0$ case. Fig. 4.7 shows the resulting filtered fields and the corresponding objectives. Comparing Fig. 4.7 and 4.6, we see once again that the objectives are diminished by the removal of the "Stark" component. However, this diminution becomes smaller as ν increases, from a factor 1.91 for $\nu = 0$ to a factor 1.39 for

$\nu = 0.10$[†]: since the constraint on the area partly prevents the appearance of the "Stark" component, the effect of its removal on the objective becomes less marked for high values of ν.

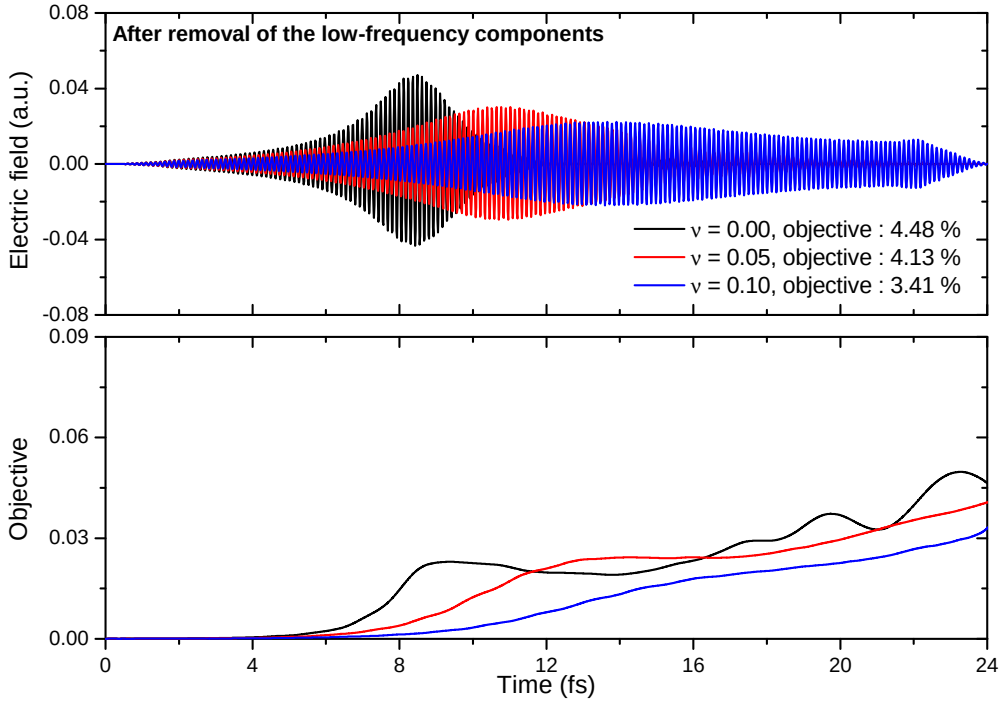

Figure 4.7: Upper panel: LCT-optimized fields for the control of the photodissociation of HeH^+, obtained with parameters $\lambda = 4.2$ and $\nu = 0$ (black curve), $\nu = 0.05$ (red curve) and $\nu = 0.10$ (blue curve), after removal of their "Stark" component. Lower panel: Corresponding objectives as a function of time. Results are shown on the same scale as in Fig. 4.6.

It is interesting to compare the effect that the constraint ν and the removal of the "Stark" components have on the area of the optimized fields. Fig. 4.8 shows the values of A_{norm} and B_{norm} for our optimized pulses as a function of ν, before (upper panel) and after (lower panel) removal of their low-frequency, "Stark" component. The evolution of A_{norm} and B_{norm} as a function of ν is not monotonic: the best correction is obtained around $\nu = 0.08$, which leads to a value of B_{norm} that is almost equal to zero. The efficiency of the area constraint in Local Control cannot be denied, however, finding the optimal value of the constraint ν that minimizes the area requires several calculations.

Moreover, comparing the upper and lower panels of Fig. 4.8 shows that filtering the low-frequency contributions of the optimized fields is much more efficient at reducing their area than the use of the constraint ν in the present case. Strangely enough, the fields optimized with high values of ν actually have a higher area than their $\nu = 0$ counterparts after filtering, although their area is so small that these differences may not be significant.

It is also worth noting that the inclusion of a constraint on the area ($\nu \neq 0$) and the suppression of the "Stark" components of the fields both lead to a non-monotonic evolution of the

[†]The ratios between the objectives before and after filtering are given by: 8.55%/4.48% = 1.91 for $\nu = 0$, and 4.75%/3.41% = 1.39 for $\nu = 0.10$.

objective as a function of time, as illustrated by the lower panels of Figs. 4.6 and 4.7.

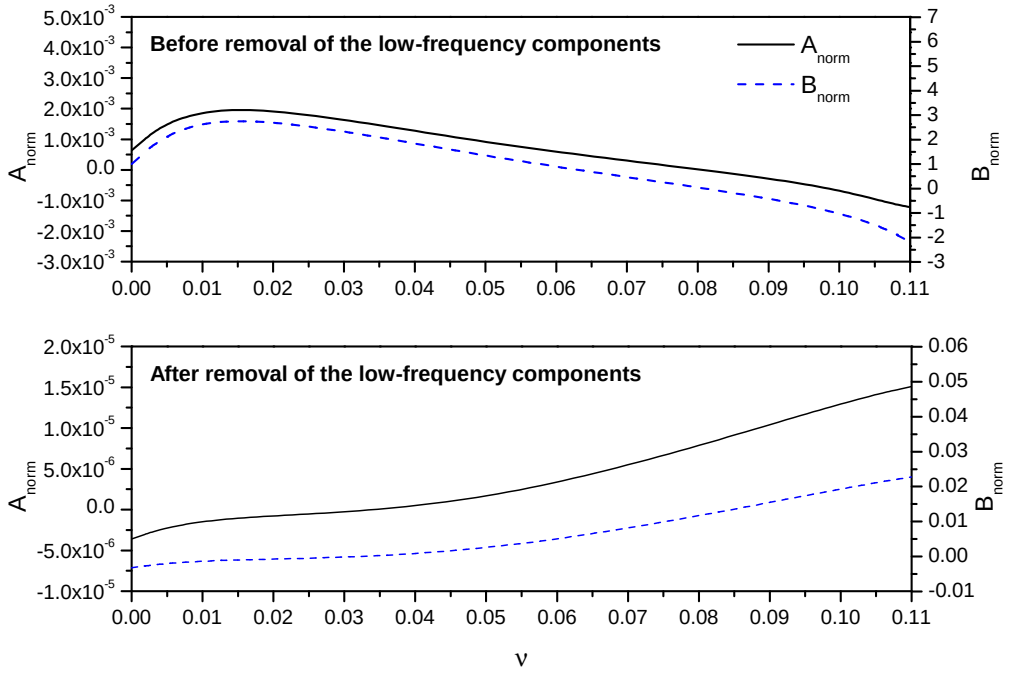

Figure 4.8: A_{norm} and B_{norm} (see Eq. 4.57) of our LCT-optimized pulses for the photodissociation of HeH^+ as a function of the area constraint ν. Upper panel: Results for the original fields (Fig. 4.6). Lower panel: Results after removal of the "Stark" components (Fig. 4.7).

4.3.2 Optimal Control of HeH^+

As mentioned in Section 4.1.3 (p. 122), the optimization of laser fields using Optimal Control Theory requires the selection of a total duration t_f for the control process and of an "initial guess" field which serves as a starting point for the algorithm. In this work, we used two kinds of initial guess: the Local Control fields described in the previous section and Gaussian pulses with frequencies corresponding to those of the Franck-Condon transitions towards the target states.

The duration of the optimized pulses was chosen to be a bit longer than the Local Control field: $t_f = 1638.4$ a.u. of time, *i.e.* ≈ 40 fs. All calculation where therefore performed from $t = 0$ to $t_f = 1638.4$ a.u. with a time step $\delta t = 0.05$ a.u. of time.

4.3.2.1 OCT of HeH^+ using Gaussian pulses as trial fields

Preliminary tests with Gaussian pulses, without optimization

We performed simple control tests using Gaussian pulses, since their area is equal zero and since they can easily be created experimentally. The carrier frequency of our test pulses were chosen to correspond to a Franck-Condon transition from the initial state to the target states.

Two series of calculations were performed: one with a fixed maximum value ($E(t)_{\max} = 0.05$ a.u.) of the pulses and one with a fixed fluence equal to that of the $v = 0$ LCT field after removal of its "Stark" component ($F = 0.06$ a.u.).

For each series, three type of pulses were tried: a single Gaussian whose carrier frequency corresponds to a resonant transition from state $X\ ^1\Sigma^+$ to state $B\ ^1\Sigma^+$ ($E_{hv} = 1.2097$ hartree = 32.92 eV), a Gaussian pulse whose carrier frequency corresponds to a transition towards state $E\ ^1\Sigma^+$ ($E_{hv} = 1.3803$ hartree = 37.56 eV), and a sum of two such pulses. Fig. 4.9 shows the corresponding pulses while Table 4.1 shows the results of these calculations.

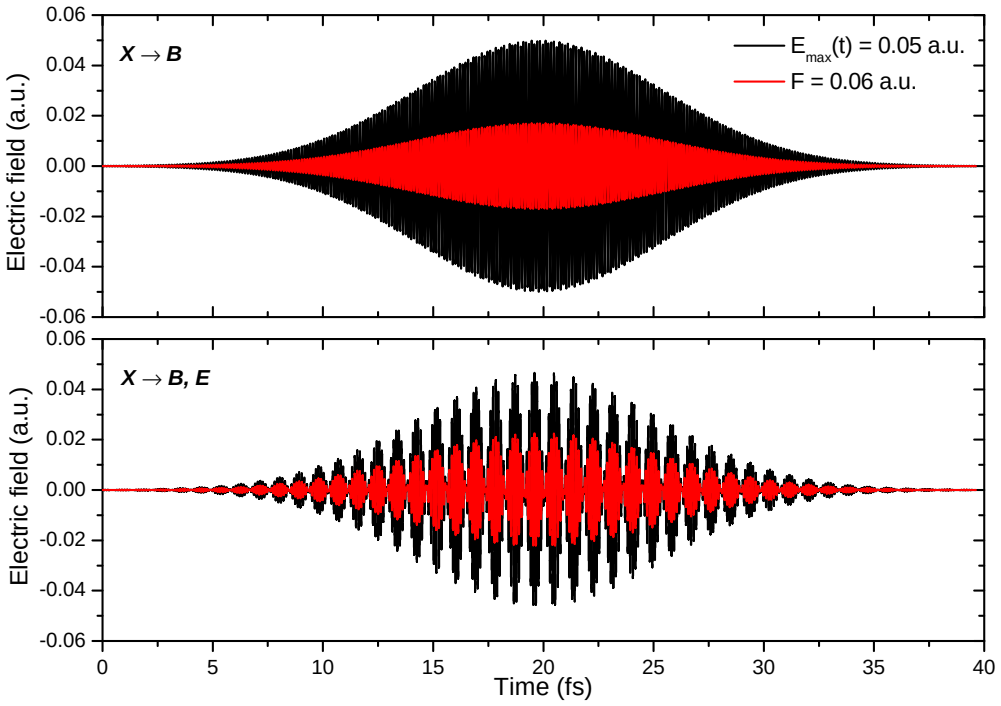

Figure 4.9: Four of the Gaussian pulses used as initial guess in our OCT calculations for the photodissociation of HeH^+, corresponding to resonant transitions towards the $B\ ^1\Sigma^+$ state (upper panel) or the B and $E\ ^1\Sigma^+$ states (lower panel), with a predefined peak value $E(t)_{\max} = 0.05$ a.u. (black curves) or a predefined fluence $F = 0.06$ a.u. (red curves).

Using resonant Gaussian pulses with a predefined peak value $E(t)_{\max} = 0.05$ a.u. as the only constraint leads to relatively high objectives: up to 13.77%, as illustrated by the left column of Table 4.1. Interestingly, using the sum of two resonant Gaussian pulse instead of one does not increase the objective but actually leads to as significant decrease due to interference effects.

These results may appear better than those obtained using Local Control Theory, since the objectives are significantly higher. The comparison of pulses that have different durations and intensity is however uneasy: it is well-known that longer and more intense pulses lead to better results than short weaker ones. In order to facilitate the comparison, we chose to compare fields with the same fluence F (as defined in Eq. 4.50).

When we impose their maximum value $E(t)_{\max} = 0.05$ a.u., the Gaussian pulses indeed have a much higher fluence than our Local Control pulse ($F \approx 0.40$ a.u. in contrast to ≈ 0.06a.u.).

Table 4.1: Objectives for the control of the photodissociation of HeH^+ using resonant Gaussian pulses with a predefined peak value $E(t)_{max} = 0.05$ a.u. or a predefined fluence $F = 0.06$ a.u.

	$E(t)_{max} = 0.05$ a.u.	$F = 0.06$ a.u.
$\text{Gaussian}_{X\rightarrow B}$	13.77 %	2.37 %
$\text{Gaussian}_{X\rightarrow E}$	11.77 %	1.56 %
$\text{Gaussians}_{X\rightarrow B,E}$	6.82 %	2.04 %

Imposing a fixed fluence $F_0 \approx 0.06$ a.u. for the Gaussian pulses leads to a very sharp decrease of the objective, as seen in the right column of Table 4.1. For a given amount of energy provided by a laser, the Local Control pulse therefore achieves significantly higher objectives than simple Gaussian pulses. Moreover, the selectivity of the Gaussian pulses is lower than that of our Local Control pulses (on the order of ≈ 0.7 instead of ≈ 1.2 for $v = 0$).

OCT using Gaussian pulses as initial guess

A series of OCT calculations were performed using these Gaussian pulses as initial guesses, with fixed fluence $F_0 = 0.06$ a.u. The corresponding values of the objective after 100 iterations are given in Table 4.2. As can readily be seen, the highest objectives are obtained for the trial pulses that themselves led to the highest objective. No constraint on the area was used for this series of calculation, as the objective was found to raise very little from one iteration to another even for $v = 0$.

Table 4.2: Objectives obtained after 100 OCT iterations with a fixed fluence $F_0 = 0.06$ a.u. for the control of the photodissociation of HeH^+ using Gaussian pulses as initial guess.

	Objective after 100 iterations
$\text{Gaussian}_{X\rightarrow B}$	5.21 %
$\text{Gaussian}_{X\rightarrow E}$	3.02 %
$\text{Gaussians}_{X\rightarrow B,E}$	4.19 %

Accordingly, only the optimization using the Gaussian with a carrier frequency corresponding to the $X \rightarrow B$ transition was carried on for more than 100 iteration, eventually reaching an objective of 16.48 % after 300 iterations. However, this optimized field contained an obvious

"Stark" component, as seen in the upper panel of Fig. 4.10, whose removal caused a drop of the objective to 12.35 %. Interestingly, it also led to a field area that is for all intent and purposes equal to zero ($A_{\mathrm{norm}} = 3.14 \times 10^{-17}$) and to a slight increase in selectivity $p_{\mathrm{H^+ + He}}/p_{\mathrm{H + He^+}}$, from 1.07 to 1.12.

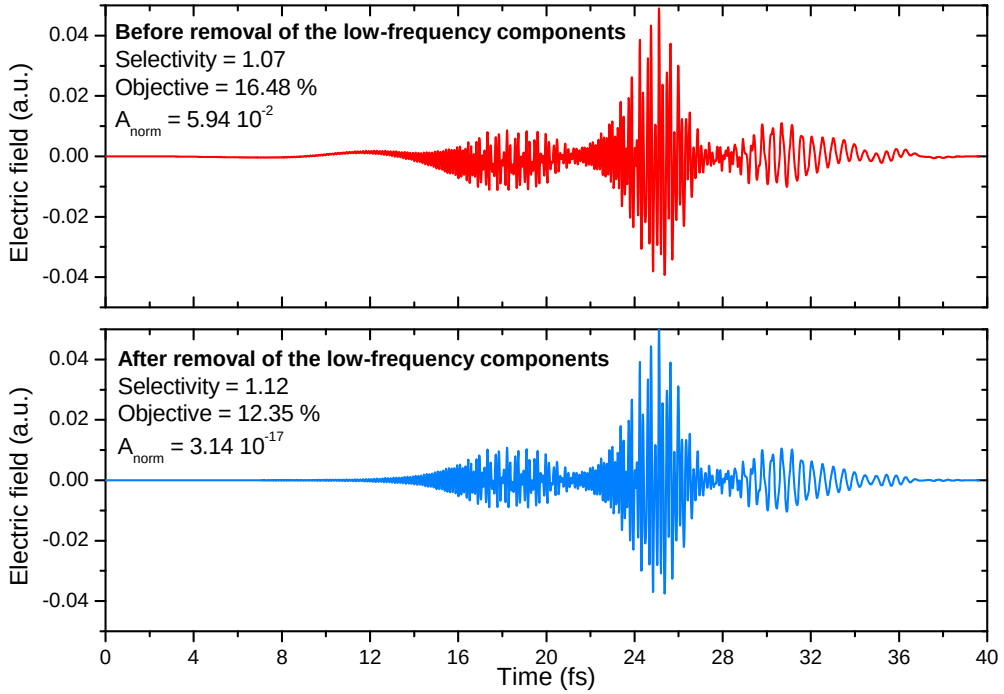

Figure 4.10: OCT-optimized fields for the control of the photodissociation of HeH^+ using a Gaussian pulse as initial guess, before (upper panel) and after (lower panel) removal of the "Stark" components.

Although the OCT algorithm led to significant improvement of the Gaussian trial pulse, even better results were obtained (at equal fluence) by using the best Local Control pulse as initial guess, as discussed in the next section.

4.3.2.2 OCT of HeH^+ using LCT pulses as trial fields

Finally, our LCT-optimized pulse were used as initial guess for the Optimal Control algorithm. The best results were obtained when the $\lambda = 4.2$, $\nu = 0$ Local Control field (filtered to remove the "Stark" component) was used as initial guess, which is unsurprising given that it has both the highest objective and the lowest area of all our LCT-optimized fields.

To allow for easy comparison with our other results, the fluence of the optimized pulses was fixed at $F_0 = 0.06$ a.u. The constraint on the area ν was varied from $\nu = 0$ to $\nu = 0.40$ from one calculation to another. However, choosing a value of ν greater than 0.20 was found to lead to convergence problems as the second term of equation 4.54 (p. 131) becomes dominant and leads to field intensities which are far too high to be realistic.

The upper panel of Fig. 4.11 shows the fields obtained after 300 iterations for $\nu = 0$ and

$\nu = 0.20$[†]. Every 100 iteration, the optimization was interrupted and the low-frequency components were filtered to prevent the appearance of a significant Stark component in the field. Interestingly, although the fields obtained for all values of ν are almost identical visually and lead to the same objective (21.55%–21.54%), their areas A_{norm} and B_{norm} significantly diminish with increasing ν, as shown in Fig. 4.12.

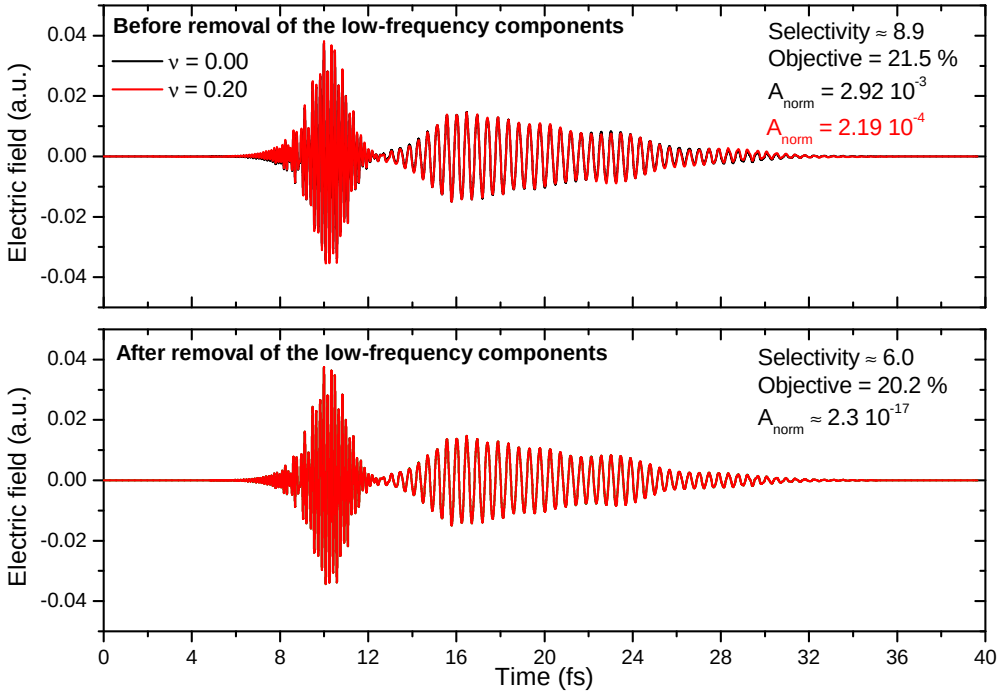

Figure 4.11: OCT-optimized fields for the control of the photodissociation of HeH^+ using the LCT field as initial guess, before (upper panel) and after (lower panel) removal of the "Stark" components. The results for $\nu = 0$ and $\nu = 0.20$ are almost perfectly superposed.

However, these fields contain once again a very small "Stark" component, too small to be detected by the naked eye. Suppressing it leads to a very small diminution of the objective (20.24% for both $\nu = 0$ and $\nu = 0.20$) and to a significant diminution of the area, which becomes virtually equal to 0 ($A_{\text{norm}} \approx 2.5 \times 10^{-17}$ a.u.). Again, the resulting fields for $\nu = 0$ and $\nu = 0.20$ are almost identical and have very similar properties. Moreover, these fields have excellent selectivity: the final populations of the two target states are slightly diminished, but those of the other $^1\Sigma^+$ are more significantly decreased, leading to a selectivity $p_{H^+ + He} / p_{H + He^+} \approx 6$.

As in the case of Local Control Theory, the area constraint in Optimal Control Theory was thus found to be efficient in reducing the final area of the optimized pulse without significantly affecting the objective. However, simply filtering the low-frequency components of the fields was once again found to be more efficient in the present case, as it leads to zero-area fields with reasonably high objectives (given the nature of the test system) and, more importantly, high selectivity.

[†]Note that the fields are almost identical and that the slight differences may not be perceptible in the printed version of his work.

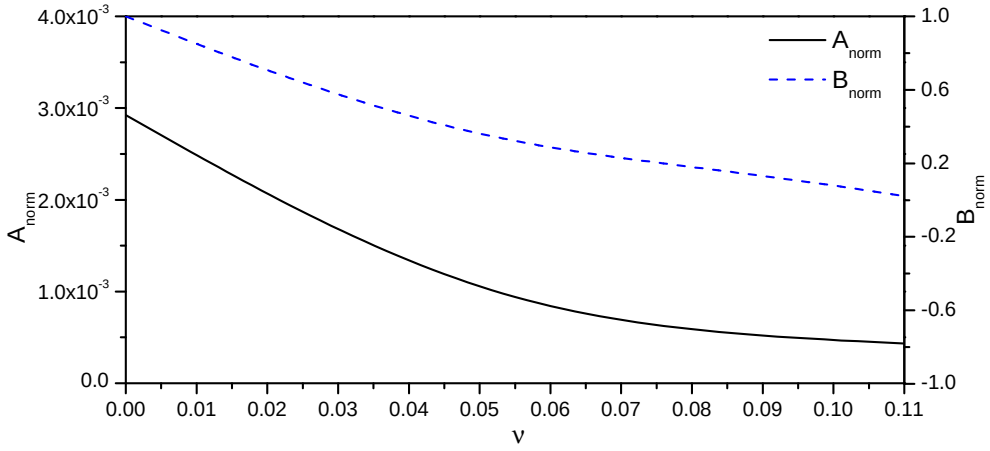

Figure 4.12: A_{norm} and B_{norm} of our OCT-optimized pulses for the photodissociation of HeH^+ as a function of the area constraint ν.

In terms of mechanism, the original Local Control field's main frequency corresponds to a photon energy of around 32.5 eV (Fig. 4.13, lower-left panel). This matches the energy region where the partial cross sections for the desired B and E channels are maximal (as seen earlier in Fig. 4.3, p. 134). However, since the cross sections for the unwanted channels still dominate even in that region, a significant population transfer occurs towards them, hence the low selectivity of the LCT pulse (Fig. 4.13, upper-left panel).

By contrast, the final Optimal Control field first contains a very intense component in the 20–30 eV energy range, *i.e.* in the region where the photodissociation only occurs through the A channel (Fig. 4.13, lower-right panel). After about 14 fs, when the wavepacket has left the Franck-Condon region, a second component then transfers population from the unwanted A state to the target B channel: the lower frequency of that second contribution indeed matches the asymptotic energy difference between the A and B states.

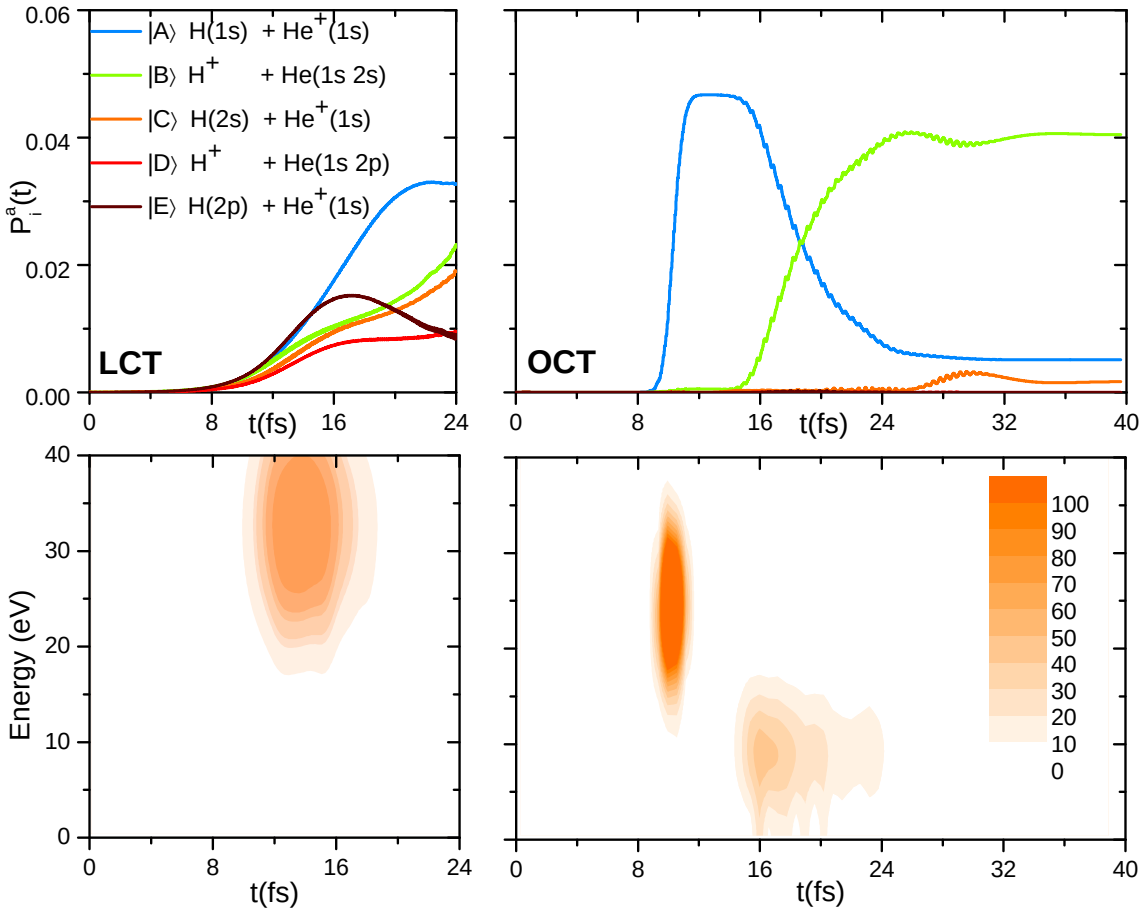

Figure 4.13: Upper panels: Population evolution for the filtered LCT-optimized field with $\lambda = 4.2$, $\nu = 0$ and the final OCT-optimized field (left and right panels, respectively). Lower panels: corresponding Gabor transforms of the control fields (in arbitrary units). State designation follows the convention given in Table 2.1 (p. 57).

4.3.3 Summary: Control of the photodissociation of HeH^+

To summarize, Table 4.3 shows the best results we obtained for each kind of pulse: the LCT-optimized pulses with parameters $\lambda = 4.2$, $\nu = 0$ and $\nu = 0.10$, the resonant Gaussian pulses with fixed maximum intensity $E_{\max}(t)$ and with fixed fluence $F_0 = 0.06$ a.u., and the OCT-optimized pulses with fixed fluence $F = 0.06$ a.u. obtained by using either a Gaussian pulse or the $\nu = 0.0$ LCT pulse as initial guess. Results are shown for the original fields and their counterpart with the "Stark" component removed.

Table 4.3: Summary of the main pulses optimized for the control of the photodissociation of HeH^+. The final time t_f, the maximum value of the electric field $E_{max}(t)$ and the fluence F are all expressed in atomic units.

Field	Objective	t_f	$E_{max}(t)$	Selectivity	A_{norm}	F	Fig.
LCT, $\nu = 0$	8.55 %	1000	0.068	1.067	6.39×10^{-4}	0.102	4.6, p. 137
LCT $\nu = 0$, no "Stark"	4.48 %	1000	0.047	1.243	-3.59×10^{-4}	0.049	4.6, p. 137
LCT, $\nu = 0.10$	4.75 %	1000	0.024	0.797	-4.30×10^{-4}	0.045	4.6, p. 137
LCT $\nu = 0.10$, no "Stark"	3.41 %	1000	0.022	0.563	1.32×10^{-5}	0.058	4.6, p. 137
Gaussian$_{X\rightarrow B}$, $E_{max}(t)$=0.05	2.37 %	1638.4	0.050	0.853	0	0.376	4.9, p. 140
Gaussian$_{X\rightarrow B}$, F=0.06	13.77 %	1638.4	0.017	0.722	0	0.060	4.9, p. 140
OCT, Guess = Gaussian$_{X\rightarrow B}$, F_0=0.06	16.48 %	1638.4	0.049	1.067	5.94×10^{-2}	0.060	4.10, p. 142
OCT, Guess = Gaussian$_{X\rightarrow B}$, F_0=0.06, no "Stark"	12.35 %	1638.4	0.051	1.119	3.14×10^{-17}	0.058	4.10, p. 142
OCT, Guess = LCT$_{\nu=0}$, $\nu = 0.20$, F_0=0.06	21.54 %	1638.4	0.039	8.894	2.19×10^{-4}	0.060	4.11, p. 143
OCT, Guess = LCT$_{\nu=0}$, $\nu = 0.20$, F_0=0.06, no "Stark"	20.24 %	1638.4	0.039	5.952	2.35×10^{-17}	0.060	4.11, p. 143

4.4 Laser control of the photodissociation of CO^{2+}

As previously stated, CO^{2+} is a species of particular interest in quantum control experiments due to the fact that the $v = 0$ level of its $X\ ^3\Pi$ state has a relatively long lifetime ($\tau > 3.8$ s, long enough to perform control experiments), whereas its excited vibrational levels predissociate very quickly. In the following calculations, CO^{2+} is assumed to initially be exclusively in the $v'', J'' = 0$ level of its $X\ ^3\Pi$ state.

All the following computations were performed using the potential energy curves, transition dipole moments and nonadiabatic couplings of the $X\ ^3\Pi$ and the eleven first $^3\Sigma^-$ states we computed in Chapter 2 of this work, expressed on a spatial grid of 2^{12} points ranging from $R_{\text{min}} = 1.5\ a_0$ to $R_{\text{max}} = 100.0\ a_0$.

Our goal in this study of CO^{2+} is to optimize laser fields that will photodissociate the dication through its $^3\Sigma^-$ channels into the fragments C^{2+} + O. As seen in Chapter 2, this amounts to favoring the dissociation of CO^{2+} through its ninth $^3\Sigma^-$ channel. The scattering projector used in our definition of the control field is therefore[†]:

$$P_9^{sc} = \int |\phi_9^-(p)\rangle \langle \phi_9^-(p)|\ dp. \tag{4.60}$$

Since the ten other $^3\Sigma^-$ states included in our calculations correspond to the fragments C^+ + O^+, the selectivity is given by the expression:

$$\begin{aligned} \text{Selectivity} &= p_{C^{2+}+O} \Big/ p_{C^+ + O^+} \\ &= p_9^{^3\Sigma^-} \Big/ \sum_{i=1, i\neq 9}^{11} p_i^{^3\Sigma^-}, \end{aligned} \tag{4.61}$$

where $p_{C^{2+}+O}$ and $p_{C^+ + O^+}$ are the populations in the dissociating channels leading to fragments C^{2+} + O and C^+ + O^+, respectively, and where $p_i^{^3\Sigma^-}$ is the population in the $i^{\text{th}}\ ^3\Sigma^-$ channel at time t_f.

When compared to HeH^+, additional difficulties in the optimization of photodissociation control pulses of CO^{2+} arise from three factors:

1. The higher number of states included in the calculations (12 instead of 6), which increases the required computational resources.

2. The fact that our aim is to dissociate the molecule through a single channel instead of two, in the presence of 10 undesired channels instead of 3, leading to lower objectives and selectivity.

3. The fact that the photodissociation cross section for this channel does not dominate in any energy range (as shown in Fig. 3.26, p. 110), which complicates the control and limits

[†]Note: In this equation, 9 denotes the ninth $^3\Sigma^-$ state. For convenience, the $^3\Pi$ state was assigned the number 0 so that the first, second, third, ... $^3\Sigma^-$ state could be assigned the numbers 1, 2, 3, ... to ensure that the state numbering follows the same convention as in Table 2.6, p. 69.

its yield.

To facilitate the comparison between our different results, a summary of the properties of our most efficient optimized pulses will be given in Table 4.4, p. 154.

4.4.1 Local Control of CO^{2+}

We first computed laser control pulses using Local Control Theory, as we did for HeH^+, in order to assess the efficiency of this approach and to use the resulting fields as a starting point for the Optimal Control calculations. As in the case of HeH^+, a timestep $\delta t = 0.05$ a.u. of time for the determination of the laser field $E(t)$ was chosen, with a longer timestep $\delta t_{\text{free}} = 0.2$ a.u. for the field-free propagations.

Unlike in the case of HeH^+, the value of the intensity parameter λ was varied from one calculation to the next. However, since our results for $\nu = 0$ contained no significant "Stark" contribution and had a very low area ($A_{norm} = 7.92 \times 10^{-5}$), no calculations with higher values of the area constraint parameter ν were performed.

The best results were obtained for $\lambda = 7.5$, which corresponds to a good compromise between the need for keeping the field intensity reasonably low and the need for reaching good values of the objective. The resulting field, which reaches an objective of 16.49% after 6500 a.u. of time ($\approx$ 157.27 fs), is shown in Fig. 4.14.

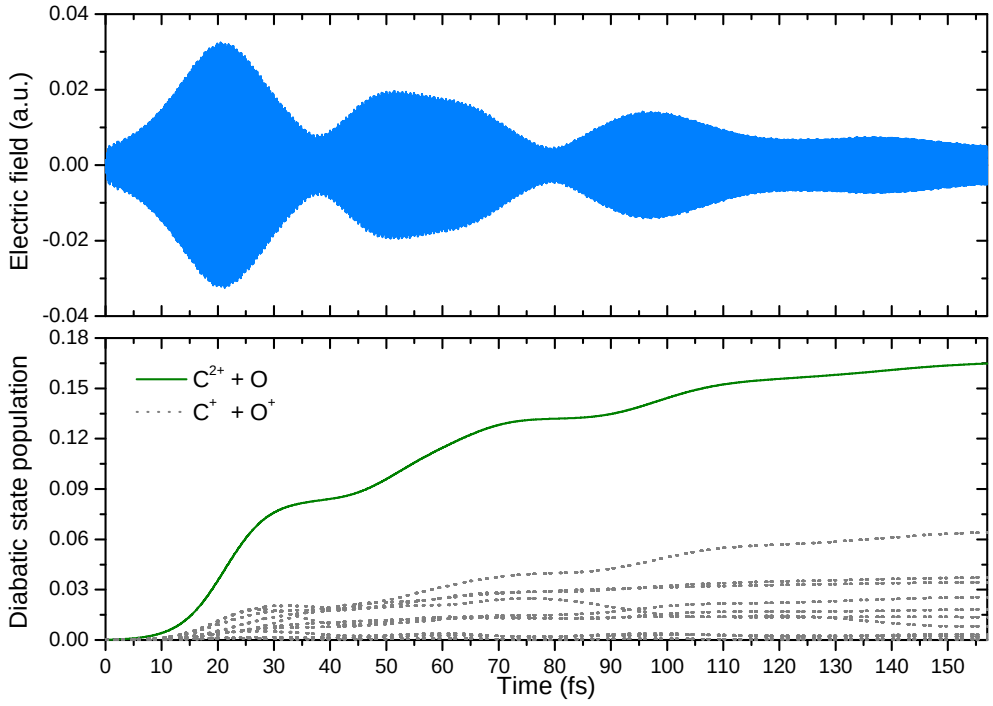

Figure 4.14: Upper panel: LCT-optimized field to guide the photodissociation of CO^{2+} towards the C^{2+} + O channel, obtained with parameters $\lambda = 7.5$, $\nu = 0$. Lower panel: Corresponding diabatic populations.

Remarkably, despite the fact that the partial photodissociation cross section for the ninth $^3\Sigma^-$ state is significantly smaller than those of all other $^3\Sigma^-$ states (Fig. 3.26, p. 110), the opti-

mized pulse strongly favors the dissociation through that channel, as illustrated by the evolution of the populations in the lower panel of Fig. 4.14.

However, although the C^{2+} + O channel is the most populated, summing the final populations in the 10 other $^3\Sigma^-$ states included in our calculations leads to a higher result: 20.69%. The pulse therefore slightly favors the dissociation through the C^+ + O^+ channels instead of C^{2+} + O, with a selectivity $p_{C^{2+}+O}/p_{C^+ + O^+} = 0.797$. This is however more than ten times higher than the selectivity observed in simple photodissociation calculations, $p_{C^{2+}+O}/p_{C^+ + O^+} = 0.0612$. The remaining 62.82% of the population is still in the ground $X\ ^3\Pi$ state and could be photodissociated through a new application of the optimized pulse.

Interestingly, our Local Control fields do not contain any obvious-to-the-naked-eye Stark contribution even for $v = 0$, unlike in the case of HeH^+. Accordingly, their spectrum does not contain any low-frequency contribution.

It is also interesting to note that, unlike in the case of HeH^+, the control field does not spontaneously stop: even after 6500 a.u. of time ($\approx$ 157.27 fs), the algorithm still finds ways to keep populating the target dissociation channel. However, by that point, the part of the wavepacket that was first promoted to the excited states is very close the end of the spatial grid used in our numerical calculations and the number of steps in the field-free propagations is getting close to zero, preventing us from pursuing the calculations much further with our chosen set of parameters (hence the abrupt end of the field shown in Fig. 4.14). The control dynamics could however be simulated further by extending the spatial grid.

It might however not be reasonable to optimize very long control pulses as their experimental implementation would likely be very complex. Instead, it may be preferable to optimize a shorter pulse with lower fidelity that could be repeatedly applied on the molecule to progressively depopulate the initial state (in other words, using repeatedly a short but simple pulse may be preferable to using a long and complex pulse).

We chose to pursue this strategy using Optimal Control Theory, by using either Gaussian pulses or the first part of the Local Control pulse as trial field.

4.4.2 Optimal Control of CO^{2+}

Two series of Optimal Control calculations were performed for CO^{2+}, differing by the nature of the trial fields $E^{(0)}(t)$: resonant Gaussian pulses for the first, and a variant of the LCT-optimized field for the second.

4.4.2.1 OCT of CO^{2+} using Gaussian pulses as trial fields

As in the case of HeH^+, our first Optimal Control calculations for the photodissociation of CO^{2+} were performed with resonant Gaussian pulses as initial guess. The peak value of the electric fields was fixed at 0.05 a.u. (2.57×10^{10} V·m^{-1}). Two carrier frequencies were tested: one corresponding to the energy of a vertical transition from the initial $X\ ^3\Pi$ state to the target ninth $^3\Sigma^-$ adiabatic state at the internuclear distance where the vibrational wavefunction is maximal

($E_{h\nu}$ = 16.78 eV, see Fig. 2.14 on p. 74), and one corresponding to the maximum of the partial photodissociation for the target channel ($E_{h\nu}$ = 14.43 eV, see Fig. 3.26 on p. 110).

These calculations however proved completely unsuccessful: the objective never reached more than 0.4% in the former case and 1.3% in the latter, even after dozens of iterations, as each of them only brought negligible improvement. This lack of significant progress from one iteration to another is usually observed when a "bad" trial pulse is used, preventing the algorithm from finding an efficient pathway to go from the initial state Ψ_i to the desired final state Ψ_f using the provided trial pulse as a starting point.

Additionally, the selectivity of the pulses was also found to be very low: the initial $^3\Pi$ state is almost completely depopulated, but the dissociation occurs predominantly through $C^+ + O^+$ channels, leading to a selectivity $p_{C^{2+}+O}/p_{C^+ + O^+} \approx 0.025$ in the target $C^{2+} + O$ channel at best.

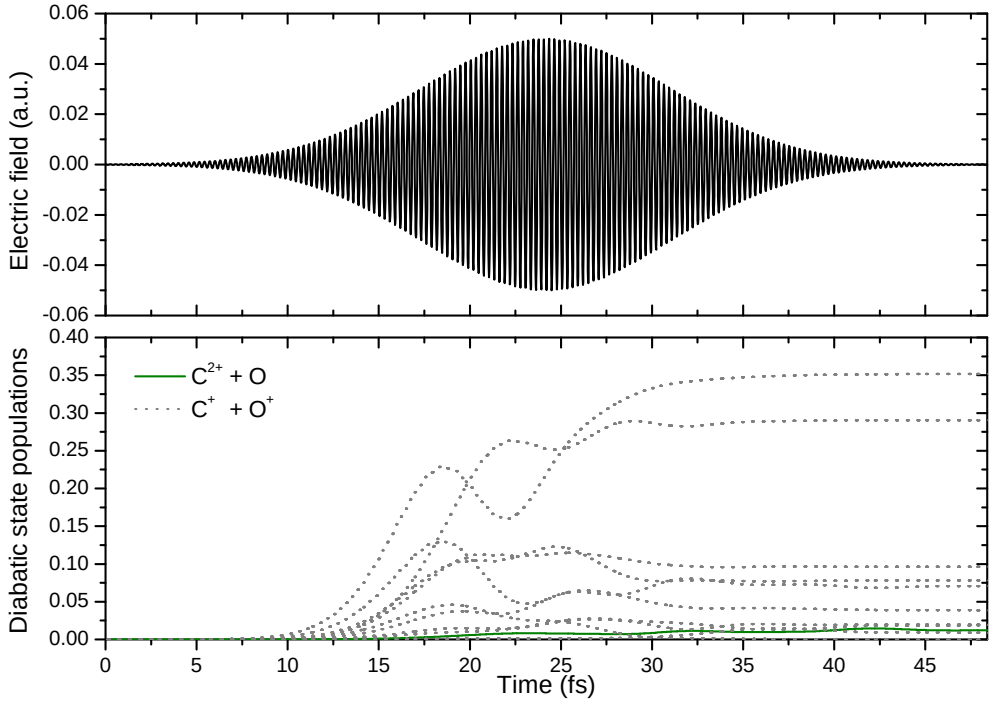

Figure 4.15: Upper panel: One of the Gaussian pulses used as initial guess in our OCT calculations for the control of the photodissociation of the $X\ ^3\Pi$ state of CO^{2+} through the $^3\Sigma^-$ channels. Lower panel: corresponding diabatic state populations as a function of time.

Although improvements might possibly have been obtained by using a combination of Gaussian pulses with different frequencies instead of one, we chose not to persevere in that direction: the inefficiency of the Gaussian pulse was no surprise, given the fact that the partial cross section for the photodissociation in the desired channel is very small.

4.4.2.2 OCT of CO^{2+} using LCT pulses as trial fields

Instead, we chose to use our Local Control field as a trial pulse for the Optimal Control algorithm, since it was clearly more efficient than any Gaussian pulse of equal intensity could ever be and since this approach had proved efficient in the case HeH^+. However, as noted in

Section 4.4.1, the Local Control field we computed has a relatively long duration: 6500 a.u. of time (≈ 157.27 fs). Since the optimization of such a long field using OCT with a reasonably short timestep δt in such a large basis of states would require an enormous amount of computing resources, we chose to limit the duration of our OCT pulse to 2000 atomic units of time (≈ 48.38 fs). In order to ensure a smooth start and end of the guess pulse, a modified sine square envelope (Eq. 4.28, p. 124) was added to the LCT field with parameters $t_f = 2000$, $t_{\text{sine}} = 200$ a.u. of time, as shown earlier in Fig. 4.2, p. 124. The resulting guess field is shown in Fig. 4.16 and leads to a final population of 9.01% in the target C^{2+} + O channel (a sharp drop from the 16.49% of the original LCT field, due to its much shorter duration and the addition of the envelope – although interestingly, the selectivity $p_{C^{2+}+O}/p_{C^{+}+O^{+}} \approx 0.799$ remains almost unaffected).

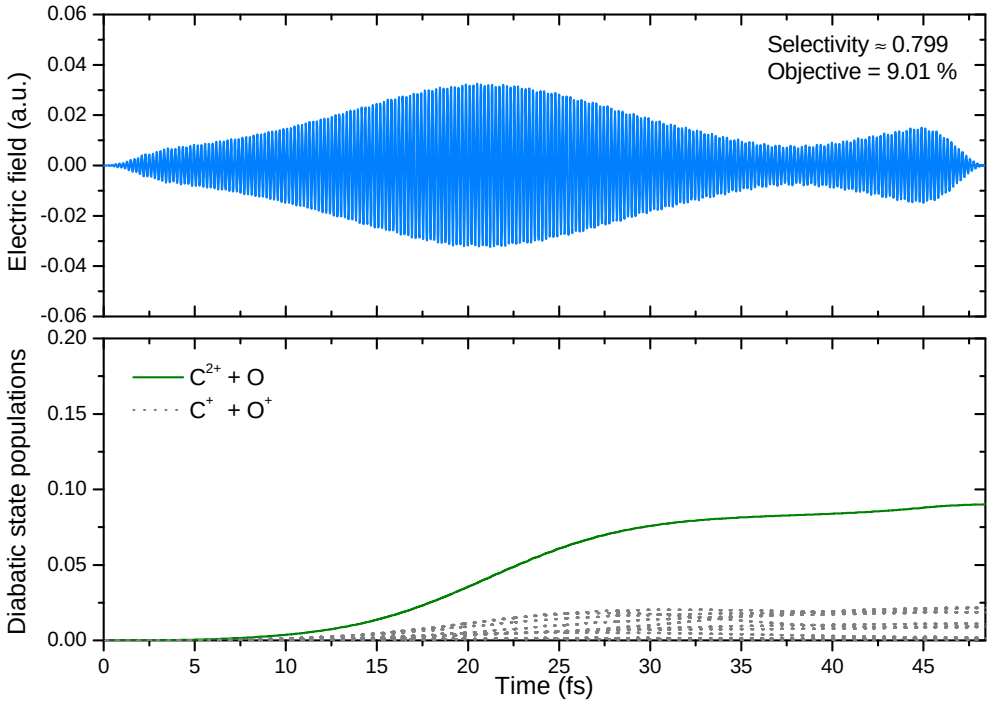

Figure 4.16: Upper panel: Modified LCT pulse used as initial guess in our OCT calculations for the control of the photodissociation of the $X\ ^3\Pi$ state of CO^{2+} through the $^3\Sigma^-$ channels. Lower panel: diabatic state populations as a function of time.

Additionally, the constraints on the fluence and the area of the pulse were found to stifle its optimization by Optimal Control Theory, leading to fidelities that stayed very low even after numerous iterations. This is likely due to the relatively small transition dipole moments of CO^{2+} compared to those of HeH^+.

The parameter α_0 was varied from one computation to another. The best results were obtained for $\alpha_0 = 200$: although this occasionally led to peak field $E_{\max}(t)$ values higher than 0.05 a.u., we circumvented this problem by dividing the whole field by a constant factor when its intensity became too high, as previously done in other studies of this kind (see for example [196]). This allowed us to prevent the field from becoming too intense while still giving "breathing room" to the optimization algorithm.

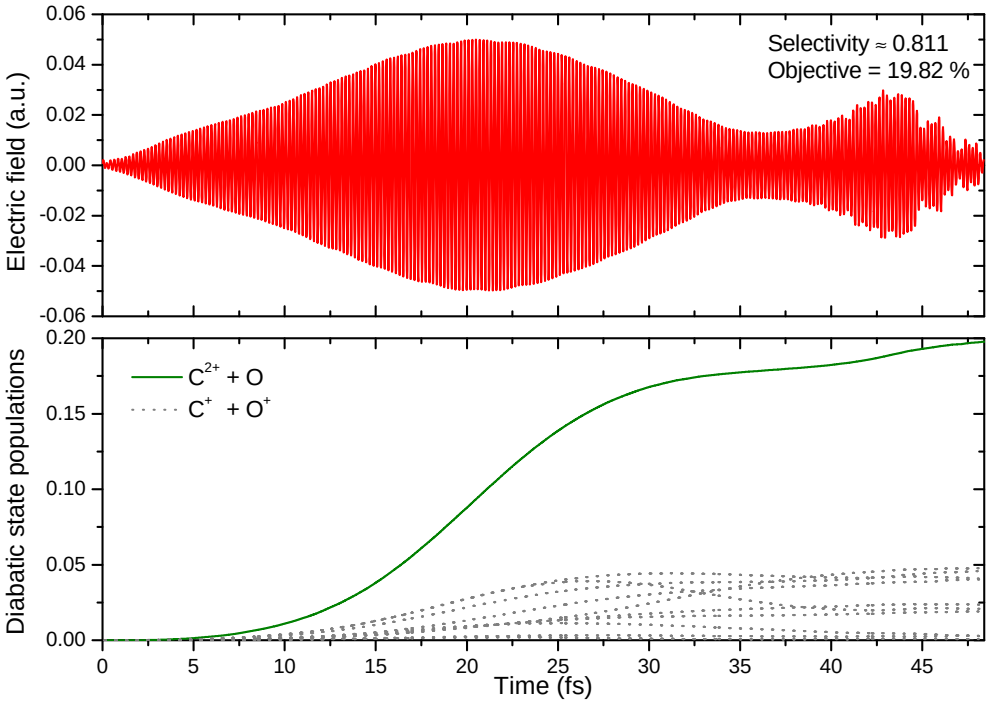

Figure 4.17: Upper panel: OCT-optimized pulse for the photodissociation of CO^{2+} using the LCT field (Fig. 4.16) as initial guess with $\alpha_0 = 200$. Lower panel: diabatic state populations as a function of time.

The resulting field, obtained after 158 iterations, is shown in the upper panel of Fig. 4.17 and leads to an objective of 19.82%. This is slightly higher than the final objective of the LCT field (16.49 %), which is notable given that the OCT pulse is about three times shorter and only has a 1.5 time bigger amplitude at most.

However, as in the case of the LCT-optimized pulse, summing the final populations in the 10 other $^3\Sigma^-$ states included in our calculations leads to a higher result than in the selected channel: 24.4%. The pulse therefore still slightly favors the dissociation towards $C^+ + O^+$ channel instead of $C^{2+} + O$, with a selectivity marginally higher than that of the LCT pulse: $p_{C^{2+}+O}/p_{C^+ + O^+} = 0.81136$.

Interestingly, although the optimized pulse outwardly appears rather close in appearance to the trial pulse shown in Fig. 4.16, a comparison of their Fourier transforms shows that it contains several new frequencies that account for its higher efficiency. These frequencies correspond to different transitions towards various excited $^3\Sigma^-$ channels, as can be deduced by comparing that figure with the partial cross sections shown in Fig. 3.26, p. 110.

Originally, our intent was to filter the low-frequency components of the field then re-optimize it with the area constraint to minimize its area. This however proved unnecessary as the field was found to contain no low-frequency "Stark" component, and to possess a very small area even without area constraint: $A_{\text{norm}} = 4.46 \times 10^{-6}$.

In order to make the area strictly equal to zero, we simply divided the area of the pulse by its number of points on our spatial grid and subtracted this small and constant result from each

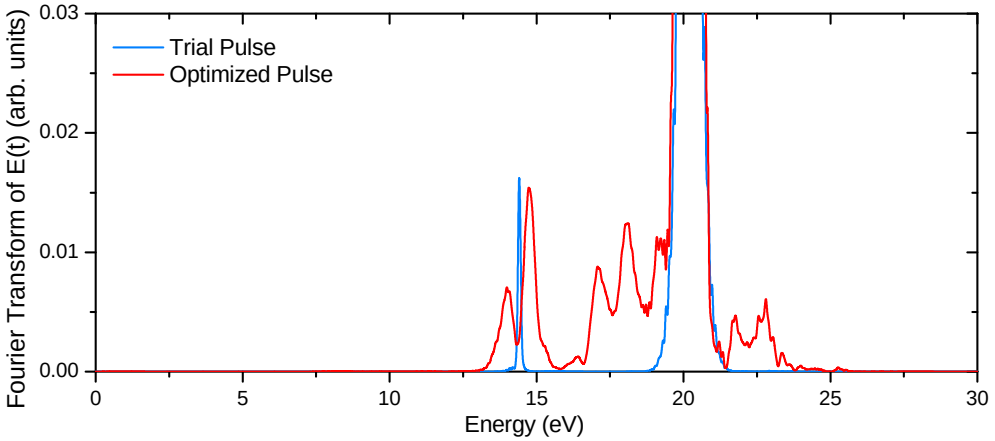

Figure 4.18: Zoom on the Fourier Transform of the initial (blue curve) and OCT-optimized pulses (red curve) for the photodissociation of the $X\ ^3\Pi$ state of CO^{2+} through the $^3\Sigma^-$ channels.

point of the electric field as computed on our spatial grid. The resulting field is visually indistinguishable to that shown in Fig. 4.17 and leads to results that are identical[†] to those obtained with the field before applying this correction. This demonstrates that the original optimized pulse can safely be considered as having an area equal to zero, for all intents and purposes.

4.4.3 Summary: Control of the photodissociation of CO^{2+}

To summarize, Table 4.4 shows the best results we obtained for each kind of pulse for the control of the photodissociation of the $X\ ^3\Pi$ state of CO^{2+} through its $^3\Sigma^-$ channels: the LCT-optimized pulses with parameters $\lambda = 7.5$ and $\nu = 0$, the resonant Gaussian pulse, the shortened LCT pulse used as initial guess for the OCT algorithm and the OCT-optimized pulse obtained with parameter $\alpha_0 = 200$. Note that all optimized fields have significantly higher fluence than in the case of HeH^+, to compensate for the smaller transition dipole moments.

[†]Negligible differences were obtained in the state populations, on the order of 5×10^{-6} % at most.

Table 4.4: Summary of the main pulses optimized for the control of the photodissociation CO^{2+}. The final time t_f, the maximum value of the electric field $E_{\max}(t)$ and the fluence F are all expressed in atomic units.

Field	Objective	t_f	$E_{\max}(t)$	Selectivity	A_{norm}	F	Fig.
LCT $\lambda = 7.5$, $\nu = 0$	16.49 %	6500	0.032	0.797	7.92×10^{-5}	0.627	4.14, p. 148
Gaussian$_{X\to 9}$, $E_{\max}(t)$=0.05	1.30 %	2000	0.050	0.025	0	0.627	4.15, p. 150
LCT, shortened, with envelope	9.01 %	2000	0.032	0.799	8.27×10^{-6}	0.347	4.16, p. 151
OCT, Guess = Shortened LCT, $\alpha_0 = 200$	19.82 %	2000	0.050	0.811	0	0.905	4.17, p. 152

4.5 General conclusion of the photodissociation control simulations

The following conclusions can be drawn from the simulations we performed for the photodissociation control of the cations HeH^+ and CO^{2+}:

- Although Gaussian pulses may at first glance occasionally appear to lead to higher objectives than pulses optimized with Local Control Theory, comparing pulses with the same fluence demonstrates that Gaussian pulses are much less efficient. Moreover, Gaussian pulses tend to lead to relatively low photodissociation selectivity in systems where the dynamics is strongly affected by nonadiabatic couplings, such as HeH^+ and CO^{2+}.

- The addition of a constraint on the area of the pulses is efficient in both Local Control Theory and Optimal Control Theory, but finding a value of the parameter ν that leads to very small area while still leading to a reasonable final value of the objective requires several calculations. In the cases studied here, simply filtering the low-frequency components of the optimized fields has a much more significant effect on their total area.

- The Optimal Control algorithm leads to much more efficient pulses when Local Control pulses are used as initial guess instead of simple resonant Gaussian pulses, indicating that a prior calculation of the field using Local Control Theory is worth the computational effort.

- Although pulses optimized using Local Control Theory lead to lower objectives than those optimized using Optimal Control Theory, their spectrum tends to be simpler, potentially simplifying their experimental realization.

Note that better selectivity could certainly be achieved by using additional constraints, for example by penalizing the population of other states than the desired ones, or by using strategies inspired either by the "optical paralysis" scheme proposed by Malinovsky *et al.* [197] or by the definition of a forbidden subspace of states by Palao *et al.* [198]. However, the inclusion of certain of these constraints would require using the Chebyshev method instead of the split-operator approach, which would significantly increase the duration of our calculations. Furthermore, other modifications could be brought to the OCT algorithm to make our pulses more experimentally realistic, for example by adding a frequency constraint [194, 199] or by reducing their complexity by identifying and selecting the frequencies that correspond to the most stable control pathways [200].

CHAPTER

5

QUANTUM COMPUTING

In this chapter, we study the possible use of ultracold polar molecules as a physical support for quantum computing, and more specifically the implementation of intra- and intermolecular versions of Grover's algorithm on the hyperfine states of trapped $^{41}K^{87}Rb$ molecules. It is split into two parts:

- We start by explaining the basic principles of quantum computing, the inner workings of quantum algorithms such as Grover's, the current state of the art in the field and more particularly in the domain of molecular quantum computing. The model used in our simulation is also described (Section 5.2.1, p. 172).
- We then present our results for the implementation of two- and three-qubit versions of Grover's algorithm on a single $^{41}K^{87}Rb$ molecule (Section 5.2.2.1, p. 178 and 5.2.2.2, p. 180) and of a two-qubit version of Grover's algorithm on two interacting $^{41}K^{87}Rb$ molecules (Section 5.2.2.3, p. 182).

5.1 Basic principles of quantum computing

In the very first pages of this thesis, we mentioned Moore's law as having been well-verified so far: the evolution of computing power for a given cost approximately follows the exponential curve predicted by Gordon E. Moore (a physical chemist!) in 1965 [11]. It is however widely predicted that Moore's law will not stay valid for much longer, as the current trend in processor power evolution relies heavily on their progressive miniaturization. Indeed, not only does miniaturization seem impossible beyond the scale of a few atoms, quantum effects also become predominant at scales of tens of nanometers and below [201].

While quantum effects might cause the end of this era of exponential computing power growth, they might also allow for an unprecedented speedup of certain types of calculations by being directly exploited in *quantum computers*. The general concept of a quantum computer was first formulated by Richard Feynman in 1982, who noted that there were two ways to go about simulating a quantum system:

1. "Imitating" the laws of quantum mechanics using a "classical" computer (as is done in all simulations presented in this work).

2. Using a computer made out of quantum mechanical elements which obey these laws themselves [202].

Today's concept of the quantum computer however has potential applications that are not limited to the simulation of quantum systems and can be generally defined as a computing machine which uses purely quantum phenomena, such as quantum superposition and entanglement, to solve specific problems much faster than classical computers.

5.1.1 Bits and qubits

The most commonly used smallest unit of information is the *binary digit* or *bit*, *i.e.* a value equal to either 0 or 1. Any amount of information, no matter its nature or complexity, may be represented in a sufficiently large basis of bits. The whole LaTeX code of this thesis is for example encoded in 595844 bytes, or 4766752 bits. Although some defend the use of ternary digits (*trits*) or beyond for encoding information [203], bits are very convenient to use in electronics because of the ease with which they can be physically implemented, for example as the electrical state of a flip-flop circuit, as the presence of absence of a hole in a punch card or of small indentations on the surface of a disk, as the direction of polarization on a magnetic band, ...

However, the use of quantum systems as computing machines offer a much more powerful basic unit of data, the *quantum binary digits* or *qubits*. Whereas a bit can either be equal to 0 *or* 1, a qubit could be equal to any *superposition* of a "0" *and* a "1" state:

$$\left|\Psi_{1-\text{qubit}}\right\rangle = a\,|0\rangle + b\,|1\rangle\,, \tag{5.1}$$

where a and b are two complex numbers, with $|a|^2$ and $|b|^2$ respectively representing the probabilities of measuring the $|0\rangle$ and $|1\rangle$ states (and thus respecting the normalization relation $|a|^2 + |b|^2 = 1$).

The state of a single qubit can thus be characterized by a two-dimensional complex vector with elements a and b:

$$\begin{pmatrix} a \\ b \end{pmatrix}. \tag{5.2}$$

Similarly, the state of a two-qubit system will be characterized by a four-dimensional complex vector (a, b, c, d):

$$\left|\Psi_{2-\text{qubit}}\right\rangle = a\,|00\rangle + b\,|01\rangle + c\,|10\rangle + d\,|11\rangle\,, \tag{5.3}$$

where the leftmost digit in the kets represent the values of the first qubit and the rightmost digit represents the values of the second qubit. Note that for most values of the coefficients a, b, c and d, this wavefunction describes *entangled states, i.e.* it cannot be rewritten as a tensor product of the states of two independent qubits, and the state of the two qubits are not independent. This is especially obvious if we look at the case where both b and c are equal to zero:

$$\left|\Psi_{2-\text{qubit},\ b=0,\ c=0}\right\rangle = a\,|00\rangle + d\,|11\rangle\,. \tag{5.4}$$

In this situation, the values of the two qubits are intrinsically linked: if one measures the value of the first qubit, one can be certain that the second qubit will have the exact same value. Conversely, if c and d are equal to zero, the state of the second qubit is completely independent from the state of the first one and the wavefunction can be rewritten as a tensor product of the state of the two qubits:

$$\begin{aligned}\left|\Psi_{2-\text{qubit},\ c=0,\ d=0}\right\rangle &= a\,|00\rangle + b\,|01\rangle \\ &= |0\rangle_{\text{qubit 1}} \otimes \left(a\,|0\rangle_{\text{qubit 2}} + b\,|1\rangle_{\text{qubit 2}}\right).\end{aligned} \tag{5.5}$$

In this case, measuring the value of the first qubit yields no information about the value of the second qubit.

Quantum superposition and quantum entanglement are the two main quantum phenomena on which quantum computing is based, along with quantum interference [204, 205]. It is through the careful exploitation of these purely quantum phenomena that computational speedup is achieved over classical computations. The fact that a qubit can be placed in a superposition of several logical states is one of the main factors behind the computational speedup offered by quantum computing, as can be understood intuitively: in a way, it is as if a quantum computer could be in "several states at once" and could be used to realize logical operations on all these states simultaneously, whereas a classical computer could only be in a single logical state at a time. This phenomenon is called *quantum parallelism*.

For this speedup to be significant, a quantum computer however needs to manipulate a large number of qubits. The general wavefunction for an n-qubit system is a quantum superposition of 2^n states $|k\rangle$:

$$\left|\Psi_{n-\text{qubit}}\right\rangle = \sum_{k=0}^{2^n-1} c_k\,|k\rangle\,. \tag{5.6}$$

Such an n-qubit system is thus characterized by a 2^n-dimensional complex vector:

$$\begin{pmatrix} c_0 \\ c_1 \\ c_2 \\ \vdots \\ c_{2^n-1} \end{pmatrix}, \tag{5.7}$$

where the coefficients c_k respect the normalization relation:

$$\sum_{k=0}^{2^n-1} |c_k|^2 = 1. \tag{5.8}$$

For convenience, it is customary to start numbering them at 0 instead of 1, to ensure that their subscript (expressed in a decimal base) matches the value of the corresponding state $|k\rangle$ of the qubit register (expressed in a binary base): c_0 for $|0...00\rangle$, c_1 for $|0...01\rangle$, c_2 for $|0...10\rangle$ and so on.

To fully exploit the potentials of qubits, quantum logical operations are needed.

5.1.2 Logic gates and quantum gates

While representing information as bits is useful for the sake of its storage in physical supports, it also has a much more interesting application: data encoded in bits can easily be manipulated using logical operations called *logic gates*. These can be as simple as switching the value of a bit (NOT gate) or making it equal to 0 or 1 depending on the values of two other bits, for example if either of them are equal to 1 (OR gate), if they are both equal to 1 (AND gate) or if only one of them is equal to 1 ("exclusive or" or XOR gate). The output of these gates and their negation NOR, NAND and XNOR as a function of the input bits A and B is shown in Tables 5.1 and 5.2). Interestingly, all binary logical operations can be realized by using combination of either NOR and NAND gates, which are thus said to be *universal gates*.

Table 5.1: Truth table of the NOT gate, which simply switches the binary value of a bit A.

Input	Output
A	NOT A
0	1
1	0

Table 5.2: Truth table of the most commonly-used 2-bit gates: OR, AND, XOR and their negation NOR, NAND and XNOR.

Input		Output					
A	B	OR	AND	XOR	NOR	NAND	XNOR
0	0	0	0	0	1	1	1
0	1	1	0	1	0	1	0
1	0	1	0	1	0	1	0
1	1	1	1	0	0	0	1

Even very complex problems can be solved by breaking them down into a series of such simple logical operations which only affect a small number of bits each, *i.e.* into an *algorithm*. Physically, logic gates can be implemented in various ways, for example by using transistors which manipulate the electrical current associated to the value of the bits. This is how today's

computers work: their microprocessors contain hundreds of millions or billions of transistors which realize the required logical operations with tremendous speed.

In quantum computing, conventional logic gates are replaced by *quantum logic gates* (or simply "*quantum gates*"). "Classical" logic gates cannot be directly transposed in the quantum world, as the laws of quantum mechanics require them to be reversible and representable by unitary matrices. For example, the quantum counterpart of the 1-bit NOT gate is the 1-qubit quantum gate X, represented by the following 2×2 matrix [206]:

$$\mathbf{X}_{1-\text{qubit}} = \begin{pmatrix} 0 & 1 \\ 1 & 0 \end{pmatrix}. \tag{5.9}$$

When applied to the state vector of a qubit, it indeed swaps the coefficients of $|0\rangle$ and $|1\rangle$:

$$\begin{pmatrix} 0 & 1 \\ 1 & 0 \end{pmatrix} \begin{pmatrix} a \\ b \end{pmatrix} = \begin{pmatrix} b \\ a \end{pmatrix}, \tag{5.10}$$

or, in other words,

$$a|0\rangle + b|1\rangle \xrightarrow{\mathbf{X}} b|0\rangle + a|1\rangle. \tag{5.11}$$

Moreover, the significant speedup offered by quantum computing comes from the exploitation of quantum mechanical phenomena, which requires logical operations that have no equivalent in classical logic. The *Hadamard Gate*, for example, is commonly used to create quantum superpositions:

$$\mathbf{H}_{1-\text{qubit}} = \frac{1}{\sqrt{2}} \begin{pmatrix} 1 & 1 \\ 1 & -1 \end{pmatrix}. \tag{5.12}$$

When applied on a qubit in its pure state $|0\rangle$, it indeed creates an equal superposition of $|0\rangle$ and $|1\rangle$:

$$1|0\rangle + 0|1\rangle \xrightarrow{\mathbf{H}_{1-\text{qubit}}} \frac{1}{\sqrt{2}}|0\rangle + \frac{1}{\sqrt{2}}|1\rangle. \tag{5.13}$$

There are many other commonly-used quantum gates. Unlike in classical logic, where all gates can be re-expressed as combinations of NOR or of NAND gates, no single quantum gate is universal: a *universal set* of quantum gates is required if one wants to be able to realize all possible qubit manipulations [206]. The ability to implement a universal set of quantum gates is one of the criteria a quantum computer must meet, which will be further discussed in Section 5.1.5, p. 168.

In the same way that conventional logic gates can be stringed together to form specific algorithms, a series of quantum gates can be used to realize *quantum algorithms*.

5.1.3 Quantum algorithms

A series of quantum algorithms which exploit the quantum properties of qubits to speed up certain type of calculations have been developed [207]. Their execution always follows the same basic sequence:

(A) The system is initially placed in a pure state, typically the one corresponding to $|0...00\rangle$.

(B) The quantum algorithm itself is executed through the sequential application of several quantum gates.

(C) Finally, the state of the system is measured, which serves as output of the quantum algorithm.

Given the quantum mechanical nature of the system, its state cannot be measured during step (B) as it would induce the collapse of the wavefunction, destroying the quantum superposition. Moreover, the algorithms must ideally be designed in such a way that the system ends up in a pure state at the end of step (B) to ensure that the measurement in step (C) yields a deterministic result. This is however not the case of all quantum algorithms: in some of them, the system remains in a quantum superposition even at the end of step (B), which means that the measurement yields a probabilistic result — yet they are devised to ensure that the probability of measuring the correct state is high. In that case, multiple executions of the algorithm may be necessary to ensure that the correct result was obtained with a reasonable uncertainty margin.

Chronologically, the first quantum algorithm is Deutsch's algorithm, which allows to check whether a Boolean function $f\colon \{0,1\} \to \{0,1\}$ is "constant" (equal to either 0 or to 1 on it whole domain) or "balanced" (equal to 0 on half of its domain and to 1 on its other half). Whereas a classical algorithm would have to compute $f(0)$ and $f(1)$ then compare the results, Deutsch's algorithm only needs to evaluate the function f once to determine whether it is constant or balanced [208].

Initially proposed for a Boolean function with a 1-bit input $f\{0,1\} \to \{0,1\}$, the algorithm was later generalized to the case of an n-bit input function $f\colon \{0,1\}^n \to \{0,1\}$ [209] and improved upon [204]. Once again, whereas a classical algorithm would require up to $2^{n-1}+1$ evaluations of the function (*i.e.* it would have to compute the function for up to half of all possible inputs plus one), Deutsch-Jozsa's generalized algorithm only requires a single evaluation of the function, potentially speeding up the process dramatically for large values of n. Although it has little practical application, the Deutsch-Jozsa algorithm was the first quantum algorithm to exhibit such a clear speedup over the best possible classical algorithm.

However, the most famous quantum algorithm is probably Shor's algorithm, [210], which allows the prime factorization of large numbers in polynomial time instead of (sub-)exponential time as in the case of classical algorithms[†]. It is of particular interest in the domain of crypt-

[†]The time complexity of algorithms is often expressed using the "Big O notation", which denotes how their execution time scales with a change in input size N. Polynomial-time algorithms for example scale as $O(N^k)$ and

analysis, as a lot of public-key encryption systems, such as the widely-used RSA algorithm[†], rely on the fact that while it is very easy to multiply two prime numbers, it is very difficult (read: very time-consuming on a classical computer) to factorize the result [211]. If implemented on a sufficiently powerful quantum computer, Shor's algorithm could however factorize very large numbers into their prime factors, thus breaking RSA-like encryption — a perspective that allegedly spurred the interest in quantum computing of organizations such as the NSA[‡] [212].

A variety of other quantum algorithms have been developed throughout the years, such as Simon's algorithm [213], Hallgren's algorithm [214], the quantum approximate counting algorithm [215] and various others (the American *National Institute of Standards and Techniques* maintains an exhaustive list of known quantum algorithms [216] and a reasonably recent review of quantum algorithms can be found in Ref. [217]). A large fraction of these algorithms are based on Shor's factorization algorithm and/or Grover's search algorithm, on which we focus in this work.

5.1.4 Grover's algorithm

This fundamental quantum algorithm was conceived in 1997 by Lov Kumar Grover [218]. Its function is simple: find a specific element among an unsorted database containing N randomly-ordered elements (for example a phone directory of N names arranged in a completely random order). Since the order of the elements in the database cannot be assumed to follow any logic, there exists no "smart" way of solving this problem using a classical computer: finding the right element would be a matter of checking each element sequentially until finding the correct one, which would on average require $N/2$ accesses to the database. Grover's algorithm, however, requires only $O(\sqrt{N})$ accesses to find the desired element, thus providing a quadratic speedup, and was shown to be optimal (*i.e.* for a given number of accesses to the database, no other quantum algorithm can give a better probability of measuring the target state than Grover's) [219].

The trick, in a nutshell, consists in placing the system in an equal superposition of states which each correspond to one of the elements of the database, in order to consider all of them "at once", then to exploit constructive and destructive quantum interference to progressively augment the amplitude of the sought-after state and decrease those of the others. In a last step, the resulting state is measured, which yields the desired state with a probability of at least 50%.

In practice, the algorithm can be split in the following steps:

(A) State mapping and initialization

For an N-element database, an n-qubit basis is chosen so that each of its $N = 2^n$ logical values $S_0 = |0\ldots00\rangle$, $S_1 = |0\ldots01\rangle$, $\ldots S_{N-1} = |1\ldots11\rangle$ is associated to one of the database

exponential-time algorithms as $O(2^{N^k})$, while the execution time of sub-exponential algorithms increases faster than any polynomial but slower than an exponential.

[†] Named after the initials of its inventors Ron Rivest, Adi Shamir, and Leonard Adleman.

[‡] *National Security Agency.*

elements. The system is then placed in a pure quantum state, typically the one associated to $|0\ldots00\rangle$.

(B1) Creation of the quantum superposition

The system is placed in an equal superposition of all $N = 2^n$ states through the use of the N successive Hadamard gates each acting on a single qubit or of the *(Walsh-)Hadamard transform*, which acts as an n-qubit Hadamard gate and creates the same superposition in one step. Its effect on the state vector is represented by a $(N \times N)$ matrix with elements [206]:

$$(\mathbf{H}_{n-\text{qubit}})_{i,j} = \frac{1}{\sqrt{2^n}}(-1)^{i\cdot j}, \tag{5.14}$$

where $i \cdot j$ is the bitwise inner product[†] of the binary representation of indices i and j, which range from 0 to $N-1$. In this work, we will consider Hadamard transforms of two and three qubits:

$$\mathbf{H}_{2-\text{qubit}} = \frac{1}{2}\begin{pmatrix} 1 & 1 & 1 & 1 \\ 1 & -1 & 1 & -1 \\ 1 & 1 & -1 & -1 \\ 1 & -1 & -1 & 1 \end{pmatrix}, \tag{5.15}$$

$$\mathbf{H}_{3-\text{qubit}} = \frac{1}{\sqrt{8}}\begin{pmatrix} 1 & 1 & 1 & 1 & 1 & 1 & 1 & 1 \\ 1 & -1 & 1 & -1 & 1 & -1 & 1 & -1 \\ 1 & 1 & -1 & -1 & 1 & 1 & -1 & -1 \\ 1 & -1 & -1 & 1 & 1 & -1 & -1 & 1 \\ 1 & 1 & 1 & 1 & -1 & -1 & -1 & -1 \\ 1 & -1 & 1 & -1 & -1 & 1 & -1 & 1 \\ 1 & 1 & -1 & -1 & -1 & -1 & 1 & 1 \\ 1 & -1 & -1 & 1 & -1 & 1 & 1 & -1 \end{pmatrix}. \tag{5.16}$$

(B2) Phase shift of the target state

As in any search problem, we assume we have a function $C(S_i)$ that allows to discriminate between the desired state S_v and all other states (for example $C(S_v) = 1$ while $C(S_{i\neq v}) = 0$). The result of this "oracle"[‡] is then used to rotate by π radians the phase of the amplitude of the desired state S_v only, while leaving all other phases unchanged. In other words,

[†]The bitwise inner product is computed by first converting the indices i and j to vectors in base 2, for example $0 \to (0), 1 \to (1), 2 \to (1,0), 3 \to (1,1)$, ... ; then computing their scalar product. For example, $(\mathbf{H}_n)_{2,3} = \frac{1}{\sqrt{2^n}}(-1)^{(1,0)\cdot(1,1)} = \frac{1}{\sqrt{2^n}}(-1)^{0+1} = \frac{-1}{\sqrt{2^n}}$.

[‡]In this context, the term "oracle" has a very general meaning: Ref. [219] describes it as "*a black box subroutine into which we are not allowed to look*". In the present case, it is any function that allows to discriminate between the desired state and the others: its inner workings are irrelevant to Grover's algorithm as a whole. Note that by metonymy, step (B2) as a whole is sometimes called "oracle".

it switches the sign of the coefficient of the target state and leaves all other untouched, which corresponds to a diagonal matrix with element -1 for the target state and $+1$ for all the others (*i.e.* $(-1)^{C(S_i)}$ elements on the diagonal). For example, in the 2-qubit case with state $|10\rangle$ as a target, it reads:

$$\mathbf{O}_{2-\text{qubit}} = \begin{pmatrix} 1 & 0 & 0 & 0 \\ 0 & 1 & 0 & 0 \\ 0 & 0 & -1 & 0 \\ 0 & 0 & 0 & 1 \end{pmatrix}. \tag{5.17}$$

(B3) Inversion about average

Next, we perform an "inversion about average" of the amplitudes. This means we modify their value in such a way that the difference between each amplitude and their average changes sign, while the average itself remains unchanged. This is better understood through the use of an example, such as the one encountered in the 2-qubit case (see Table 5.3).

Table 5.3: State amplitudes before and after the inversion about average in the first iteration of the two-qubit version of Grover's algorithm.

	$\|00\rangle$	$\|01\rangle$	$\|10\rangle$	$\|11\rangle$	Average
Amplitudes before the operation	$\frac{1}{2}$	$\frac{1}{2}$	$-\frac{1}{2}$	$\frac{1}{2}$	$\frac{1}{4}$
Differences with the average	$\frac{1}{4}$	$\frac{1}{4}$	$-\frac{3}{4}$	$\frac{1}{4}$	
Amplitudes after the operation	0	0	1	0	$\frac{1}{4}$
Differences with the average	$-\frac{1}{4}$	$-\frac{1}{4}$	$\frac{3}{4}$	$-\frac{1}{4}$	

This transformation corresponds to the diffusion transform D which can be represented by the following matrix:

$$\mathbf{D} \equiv \begin{cases} D_{i,j} = \frac{2}{N} & \text{for off-diagonal elements (i} \neq \text{j)}, \\ D_{i,i} = -1 + \frac{2}{N}. \end{cases} \tag{5.18}$$

For example, in the 2-qubit case, we have:

$$\mathbf{D}_{2-\text{qubit}} = \frac{1}{2}\begin{pmatrix} -1 & 1 & 1 & 1 \\ 1 & -1 & 1 & 1 \\ 1 & 1 & -1 & 1 \\ 1 & 1 & 1 & -1 \end{pmatrix}. \tag{5.19}$$

In his original paper, Grover notes that the matrix representing this transformation is not local, since there are transitions from each state to all other N states, and suggests splitting it into the successive application of a Walsh-Hadamard transform $\mathbf{H}_{n-\text{qubit}}$, a phase shift $\mathbf{R}_{n-\text{qubit}}$ of the $|0...00\rangle$ state and a Walsh-Hadamard transform [218]:

$$\mathbf{D}_{n-\text{qubit}} = \mathbf{H}_{n-\text{qubit}}\,\mathbf{R}_{n-\text{qubit}}\,\mathbf{H}_{n-\text{qubit}}. \tag{5.20}$$

In the present theoretical implementation, this is however not necessary and the inversion about average is realized in a single step.

Repeated iterations

Steps (B2) and (B3) are repeated $O(\sqrt{N})$ times in order to maximize the amplitude of the desired state. In the 2-qubit case, only one such iteration is necessary, while three iterations are necessary in the 3-qubit case, *etc.*

(C) Measurement

Finally, the state of the system is measured, thus providing the answer to the search problem. Note however that multiple executions of the algorithm might be necessary to obtain the answer with a reasonable uncertainty margin, depending on the fidelity of the quantum gates and on the dimension of the database, as Grover's algorithm yields a probabilistic result for certain values of N. Luckily, this is not the case for the 2 and 3-qubit cases considered here.

The maximum probability amplitude for the target state is obtained after a number of iterations $k = \pi\sqrt{N}/4$ [220], thus indeed providing a quadratic speedup compared to the classical algorithm, which scales as $N/2$. Note that the amplitude of the target state follows a sinusoid as a function of the number of repetitions k of steps (B2) and (B3) [201]:

$$|\Psi\rangle = \sin\left(\frac{(2k+1)\theta}{2}\right)|\text{target state}\rangle + \cos\left(\frac{(2k+1)\theta}{2}\right)|\text{other states}\rangle\,, \tag{5.21}$$

where the angle θ is given by the relation:

$$\sin\left(\frac{\theta}{2}\right) = \frac{1}{\sqrt{N}}. \tag{5.22}$$

The amplitude of the target state and the probability of measuring it for the first fifteen iterations of the 2- and 3-qubit versions of Grover's algorithm are given in Table 5.4. The number of iterations required to reach a certain probability is discussed in Ref. [221], and it bears mention

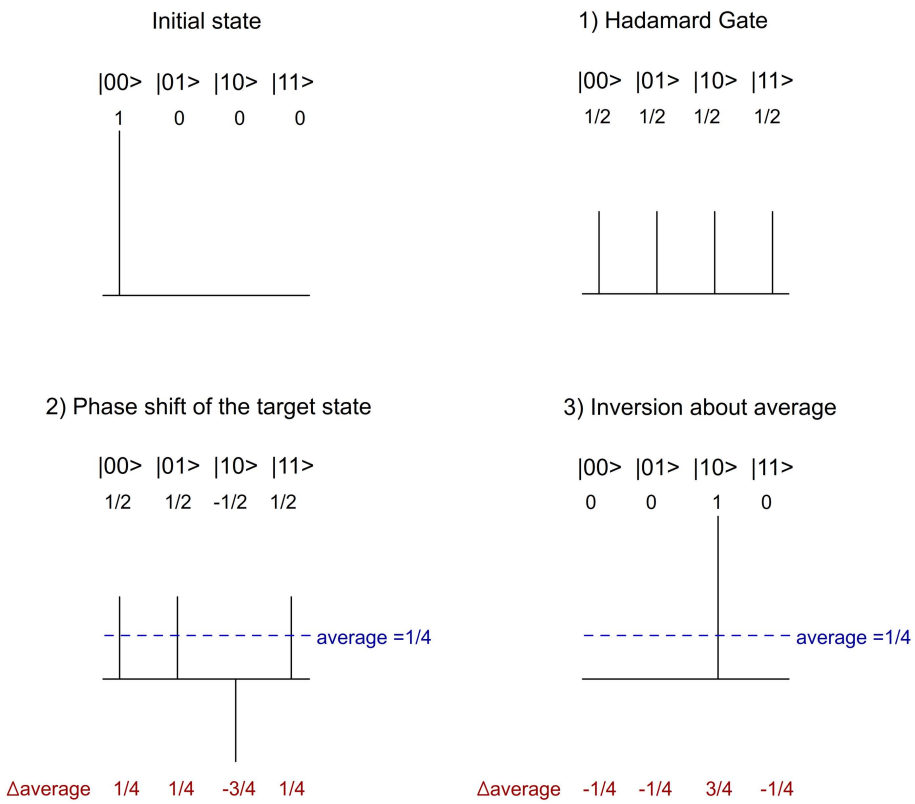

Figure 5.1: One iteration of the two-qubit Grover algorithm, with $|00\rangle$ as initial state and $|11\rangle$ as target state. From left to right, the vertical lines represent the amplitudes for $|00\rangle$, $|01\rangle$, $|10\rangle$ and $|11\rangle$. Note that the average amplitude does not vary between steps 2) and 3), but that the differences between each amplitude and the average change sign.

that unlike the Deutsch-Jozsa or Shor algorithms, Grover's algorithm is probabilistic: it yields the correct answer with a certain probability which may be lower than 100%, thus often requiring multiple executions of the algorithm in order to obtain the desired result with a satisfying margin of confidence. In practice, this is however likely to hold true even for "deterministic" quantum algorithms (which are supposed to lead to the correct answer with a probability of 100%), as interactions with the environment may affect the amplitudes of the state superposition of the system and lead to a probabilistic instead of deterministic result upon measurement. *Quantum Error Correction* (QEC) strategies have however been developed to mitigate the effect of decoherence and inaccuracies within reasonable limits [222–225], and a scheme that allows for the loss of some qubits has been developed [226].

Along with Shor's, Grover's algorithm is often considered the most important quantum algorithm (with some even quipping that "*there are really only two quantum algorithms: Shor's and Grover's*", quite mistakenly [217]). It serves indeed as the basis for many other quantum algorithms and protocols with a wide variety of applications, ranging from the resolution of physical and mathematical problems to quantum cryptography (see for example Refs. [215, 227–233]).

However, while Grover's algorithm is one of the clearest examples of the potential speedup offered by quantum computing and the cornerstone of many subsequent quantum algorithms,

Table 5.4: Amplitude and probability of the target state in the 2- and 3-qubit versions of Grover's algorithm as a function of the number of iterations.

	2-qubit		3-qubit	
Iteration k	Amplitude	Probability	Amplitude	Probability
1	1.000000	1.000000	0.883883	0.781250
2	0.500000	0.250000	0.972272	0.945313
3	-0.500000	0.250000	0.574524	0.330078
4	-1.000000	1.000000	-0.110485	0.012207
5	-0.500000	0.250000	-0.740252	0.547974
6	0.500000	0.250000	-0.999893	0.999786
7	1.000000	1.000000	-0.759587	0.576973
8	0.500000	0.250000	-0.139488	0.019457
9	-0.500000	0.250000	0.550356	0.302891
10	-1.000000	1.000000	0.965021	0.931266
11	-0.500000	0.250000	0.897176	0.804925
12	0.500000	0.250000	0.380743	0.144965
13	1.000000	1.000000	-0.326062	0.106316
14	0.500000	0.250000	-0.869835	0.756614
15	-0.500000	0.250000	-0.978692	0.957837

and although it already has been implemented experimentally as early as 1998 [234], it has not yet been used to crack problems beyond the capabilities of conventional computers. So far, 2- and 3-qubit versions of the algorithm have been implemented experimentally on various physical systems [235–239], thus allowing a search in a database of eight elements at most (a trivial problem easily solvable at a glance), as well as a 7-qubit version [240] using liquid NMR (as we will see, the "quantumness" of this approach has however been called into question).

Despite their elegance and deceptive simplicity on paper, quantum algorithms are indeed very hard to implement experimentally. Although the theoretical bases of quantum computing are well-established, the nature of the best physical support to encode quantum information and ensure its easy manipulation is still debated.

5.1.5 Current realizations in quantum computing and requirements

The concept of quantum computer is a very general one: many different kind of microscopic physical systems have therefore been considered as potential quantum computers. In this section, we will give a very brief overview of the current state of the art in quantum computing and of the main obstacles to the realization of powerful quantum computers, able to manipulate a large enough number of qubits to solve problems beyond the abilities of current "classical" computers.

In 2000, David P. DiVincenzo proposed the following list of requirements a physical system should meet in order to be used in efficient quantum computation [241]:

1. Scalability, with well-characterized qubits

It should be possible to encode a large number of qubits in the system and to manipulate them individually.

2. The ability to initialize the qubits to a simple state

Before attempting any computation, it should be possible to "initialize" the system by placing it into a specific state (typically, the physical state associated with the pure $|000...0\rangle$ value of the qubit register).

3. Decoherence times much longer than the gate operation time

The decoherence time characterizes how long it takes for the interaction between the quantum system and its environment to significantly affect its state amplitudes. To minimize the effects of decoherence, it should occur on much longer timescales than that of the algorithm execution.

4. A "universal" set of quantum gates

All possible quantum logical operations should be implementable on the system through the combination of a finite set of quantum gates.

5. A qubit-specific measurement capability

Last but not least, it should be possible to measure specific qubits in order to read out the result of the quantum computation.

The matters of scalability and decoherence tend to be the most problematic. The estimated number of qubits necessary in a "useful" quantum computer depends on its projected application: it varies from a few tens for some quantum chemistry and physics problems [242–244] to hundreds or thousands for the cryptanalysis of typical public-key cryptosystems [245]. Decoherence is also very troublesome because it essentially disrupts the purely quantum behaviour of the isolated system, modifying the coefficients of the superposition or destroying it entirely. Although Quantum Error Correction techniques allow for the correction of a certain amount of decoherence per gate, which is inevitable in any real experiment, they are unable to cope with large amount of decoherence (see Ref. [225] for an introduction to the subject).

We thus appear to be several major breakthroughs away from "useful" quantum computers, (*i.e.* quantum computers which manipulate enough qubits to outperform current classical computers in the resolution of specific problems). However, very encouraging results have been obtained on a variety of physical systems.

For example, *liquid-phase NMR quantum computing* uses nuclear spin states of a liquid sample of molecules as qubits. However, unlike most other physical implementations of quantum computers, it uses the average properties of a macroscopic ensemble of molecules as support for the quantum information instead of the individual properties of microscopic, quantum systems. Although it yielded very promising results in the early day of experimental quantum computing, it was quickly realized that it could not be used to implement useful quantum computers because of bad scaling properties caused by low signal-to-noise ratio [246]. Worse, recent

studies have called the "quantumness" of this approach into question, as it appears not to allow for entangled states and can be modeled using a classical statistical model [247, 248].

Another popular approach is the use of *superconducting qubits*, *i.e.* the encoding of qubits in the charge or phase properties (or both) of superconducting circuits [249]. While comparatively closer in spirit to the functioning of "classical" computers than other quantum computing schemes, and despite recent progresses, this approach still suffers from short decoherence times due to the strong coupling with the environment [239, 250].

Linear optical quantum computing constitutes another leading approach [251]. It relies on the encoding of qubits in the properties of photons (typically, their polarization) and on the implementation of logic gates using circuits of linear optical elements such as beach splitters, phase shifters, *etc.* [252, 253].

The encoding of qubits in the energy levels of cold trapped atomic ions as well as in their collective motion states is yet another very promising approach, as it benefits from long decoherence time, high fidelity qubit manipulation with lasers and easy readout [254]. Very impressive experiments have been realized in recent years with the encoding of up to 14 qubits [255], as well as the implementation of some quantum gates and of the Deutsch-Jozsa algorithm [256]. The work of David Wineland and his group is of particular interest, and led to his selection as co-recipient of the 2012 Nobel Prize in physics [257–259].

Similarly, arrays of ultracold neutral atoms trapped in an optical lattice as well as atoms placed in reflective cavities are also being considered as potential quantum computers [260]. Approaches that combine the encoding of qubits in registers of atoms or ions, with the use of photons to transfer qubits from one register to another, appear particularly promising [261, 262].

Other approaches of quantum computing currently being developed include the use of solid-state NMR, Bose-Einstein condensates, and many other physical systems. Note that in addition to the "standard" implementation of quantum computing based on the successive application of few-qubit quantum gates which has been presented here, other approaches have also been proposed, such as the *adiabatic quantum computer* [263], the *one-way quantum computer* [238, 264] and the *topological quantum computer* [265], which will not be discussed in detail in this thesis.

While their exact nature remains somewhat mysterious and controversial, the supposedly "quantum" computers developed by D-Wave Systems and recently sold to Google Inc. and NASA[†] to much media attention must also be mentioned here. Although the Canadian company boldly claims to offer "*a superconducting 512-qubit processor chip [...] housed inside a cryogenics system within a 10 square meter shielded room*" [266], skeptics such as Massachusetts Institute of Technology professor Scott Aaronson have tempered these assertions [267] and a team led by Matthias Troyer from ETH Zurich[‡] recently found no conclusive evidence of quantum speedup during a comparison between D-Wave and a classical computer running an optimized algorithm [268].

[†] *National Aeronautics and Space Administration.*

[‡] *Eidgenössische Technische Hochschule Zürich.*

For the curious, note that Prof. Aaronson also published on his blog very interesting rebuttals [269] to some of the critics of quantum-computing skeptics such as Prof. Dyakonov, who questions whether fault-tolerant quantum computing with a large number of qubits will ever be experimentally feasible and whether they would be useful [270]. While it is true we are still several breakthroughs away from "useful" quantum computers, we do not believe that research on the subject amounts to wasted time — quite the contrary, as it furthers our understanding of matter and drives the amelioration of quantum control techniques.

Given today's state of matters, it is very difficult to determine what physical support the first "useful" quantum computers will use. In addition to those mentioned above, molecular systems are possible candidates.

5.1.6 Molecular quantum computing

In this work, we explore the potential role of laser-controlled molecules as quantum computers. Molecules indeed seem like a logical choice for quantum computing: they are small enough to obey the laws of quantum mechanics while having a rich internal energy structure that could potentially allow the encoding of a large number of qubits. Moreover, the development of laser control techniques also opens interesting perspectives in the coherent manipulation of these qubits.

Since the early 2000s, a growing number of articles exploring the use of molecules in quantum computing have been published, starting with de Vivie-Riedle's group pioneering work on the encoding of qubits in vibrational levels of acetylene [190, 271], followed by theoretical simulations using electronic states [189, 192, 272–275] or (ro-)vibrational levels [7, 8, 10, 276–285] as physical support for the qubits.

In this approach, the populations of $N = 2^n$ specific energy levels of the molecules are associated to the N logical values of the n-qubit register (for example, the population of a given rovibrational level v, J would correspond to the coefficient c_0 of logical state $|0...00\rangle$ while the population of another level $v', J' = 0$ would correspond to the coefficient c_1 of logical state $|0...01\rangle$, and so forth). Quantum gates are then implemented on these qubits through the use of laser pulses which guide the desired population transfers among the chosen states. Since quantum gates are described by unitary matrices, these population transfers correspond to unitary transformations.

The control pulses can be based on techniques such as Stimulated Raman Adiabatic Passage (STIRAP) [284] or be optimized theoretically by Optimal Control Theory [189] or through the use of genetic algorithms [282, 286, 287]. At the end of the computation, the state of the system is measured with standard spectroscopic techniques, yielding the result of the quantum algorithm [190].

However, as seen in Chapter 4, theoretical control pulses are extremely sensitive to the accuracy of the *ab initio* data — and quantum computing of course requires extremely high fidelity transitions, as even a very small loss of population with each quantum gate leads to errors which quickly accumulate in the course of a full algorithm. Furthermore, the decoherence time of

molecular states tends to be shorter than those of atoms and the quantity of qubits that can be encoded on a single molecule then "addressed" individually using laser pulses cannot be infinitely stretched.

This last problem could however be circumvented by encoding the qubits on several molecules instead of a single one and by exploiting the interaction between molecules to entangle the qubits they bear. Note that hybrid approaches, using for example molecules interacting with atoms [288] or with solid state quantum processors [289], have also been proposed.

5.2 Theoretical implementation of quantum algorithms on ultracold $^{41}K^{87}Rb$ molecules

Let us preface with a disclaimer that Rolf Landauer, famous for its contributions to the physics of information, suggested all works on quantum computing should contain:

"*This scheme, like all other schemes for quantum computation, relies on speculative technology, does not in its current form take into account all possible sources of noise, unreliability and manufacturing error, and probably will not work.*"

— Prof. Rolf Landauer (1927 – 1999) [290]

What Prof. Landauer meant by this was of course not that all research in quantum computing is useless, but that we should keep the current technical limitations in mind when discussing quantum computing and refrain from overselling our results.

Let us thus define clearly our intention here: our aim is not to provide a working scheme for quantum computation with a high number of qubits, but to explore possible answers to some of the challenges it poses. More precisely, we theoretically study the possibility of implementing intermolecular logical operations on qubits encoded in hyperfine levels of trapped polar molecules, using a simplified model.

5.2.1 Model

We chose to explore the possibility of using trapped diatomic molecules interacting with each other through their electric dipole-dipole interaction as quantum computers, as first proposed by DeMille [70]. Such molecules indeed present several advantages:

- First and foremost, their large and long range permanent electric dipole moment allows the transmission of information between molecules through their dipole-dipole interaction, as well as the transmission of information to other kind of systems such as atoms, solid-state systems, *etc.* [288, 289, 291].

- They can be created at ultracold temperatures (*i.e.* with translational temperatures on the order of μK or less) by photoassociation of laser-cooled atoms [292–294] or by mag-

netically tuning through Feschbach resonances [71, 72, 295, 296] (for a review of these approaches, see Refs. [297] and [298] respectively).

– They possess a rich internal level structure and strong optical and microwave transitions, allowing for the encoding of several qubits on a single molecule and their coherent manipulation through laser control techniques [291].

– Furthermore, their hyperfine levels have a long decoherence time (on the scale of several seconds [70]), several orders of magnitude larger than the gate operation time (on the scale of tens or hundreds of microseconds [70, 299]), making them good support for quantum information (both in the context of qubit manipulation and of their storage in a "quantum memory" [289]).

For these reasons, Kuznetsova *et al.* [291] note that polar molecules combine some of the advantages of ions and neutral atoms and of quantum dots and superconducting circuits, "*making them compatible with various architectures, including optical lattices, microwave, static and ac electric and magnetic traps and solid state-systems*". Recent reviews of the state of the art in the field of polar molecules and in the control of ultracold molecules can be found in Refs. [300] and [301] respectively.

We chose to focus on KRb molecules, which can be obtained at ultracold temperatures in their absolute ground state (*i.e.* their lowest electronic, vibrational, rotational and hyperfine state) by association of their constituting atoms through a Fano-Feshbach resonance, followed by a population transfer to the lowest rotational manifold by STIRAP and a microwave transition to its lowest hyperfine state (see Refs. [71–74] for more details).

As in the model initially proposed by DeMille, we assume that the molecules are held in a one-dimensional optical trap array [302] created by a standing-wave laser beam. An electric field with a gradient along the trapping axis is added to allow the spectroscopic addressing of each molecule [70].

We use a simplified model in which the molecules are assumed to be fixed in space in the optical lattice and to be aligned along the Z axis of a laboratory frame coinciding with the intermolecular axis, as illustrated in Fig. 5.2. An intermolecular distance of 100 nm between the centers of mass is used to ensure a high dipole-dipole interaction. Quantum tunneling from one site to another is assumed not to take place on the considered timescales.

The molecules are also assumed to be initially placed in their pure absolute ground state and stay at all time in the lowest vibrational level $v = 0$ of their ground $X\ ^1\Sigma^+$ electronic state. Only hyperfine levels or the first two lowest rotational manifolds $J = 0, 1$ are considered here.

We implement not only *intra*molecular but also *inter*molecular quantum gates, *i.e.* conditional gates operating on qubits encoded in energy levels of two interacting molecules. This constitutes an important step towards scalability, as a large qubit register could be created by working with networks of interacting molecules, each carrying a small number of qubits [9].

As earlier, this first requires the resolution of the time-independent Schrödinger equation by diagonalizing the Hamiltonian. This was achieved by Philippe Pellegrini in the course of

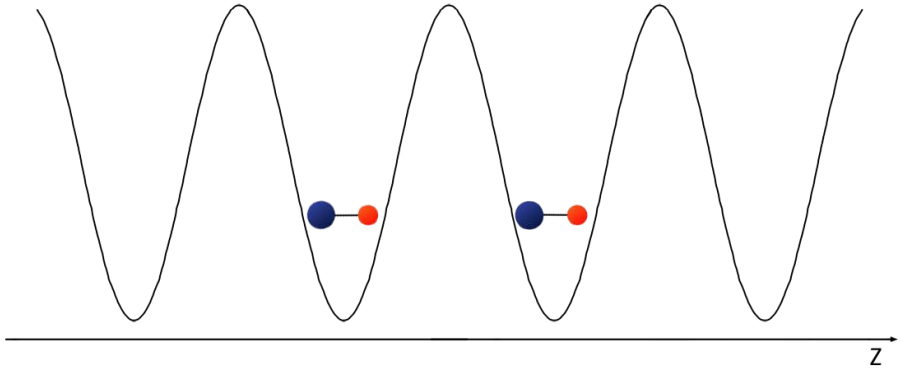

Figure 5.2: Model used in this work: two diatomic molecules placed in neighbouring sites of an optical trapping potential (black curve). The trapping field, the control field and the internuclear axis are all aligned with the Z axis of the laboratory-fixed frame.

his postdoctoral work at the *Laboratoire de Chimie Physique* using the model described Sections 5.2.1.1 and 5.2.1.2.

5.2.1.1 Hamiltonian for a single diatomic molecule

In the one-molecule case, only a magnetic field is applied: an additional electric field with a gradient along the Z axis is only added in the two-molecule case to differentiate the energy levels of the two molecules.

Since we restrict our basis of states to the $v = 0$ levels of the ground electronic state, the electronic and vibrational contributions are constant. The field-free Hamiltonian H_0, which is equal to the internal Hamiltonian of the molecule, can thus simply be written as:

$$\begin{aligned} H_0 &= H_{\text{in}} \\ &= H^{\text{rot}} + H^{\text{hf}} + H^{\text{Z}} \end{aligned} \tag{5.23}$$

where H^{rot} is the rotational Hamiltonian, H^{hf} is the hyperfine Hamiltonian and H^{Z} is the Zeeman Hamiltonian.

Let us develop each of these terms, starting with H^{rot}:

$$H^{\text{rot}} = B\,\mathbf{N}^2, \tag{5.24}$$

where B is the rotational constant and $\mathbf{N}$ is the rotational angular momentum. In the present study, we neglect the centrifugal distortion term and beyond, as only small values of the rotational quantum number J are considered.

The hyperfine Hamiltonian H^{hf} is given by:

$$H^{\text{hf}} = \sum_{i=1}^{2} \mathbf{V}_i \cdot \mathbf{Q}_i + \sum_{i=1}^{2} c_i\,\mathbf{N}\cdot\mathbf{I}_i + c_3\,\mathbf{I}_1\cdot\mathbf{T}\cdot\mathbf{I}_2 + c_4\,\mathbf{I}_1\cdot\mathbf{I}_2, \tag{5.25}$$

where:

– the first term is the electric quadrupole coupling, arising from the interaction between the nonzero electric field gradient $\mathbf{V}_i$ and the nuclear quadrupole electric moments $\mathbf{Q}_i$ of the nuclei of the i atoms;

– the second term is the spin-rotation interaction between the nuclear spin $\mathbf{I}_i$ of atom i and the angular momentum $\mathbf{N}$ of the molecule;

– the third term is the tensor nuclear spin-spin interaction ($\mathbf{T}$ being the tensor describing the angle dependence of the spin-spin interaction), which is neglected in this work as it was found to be an order of magnitude smaller than the fourth and last term, the scalar nuclear spin-spin coupling interaction.

An interesting description of these terms and of their connection to physical quantities commonly used in NMR spectroscopy can be found in Ref. [303]. The value of constants B, c_1, c_2, c_3 and c_4 used in this work were taken from Ref. [304].

The last term of Eq. 5.23, the Zeeman Hamiltonian H^{Z}, is defined as:

$$H^{\mathrm{Z}} = g_r \mu_N \, \mathbf{N}\cdot\mathbf{B} - \sum_{i=1}^{2} g_i \, \mu_N \, \mathbf{I}_i \cdot \mathbf{B}, \tag{5.26}$$

where μ_N is the nuclear magneton, $\mathbf{B}$ is the magnetic field, g_r is the rotational g-factor of the molecule and g_i is the nuclear g-factor for nucleus i[†].

The inner Hamiltonian H^{in} is expressed in the uncoupled basis of states $|J, m_J, m_{I_1}, m_{I_2}\rangle$. Each state is characterized by its rotational quantum number J, its projection m_J on axis Z as well as the projections m_{I_1} and m_{I_2} of the nuclear spins I_1 and I_2 of the two atoms. The hyperfine eigenstates $|\phi_k\rangle$ found by diagonalizing the Hamiltonian are a mixture of these basis states:

$$|\phi_k\rangle = \sum_{J, m_J, m_{I_1}, m_{I_2}} \alpha^k_{J, m_J, m_{I_1}, m_{I_2}} \, |J, m_J, m_{I_1}, m_{I_2}\rangle \, . \tag{5.27}$$

This state mixing allows certain transitions between hyperfine states whose main constituent $|J, m_J, m_{I_1}, m_{I_2}\rangle$ is such that these transitions would normally be forbidden by rotational selection rules.

The number of states in each rotational manifold J is equal to:

$$(2J+1)(2I_1+1)(2I_2+1). \tag{5.28}$$

For ^{41}K^{87}Rb, we have $I_{^{41}\mathrm{K}} = I_{^{87}\mathrm{Rb}} = 3/2$, leading to 16 states in the $J = 0$ manifold and 48 states in the $J = 1$ manifold, for a total of 64 states in the first two rotational manifolds. No higher energy level was considered in the present calculations.

In our simulations, the system is initially placed in a single hyperfine level associated to the pure $|00...0\rangle$ state of the quantum register. The time-dependence is induced by the microwave

[†]The *g-factor*, or *dimensionless magnetic moment*, is a dimensionless quantity that relates the magnetic moment of a molecule or a particle to its angular momentum. It is linked to the gyromagnetic ratio γ by the relation $\gamma = g\mu_N/\hbar$. More details about its form for diatomic molecules can for example be found in Refs. [305, 306].

electric field we use to control its dynamics:

$$H(t) = H^{\text{in}} + W(t). \tag{5.29}$$

In the dipolar approximation, the interaction between the molecule and the control field $\mathbf{E}(t)$ is given by:

$$W(t) = -\boldsymbol{\mu}\mathbf{E}(t). \tag{5.30}$$

Since we consider that the control pulse is polarized along the Z axis of the laboratory frame, we can also write this as:

$$W(t) = -\mu_0 E(t) cos\theta, \tag{5.31}$$

where μ_0 is the component of the dipole moment of the molecule along its internuclear axis and θ is the angle between that axis and the direction of polarization of the control field.

5.2.1.2 Hamiltonian for two molecules

The time-independent Hamiltonian for the two-molecule system is simply the sum of the two internal Hamiltonians H^1_{in} and H^2_{in} and of their electric dipole-dipole interaction term V_{dd}:

$$H_0 = \sum_{i=1}^{2} H^i_{\text{in}} + V_{\text{dd}}. \tag{5.32}$$

The dipole-dipole interaction term takes the form [307]:

$$V_{\text{dd}} = \frac{\boldsymbol{\mu}^1 \cdot \boldsymbol{\mu}^2 - 3(\boldsymbol{\mu}^1 \cdot \mathbf{1_Z})(\boldsymbol{\mu}^2 \cdot \mathbf{1_Z})}{R^3}, \tag{5.33}$$

where the intermolecular axis is assumed to coincide with Z and where $\mathbf{1_Z}$ is the unit vector in that direction.

As in the one-molecule case, the electronic and vibrational contributions to the internal Hamiltonians H^i_{in} are constant. However, since we add a static electric field along Z to differentiate the energy levels of the two molecules, a Stark Hamiltonian H^i_{S} must now be included in the internal Hamiltonians H^i_{in}:

$$H^i_{\text{in}} = H^i_{\text{rot}} + H^i_{\text{hf}} + H^i_{\text{Z}} + H^i_{\text{S}}. \tag{5.34}$$

This new term takes the form:

$$H^i_{\text{S}} = -\mu^i E^i \cos\theta_i - \frac{1}{2}\alpha_{\parallel}(E^i)^2 \cos^2\theta_i - \frac{1}{2}\alpha_{\perp}(E^i)^2 \cos^2\theta_i, \tag{5.35}$$

where E^i is the value of the static electric field experienced by molecule i, while $\alpha_{\parallel}$ and $\alpha_{\perp}$ are its parallel and perpendicular polarizabilities, whose values were taken from Ref. [308].

In the dipolar approximation, the interaction between the molecules and the control field $\mathbf{E}(t)$ we optimize is given by:

$$W(t) = -\boldsymbol{\mu}^1 \mathbf{E}(t) + \boldsymbol{\mu}^2 \mathbf{E}(t), \tag{5.36}$$

or, since the control pulse is polarized along the Z axis,

$$W(t) = -\mu^1 E(t) \cos\theta_1 + \mu^2 E(t) \cos\theta_2. \tag{5.37}$$

Using this model, all calculations of the energy levels used in the following field optimizations were performed by Philippe Pellegrini during his postdoctoral research in the *Laboratoire de Chimie Physique*.

5.2.1.3 Optimization of the microwave control field

In order to implement a logical operation acting on n qubits, each control field must guide the population of the 2^n hyperfine levels used in the quantum register from their 2^n input values to the 2^n desired outputs:

$$|\phi_k(t=0)\rangle \xrightarrow{E(t)} |\phi_k^{\text{target}}(t_f)\rangle\,, \tag{5.38}$$

with $k = 1,2,...2^n$. The simultaneous optimization of these 2^n transitions was achieved using Multi-Target Optimal Control Theory, as described in Section 4.1.3.6 (p. 127). The time dependent coupled equations were expressed in the interaction representation [309] in the basis set of eigenstates of the field-free Hamiltonian H_0 and were solved using the fourth-order Runge-Kutta method [310].

However, unless an additional constraint is added, each state ends up with a different phase $e^{i\gamma_k}$ by the end of the control pulse. This is problematic as the *relative* phases of the states involved in a quantum superposition must be kept equal, to avoid unwanted interferences effects [191, 311]. This can be achieved by optimizing an additional transition, this time involving the sum of all 2^n input states and the corresponding 2^n output states at once to ensure that their phases stay equal [191]:

$$\sum_{k=1}^{2^n+1} |\phi_k(t=0)\rangle \xrightarrow{E(t)} \sum_{k=1}^{2^n+1} |\phi_k^{\text{target}}(t_f)\rangle\, e^{i\gamma}, \tag{5.39}$$

where γ is the phase.

Using these 2^n+1 equations, the microwave fields were optimized by Optimal Control Theory generalized to the multi-target case. The fidelity was computed as:

$$F = \frac{1}{2^n+1}^2 \left| \sum_k^{2^n+1} \langle \phi_k(t_f) | \phi_k^{\text{target}}(t_f) \right|^2, \tag{5.40}$$

where $\phi_k(t_f)$ is the wavefunction in state k at time t_f and $\phi_k^{\text{target}}(t_f)$ is the target wavefunction for that state. Field optimizations were pursued until the fidelity reached at least 99 %, as quan-

tum computations require very high fidelity operations to limit the accumulation of errors. No additional constraints on the fluence or the area of the field were imposed in order to ensure a reasonably quick convergence to high fidelity.

5.2.2 Results

5.2.2.1 Intramolecular 2-qubit Grover algorithm

For the 2-qubit intramolecular version of Grover's algorithm, we use a single $^{41}K^{87}Rb$ molecule in a magnetic field of 500 gauss. The 64 states of its first two rotational manifolds were included in all computations presented here.

The four possible states $|00\rangle, |01\rangle, |10\rangle$ and $|11\rangle$ of the 2-qubit register were associated to states $k = 4, 7, 10, 13$ (numbered in order of ascending energy) of the $J = 0$ rotational manifold (see Table 5.5 and Fig. 5.3). These states were chosen because they are coupled through transitions involving states $k = 36$ and $k = 41$ of the $J = 1$ manifold. The $|10\rangle$ state was arbitrarily chosen as target for the algorithm, but any other state could be selected instead by simply optimizing another phase shift gate.

A control pulse was optimized separately for each of the three quantum gates of Grover's algorithm using OCT. The same initial field was chosen for each quantum gate: eight sine square pulses of amplitude $E_0 = 10^{-8}$ a.u. with frequencies corresponding to transitions from states $k = 4, 7, 10, 13$ to states $k = 36$ and 41. The qubits are thus only coupled by transitions towards two specific external states, but not by direct transitions.

After optimization, we reached fidelities of 99.90% for the Hadamard after 530 iterations, 99.71% for the phase shift gate after 750 iterations and 99.94% for the inversion about average gate after 540 iterations. The corresponding fields and the population evolution of target state $|10\rangle$ throughout the single iteration of Grover's algorithm necessary to obtain the desired result can be found in Fig. 5.4.

Table 5.5: Assignment of the logical states for the 2-qubit Grover algorithm implemented on a single $^{41}K^{87}Rb$ molecule in a magnetic field of 500 gauss. The k states are numbered in the order of increasing energy and their main constituent J, m_J, m_{I_1}, m_{I_2} is given.

$\|Q_1 Q_2\rangle$	k	$\|J, m_J, m_{I_1}, m_{I_2}\rangle$
$\|00\rangle$	4	$\|0, 0, -3/2, 3/2\rangle$
$\|01\rangle$	7	$\|0, 0, -1/2, 1/2\rangle$
$\|10\rangle$	10	$\|0, 0, 1/2, -1/2\rangle$
$\|11\rangle$	13	$\|0, 0, 3/2, -3/2\rangle$

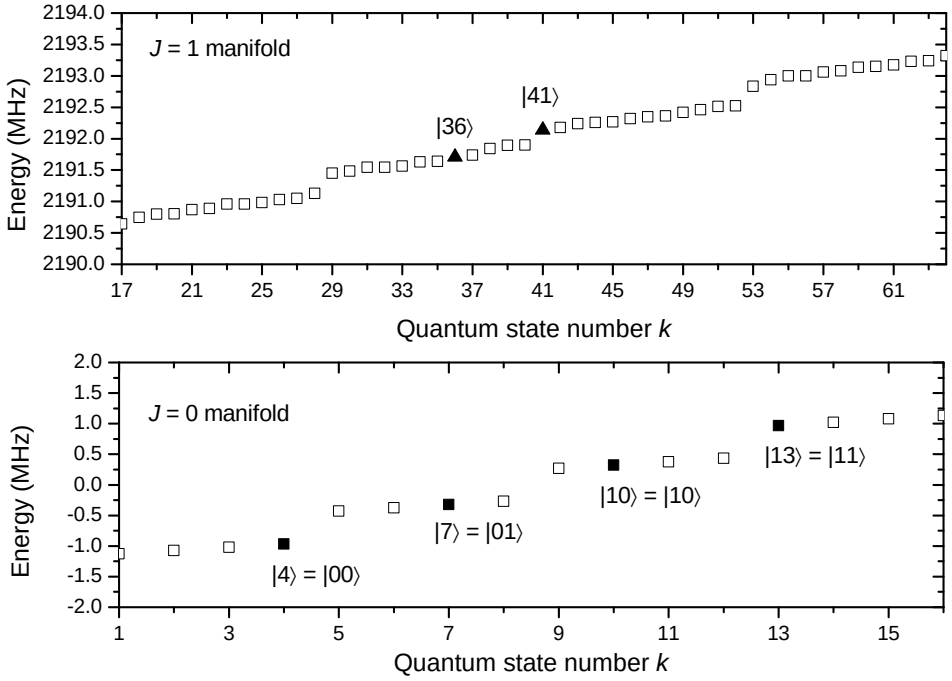

Figure 5.3: Hyperfine levels of the first $J = 0$ and $J = 1$ rotational manifolds of a $^{41}K^{87}Rb$ molecule exposed to a magnetic field of 500 gauss. The black squares represent the four levels on which the four possible pure values of the 2-qubit register were encoded, while the black triangles denote the levels with which they have strong transition dipole moments.

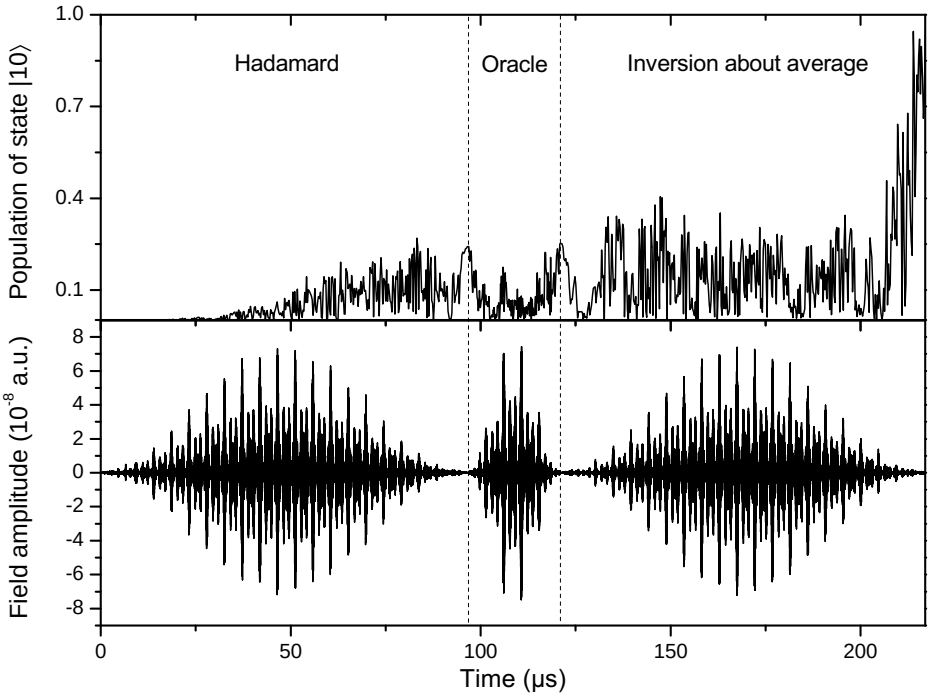

Figure 5.4: Optimized fields (bottom) and evolution of the population in the target state $|10\rangle$ (top) as a function of time for the first iteration of our theoretical implementation of the 2-qubit Grover algorithm on a single $^{41}K^{87}Rb$ molecule.

5.2.2.2 Intramolecular 3-qubit Grover algorithm

Similarly, we implemented a 3-qubit intramolecular version of Grover's algorithm on a single $^{41}K^{87}Rb$ molecule exposed to a magnetic field of 500 gauss, as in the 2-qubit case. This time, $2^3 = 8$ states are needed to encode the three qubits: in addition to those used in the 2-qubit case, states $k = 30$, 36, 41 and 47 were associated to the values $|100\rangle, |101\rangle, |110\rangle, |111\rangle$ of the quantum register (Table 5.6 and Fig. 5.5). As in the 2-qubit case, the $|010\rangle$ state was arbitrarily chosen as the target of the search algorithm.

Table 5.6: Assignment of the logical states for the 2-qubit Grover algorithm implemented on a single $^{41}K^{87}Rb$ molecule in a magnetic field of 500 gauss. The k states are numbered in the order of increasing energy and their main constituent $|J, m_J, m_{I_1}, m_{I_1}\rangle$ is given.

$\|Q_1Q_2Q_3\rangle$	k	$\|J, m_J, m_{I_1}, m_{I_1}\rangle$
$\|000\rangle$	4	$\|0,0,-3/2,3/2\rangle$
$\|001\rangle$	7	$\|0,0,-1/2,1/2\rangle$
$\|010\rangle$	10	$\|0,0,1/2,-1/2\rangle$
$\|011\rangle$	13	$\|0,0,3/2,-3/2\rangle$
$\|100\rangle$	30	$\|1,-1,1/2,1/2\rangle$
$\|101\rangle$	36	$\|1,0,-3/2,1/2\rangle$
$\|110\rangle$	41	$\|1,-1,3/2,-1/2\rangle$
$\|111\rangle$	47	$\|1,-1,-1/2,-1/2\rangle$

As in the previous case, the states are coupled by their transition to states $k = 36$ and 41. We thus chose 16 sine square pulses with frequencies corresponding to the transitions between the 8 states of our basis and these two intermediary states as initial guess for the OCT algorithm. For the three gates, fidelities superior to 99.9% were obtained after 1500 iterations of the optimization algorithm. The three optimized pulses and the evolution of the population in the target state $|010\rangle$ during the first iteration of Grover's algorithm are shown in Fig. 5.6.

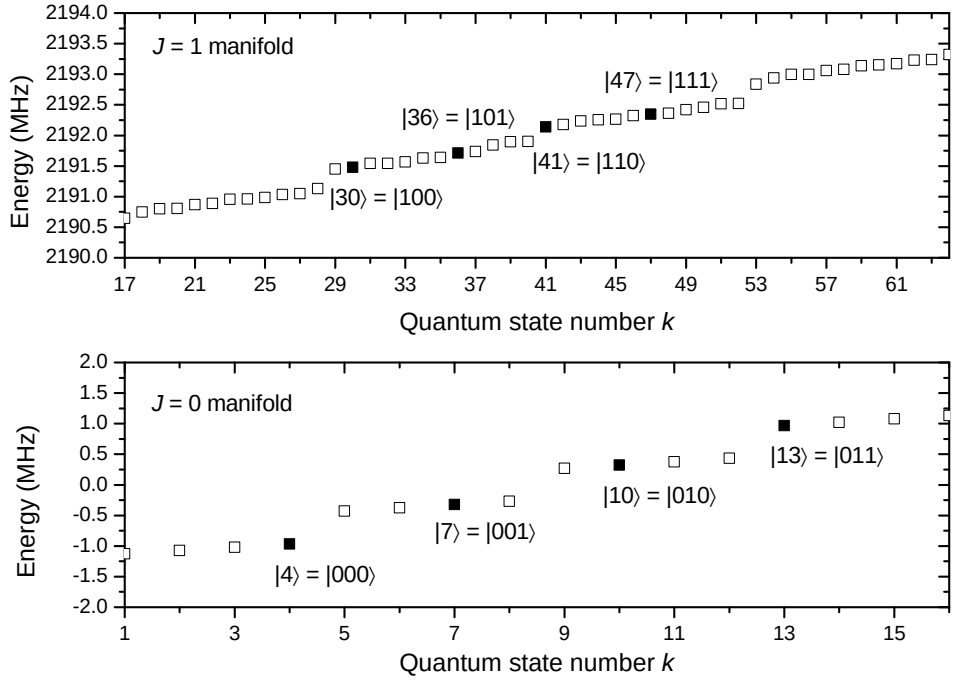

Figure 5.5: Hyperfine levels of the first $J = 0$ and $J = 1$ rotational manifolds of a $^{41}K^{87}Rb$ molecule exposed to a magnetic field of 500 gauss. The black shapes represent the four levels on which the eight possible values of the 3-qubit register were encoded, while the black triangles denote the levels with which they have strong transition dipole moments.

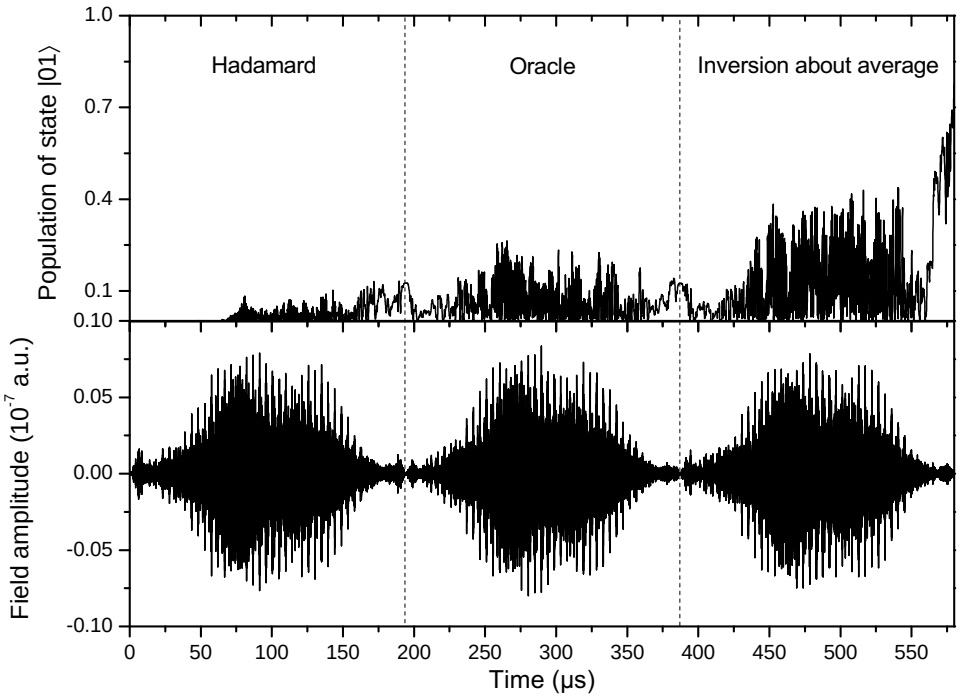

Figure 5.6: Optimized fields (bottom) and evolution of the population in the target state $|010\rangle$ (top) as a function of time for the first iteration of our theoretical implementation of the 3-qubit Grover algorithm on a single $^{41}K^{87}Rb$ molecule. The population reaches the expected value of 0.78125, as predicted in Table 5.4 (p. 168).

5.2.2.3 Intermolecular 2-qubit Grover algorithm

Finally, we simulated the implementation of a 2-qubit version of Grover's algorithm in hyperfine levels of two interacting $^{41}K^{87}Rb$ molecules. As explained in the description of the model, the distance between the centers of mass of the two molecules is assumed to stay constant at 100 nm. The two molecules are exposed to different magnetic and electric fields to differentiate their energy levels and allow individual addressing: 500 gauss and 1 kV/cm for the first one, 400 gauss and 0.8 kV/cm for the second.

The addition of a molecule in our model of course complicates the problem significantly: even by limiting ourselves to the $J = 0, 1$ rotational manifolds, which contain 64 states for each molecules, we have a total of $64^2 = 4096$ different states to consider for the two interacting molecules. These states can be divided in three manifolds: one where both molecules are in their lowest rotational manifold $J = 0$, one where one molecule is in $J = 1$ while the other is in $J = 0$, and one where both molecules are in $J = 1$ (Fig. 5.7).

We assigned the $|00\rangle$ logical state of our qubit register to the lowest energy state of the system, where both molecules are in their absolute lowest energy level. Because of the external electric fields we impose, this state only couples to a few states in the second manifold, which themselves only couple to a few states in the third manifold. The state $|00\rangle$ does not couple directly to any state in the third manifold. The four logical states $|00\rangle, |01\rangle, |10\rangle, |11\rangle$ of our 2-qubit register were assigned to the hyperfine states numbered (in order of ascending energy) $k = 1$ (first manifold), 1249, 1537 (second manifold) and 3841 (third manifold) respectively (Table 5.7).

Table 5.7: Assignment of the logical states for the 2-qubit Grover algorithm implemented on two $^{41}K^{87}Rb$ molecules in a magnetic field of 500 and 400 gauss respectively. The k states are numbered in the order of increasing energy and their main constituents J, m_J, m_{I_1}, m_{I_2} are given.

$\|Q_1Q_2\rangle$	k	$\|J^{(1)}, m_J^{(1)}, m_{I_1}^{(1)}, m_{I_2}^{(1)}\rangle \otimes \|J^{(2)}, m_J^{(2)}, m_{I_1}^{(2)}, m_{I_2}^{(2)}\rangle$
$\|00\rangle$	1	$\|0,0,3/2,3/2\rangle \otimes \|0,0,3/2,3/2\rangle$
$\|01\rangle$	1249	$\|1,0,3/2,3/2\rangle \otimes \|0,0,3/2,3/2\rangle$
$\|11\rangle$	1537	$\|0,0,3/2,3/2\rangle \otimes \|1,0,3/2,3/2\rangle$
$\|11\rangle$	3841	$\|1,0,3/2,-3/2\rangle \otimes \|1,0,3/2,3/2\rangle$

Given the fact that a field optimization with 4096 states would require a huge amount of computational resources, only those possessing a significant transition dipole moment with the states used to encode the qubits were included in the calculations, for a total of 16 states (see Fig. 5.7 for a complete vision of all 4096 states and of those used in our calculations).

We reached a fidelity of 99.995% for the Hadamard gate after 630 OCT iterations with a trial

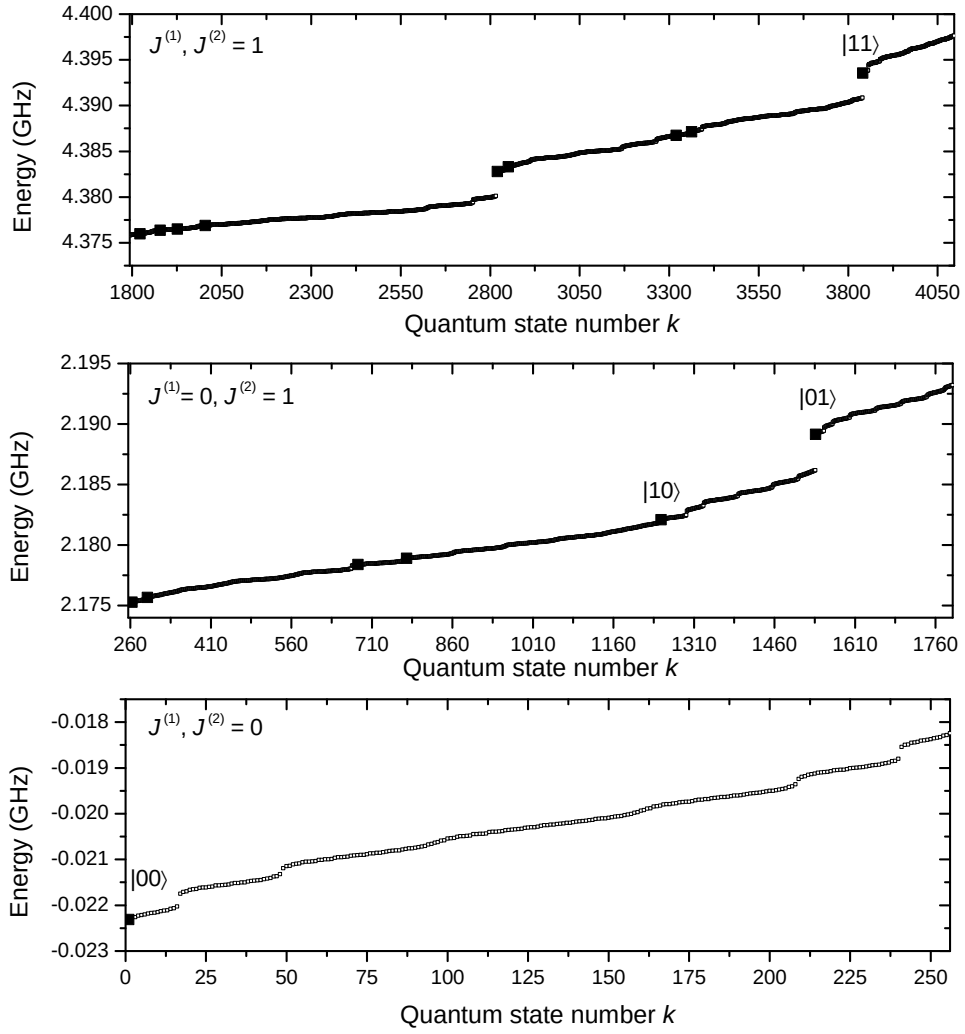

Figure 5.7: The energy levels of two $^{41}K^{87}Rb$ molecules exposed to a magnetic field of 500 and 400 gauss, respectively. The black squares represent the 16 levels included in our calculations.

amplitude of 10^{-8} a.u., of 99.74% for the phase shift after 7700 iterations and of 99.53% for the inversion about average after 7600 iterations, with a trial amplitude of 10^{-9} a.u. for both. The resulting optimized fields and the corresponding evolution of the population in the target state $|10\rangle$ is shown in Fig. 5.8.

Note that the population displays strong oscillations, especially during the inversion about average pulse. A smoother evolution can be obtained by using lower field intensities, but the number of iterations required to reach a good fidelity then rises significantly. Similarly, a shorter duration could be chosen for the pulses at the cost of longer field optimization times.

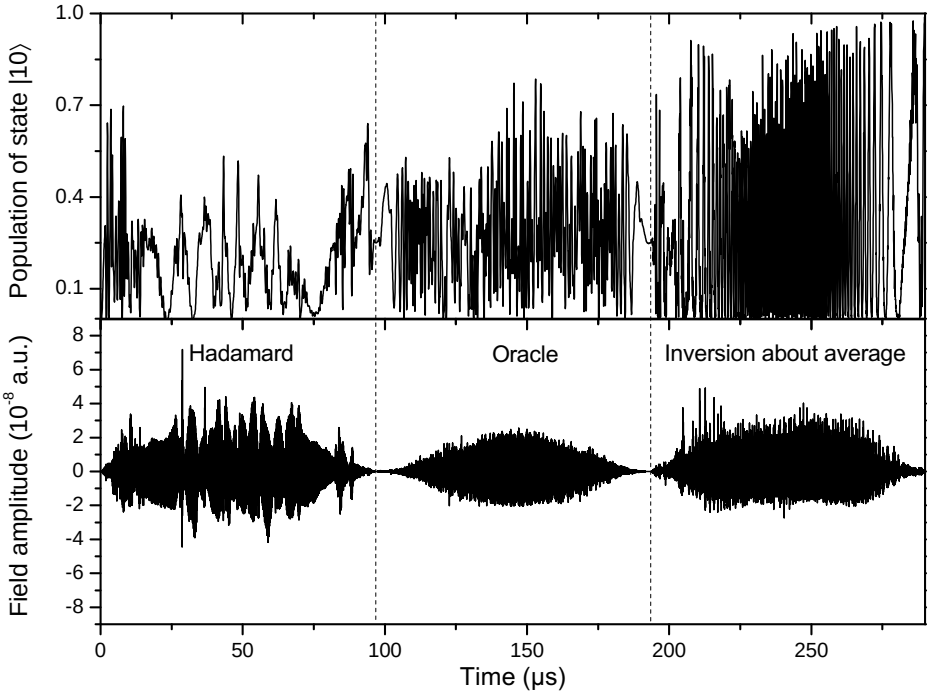

Figure 5.8: Optimized fields (bottom) and evolution of the population in the target state $|10\rangle$ (top) as a function of time for our theoretical implementation of the 2-qubit Grover algorithm on two interacting $^{41}K^{87}Rb$ molecules.

5.2.2.4 Discussion

The high fidelity of our optimized pulses was put to the test by simulating multiple successive iterations of the algorithm. The probability of measuring the target state as a function of the number of iterations is shown in Fig. 5.9 and compared with the expected behavior in an ideal case with 100% fidelities for all gates.

The good agreement between the ideal case and our simulations even after a relatively large number of gate operations is granted by the high fidelities of the field we optimized. As expected, this agreement however breaks down for high number of iterations as the small errors in each step gradually accumulate.

Note that the mixing between hyperfine states varies with the values of the external field, with high intensities leading to a simplification of the hyperfine spectrum (*i.e.* lower transition probabilities between the states [312,313]). Conversely, high field intensities ensure a large splitting between states, leading to easier addressing. A compromise such as the one presented here must thus be found in order to preserve a strong state mixing to allow the implementation of complex operations, while ensuring a sufficient splitting.

Also note that the general concept of implementing intermolecular operations on two neighboring trapped molecule does not depend on the parameters used in the present simulations: we chose an intermolecular distance of 100 nm to make the dipole-dipole interaction very significant, and a sharp field gradient to ensure easy state addressing, but these values were chosen out of numerical convenience and similar results can be obtained for other conditions.

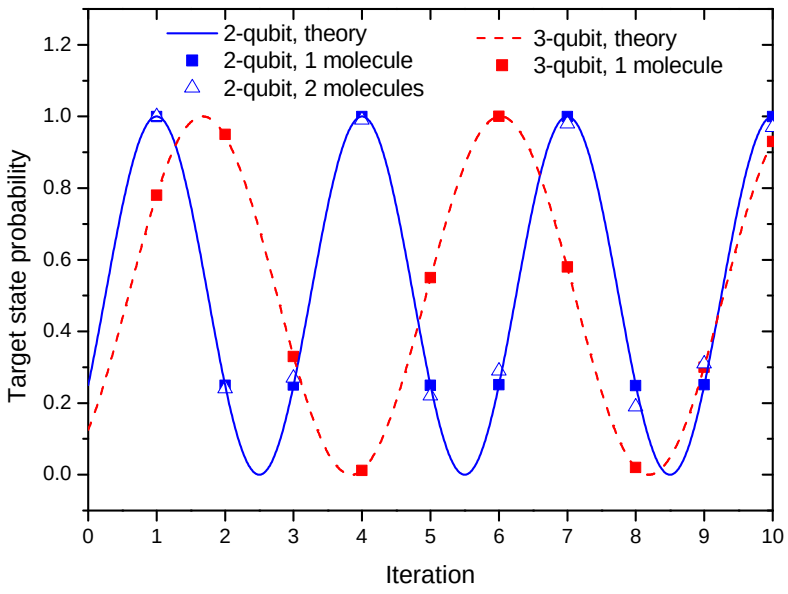

Figure 5.9: Probability of measuring the target state as a function of the number of iteration of the 2-qubit (blue) and 3-qubit (red) Grover algorithm. Lines: theoretical predictions (see Table 5.4 p. 168), Squares: results of our simulations on one ^{41}K^{87}Rb molecule, Triangles: results of our simulations on two ^{41}K^{87}Rb molecules.

However, several ameliorations could be brought to our calculations, that were chronologically the first field optimizations realized in this thesis. Additional constraints could for example be used in the optimizations to minimize the area and the fluence of the control fields. Lower field intensities may also help avoid the strong population oscillations observed for certain operations. Additional calculations with modified parameters (such as different values of the magnetic and electric fields), or with the addition of "noise" to our optimized pulses, could also be performed to test their robustness and their sensitivity to experimental conditions.

CHAPTER

6

CONCLUSIONS AND PERSPECTIVES

In this work, we theoretically studied the static properties of small molecular systems, their field-free photodissociation and radiative association dynamics, the control of their photodissociation dynamics using laser pulses, and the potential application of laser control to the use of molecules as quantum computers. Our calculations thus ranged from the fundamental, *ab initio* description of molecular properties on the basis of the basic principles of quantum mechanics, up to the theoretical determination of control pulses susceptible to inform future experiments.

Three diatomic species were studied:

– HeH^+, a species that plays an important role in astrochemistry,

– CO^{2+}, a metastable dication of interest in quantum control experiments,

– $^{41}K^{87}Rb$, a promising polar molecule for molecular quantum computing schemes.

In a first step, we computed the *ab initio* data required to perform the subsequent dynamical calculations. For HeH^+, the calculations previously performed by Loreau *et al.* [2] were expanded upon by computing more accurate potential energy curves for its three lowest $^1\Sigma^+$ states and for its two lowest $^3\Sigma^+$ states. For CO^{2+}, the potential energy curves of the $X\,^3\Pi$ state and of the 11 lowest $^3\Sigma^-$ states were computed, as well as the corresponding radial nonadiabatic couplings and electric transition dipole moments. This constitutes the first detailed *ab initio* study of the excited $^3\Sigma^-$ states of CO^{2+}.

In a second step, we studied the photodissociation dynamics of both HeH^+ and CO^{2+} using this *ab initio* data. The partial photodissociation and radiative association cross sections from

all vibrational levels of the a and $b\ ^3\Sigma^+$ states of HeH^+ towards the higher n =2–3 $^3\Sigma^+$ and $^3\Pi$ states were determined, using an approach that allows the extraction of the photodissociation cross sections and of the corresponding radiative association cross section from a dissociative calculation. The effect of the vibrational dependence of the cross sections was found to be very significant, and special care was taken to ensure the suppression of Gibbs oscillations near the threshold energies of the photodissociation cross sections. Resonances and the rotational dependence of the cross sections however had to be neglected in our calculations. Our results were used to compute the corresponding photodissociation and radiative association for physical conditions typically met in relevant astrophysical environments, which had never been done before for triplet states of HeH^+. Although our results show that the density of HeH^+ in its triplet states is likely to be low in astrophysical environments, it may influence the abundances of other species. Additionally, the partial photodissociation cross sections from the $v = 0$ level of the $X\ ^3\Pi$ state of CO^{2+} through its $^3\Sigma^-$ channels were also determined.

Next, we computed laser pulses that enhance the photodissociation of the ground electronic states HeH^+ and CO^{2+} through specific channels. Three kind of control fields were tested in our simulations: simple Gaussian pulses, pulses computed using Local Control Theory and pulses optimized using Optimal Control Theory. We more specifically focused on the introduction, in the two latter approaches, of a new constraint that allows the minimization of the area of the control field. Although our results show that this constraint is efficient in reducing the area of the optimized fields, filtering the low-frequency components of their Fourier transform during the optimization or after was found to more significantly reduce their final area, in the presently studied cases. Our best results in terms of maximization of the objective and of minimization of the area were obtained when using Optimal Control Theory with the Local Control pulse as initial guess, both for HeH^+ and for CO^{2+}.

Finally, we ran simulations for a potential application of such quantum control techniques: the use of molecular systems as quantum computers. We more precisely theoretically implemented 2- and 3-qubit versions of Grover's quantum search algorithm on hyperfine states of ultracold trapped $^{41}K^{87}Rb$ molecules exposed to a static magnetic field. Although they are likely not experimentally predictive, these calculations show that logical operations may be implemented between qubits encoded in states of different molecules, interacting through their dipole-dipole interaction.

In conclusion, although current trends in research thematics may appear to favor the description of still bigger and more complex molecular systems (often at the cost of rough approximation), much research remains to be done even on small molecular systems: their theoretical description is very far from trivial even today, as our calculations have shown. Computational chemistry for small molecular systems therefore still has a bright future ahead of itself – especially since accurate *ab initio* data is essential to the accurate theoretical calculation of reaction cross sections and quantum control laser pulses.

The laser control of chemical processes is a very promising field of research both theoretically and experimentally. However, as we have seen, theoretically optimized pulses are often not

experimentally realistic. We have focused here on a specific aspect that may help bridge the gap between theory and experiment, the need for zero-area pulses, but other factors need to carefully be taken into account to theoretically optimize experimentally usable pulses, such as their spectral properties and their robustness against experimental noise. Close collaborations between theoreticians and experimentalists will surely play a crucial role in future developments of this domain of research, which may eventually lead to the realization of quantum computers capable of outperforming even the most powerful classical computers.

If efficient molecular quantum computing schemes are to become a reality, important progresses first need to be achieved. As illustrated here, the theoretical description of even small systems can be difficult – and needs to be realized with a high degree of precision to be of use in the theoretical optimization of control pulses. Although the laser control of molecular processes has come a long way since its inception, both theoretically and experimentally, there remains a lot of progress to be done, especially if the gap between theoretical predictions and experimental implementations is to be bridged. It might however pave the way to revolutionary applications, including the use of trapped molecules as quantum computers – which might themselves revolutionize the way we theoretically describe molecules.

Since this thesis was partly realized in France, it is only appropriate to end it with a quote attributed to one of its kings:

"*If we only cared about the completion of things, we would never undertake anything noteworthy.*"

— King *François I*^{er} (1494 – 1547),
about the construction of the *Château de Chambord.*

APPENDIX

A

ADDITIONAL INFORMATION

A.1 Properties of the nonadiabatic radial coupling matrices

In this section, we give mathematical proof of the properties of the nonadiabatic radial couplings matrices $\mathcal{F}$ and $\mathcal{G}$ used in Section 1.4.3 (p. 35).

A.1.1 Antisymmetry

Let us first prove that $F_{kj} = -F_{jk}$. We know that the electronic wavefunctions are orthonormal:

$$\left\langle \Psi_j^{\text{el}} \middle| \Psi_k^{\text{el}} \right\rangle = \delta_{jk} \tag{A.1}$$

Deriving this expression with respect to R for $j \neq k$ leads to:

$$\left\langle \frac{\partial}{\partial R}\Psi_j^{\text{el}} \middle| \Psi_k^{\text{el}} \right\rangle + \left\langle \Psi_j^{\text{el}} \middle| \frac{\partial}{\partial R}\Psi_k^{\text{el}} \right\rangle = 0, \tag{A.2}$$

which amounts to:

$$\left\langle \Psi_k^{\text{el}} \middle| \frac{\partial}{\partial R}\Psi_j^{\text{el}} \right\rangle^* + \left\langle \Psi_j^{\text{el}} \middle| \frac{\partial}{\partial R}\Psi_k^{\text{el}} \right\rangle = 0. \tag{A.3}$$

Given the definition of the elements F_{kj} (Eq. 1.29, p. 38), this implies that:

$$F_{kj} + F_{jk} = 0, \tag{A.4}$$

and therefore that $F_{kj} = -F_{jk}$.

A.1.2 Relation between $\mathcal{F}$ and $\mathcal{G}$

Let us now derive an element F_{kj} with respect to R:

$$\begin{aligned}\frac{\partial}{\partial R}\left\langle \Psi_k^{\mathrm{el}} \middle| \frac{\partial}{\partial R} \middle| \Psi_j^{\mathrm{el}} \right\rangle &= \left\langle \frac{\partial}{\partial R}\Psi_k^{\mathrm{el}} \middle| \frac{\partial}{\partial R} \middle| \Psi_j^{\mathrm{el}} \right\rangle + \left\langle \Psi_k^{\mathrm{el}} \middle| \frac{\partial^2}{\partial R^2} \middle| \Psi_j^{\mathrm{el}} \right\rangle \\ &= \left\langle \frac{\partial}{\partial R}\Psi_k^{\mathrm{el}} \middle| \frac{\partial}{\partial R}\Psi_j^{\mathrm{el}} \right\rangle + G_{kj}. \end{aligned} \tag{A.5}$$

Since the electronic wavefunctions Ψ_l^{el} form a complete set, we can write:

$$\begin{aligned}\left\langle \frac{\partial}{\partial R}\Psi_k^{\mathrm{el}} \middle| \frac{\partial}{\partial R}\Psi_j^{\mathrm{el}} \right\rangle &= \left\langle \frac{\partial}{\partial R}\Psi_k^{\mathrm{el}} \middle| \sum_l \middle| \Psi_l^{\mathrm{el}} \right\rangle \left\langle \Psi_l^{\mathrm{el}} \middle| \frac{\partial}{\partial R}\Psi_j^{\mathrm{el}} \right\rangle \\ &= \sum_l \left\langle \frac{\partial}{\partial R}\Psi_k^{\mathrm{el}} \middle| \Psi_l^{\mathrm{el}} \right\rangle \left\langle \Psi_l^{\mathrm{el}} \middle| \frac{\partial}{\partial R}\Psi_j^{\mathrm{el}} \right\rangle \\ &= \sum_l F_{kl}F_{lj}. \end{aligned} \tag{A.6}$$

Inserting this into Eq. A.5, we can write the general relationship between the $\mathcal{F}$ and $\mathcal{G}$ matrices:

$$\mathcal{G} = \mathcal{F}^2 + \frac{\partial}{\partial R}\mathcal{F}. \tag{A.7}$$

A.1.3 Radial couplings as a function of the potential energy

Finally, let us demonstrate Eq. 1.33 (p. 39). We start from the fact that the electronic Hamiltonian H^{el} is diagonal for the electronic wavefunctions Ψ_l^{el}:

$$\left\langle \Psi_k^{\mathrm{el}} \middle| H^{\mathrm{el}} \middle| \Psi_j^{\mathrm{el}} \right\rangle = 0. \tag{A.8}$$

The derivative with respect to R yields:

$$\left\langle \frac{\partial}{\partial R}\Psi_k^{\mathrm{el}} \middle| H^{\mathrm{el}} \middle| \Psi_j^{\mathrm{el}} \right\rangle + \left\langle \Psi_k^{\mathrm{el}} \middle| \frac{\partial}{\partial R}H^{\mathrm{el}} \middle| \Psi_j^{\mathrm{el}} \right\rangle + \left\langle \Psi_k^{\mathrm{el}} \middle| H^{\mathrm{el}} \middle| \frac{\partial}{\partial R}\Psi_j^{\mathrm{el}} \right\rangle = 0, \tag{A.9}$$

where we see appearing the elements F_{jk} and F_{kj} as well as the electronic energies E_j^{el} and E_k^{el}:

$$E_j^{\mathrm{el}}F_{jk} + \left\langle \Psi_k^{\mathrm{el}} \middle| \frac{\partial}{\partial R}H^{\mathrm{el}} \middle| \Psi_j^{\mathrm{el}} \right\rangle + E_k^{\mathrm{el}}F_{kj} = 0. \tag{A.10}$$

Since $F_{jk} = -F_{kj}$, we obtain the relation:

$$F_{kj} = \frac{\left\langle \Psi_k^{\mathrm{el}} \middle| \frac{\partial}{\partial R}H^{\mathrm{el}} \middle| \Psi_j^{\mathrm{el}} \right\rangle}{E_k^{\mathrm{el}} - E_j^{\mathrm{el}}}. \tag{A.11}$$

A.2 Area of the electric component of an electromagnetic wave

Note: The following demonstration was put forward by Prof. O. Atabek (*Institut des Sciences Moléculaire d'Orsay, Université Paris-Sud*) [179].

The wave equation for the electric component $E(\mathbf{r}, t)$ of an electromagnetic wave is:

$$\nabla^2 E(\mathbf{r}, t) = \frac{1}{c^2} \frac{\partial^2}{\partial t^2} E(\mathbf{r}, t), \tag{A.12}$$

where c is the speed of light. Its solutions take the form:

$$E(\mathbf{r}, t) = g(\omega t - \mathbf{k} \cdot \mathbf{r}), \tag{A.13}$$

where $\mathbf{k} = \omega / c$ is the wave vector, $\omega = 2\pi\nu$ is the angular frequency, and the function g is a monochromatic sinusoidal wave or any linear superposition of sine waves with different angular frequencies ω [314]. Since we consider here the electric field associated to one or several photons, these frequencies can take any value except 0 as that would imply that $k = 0$ and that the wave does not propagate.

As a consequence, the integral of the field over time $\int_{-\infty}^{+\infty} E(\mathbf{r}, t) dt$ must be strictly equal to zero. This can be understood intuitively as the integration of each individual sine wave corresponding to a particular frequency would yield zero.

For a more rigorous demonstration, let us consider a time-dependent function $f(t)$ and its Fourier Transform $F(\omega)$:

$$f(t) = \int F(\omega) e^{i\omega t} d\omega. \tag{A.14}$$

Integrating over t leads to:

$$\int_{-\infty}^{+\infty} f(t)\ dt = \int_{-\infty}^{+\infty} \int F(\omega) e^{i\omega t}\ d\omega\ dt, \tag{A.15}$$

where the integral over time in the right-hand side can be rewritten as:

$$\int_{-\infty}^{+\infty} e^{i\omega t}\ dt = 2\pi\delta(\omega). \tag{A.16}$$

Knowing that for any function $a(b)$, $\int \delta(b)\ a(b)\ db = a(0)$, Eq. A.15 becomes:

$$\int_{-\infty}^{+\infty} f(t)\ dt = 2\pi F(\omega = 0). \tag{A.17}$$

In other words, the only non-zero contribution to the integral over time comes from the $\omega = 0$, non-periodical part of the function. Since the frequency of the electric field associated to the propagation of photons must be strictly different from zero, its area must therefore be strictly equal to zero.

APPENDICE

B

RÉSUMÉ DE LA THÈSE EN FRANÇAIS

Conformément à la loi française, cette annexe présente un résumé dans la langue de Voltaire des recherches réalisées lors de ma thèse. Dans un souci de concision, seuls les résultats principaux de ce travail seront présentés dans cette section : les détails théoriques et méthodologiques peuvent être trouvés (en anglais) dans les pages qui précèdent.

B.1 Introduction et choix des systèmes étudiés

Le présent travail porte sur l'étude théorique des propriétés de petits systèmes moléculaires et sur le contrôle de leur dynamique à l'aide de champs lasers. Il a été réalisé dans le cadre d'une cotutelle internationale entre le Service de Chimie Quantique et Photophysique (CQP) de l'Université Libre de Bruxelles et le Laboratoire de Chimie Physique (LCP) de l'Université Paris-Sud, et se place dans la continuité de travaux réalisés dans les deux laboratoires : l'étude détaillée des propriétés du cation HeH^+ entreprise par Jérôme Loreau [2–5] ainsi que les simulations de dynamique quantique et de contrôle quantique du groupe ThéoSim du LCP [6–10].

Nous étudions plus précisément trois systèmes : le cation hydrohélium HeH^+, le dication du monoxyde de carbone CO^{2+} et la molécule polaire $^{41}K^{87}Rb$.

B.1.1 Le cation hydrohélium HeH^+

HeH^+ est un système de grand intérêt en astrochimie : composé d'hydrogène et d'hélium, les deux éléments les plus abondants de l'univers, on pense qu'il est la première espèce moléculaire qui s'est formée dans l'histoire de l'univers, par association radiative de H^+ et He [25–27]. Des prédictions théoriques indiquent que HeH^+ devrait avoir, aujourd'hui encore,

une abondance fractionnelle suffisamment grande pour être observable dans certaines régions de l'espace [28], notamment dans certaines nébuleuses [25, 29, 30], certaines supernovæ [31] et dans certaines étoiles pauvres en métaux [32] (en particulier les naines blanches riches en hélium [33]). À l'heure actuelle, aucune des tentatives de détection de HeH^+ dans l'espace n'a toutefois été concluante [34, 35].

Son état $a\ ^3\Sigma^+$ est toutefois métastable (avec un temps de vie radiatif de 149 s pour son niveau rovibrationel le plus bas), ce qui suggère que HeH^+ pourrait peut-être être détecté dans cet état dans des environnements astrophysiques où le taux de collision est très bas [3]. Dans cette thèse, nous avons donc poursuivi le travail commencé par Loreau *et al.* en étudiant l'astrochimie de HeH^+ dans ses deux premiers états triplets. Nous avons tout d'abord calculé les sections efficaces caractérisant la destruction de ces deux états par photodissociation et leur formation par association radiative. Nous avons ensuite optimisé théoriquement des champs laser permettant de guider la photodissociation de HeH^+ vers des fragments spécifiques, dans la continuité du travail entrepris par Bomble *et al.* [43] : la dynamique de photodissociation de HeH^+ est loin d'être triviale en raison du grand rôle qu'y jouent les couplages non-adiabatiques, ce qui en fait un bon cas d'étude pour les méthodes de contrôle quantique.

B.1.2 Le dication CO^{2+}

CO^{2+} est un autre ion diatomique qui suscite l'intérêt dans plusieurs domaines de recherche : premier dication détecté expérimentalement [44], il s'agit à la fois d'une espèce d'intérêt en astrochimie [57] et dans le domaine du contrôle quantique [102]. Le niveau vibrationnel le plus bas de son état électronique fondamental $X\ ^3\Pi$ a en effet un temps de vie significativement plus long (de l'ordre de plusieurs secondes au moins [49]) que ses niveaux vibrationnels excités, ce qui signifie qu'il est relativement aisé d'obtenir du CO^{2+} pur vibrationnellement.

Pour cette raison, le groupe d'expérimentateurs du Prof. Urbain (Université catholique de Louvain), qui a précédemment étudié la formation de CO^{2+} par impact d'électrons sur CO^+ [50], souhaite réaliser des expériences de contrôle laser de la photodissociation de CO^{2+}. Dans cette optique, nous avons déterminé théoriquement des champs de contrôle laser permettant de guider sa photodissociation à travers ses canaux $^3\Sigma^-$ de façon à favoriser la formation des fragments $C^{2+} + O$ plutôt que $C^+ + O^+$. Pour y parvenir, nous avons tout d'abord calculé les données *ab initio* nécessaires, qui n'avaient encore jamais été déterminées auparavant.

B.1.3 La molécule polaire $^{41}K^{87}Rb$

Parmi les nombreux systèmes moléculaires considérés comme supports potentiels pour l'information dans le domaine de "l'informatique quantique moléculaire", les molécules diatomiques polaires font partie des candidats les plus prometteurs grâce à leur long temps de cohérence et leur forte interaction dipôle-dipôle [70].

Les molécules de $^{41}K^{87}Rb$ présentent plus particulièrement l'avantage de pouvoir être obtenues dans leur état d'énergie le plus bas et piégées [71–74], ce qui en fait d'excellentes can-

didates pour la réalisation d'expériences de contrôle de façon générale et dans le domaine de l'informatique quantique en particulier.

Dans cette thèse, nous simulons l'implémentation de l'algorithme quantique de Grover sur des qubits encodés dans des états hyperfins de molécules de $^{41}K^{87}Rb$ piégées. Nous mettons plus particulièrement l'accent sur la réalisation d'opérations logiques *inter*moléculaires, c'est-à-dire agissant sur des qubits encodés sur deux molécules différentes, qui interagissent l'une avec l'autre par le biais de leur moment dipolaire (ce qui ouvre des perspectives intéressantes en terme d'extensibilité).

B.2 Calculs *ab initio*

B.2.1 Calculs *ab initio* pour HeH^+

Tous les calculs de dynamique de réaction de HeH^+ présentés dans ce travail ont été réalisés avec les courbes d'énergie potentielle, les couplages non-adiabatiques radiaux et les moments dipolaires électriques calculés par Loreau *et al.* [2]. Les figures B.1 et B.2 montrent les courbes d'énergie potentielle adiabatiques et diabatiques pour les états singulets et triplets de HeH^+, respectivement.

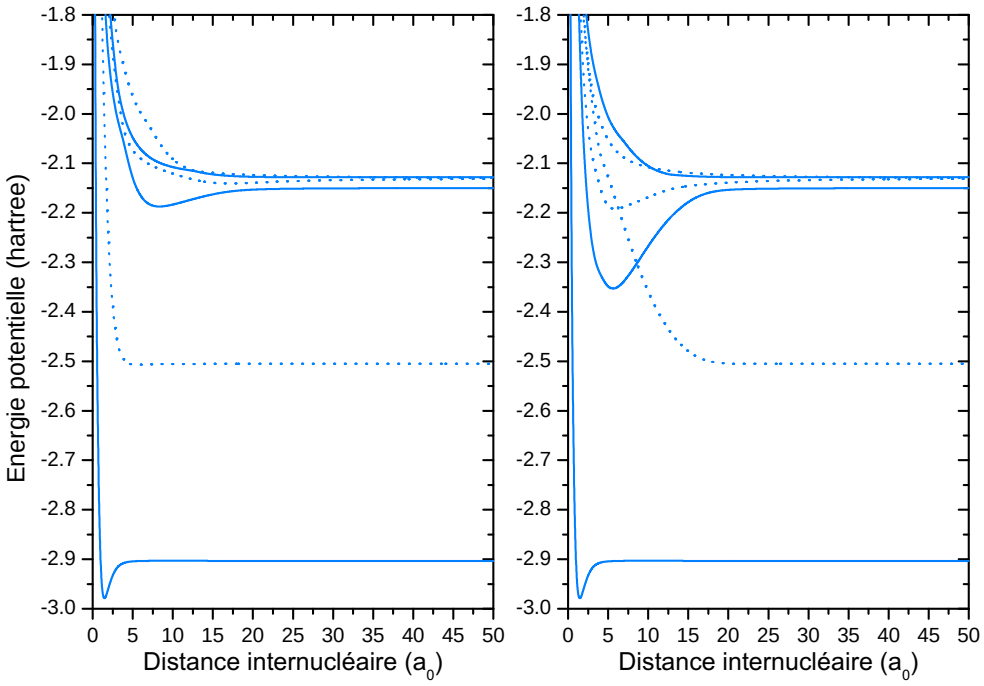

Figure B.1: Courbes d'énergie potentielle adiabatiques (à gauche) et diabatiques (à droite) des états $n = 1$–$3\ ^1\Sigma^+$ de HeH^+. Lignes pleines : états qui se dissocient en $He + H^+$, lignes pointillées : états qui se dissocient en $He^+ + H$.

Puisque notre objectif était d'étudier la dynamique de photodissociation des états $X\ ^1\Sigma^+$, $a\ ^3\Sigma^+$ et $b\ ^3\Sigma^+$ de HeH^+ ; ce qui nécessite la détermination de leurs fonctions d'onde rovibra-

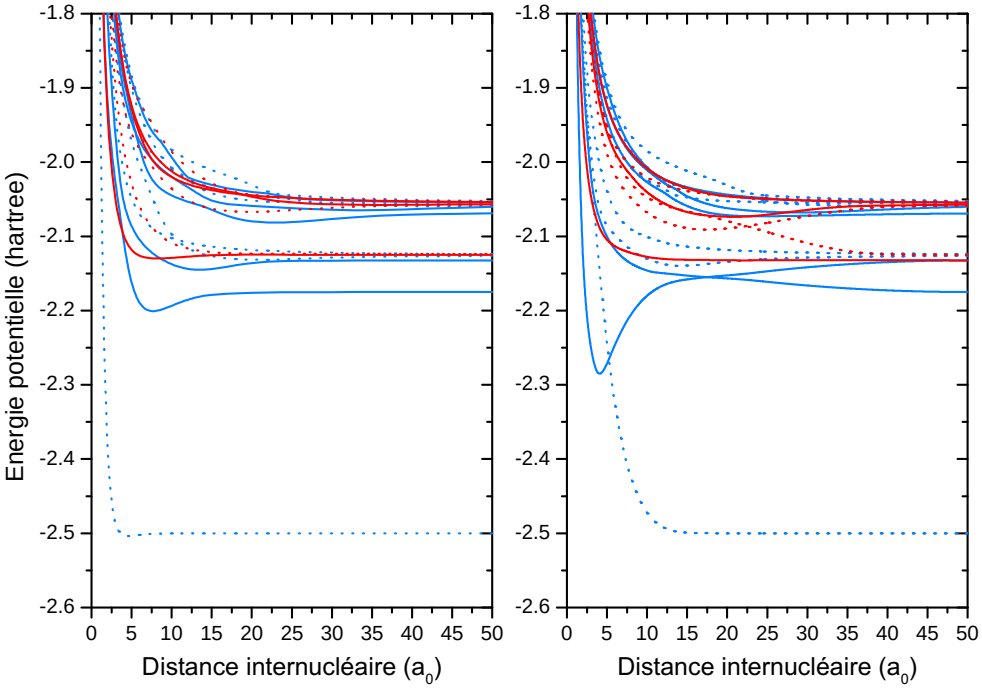

Figure B.2: Courbes d'énergie potentielle adiabatiques (à gauche) et diabatiques (à droite) des états $n = 1$–$3\ ^3\Sigma^+$ (en bleu) et $^3\Pi$ (en rouge) de HeH^+. Lignes pleines : états qui se dissocient en $He + H^+$, lignes pointillées : états qui se dissocient en $He^+ + H$.

tionelles avec haute précision, nous avons effectué une série de calculs supplémentaires des courbes d'énergie potentielle de ses états $X, A, B\ ^1\Sigma^+$ et $a, b\ ^3\Sigma^+$ durant notre mémoire de Master en utilisant les mêmes paramètres que Loreau *et al.*, en dehors de la base, qui a été variée de AVTZ à AV6Z. Ces séries de résultats dans des bases de tailles croissantes ont ensuite été extrapolées à base complète (CBS). Étant donné l'excellent accord entre les courbes CBS et celles obtenues par Loreau *et al*, ces dernières ont été utilisées dans tous nos calculs de dynamique, mais ce sont les courbes CBS qui ont été employées pour calculer les énergies des niveaux rovibrationnels des états X, a et b ainsi que leurs fonctions d'onde (représentées sur la figure B.3 pour l'état $b\ ^3\Sigma^+$).

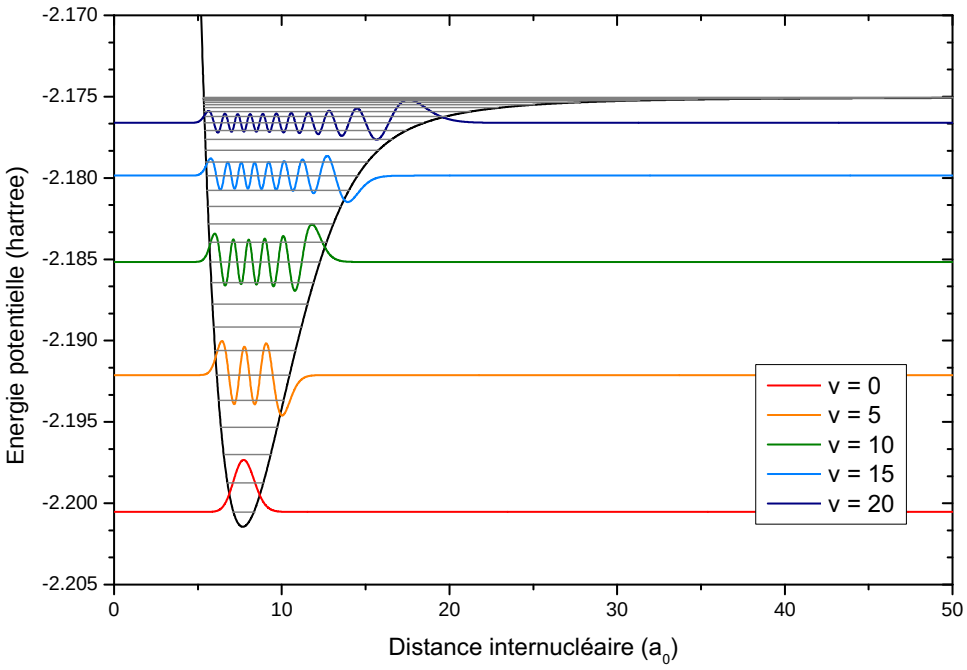

Figure B.3: Courbe d'énergie potentielle, niveaux vibrationnels et fonctions d'onde de l'état $b\,^3\Sigma^+$ de HeH^+ pour $J = 0$.

B.2.2 Calculs *ab initio* pour CO^{2+}

Notre but dans ce travail n'était pas d'améliorer la précision des courbes de potentiel adiabatiques calculées précédemment dans d'autres études [62–64, 67, 69, 98, 104–106], mais de calculer les courbes d'énergie potentielle, les couplages non-adiabatiques radiaux ainsi que les dipôles permanents et de transition de l'état fondamental $X\,^3\Pi$ et des onze premiers états $^3\Sigma^-$ de CO^{2+}.

Cette tâche a été rendue difficile par de nombreux problèmes de convergence, qui nous ont poussé à choisir un très petit pas spatial ΔR entre nos différents calculs (jusqu'à 0.001 a_0 dans certaines régions) afin de faciliter leur convergence. Ceci nous a permis par la suite de corriger plus facilement le signe des dipôles de transition et des couplages non-adiabatiques radiaux entre nos états, grandeurs qui sont obtenues au signe près dans la suite MOLPRO [84]. Toutes ces données ont été calculées dans la base AVTZ avec un espace actif (6 a_1, 2 b_1, 2 b_2) pour des distances internucléaires allant de $R = 1.5$ à 100 a_0. Des calculs dans les bases AVQZ, AV5Z et AV6Z ont également été réalisés et, bien que les énergies absolues des états varient d'une base à l'autre (jusqu'à ≈ 0.010 hartree), les différences d'énergie entre les états varient comparativement peu (≈ 0.003 hartree au maximum).

Les signes des 78 couplages non-adiabatiques radiaux et des 91 moments dipolaires de transition entre les états étudiés ont été corrigés manuellement. Les courbes d'énergie potentielle et les dipôles de transition ont ensuite été diabatisés : la figure B.4 montre les courbes d'énergie potentielle des états $^3\Sigma^-$ avant et après diabatisation, tandis que la figure B.5 montre la courbe

d'énergie potentielle de l'état fondamental $X\,^3\Pi$ et la fonction d'onde de son niveau $v, J = 0$.

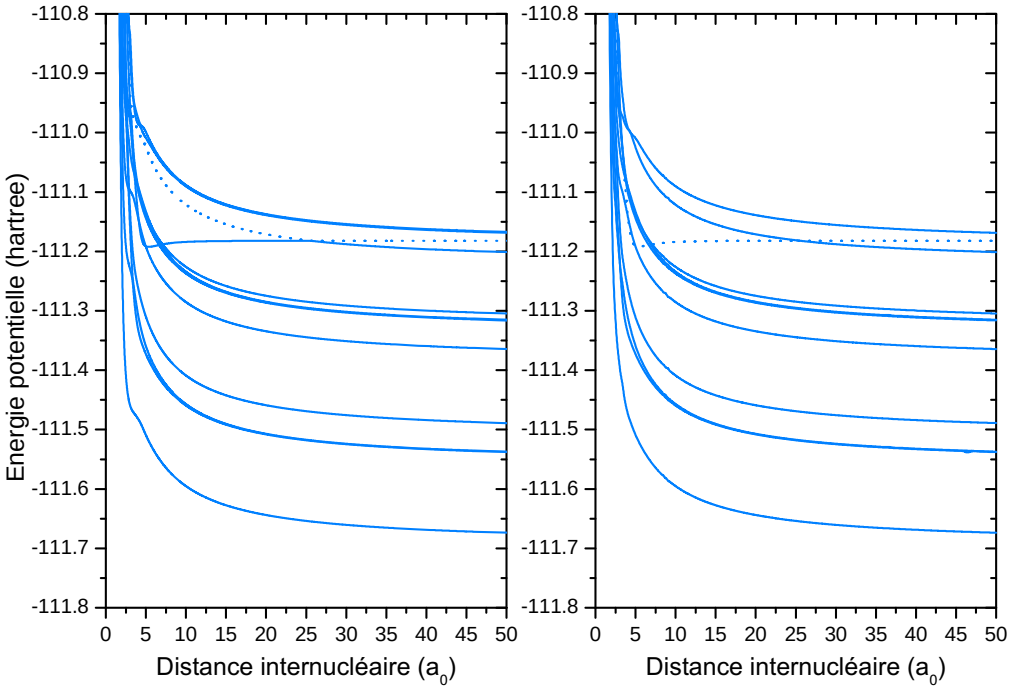

Figure B.4: Courbes d'énergie potentielle adiabatiques (gauche) et diabatiques (droite) des 11 premiers états $^3\Sigma^-$ de CO^{2+}. Lignes pleines : états qui se dissocient en $C^+ + O^+$, lignes pointillées : états qui se dissocient en $C^{2+} + O$.

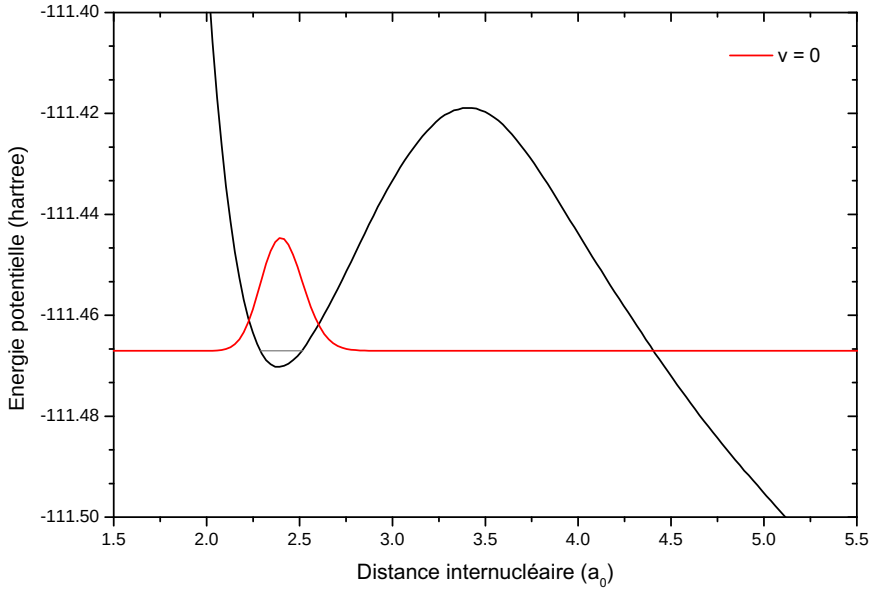

Figure B.5: Courbe d'énergie potentielle de l'état $X\,^3\Pi$ de CO^{2+} et fonction d'onde de son niveau $v = 0, J = 0$.

B.3 Dynamique libre

Nous avons ensuite utilisé ces données *ab initio* afin de décrire la dynamique de photodissociation de HeH^+ et de CO^{2+} ainsi que la formation de HeH^+ par association radiative. Nous avons pour cela utilisé une approche dépendante du temps basée sur la propagation de paquets d'ondes.

B.3.1 Dynamique libre pour HeH^+

Nous avons déterminé les sections efficaces de photodissociation des états a et $b\,^3\Sigma^+$ de HeH^+ vers les états $^3\Sigma^+$ et $^3\Pi$ n =2–3 supérieurs ainsi que les sections efficaces d'association radiative correspondantes, en utilisant une méthode dépendante du temps basée sur la propagation de paquets d'ondes. Les sections efficaces de photodissociation ont été calculées pour chaque niveau vibrationnel initial possible, en combinant deux méthodes de calcul différentes : la première se base sur la fonction d'autocorrélation du paquet d'ondes afin de déterminer les sections totales, tandis que la seconde se base sur la valeur du paquet d'ondes à une certaine distance internucléaire R_∞ afin de déterminer les sections partielles. Nous avons montré que ces deux méthodes peuvent être utilisées de façon complémentaire afin de corriger les oscillations de Gibbs [139] qui apparaissent dans les sections partielles lorsqu'elles ont une contribution non nulle à proximité de l'énergie de seuil. Les résonances ont toutefois dû être négligées en raison des temps de calcul considérables qui auraient été nécessaires à leur détermination pour chacun des niveaux rovibrationnels initiaux.

Les sections efficaces d'association radiative ont ensuite été déterminées sur base des sections efficaces de photodissociation correspondantes. Enfin, ces résultats ont été utilisés pour estimer les constantes de vitesse de photodissociation et d'association radiative dans les conditions typiquement rencontrées dans les environnements astrophysiques où HeH^+ devrait pouvoir être détecté. Nos résultats indiquent que l'abondance fractionnelle de HeH^+ dans des états triplets doit y être beaucoup plus petite que celle de HeH^+ dans des états singulets, tout en étant toutefois suffisante pour influencer les abondances d'autres espèces chimiques.

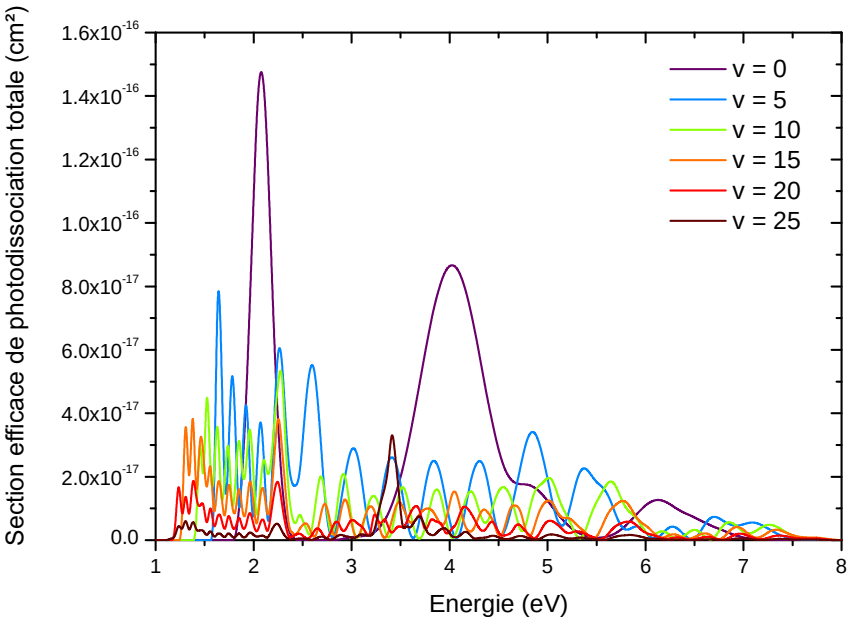

Figure B.6: Sections efficaces de photodissociation de différents niveaux vibrationnels de l'état $b\,^3\Sigma^+$ de HeH^+ vers les canaux $^3\Sigma^+$ supérieurs.

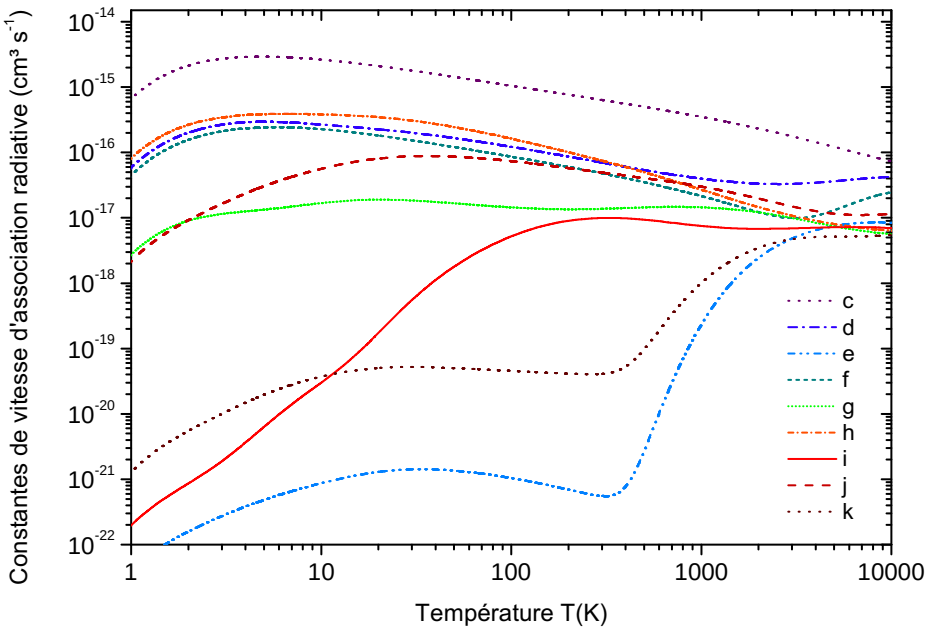

Figure B.7: Constantes de vitesse d'association radiative vers l'état $b\,^3\Sigma^+$ de HeH^+ depuis ses canaux $^3\Sigma^+$ $n = 2$–3.

B.3.2 Dynamique libre pour CO^{2+}

Les sections efficaces partielles de photodissociation du niveau $v'' = 0$ de l'état $X\ ^3\Pi$ de CO^{2+} vers les canaux $^3\Sigma^-$ ont également été calculées. La figure B.8 montre les sections efficaces partielles que nous avons obtenues. La section efficace de photodissociation vers le neuvième état $^3\Sigma^-$, le premier qui se dissocie en C^{2+} + O plutôt qu'en C^+ + O^+ , est très petite et ne domine dans aucun domaine d'énergie, d'où la nécessité d'utiliser des méthodes de contrôle quantique afin de calculer des champs laser permettant de favoriser la dissociation dans ce canal.

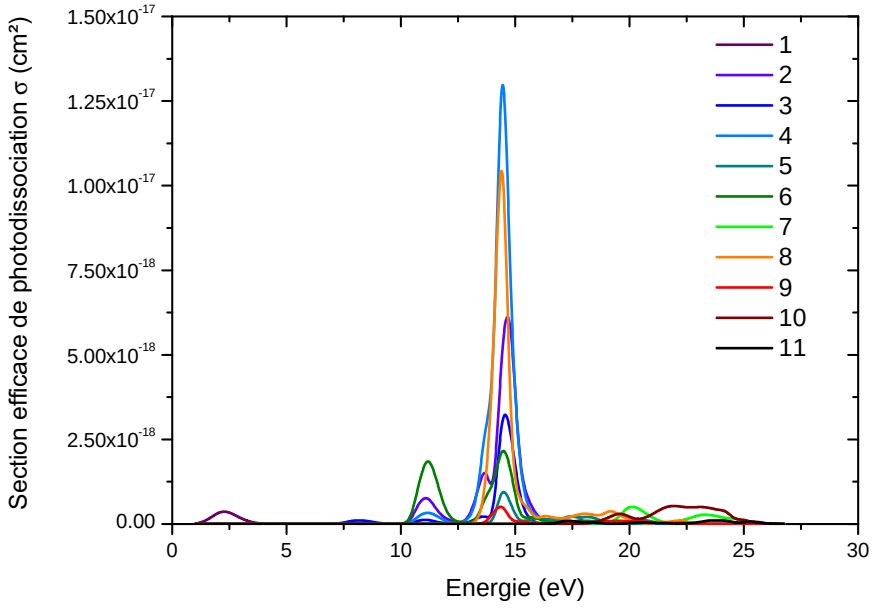

Figure B.8: Sections efficaces de photodissociation partielles du niveau $v'' = 0$ de l'état $X\ ^3\Pi$ de CO^{2+} vers les 11 premiers canaux $^3\Sigma^-$. La nomenclature des états suit celle donnée dans le tableau 2.6 (p. 69).

B.4 Contrôle laser de réactions de photodissociation

Après avoir décrit la dynamique de photodissociation libre de HeH^+ et CO^{2+}, nous sommes allés un cran plus loin en calculant des champs laser guidant la dynamique de photodissociation vers des canaux spécifiques, de façon à favoriser leur dissociation en He^+ + H et C^{2+} + O plutôt qu'en He + H^+ et en C^+ + O^+. Pour y parvenir, nous avons utilisé deux techniques d'optimisation des champs de contrôle : la théorie du contrôle optimal (OCT) [181, 184] et une variante du contrôle local (LCT) [166–168] basée sur les opérateurs de Møller (développée précédemment lors d'une collaboration entre le Prof. Meier du laboratoire LCAR-IRSAMC de l'Université Paul Sabatier et le Laboratoire de Chimie Physique de l'Université Paris-Sud [43]).

B.4.1 Contrainte sur l'aire

Les champs lasers de contrôle optimisés théoriquement à l'aide de ces méthodes ne sont cependant pas toujours expérimentalement réalistes. L'un de ceux déterminés par Bomble *et al.* dans le premier article sur le contrôle de la photodissociation de HeH^+ a par exemple une aire totale non nulle, comme illustré dans la figure B.9 (courbe noire).

L'aire totale du champ électrique associé à une onde électromagnétique devrait pourtant en principe être nulle[†], p. 193), ce qui a motivé les Prof. Sugny (Laboratoire Interdisciplinaire Carnot de Bourgogne, Université de Bourgogne) et Atabek (Institut des Sciences Moléculaires d'Orsay, Université Paris-Sud) à proposer une contrainte, pondérée par un paramètre ν, permettant de minimiser l'aire des champs de contrôle lors de leur optimisation par la théorie du contrôle local ou la théorie du contrôle optimal [180].

Nous présentons dans ce travail les premiers résultats obtenus en implémentant cette contrainte en contrôle local, ainsi que nos résultats obtenus en l'implémentant en contrôle optimal. Nous combinons à cela une autre approche de la minimisation de l'aire de nos champs après optimisation, qui consiste à filtrer les basses fréquences dans leur transformée de Fourier (comme illustré sur la figure B.9), qui correspondent à une contribution non-oscillante dite "Stark".

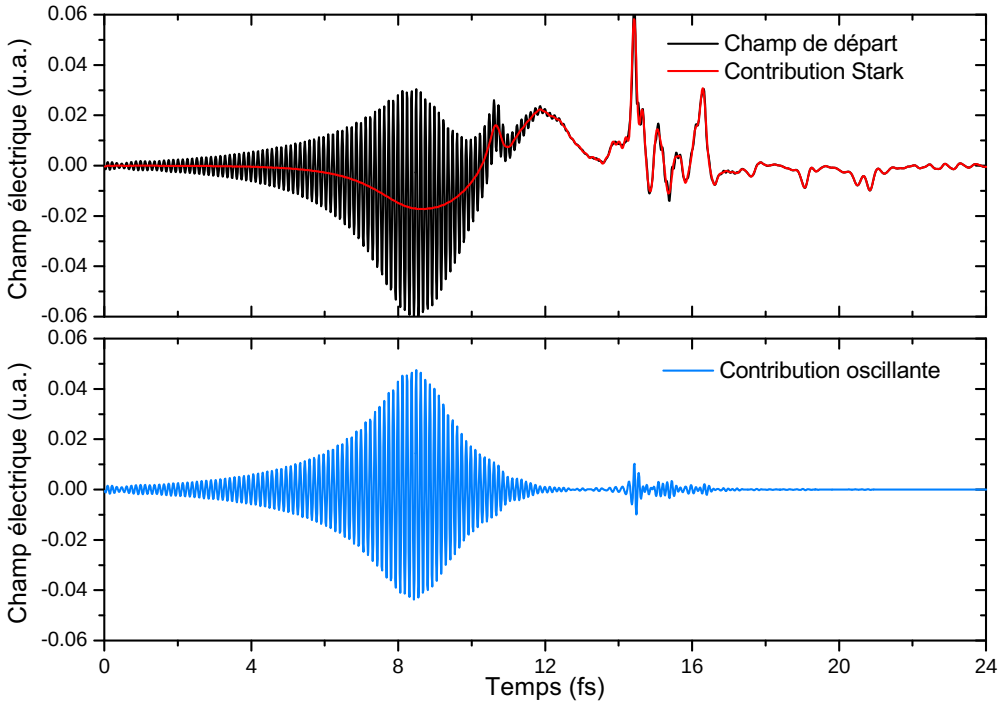

Figure B.9: Le champ de contrôle de la photodissociation de HeH^+ optimisé par Bomble *et al.* avec les paramètres $\lambda = 4.2$, $\nu = 0$ (en haut, courbe noire) peut être séparé en une contribution "Stark" (en haut, courbe noir) et une partie oscillante (en bas, courbe bleue) en filtrant sa transformée de Fourier.

[†]Une démonstration proposée par le Prof. Atabek est donnée (en anglais) au début de l'annexe A.2.

B.4.2 Contrôle de la photodissociation de HeH^+

Le tableau B.1 montre les meilleurs résultats que nous avons obtenus avec différents types d'impulsions laser: les champs LCT obtenus avec les paramètres $\lambda = 4.2$, $\nu = 0$ et $\nu = 0.10$, des champs gaussiens dont la fréquence correspond à des transitions résonnantes (avec soit une valeur maximale du champ $E_{\max}(t)$ imposée, soit une fluence F_0 imposée), et les champs optimisés par OCT avec une fluence imposée fixe $F_0 = 0.06$ u.a. obtenus en utilisant soit une impulsion gaussienne, soit le champ LCT à $\nu = 0$ comme champ de départ (figure B.10). Les résultats sont présentés pour les champs avant et après filtrage des composantes "Stark".

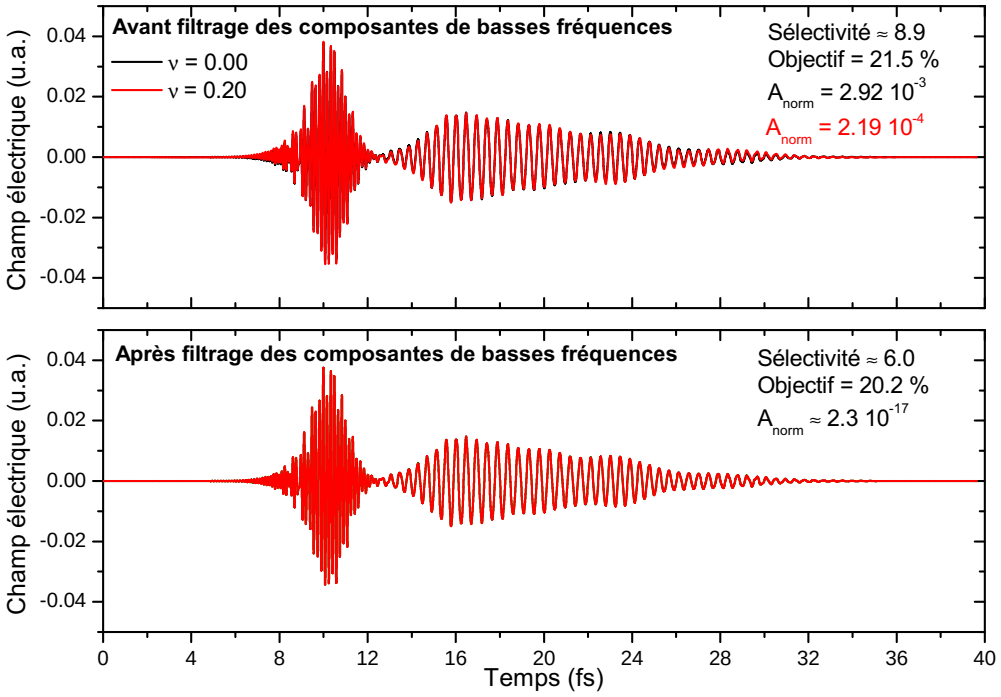

Figure B.10: Champs optimisés à l'aide la théorie du contrôle optimale pour le contrôle de la photodissociation de HeH^+, obtenus en utilisant le champ LCT comme point de départ, avant (en haut) et après (en bas) filtrage des composantes "Stark".

Tableau B.1: Propriétés des meilleurs champs optimisés pour le contrôle de la photodissociation de HeH^+. La durée t_f, la valeur maximale du champ électrique $E_{\max}(t)$ et la fluence F sont toutes exprimées en unités atomiques.

Champ	Objectif	t_f	$E_{\max}(t)$	Sélectivité	A_{norm}	F	Fig.
LCT, $v = 0$	8.55 %	1000	0.068	1.067	6.39×10^{-4}	0.102	4.6, p. 137
LCT $v = 0$, sans “Stark”	4.48 %	1000	0.047	1.243	-3.59×10^{-4}	0.049	4.6, p. 137
LCT, $v = 0.10$	4.75 %	1000	0.024	0.797	-4.30×10^{-4}	0.045	4.6, p. 137
LCT $v = 0.10$, sans “Stark”	3.41 %	1000	0.022	0.563	1.32×10^{-5}	0.058	4.6, p. 137
Gaussienne$_{X\to B}$, $E_{\max}(t)$=0.05	2.37 %	1638.4	0.050	0.853	0	0.376	4.9, p. 140
Gaussienne$_{X\to B}$, F=0.06	13.77 %	1638.4	0.017	0.722	0	0.060	4.9, p. 140
OCT, Champ initial = Gaussienne$_{X\to B}$, F_0=0.06	16.48 %	1638.4	0.049	1.067	5.94×10^{-2}	0.060	4.10, p. 142
OCT, Champ initial = Gaussienne$_{X\to B}$, F_0=0.06, sans “Stark”	12.35 %	1638.4	0.051	1.119	3.14×10^{-17}	0.058	4.10, p. 142
OCT, Champ initial = LCT$_{v=0}$, $v = 0.20$, F_0=0.06	21.54 %	1638.4	0.039	8.894	2.19×10^{-4}	0.060	4.11, p. 143
OCT, Champ initial = LCT$_{v=0}$, $v = 0.20$, F_0=0.06, sans “Stark”	20.24 %	1638.4	0.039	5.952	2.35×10^{-17}	0.060	4.11, p. 143

B.4.3 Contrôle de la photodissociation de CO^{2+}

Le tableau B.2 montre les meilleurs résultats que nous avons obtenus avec différents types d'impulsions laser: les champs LCT obtenus avec les paramètres $\lambda = 7.5$ et $\nu = 0$, un champ gaussien dont la fréquence correspond à une transition résonnante vers l'état-cible, le champ LCT modifié afin de servir de point de départ à l'algorithme de contrôle optimal et le champ optimisé par OCT avec le paramètre $\alpha_0 = 200$. Les champs obtenus ont une fluence plus élevée que pour HeH^+ en raison de la valeur plus petite des moments dipolaires de transition impliqués.

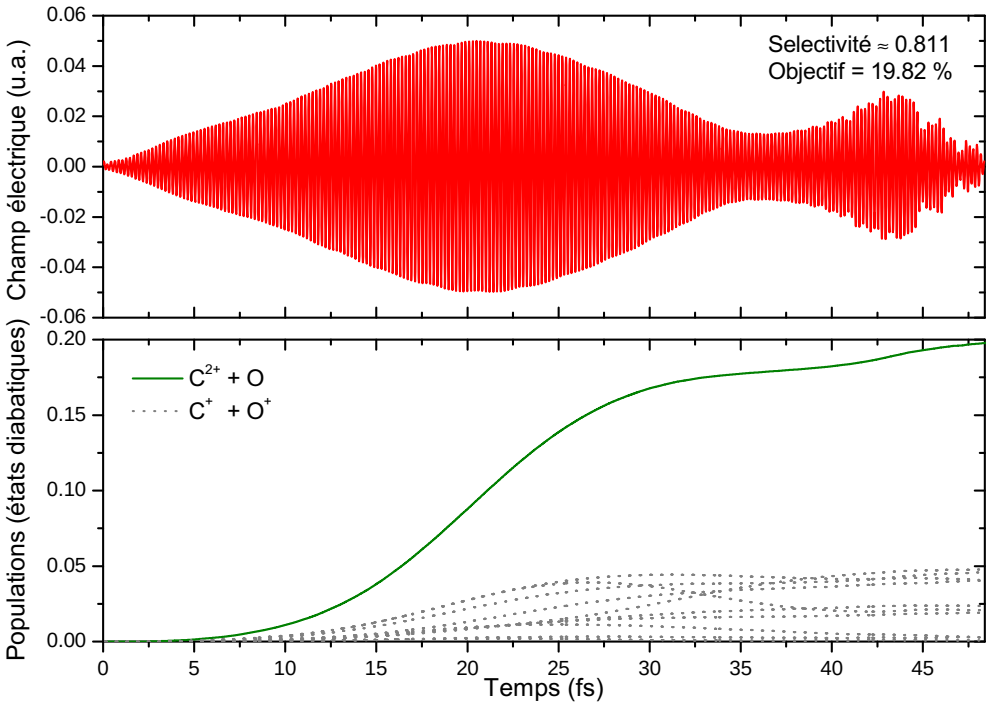

Figure B.11: En haut : champ optimisé à l'aide la théorie du contrôle optimale avec $\alpha_0 = 200$ pour le contrôle de la photodissociation de CO^{2+}, obtenu en utilisant le champ LCT comme point de départ. En bas : populations des états diabatiques en fonction du temps.

Tableau B.2: Propriétés des meilleurs champs optimisés pour le contrôle de la photodissociation de CO^{2+}. La durée t_f, la valeur maximale du champ électrique $E_{\max}(t)$ et la fluence F sont toutes exprimées en unités atomiques.

Champ	Objectif	t_f	$E_{\max}(t)$	Sélectivité	A_{norm}	F	Fig.
LCT $\lambda = 7.5$, $\nu = 0$	16.49 %	6500	0.032	0.797	7.92×10^{-5}	0.627	4.14, p. 148
Gaussian$_{X\to 9}$, $E_{\max}(t)$=0.05	1.30 %	2000	0.050	0.025	0	0.627	4.15, p. 150
LCT, raccourci, avec enveloppe	9.01 %	2000	0.032	0.799	8.27×10^{-6}	0.347	4.16, p. 151
OCT, Champ initial = LCT raccourci, $\alpha_0 = 200$	19.82 %	2000	0.050	0.811	0	0.905	4.17, p. 152

B.4.4 Conclusions : contrôle de réactions de photodissociation

Nous avons tiré les conclusions suivantes de nos calculs sur HeH^+ and CO^{2+}:

- Bien que des impulsions gaussiennes puissent, de prime abord, sembler parfois mener à des objectifs plus élevés que des impulsions laser optimisées par LCT, la comparaison d'impulsions de même fluence montrent que les gaussiennes sont beaucoup moins efficaces. De plus, elles mènent à des sélectivités relativement basses dans des systèmes où la dynamique est fortement influencée par des couplages non-adiabatiques, comme HeH^+ et CO^{2+}.

- La contrainte sur l'aire est efficace, que ce soit en contrôle local ou en contrôle optimal, mais trouver la valeur du paramètre ν qui mène à la fois à une aire très petite et à un objectif final raisonnable nécessite plusieurs calculs. Dans les cas étudiés ici, filtrer les composantes à basse fréquence de nos champs mène déjà à une diminution significative de leur aire totale.

- L'algorithme de contrôle optimal mène à des impulsions beaucoup plus efficaces quand les champs optimisés par la théorie du contrôle local sont utilisés comme point de départ plutôt que de simples impulsions gaussiennes.

- Bien que les champs obtenus en utilisant la théorie du contrôle local mènent à des objectifs moins élevés que ceux obtenus en utilisant la théorie du contrôle optimal, leur spectre est beaucoup plus simple, ce qui est susceptible de simplifier leur implémentation expérimentale.

Une meilleur sélectivité entre les différents canaux de photodissociation pourrait certainement être obtenue en utilisant des contraintes supplémentaires de façon à pénaliser ou à interdire le transfert de population vers certains états [197, 198].

B.5 Calcul quantique moléculaire

Enfin, nous nous sommes intéressés à l'une des applications potentielles des méthodes de contrôle laser : l'utilisation de molécules comme "ordinateurs quantiques". Différentes stratégies ont en effet été imaginées au cours des dernières années pour tirer parti des propriétés quantiques d'objets microscopiques, comme les molécules, afin d'effectuer certains calculs plus rapidement qu'avec n'importe quel ordinateur classique.

Notre objectif dans ce travail n'est pas de donner une stratégie fonctionnelle pour permettre l'utilisation de molécules comme ordinateurs quantiques capables de manipuler un grand nombre de bits quantiques ("qubits"), mais d'explorer une possibilité de solution à certains des obstacles qui doivent d'abord être surmontés : le problème de la décohérence (la perte de l'information quantique sous l'effet de l'interaction avec l'environnement) et le problème de l'extensibilité (la difficulté d'encoder un grand nombre de qubits dans un système quantique et

de les manipuler). Nous étudions plus précisément, à l'aide d'un modèle simplifié, la possibilité d'implémenter des opérations logiques *intermoléculaires*, c'est-à-dire sur des qubits encodés dans des états d'énergie de molécules différentes qui interagissent les unes avec les autres.

B.5.1 Modèle utilisé

Notre modèle s'inspire de celui proposé par le Prof. DeMille [70] et consiste à encoder les qubits dans les états hyperfins de molécules diatomiques polaires piégées "communiquant" par le biais de leur interaction dipôle-dipôle. Ces molécules présentent en effet de nombreux avantages : elles peuvent être créées à très basse température et piégées, leur interaction dipôle-dipôle est particulièrement forte, et leurs états hyperfins ont à la fois un temps de décohérence relativement long et une structure suffisamment complexe pour permettre l'encodage d'un grand nombre de qubits [70, 291, 299].

Dans notre modèle, les molécules de $^{41}K^{87}Rb$ sont supposées piégées dans un réseau optique : nous avons fait l'approximation qu'elles sont immobiles dans l'espace (avec une distance de 100 nm entre leurs centres de masse), et alignées sur l'axe intermoléculaire Z. Un champ magnétique intense est utilisé pour provoquer le splitting des états hyperfins. De plus, un champ électrique avec un gradient le long de l'axe de piégeage permet l'adressage individuel de chacune des molécules [70].

Les molécules se trouvent au départ dans leur niveau d'énergie le plus bas (électronique, vibrationnel, rotationnel et hyperfin) et restent tout au long du calcul dans les deux niveaux rotationnels les plus bas du niveau vibrationnel $v = 0$ de leur état électronique fondamental $X\,^1\Sigma^+$. Les autres niveaux d'énergie des molécules n'ont pas été pris en compte dans nos calculs.

B.5.2 Implémentations théoriques de l'algorithme de Grover

À l'aide de ce modèle, nous avons implémenté théoriquement une version à 2 et à 3 qubits de l'algorithme quantique de recherche de Grover, qui permet de trouver un élément précis dans une base de données désordonnée qui en contient N en un nombre d'opérations proportionnel à $\sqrt{N}$ (plutôt qu'à $N/2$, comme le ferait le plus efficace des algorithmes classiques). Les opérations logiques successives qui composent l'algorithme sont réalisées à l'aide de champs lasers optimisés par la théorie du contrôle optimal multicible [190] afin de réaliser les transferts de population appropriés entre les états dans lesquels les qubits sont encodés. Les optimisations ont été menées pendant plusieurs centaines d'itérations, jusqu'à ce que la fidélité des champs de contrôle atteigne plus de 99 %.

Trois versions de l'algorithme de Grover ont été simulées : une version à 2 et une version à 3 qubits en encodant ceux-ci dans les états hyperfins d'une même molécule de $^{41}K^{87}Rb$, et une version à 2 qubits en encodant ceux-ci dans les états hyperfins de deux molécules de $^{41}K^{87}Rb$ voisines interagissant via leurs dipôles permanents. Les figures B.12 et B.13 montrent respectivement l'encodage choisi pour les qubits et les champs de contrôle que nous avons optimisés dans ce dernier cas. La fidélité très élevée de nos champs de contrôle permet la réalisation de

plusieurs itérations successives de l'algorithme sans perte significative de population dans les états-cibles.

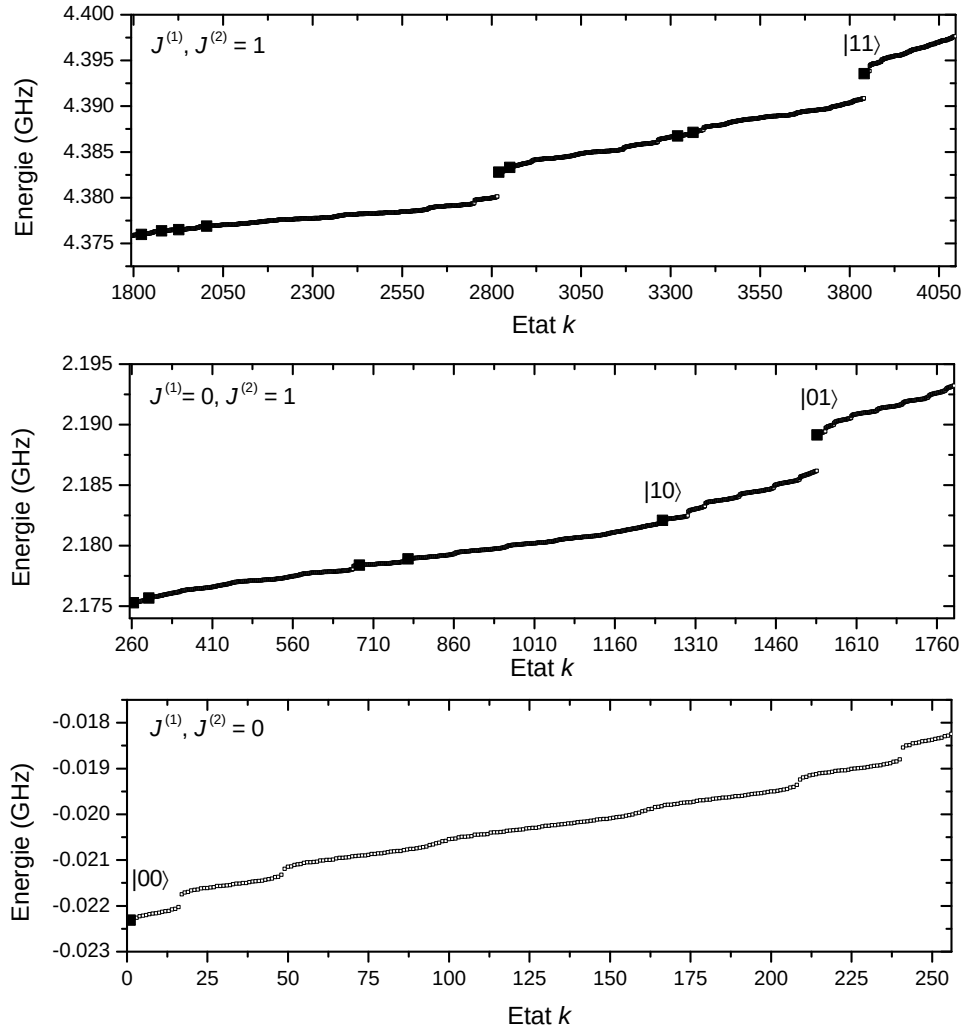

Figure B.12: Niveaux d'énergie de deux molécules de $^{41}K^{87}Rb$ exposées à un champ magnétique de 500 et 400 gauss, respectivement. Les carrés noirs représentent les seize états inclus dans nos calculs.

Nos résultats indiquent que la réalisation d'opérations logiques conditionnelles inter-moléculaires est possible, ce qui ouvre des perspectives intéressantes en terme d'extensibilité : plutôt que d'encoder un nombre important de qubits sur une seule molécule, il pourrait être intéressant d'utiliser plusieurs molécules en interaction, portant chacune un petit nombre de qubits [9].

Il faudrait toutefois vérifier que ces résultats se confirment dans des modèles plus fidèles à la réalité. De plus, nos champs optimisés (chronologiquement, les premiers calculés dans le cadre de cette thèse) induisent des oscillations importantes des populations et pourraient être améliorés de différentes façons, par exemple en ajoutant une contrainte sur leur aire et sur leur fluence.

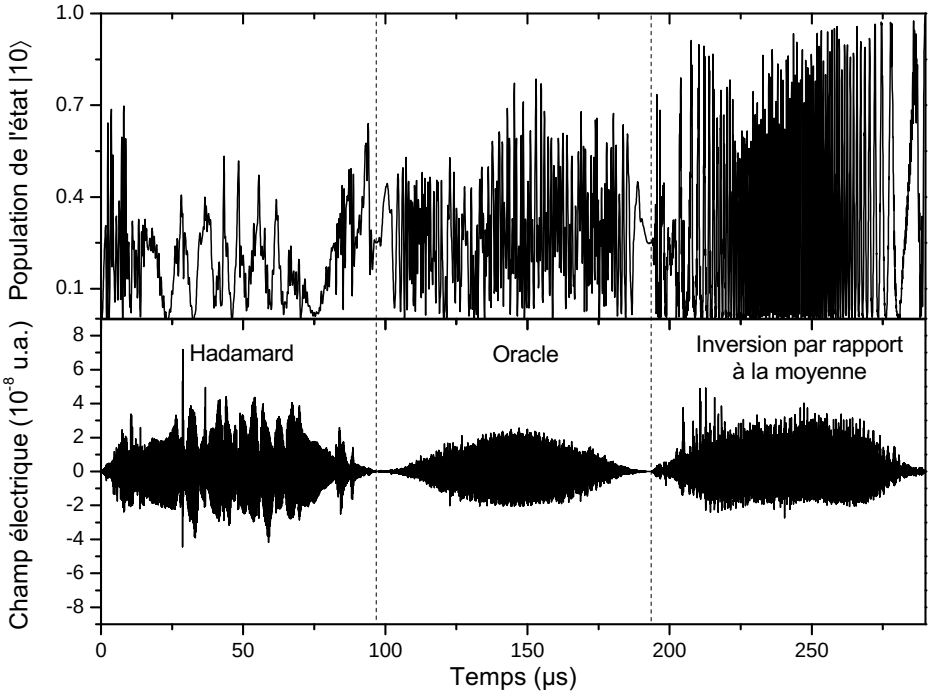

Figure B.13: Champs optimisés (en bas) et évolution de la population dans l'état-cible $|10\rangle$ (en haut) en fonction du temps pour notre implémentation de l'algorithme de Grover à deux qubits dans les états hyperfins de deux molécules de $^{41}K^{87}Rb$ en interaction.

B.6 Conclusions

Dans ce travail, nous avons étudié théoriquement les propriétés statiques de systèmes moléculaires diatomiques, leur dynamique de photodissociation et d'association radiative, le contrôle de leur photodissociation à l'aide de champs lasers, et l'application potentielle des méthodes de contrôle quantique à la réalisation d'ordinateurs quantiques moléculaires.

Des progrès important doivent toutefois encore être réalisés avant que des ordinateurs quantiques moléculaire capables de surpasser nos ordinateurs classiques ne puissent être créés. Comme l'illustre ce travail, la description théorique de petites molécules n'est pas un problème trivial, surtout lorsqu'elle doit être réalisée avec une haute précision (condition essentielle à l'optimisation théorique de champs de contrôle fiables). De plus, bien que le contrôle laser de processus chimiques ait beaucoup évolué depuis ses débuts, des progrès importants doivent encore être réalisés afin de combler l'écart qui existe souvent entre les prédictions théoriques et les réalisations expérimentales.

De tels progrès ouvriraient toutefois la voie à des applications révolutionnaires, telles que l'utilisation de molécules comme ordinateurs quantiques — qui pourraient à leur tour révolutionner la façon dont nous décrivons théoriquement les molécules.

BIBLIOGRAPHY

[1] NIST Database. URL: http://physics.nist.gov/cuu/Constants/index.html.

[2] J. Loreau, J. Liévin, P. Palmeri, P. Quinet, and N. Vaeck. *Ab initio* calculation of the 66 low lying electronic states of HeH^+ : adiabatic and diabatic representations. *J. Phys. B: At. Mol. Opt. Phys.*, 43:065101, 2010. doi:10.1088/0953-4075/43/6/065101.

[3] J. Loreau, J. Liévin, and N. Vaeck. Radiative lifetime of the $a\,^3\Sigma^+$ state of HeH^+ from *ab initio* calculations. *J. Chem. Phys.*, 133:114302, 2010. doi:10.1063/1.3481782.

[4] J. Loreau, K. Sodoga, D. Lauvergnat, M. Desouter-Lecomte, and N. Vaeck. *Ab initio* calculation of H + He^+ charge transfer cross sections for plasma physics. *Phys. Rev. A*, 82:012708, 2010. doi:10.1103/PhysRevA.82.012708.

[5] J. Loreau, J. Lecointre, X. Urbain, and N. Vaeck. Rovibrational analysis of the XUV photodissociation of HeH^+ ions. *Phys. Rev. A*, 84:053412, 2011. doi:10.1103/PhysRevA.84.053412.

[6] K. Sodoga, J. Loreau, D. Lauvergnat, Y. Justum, N. Vaeck, and M. Desouter-Lecomte. Photodissociation of the HeH^+ ion into excited fragments ($n = 2,3$) by time-dependent methods. *Phys. Rev. A.*, 80:033417, 2009. doi:10.1103/PhysRevA.80.033417.

[7] L. Bomble, D. Lauvergnat, F. Remacle, and M. Desouter-Lecomte. Vibrational computing: Simulation of a full adder by optimal control. *J. Chem. Phys.*, 128:064064110, 2008. doi:10.1063/1.2806800.

[8] L. Bomble, D. Lauvergnat, F. Remacle, and M. Desouter-Lecomte. Controlled full adder or subtractor by vibrational quantum computing. *Phys. Rev. A*, 80:022332, 2009. doi:10.1103/PhysRevA.80.022332.

[9] L. Bomble, P. Pellegrini, P. Ghesquière, and M. Desouter-Lecomte. Toward scalable information processing with ultracold polar molecules in an electric field: a numerical investigation. *Phys. Rev. A*, 82:062323, 2010. doi:10.1103/PhysRevA.82.062323.

[10] L. Bomble, D. Lauvergnat, F. Remacle, and M. Desouter-Lecomte. Controlled full adder or subtractor by vibrational computing. *Physical Chemistry Chemical Physics*, 18:15628–15635, 2010. doi:10.1039/C003687K.

[11] G. E. Moore. Cramming More Components onto Integrated Circuits. *Proceedings of the IEEE*, 86(1):82, 1965. doi:10.1109/JPROC.1998.658762.

[12] M. S. Safronova, M. G. Kozlov, W. R. Johnson, and D. Jiang. Development of a configuration-interaction plus all-order method for atomic calculations. *Phys. Rev. A*, 80:012516, 2009. doi:10.1103/PhysRevA.80.012516.

[13] C. Froese Fischer, S. Verdebout, M. Godefroid, P. Rynkun, P. Jönsson, and G. Gaigalas. Doublet-quartet energy separation in boron: A partitioned-correlation-function-interaction method. *Phys. Rev. A*, 88:062506, 2013. doi:10.1103/PhysRevA.88.062506.

[14] C. Brif, R. Chakrabarti, and H. Rabitz. Control of quantum phenomena: past, present and future. *New J. Phys.*, 12:075008, 2010. doi:10.1088/1367-2630/12/7/075008.

[15] B. G. Anex. Ground State of the HeH^+ Molecule Ion. *J. Chem. Phys.*, 38:1651, 1963. doi:10.1063/1.1776937.

[16] W. Kolos and J. M. Peek. New *ab initio* potential curve and quasibound states of HeH^+. *Chem. Phys.*, 12:381–386, 1976. doi:10.1016/0301-0104(76)87076-0.

[17] D. M. Bishop and L. M. Cheung. A theoretical investigation of HeH^+. *J. Mol. Spectrosc.*, 75(3):462–473, 1979. doi:10.1016/0022-2852(79)90090-0.

[18] M. Stanke, D. Kedziera, M. Molski, S. Bubin, M. Barysz, and L. Adamowicz. Convergence of Experiment and Theory on the Pure Vibrational Spectrum of HeH^+. *Phys. Rev. Lett.*, 96:233002, 2006. doi:10.1103/PhysRevLett.96.233002.

[19] T. A. Green, H. H. Michels, J. C. Browne, and M. M. Madsen. Configuration interaction studies of the HeH^+ molecular ion. I. Singlet sigma states. *J. Chem. Phys.*, 61:5186, 1974. doi:10.1063/1.1681864.

[20] T. A. Green, H. H. Michels, J. C. Browne, and M. M. Madsen. Configuration interaction studies of the HeH^+ molecular ion. II. Dipole and radial coupling matrix elements for the singlet sigma states. *J. Chem. Phys.*, 61:5198, 1974. doi:10.1063/1.1681865.

[21] T. A. Green, H. H. Michels, and J. C. Browne. Configuration interaction studies of the HeH^+ molecular ion. III. Singlet pi and delta states. *J. Chem. Phys.*, 64:3951, 1976. doi:10.1063/1.432025.

[22] T. A. Green, H. H. Michels, and J. C. Browne. Configuration interaction studies of the HeH^+ molecular ion. IV. The triplet sigma, pi, and delta states. *J. Chem. Phys.*, 69:101, 1978. doi:10.1063/1.436392.

[23] G. Bertschinger and O. Marchuk. *Nuclear Fusion Research – Understanding Plasma-Surface Interactions*, volume 78, chapter High-Temperature Plasmas Diagnostics by X-ray Spectroscopy in the Low Density Limit, pages 183–199. Springer Series in Chemical Physics, 2005. doi:10.1007/3-540-27362-X_8.

[24] F. B. Rosmej, R. Stamm, and V. S. Lisitsa. Convergent coupling of helium to the H/D background in magnetically confined plasmas. *Europhys. Lett.*, 73:342, 2006. doi:10.1209/epl/i2005-10405-7.

[25] W. Roberge and A. Dalgarno. The formation and destruction of HeH^+ in astrophysical plasmas. *Astrophys. J.*, 255:489–496, 1982. doi:10.1086/159849.

[26] D. Galli and F. Palla. The chemistry of the early Universe. *Astron. Astrophys.*, 335:403–420, 1998. URL: http://arxiv.org/abs/astro-ph/9803315.

[27] S. Lepp, P. C. Stancil, and A. Dalgarno. Atomic and molecular processes in the early Universe. *J. Phys. B: At. Mol. Opt. Phys.*, 35:R57–R80, 2002. doi:10.1088/0953-4075/35/10/201.

[28] I. Dabrowski and G. Herzberg. The predicted infrared spectrum of HeH^+ and its possible astrophysical importance. *Transactions of the New York Academy of Sciences*, 38(1):14–25, 1977. doi:10.1111/j.2164-0947.1977.tb02944.x.

[29] J. H. Black. Molecules in planetary nebulæ. *Astrophys. J.*, 222:125–131, 1978. doi:10.1086/156128.

[30] C. Cecchi-Pestellini and A. Dalgarno. Emission of HeH^+ in nebulæ. *Astrophys. J.*, 413:611–618, 1993. doi:10.1086/173030.

[31] S. Miller, J. Tennyson, S. Lepp, and A. Dalgarno. Identification of features due to H_3^+ in the infrared spectrum of supernova 1987A. *Nature*, 355:420–422, 1992. doi:10.1038/355420a0.

[32] A. E. Engel, N. Doss, G. J. Harris, and J. Tennyson. Calculated spectra for HeH^+ and its effect on the opacity of cool metal-poor stars. *Mon. Not. R. Astron. Soc.*, 357:471–477, 2005. doi:10.1111/j.1365-2966.2005.08611.x.

[33] G. J. Harris, A. E. Lynas-Gray, S. Miller, and J. Tennyson. The role of HeH^+ in cool helium-rich white dwarfs. *Astrophys. J.*, 617(2):L134–L146, 2004. doi:10.1086/427391.

[34] D. R. Flower and E. Roueff. On The Formation and Destruction of HeH^+ in Gaseous Nebulæ and the Associated Infra-red Emission Line Spectrum. *Astron. Astrophys.*, 72:361–366, 1979. URL: http://adsabs.harvard.edu/abs/1979A%26A....72..361F.

[35] J. M. Moorhead, R. P. Lowe, J. P. Maillard, W. H. Wehlau, and P. F. Bernath. Search for HeH^+ in NGC 7027. *Astrophys. J.*, 326:899, 1988. doi:10.1086/166147.

[36] X.-W. Liu, M. J. Barlow, A Dalgarno, J. Tennyson, T. Lim, B. M. Swinyard, J. Cernicharo, P. Cox, J.-P. Baluteau, D. Péquinot, Nguyen-Q-Rieu, R. J. Emery, and P. E. Clegg. An ISO Long Wavelength Spectrometer detection of CH in NGC 7027 and an HeH^+ upper limit. *Mon. Not. R. Astron. Soc.*, 290:L71, 1997. URL: http://adsabs.harvard.edu/abs/1997MNRAS.290L..71L.

[37] M. J. Barlow, B. M. Swinyard, P. J. Owen, J. Cernicharo, H. L. Gomez, R. J. Ivison, O. Krause, T. L. Lim, M. Matsuura, S. Miller, G. Olofsson, and E. T. Polehampton. Detection of a Noble Gas Molecular Ion, $^{36}ArH^+$, in the Crab Nebula. *Science*, 342:1343, 2013. doi:10.1126/science.1243582.

[38] T. R. Hogness and E. G. Lunn. The Ionization of Hydrogen by Electron Impact as Interpreted by Positive Ray Analysis. *Phys. Rev.*, 26:44–55, 1925. doi:10.1103/PhysRev.26.44.

[39] F. B. Yousif, J. B. A. Mitchell, M. Rogelstad, A. Le Paddelec, A. Canosa, and M. I. Chibisov. Dissociative recombination of HeH^+: A reexamination. *Phys. Rev. A*, 49:4610, 1994. doi:10.1103/PhysRevA.49.4610.

[40] D. Strasser, K. G. Bhushan, H. B. Pedersen, R. Wester, O. Heber, A. Lafosse, M. L. Rappaport, N. Altstein, and D. Zajfman. Charge-transfer dissociation of vibrationally cold HeH^+: Evidence for and lifetime of the $a\,^3\Sigma^+$ metastable state. *Phys. Rev. A*, 61:060705(R), 2000. doi:10.1103/PhysRevA.61.060705.

[41] H. B. Pedersen, S. Altevogt, B. Jordon-Thaden, O. Heber, M. L. Rappaport, D. Schwalm, J. Ullrich, D. Zajfman, R. Treusch, N. Guerassimova, M. Martins, J.-T. Hoeft, M. Wellhöfer, and A. Wolf. Crossed Beam Photodissociation Imaging of HeH^+ with Vacuum Ultraviolet Free-Electron Laser Pulses. *Phys. Rev. Lett.*, 98:223202, 2007. doi:10.1103/PhysRevLett.98.223202.

[42] J. Lecointre, J. J. Jureta, X. Urbain, and P. Defrance. Electron-impact dissociation of HeH^+: absolute cross sections for the production of He^{q+} (q = 1–2) fragments. *J. Phys. B: At. Mol. Opt. Phys.*, 47:015203, 2014. doi:10.1088/0953-4075/47/1/015203.

[43] L. Bomble, A. Chenel, C. Meier, and M. Desouter-Lecomte. Local control of non-adiabatic dissociation dynamics. *J. Chem. Phys.*, 134:204112, 2011. doi:10.1063/1.3589911.

[44] R. Conrad. *Phys. Z.*, 31:888, 1930.

[45] J. J. Thomson. *Rays of Positive Electricity, and their application to chemical analyses*. Longmans, London, 1921. URL: https://archive.org/details/raysofpositiveel00thomuoft.

[46] L. Pauling. The Normal State of the Helium Molecule-Ions He_2^+ and He_2^{++}. *J. Chem. Phys.*, 1:56, 1933. doi:10.1063/1.1749219.

[47] S. G. Cox, A. D. J. Critchley, P. S. Kreynin, I. R. McNab, R. C. Shiell, and F. E. Smith. High resolution spectroscopy and structure of molecular dications. *Phys. Chem. Chem. Phys.*, 5:663–676, 2003. doi:10.1039/b209398g.

[48] J. Senekowitsch, S. ONeil, and W. Meyer. On the bonding in doubly charged diatomics. *Theor Chim Acta*, 84:85–93, 1992. doi:10.1007/BF01117404.

[49] F. Mrugała. A computational study of metastable states of CO^{2+}. *J. Chem. Phys.*, 129:064314, 2008. doi:10.1063/1.2948389.

[50] J. Lecointre, D. S. Belic, J. J. Jureta, K. Becker, H. Deustch, J. Limtrakul, T. D. Märk, M. Probst, and P. Defrance. Absolute cross sections and kinetic energy release for doubly and triply charged fragments produced by electron impact on CO^+. *Institute of Physics Publishing*, 40:85–100, 2007. doi:10.1088/0953-4075/40/1/008.

[51] D. Mathur, L. H. Andersen, P. Hvelplund, D. Kella, and C. P. Safvan. Long-lived, doubly charged diatomic and triatomic molecular ions. *J. Phys. B: At. Mol. Opt. Phys.*, 28:3415, 1995. doi:10.1088/0953-4075/28/15/027.

[52] O. Witasse, O. Duituit, J. Lilensten, R. Thissen, J. Zabka, C. Alcaraz, S. W. Bougher, S. Engel, L. H. Andersen, and K. Seiersen. Prediction of a CO_2^{2+} layer in the atmosphere of Mars. *Geophysical Research Letters*, 29(8):1263, 2002. doi:10.1029/2002GL014781.

[53] G. Gronoff, J. Lilensten, C. Simon, O. Witasse, R. Thissen, O. Duituit, and C. Alcaraz. Modelling dications in the diurnal ionosphere of Venus. *Astron. Astrophys.*, 465:641–645, 2007. doi:10.1051/0004-6361:20065991.

[54] S. Petrie and D. K. Bohme. Ions in Space. *Mass Spectrometry Reviews*, 26(2):258–280, 2006. doi:10.1002/mas.20114.

[55] E. F. van Dishoeck and J. H. Black. The photodissociation and chemistry of interstellar CO. *Astrophys. J.*, 334:771–802, 1988. doi:10.1086/166877.

[56] W. B. Latter, C. K. Walker, and P. R. Maloney. Detection of the Carbon Monoxide Ion (CO^+) in the Interstellar Medium and a Planetary Nebula. *Astrophys. J. Lett.*, 419:L97, 1993. doi:10.1086/187146.

[57] J. D. Eland, M. Hochlaf, G. C. King, P. S. Kreynin, R. J. LeRoy, I. R. McNab, and J.-M. Robbe. Photo double ionization spectra of CO: comparison of theory with experiment. *J. Phys. B: At. Mol. Opt. Phys.*, 37:3197, 2004. doi:10.1088/0953-4075/37/15/014.

[58] A. B. Alekseyev, H.-P. Liebermann, R. Lingott, and R. J. Buenker. Long-lived diatomic dications: potential curves and radiative lifetimes for $CaBr^{2+}$ and CaI^{2+} including relativistic effects. *Mol. Phys.*, 91(5):777–778, 1997. doi:10.1080/002689797170897.

[59] J. M. Curtis and R. K. Boyd. Ion kinetic energy spectroscopy of the doubly charged ion of carbon monoxide. *J. Chem. Phys.*, 80:1150, 1984. doi:10.1063/1.446844.

[60] J. O. K. Pedersen and P. Hvelplund. Energy gain spectroscopy studies of electron capture from neon by doubly charged CO ions. *J. Phys. B: At. Mol. Phys.*, 20:L317, 1987. doi:10.1088/0022-3700/20/10/005.

[61] Z. Herman, P. Jonathan, A. G. Brenton, and J. H. Beynon. Non-dissociative single-electron capture by CO^{2+} from rare gases. *Chem. Phys. Lett.*, 141(5):433–442, 1987. doi:10.1016/0009-2614(87)85055-8.

[62] P. Lablanquie, J. Delwiche, M.-J. Hubin-Franskin, I. Nenner, P. Morin, K. Ito, J. H. D. Eland, J.-M. Robbe, G. Gandara, J. Fournier, and P. G. Fournier. Experimental and theoretical investigation of the spectroscopy and dynamics of multiply charged CO cations. *Phys. Rev. A*, 40:5673–5689, 1989. doi:10.1103/PhysRevA.40.5673.

[63] L. H. Andersen, J. H. Posthumus, O. Vahtras, H. Agren, N. Elander, A. Nunez, A. Scrinzi, M. Natiello, and M. Larsson. Very slow spontaneous dissociation of CO^{2+} observed by means of a heavy ion storage ring. *Phys. Rev. Lett.*, 71:1812–1815, 1993. doi:10.1103/PhysRevLett.71.1812.

[64] M. Hochlaf, R. I. Hall, F. Penent, P. Kjeldsen, H. AN Lablanquie, M. Lavollée, and J. H. D. Eland. Threshold photoelectrons coincidence spectroscopy of N_2^{2+} and CO^{2+} ions. *Chemical Physics*, 207:159–165, 1996. doi:10.1016/0301-0104(96)00056-0.

[65] O. Fuhurashi, T. Kinugawa, S. Masuda, C. Yamada, and S. Ohtani. Double charge transfer spectroscopy for N_2^{2+} and CO^{2+} at vibrational resolution. *Chem. Phys. Lett.*, 337(1–3):97–102, 2001. doi:10.1016/S0009-2614(01)00173-7.

[66] C. Guo. Holding molecular dications together in strong laser fields. *Phys. Rev. A*, 73:041401(R), 2006. doi:10.1103/PhysRevA.73.041401.

[67] R. W. Wetmore, R. J. Le Roy, and R. K. Boyd. Theoretical Investigation of the Diatomic Dication CO^{2+}. *J. Phys. Chem.*, 88:6318–6328, 1984. doi:10.1021/j150669a053.

[68] N. Correia, A. Flores-Riveros, H. Agren, K. Helenelund, L. Asplund, and U. Gelius. Theory of band shape formation in Auger and autoionization spectra of molecules. Numerical applications and new high-resolution spectra for CO. *J. Chem. Phys.*, 83:2035, 1985. doi:10.1063/1.449346.

[69] M. Larsson, B. J. Olsson, and P. Sigray. Theoretical Study of the CO^{2+} dication. *Chemical Physics*, 139:457–469, 1989. doi:10.1016/0301-0104(89)80157-0.

[70] D. DeMille. Quantum Computation with Trapped Polar Molecules. *Phys. Rev. Lett.*, 88:067901, 2002. doi:10.1103/PhysRevLett.88.067901.

[71] S. Inouye, J. Goldwin, M. L. Olsen, C. Ticknor, J. L. Bohn, and D. S. Jin. Observation of Heteronuclear Feshbach Resonances in a Mixture of Bosons and Fermions. *Phys. Rev. Lett.*, 93(18):183201, 2004. doi:10.1103/PhysRevLett.93.183201.

[72] K.-K. Ni, S. Ospelkaus, M. H. G. de Miranda, A. Pe'er, B. Neyenhuis, J. J. Zirbel, S. Kotochigova, P. S. Julienne, D. S. Jin, and J. Ye. A High Phase-Space-Density Gas of Polar Molecules. *Science*, 322:231–235, 2008. doi:10.1126/science.1163861.

[73] S. Ospelkaus, K.-K. Ni, G. Quéméner, B. Neyenhuis, D. Wang, M. H. G. de Miranda, J. L. Bohn, J. Ye, and D. S. Jin. Controlling the hyperfine state of rovibronic ground-state polar molecules. *Phys. Rev. Lett.*, 104:030402, 2010. doi:10.1103/PhysRevLett.104.030402.

[74] S. Ospelkaus, K.-K. Ni, D. Wang, M. H. G. de Miranda, G. Quéméner, P. S. Julienne, J. L. Bohn, D. S. Jin, and J. Ye. Quantum-State Controlled Chemical Reactions of Ultracold Potassium-Rubidium Molecules. *Science*, 327(5967):853–857, 2010. doi:10.1126/science.1184121.

[75] B. H. Bransden and C. J. Joachain. *Physics of Atoms and Molecules*. Prentice Hall, 2003.

[76] G. C. Schatz. Scattering Theory and Dynamics: Time-Dependent and Time-Independent Methods. *J. Phys. Chem.*, 100(31):12839–12847, 1996. doi:10.1021/jp953344y.

[77] F. Jensen. *Introduction to Computational Chemistry*. John Wiley & Sons, 2007.

[78] M. Born and R. Oppenheimer. Zur Quantentheorie der Molekeln. *Annalen der Physik*, 389(20):457–484, 1927. doi:10.1002/andp.19273892002.

[79] M. Born and R. Oppenheimer. On the Quantum Theory of Molecules (translation of *Zur Quantentheorie der Molekeln* by S. M. Binder, with emmendations by B. Sutcliffe and W. Geppert). *Annalen der Physik*, 389(20):457–484, 1927. URL: http://www.chm.bris.ac.uk/pt/manby/papers/bornop.pdf.

[80] F. T. Smith. Diabatic and Adiabatic Representations for Atomic Collision Problems. *Phys. Rev.*, 179:111–123, 1969. doi:10.1103/PhysRev.179.111.

[81] M. Baer. Introduction to the theory of electronic non-adiabatic coupling terms in molecular systems. *Physics Reports*, 358:75–142, 2002. doi:10.1016/S0370-1573(01)00052-7.

[82] M. Baer. Born-Oppenheimer Time-Dependent Systems: Perturbative vs Nonperturbative Diabatization. *J. Phys. Chem. A*, 107:4724–4730, 2003. doi:10.1021/jp022655n.

[83] M. Baer. *Beyond Born-Oppenheimer: Electronic Nonadiabatic Coupling Terms and Conical Intersections*. John Wiley & Sons, 2006.

[84] H.-J. Werner, P. J. Knowles, R. Lindh, F. R. Manby, M. Schütz, and al. MOLPRO, version 2006.1. A package of *ab initio* programs, 2006.

[85] G. Herzberg. *Molecular Spectra and Molecular Structure. I. Spectra of Diatomic molecules, Second Edition.* D. Van Nostrand Company, Inc., 1950. URL: https://archive.org/details/molecularspectra032774mbp.

[86] Hydra cluster at the HPC Computing Center (ULB/VUB). URL: https://cc.ulb.ac.be/hpc/hydra.php.

[87] E. Lewars. *Computational Chemistry - Introduction to the Theory and Applications of Molecular and Quantum Mechanics.* Kluwer Academic Publishers, 2004.

[88] T. H. Dunning. Gaussian Basis Set for use in correlated molecular calculations. I. The atoms Boron through Neon and Hydrogen. *J. Chem. Phys.*, 90:1007, 1988. doi:10.1063/1.456153.

[89] D. E. Woon and T. H. Dunning. Gaussian basis sets for use in correlated molecular calculations. IV. Calculation of static electrical response properties. *J. Chem. Phys.*, 100:2407–3371, 1994. doi:10.1063/1.466439.

[90] D. Feller. Application of systematic sequences of wave functions to the water dimer. *J. Chem. Phys.*, 96:6104–6114, 1992. doi:10.1063/1.462652.

[91] Z.-H. Li and M. W. Wong. Scaling of correlation basis set extension energies. *Chem. Phys. Lett.*, 337:209–216, 2001. doi:10.1016/S0009-2614(01)00188-9.

[92] C. De Boor. *A practical guide to splines.* Springer-Verlag, 1978.

[93] W. Eissner, M. Jones, and H. Nussbaumer. Techniques for the calculation of atomic structures and radiative data including relativistic corrections. *Comput. Phys. Comm.*, 8:270–306, 1974. doi:10.1016/0010-4655(74)90019-8.

[94] N. R. Badnell. Dielectronic recombination of Fe^{22+} and Fe^{21+}. *J. Phys. B: At. Mol. Phys.*, 19(22):3827, 1986. doi:10.1088/0022-3700/19/22/023.

[95] N. R. Badnell. On the effects of the two-body non-fine-structure operators of the Breit-Pauli Hamiltonian. *J. Phys. B: At. Mol. Opt. Phys.*, 30(1):1–11, 1997. doi:10.1088/0953-4075/30/1/005.

[96] E. Hille and T. D. Märk. Cross section for single and double ionization of carbon monoxide by electron impact from threshold up to 180 eV. *J. Chem. Phys.*, 69:4600, 1978. doi:10.1063/1.436411.

[97] S. Mazumdar, F. A. Rajgara, V. R. Marathe, C. Badrinathan, and D. Mathur. Formation of doubly charged CO^{2+} ions: a combined experimental and theoretical study. *J. Phys. B: At. Mol. Opt. Phys.*, 21:2815, 1988. doi:10.1088/0953-4075/21/16/007.

[98] G. Dawber, A. G. McConkey, L. Avaldi, M. A. MacDonald, G. C. King, and R. I. Hall. Threshold photoelectrons coincidence spectroscopy of doubly-charged ions of nitrogen, carbon monoxide, nitric oxide and oxygen. *J. Phys. B: At. Mol. Opt. Phys.*, 27:2191–2209, 1994. doi:10.1088/0953-4075/27/11/014.

[99] G. Dujardin, L. Hellner, M. Hamdan, A. G. Brenton, B. J. Olsson, and M. J. Besnard-Ramage. Quasibound electronic states of CO^{2+}. *J. Phys. B: At. Mol. Opt. Phys.*, 23:1165–1173, 1990. doi:10.1088/0953-4075/23/7/013.

[100] D. Mathur. Structure and dynamics of molecules in high charge states. *Physics Reports*, 391:1–118, 2004. doi:10.1016/j.physrep.2003.10.016.

[101] C. P. Safvan, M. J. Jensen, H. B. Pedersen, and L. H. Andersen. Dissociative recombination of the CO^{2+} dication. *Phys. Rev. A*, 60:R3361–R3364, 1999. doi:10.1103/PhysRevA.60.R3361.

[102] E. Wells, J. McKenna, A. M. Sayler, B. Jochim, N. Gregerson, R. Averin, M. Zohrabi, K. D. Carnes, and I. Ben-Itzhak. Closed-loop control of vibrational population in CO^{2+}. *J. Phys. B: At. Mol. Opt. Phys.*, 43:015101, 2010. doi:10.1088/0953-4075/43/1/015101.

[103] D. M. Reich and C. P. Koch. Cooling molecular vibrations with shaped laser pulses: optimal control theory exploiting the timescale separation between coherent excitation and spontaneous emission. *New J. Phys.*, 15:125028, 2013. doi:10.1088/1367-2630/15/12/125028.

[104] A. C. Hurley and V. W. Maslen. Potential Curves for Doubly Positive Diatomic Ions. *J. Chem. Phys.*, 34:1919, 1961. doi:10.1016/0022-2852(62)90209-6.

[105] T. Šedivcová, P. R. Žd'ánská, V. Špirko, and J. Fišer. Computed lifetimes of metastable states of CO^{2+}. *J. Chem. Phys.*, 124:214303, 2006. doi:10.1063/1.2198835.

[106] P. Kumar and N. Sathyamurthy. Potential energy curves for neutral and multiply charged carbon monoxide. *Pramana*, 74:49–55, 2010. doi:10.1007/s12043-010-0006-y.

[107] J. McKenna, A. M. Sayler, F. Anis, Nora G. Johnson, B. Gaire, U. Lev, M. A. Zohrabi, K. D. Carnes, B. D. Esry, and I. Ben-Itzhak. Vibrationally cold CO^{2+} in intense ultrashort laser pulses. *Phys. Rev. A*, 81(6):061401, Jun 2010. doi:10.1103/PhysRevA.81.061401.

[108] L. Veseth. Computed photoionization cross sections of CO^{+}. *J. Phys. B: At. Mol. Opt. Phys.*, 34:L773–L777, 2001. doi:10.1088/0953-4075/34/24/103.

[109] L. F. Errea, L. Fernàndez, A. Macìas, L. Méndez, I. Rabadàn, and A. Riera. Sign-consistent dynamical couplings between *ab initio* three-center wave functions. *J. Chem. Phys.*, 121:1663, 2004. doi:10.1063/1.1766010.

[110] E. J. Heller. Quantum corrections to classical photodissociation models. *J. Chem. Phys.*, 68:2066, 1977. doi:10.1063/1.436029.

[111] R. Schinke. *Photodissociation Dynamics - Spectroscopy and Fragmentation of Small Polyatomic Molecules*. Cambridge University Press, 1993.

[112] H. Guo and G. C. Schatz. Nonadiabatic effects in photodissociation dynamics: A quantum mechanical study of ICN photodissociation in the *A* continuum. *J. Chem. Phys.*, 92:1634, 1989. doi:10.1063/1.458097.

[113] Y. Zeiri, G. Katz, R. Kosloff, M. S. Topaler, D. G. Truhlar, and J. C. Polanyi. Quantum mechanism in the photodissociation of NaFH complex: a challenge to semiclassical analysis. *Chem. Phys. Lett.*, 300(5–6):523–528, 1999. doi:10.1016/S0009-2614(98)01411-0.

[114] H. Tal-Ezer and R. Kosloff. An accurate and efficient scheme for propagating the time dependent Schrödinger equation. *J. Chem. Phys.*, 81:3967, 1984. doi:10.1063/1.448136.

[115] N. Vaeck, M.-C. Bacchus-Montabonel, E. Baloïtcha, and M. Desouter-Lecomte. Time-dependent wave-packet treatment of the Si^{4+} + He collision. *Phys. Rev. A*, 63:042704, 2001. doi:10.1103/PhysRevA.63.042704.

[116] M. Ndong, H. Tal-Ezer, R. Kosloff, and C. P. Koch. A Chebychev propagator for inhomogeneous Schrödinger equations. *J. Chem. Phys.*, 130(12):124108, 2009. doi:10.1063/1.3098940.

[117] M. D. Feit, Jr. Fleck, and A. Steiger. Solution of the Schrödinger Equation by a Spectral Method. *J. Comput. Phys.*, 47:412–433, 1982. doi:10.1016/0021-9991(82)90091-2.

[118] J. Alvarellos and H. Metiu. The evolution of the wave function in a curve crossing problem computed by a fast Fourier transform method. *J. Chem. Phys.*, 88:4957, 1988. doi:10.1063/1.454707.

[119] J. F. Cornwell. *Group Theory in Physics*. Harcourt Brace & Company, 1997.

[120] D. J. Tannor. *Introduction to Quantum Mechanics: A Time-Dependent Perspective*. University Science Books, 2007.

[121] C. E. Shannon. Communication in the presence of noise. *Proc. Institute of Radio Engineers*, 37:10–21, 1949. doi:10.1109/JPROC.1998.659497.

[122] A. E. Garriz, A. Sztrajman, and D. Mitnik. Running into trouble with the time-dependent propagation of a wavepacket. *Eur. J. Phys.*, 31:785–799, 2010. doi:10.1088/0143-0807/31/4/008.

[123] R. Kosloff and D. Kosloff. Absorbing Boundaries for Wave Propagation Problems. *J. Comput. Phys.*, 63:363–376, 1986. doi:10.1016/0021-9991(86)90199-3.

[124] J. V. V. Kasper and G. C. Pimentel. Atomic Iodine Photodissociation Laser. *Appl. Phys. Lett.*, 5:231, 1964. doi:10.1063/1.1723603.

[125] K. P. Kirby. Photodissociation Processes in Diatomic Molecules of Astrophysical Interest. *Adv. At. Mol. Phys.*, 25:473–476, 1989. doi:10.1016/S0065-2199(08)60097-4.

[126] E. J. Heller. Photofragmentation of symmetric triatomic molecules: Time dependent picture. *J. Chem. Phys.*, 68:3891, 1978. doi:10.1063/1.436197.

[127] G. G. Balint-Kurti, R. N. Dixon, and C. Clay Marston. Time-dependent Quantum Dynamics of Molecular Photofragmentation Processes. *J. Chem. Soc. Faraday Trans.*, 86:1741–1749, 1990. doi:10.1039/FT9908601741.

[128] D. R. Bates. Rate of formation of molecules by radiative association. *Mon. Not. R. Astron. Soc.*, 111:303, 1951. doi:10.1111/j.1365-246X.1951.tb03008.x.

[129] C. M. Leung, E. Herbst, and W. F. Huebner. Synthesis of complex molecules in dense interstellar clouds via gas-phase chemistry. *Astrophys. J. Suppl. S.*, 56:231–256, 1984. doi:10.1086/190982.

[130] D. Gierlich and S. Horning. Experimental investigation of radiative association processes as related to interstellar chemistry. *Chem. Rev.*, 92(7):1509–1539, 1992. doi:10.1021/cr00015a003.

[131] R. Martinazzo and G. F. Tantardini. Testing wave packet dynamics in computing radiative association cross sections. *J. Chem. Phys.*, 122:094109, 2005. doi:10.1063/1.1857476.

[132] G. Barinovs and M. C. Van Hemert. CH^+ potential energy curves and photodissociation cross-section. *Chem. Phys. Lett.*, 399:406–411, 2004. doi:10.1016/j.cplett.2004.10.035.

[133] A. Hansson and J. K. G. Watson. A comment on Hönl-London factors. *J. Mol. Spectrosc.*, 233(2):169 – 173, 2005. doi:10.1016/j.jms.2005.06.009.

[134] D. Puy, V. Dubrovich, A. Lipovka, D. Talbi, and P. Vonlanthen. Molecular fluorine chemistry in the early Universe. *Astron. Astrophys.*, 476:685, 2007. doi:10.1051/0004-6361:20066934.

[135] W. P. Kraemer, V. Špirko, and M. Juřek. Formation of HeH^+ by radiative association of He^+ + H. An advanced *ab initio* study. *Chem. Phys. Lett.*, 236:177–183, 1995. doi:10.1016/0009-2614(95)00187-9.

[136] R. D. Levine. *Molecular Reaction Dynamics.* Cambridge University Press, 2005.

[137] M. I. Chibisov, F. B. Yousif, P. J. T. Van der Donk, and J. B. A. Mitchell. Radiative decay of the HeH^+ ($b\,^3\Sigma^+$) molecular ion. *Phys. Rev. A.*, 54:4997–5003, 1996. doi:10.1103/PhysRevA.54.4997.

[138] J. Loreau, S. Vranckx, M. Desouter-Lecomte, N. Vaeck, and A. Dalgarno. Photodissociation and radiative association of HeH^+ in the metastable triplet state. *J. Phys. Chem. A*, 117(39):9846–9492, 2013. doi:10.1021/jp312007q.

[139] A. J. Jerri. *The Gibbs Phenomenon in Fourier Analysis, Splines and Wavelet Approximations*. Springer, Kluwer Academic Publishers, 1998.

[140] S. J. Singer, K. F. Freed, and Y. B. Band. Low-energy resonances in photodissociation of CH^+. *Chem. Phys. Lett.*, 105:158, 1984. doi:10.1016/0009-2614(84)85640-7.

[141] N. Balakrishnan, B. D. Esry, and H. R. Sadeghpour. Quantum wave-packet dynamics of the photodissociation of LiF. *Phys. Rev. A.*, 60:1407, 1999. doi:10.1103/PhysRevA.60.1407.

[142] M. Desouter-Lecomte and J. Liévin. Memory kernels and effective Hamiltonians from time dependent methods. I. Predissociation with a curve crossing. *J. Chem. Phys.*, 107:1428, 1997. doi:10.1063/1.474497.

[143] E. F. van Dishoeck and R. Visser. Molecular photodissociation. In *Modern Concepts in Laboratory Astrochemistry*, chapter Molecular photodissociation. Springer, 2011. URL: http://arxiv.org/abs/1106.3917.

[144] M. Desouter-Lecomte, J. Liévin, and V. Brems. Avoided resonance overlapping beyond the energy independent formalism. I. Vibrational predissociation. *J. Chem. Phys.*, 103:4524, 1995. doi:10.1063/1.470641.

[145] S. Miyake, C. D. Gay, and P. C. Stancil. Rovibrationally resolved photodissociation of HeH^+. *Astrophys. J.*, 735:21, 2011. doi:10.1088/0004-637X/735/1/21.

[146] S. V. Antipov, T. Sjölander, G. Nyman, and M. Gustaffson. Rate coefficient of CN formation through radiative association: A theoretical study of quantum effects. *J. Chem. Phys.*, 131:074302, 2009. doi:10.1063/1.3196179.

[147] S. S. Bhattacharyya and D. Basu. Shape resonances and the photodissociation cross section of MgH near theshold. *Chem. Phys.*, 79:129–135, 1983. doi:10.1016/0301-0104(83)85145-3.

[148] G. Breit and E. Wigner. Capture of Slow Neutrons. *Phys. Rev.*, 49(7):519–531, 1936. doi:10.1103/PhysRev.49.519.

[149] R. A. Bain and J. N. Bardsley. Shape resonances in atom-atom collisions. I. Radiative association. *J. Phys. B: At. Mol. Phys.*, 5:277, 1972. doi:10.1088/0022-3700/5/2/024.

[150] G. W. F. Drake and R. R. Robbins. The Population of Helium Triplet States in Gaseous Nebulæ. *Astrophys. J.*, 171:55, 1972. doi:10.1086/151257.

[151] R. E. S. Clegg. Collisional effects in He I lines and helium abundances in planetary nebulæ. *Mon. Not. R. Astron. Soc.*, 229:31P–39P, 1987. URL: http://adsabs.harvard.edu/abs/1987MNRAS.229P..31C.

[152] N. Dudovich, D. Oron, and Y. Silberberg. Single-pulse coherently controlled nonlinear Raman spectroscopy and microscopy. *Nature*, 418:512–514, 2002. doi:10.1038/nature00933.

[153] I. Pastirk, J. Dela Cruz, K. A. Walowicz, V. V. Lozovoy, and M. Dantus. Selective two-photon microscopy with shaped femtosecond pulses. *Opt. Express*, 11(14):1695–1701, 2003. doi:10.1364/OE.11.001695.

[154] J. M. Dela Cruz, I. Pastirk, M. Comstock, V. V. Lozovoy, and M. Dantus. Use of coherent control methods through scattering biological tissue to achieve functional imaging. *Proc. Natl. Acad. Sci.*, 101(49):16996–17001, 2004. doi:10.1073/pnas.0407733101.

[155] L. Palliyaguru, J. Sloss, H. Rabitz, and R. J. Levis. Multicomponent control via shaped, strong laser fields mass spectrometry. *J. Mod. Opt.*, 55(1):177, 2008. doi:10.1080/09500340701350239.

[156] S. D. McGrane, R. J. Scharff, M. Greenfild, and S. D. Moore. Coherent control of multiple vibrational excitations for optimal detection. *New J. Phys.*, 11:105047, 2009. doi:10.1088/1367-2630/11/10/105047.

[157] R. S. Judson and H. Rabitz. Teaching Lasers to Control Molecules. *Phys. Rev. Lett.*, 68:1500, 1992. doi:10.1103/PhysRevLett.68.1500.

[158] H. Rabitz, R. de Vivie-Riedle, M. Motzkus, and K. Kompa. Whither the Future of Controlling Quantum Phenomena. *Science*, 288:824–828, 2000. doi:10.1126/science.288.5467.824.

[159] C. Daniel, J. Full, L. González, C. Lupulescu, J. Manz, A. Merli, Š. Vajda, and L. Wöste. Deciphering the Reaction Dynamics Underlying Optimal Control Laser Fields. *Science*, 299(5606):536–539, 2003. doi:10.1126/science.1078517.

[160] H. Rabitz. Shaped Laser Pulses as Reagents. *Science*, 299:525–527, 2003. doi:10.1126/science.1080683.

[161] R. Vijay, C. Macklin, D. H. Slichter, S. J. Weber, K. W. Murch, R. Naik, A. N. Korotkov, and I. Siddiqi. Stabilizing Rabi oscillations in a superconducting qubit using quantum feedback. *Nature*, 490:77–80, 2012. doi:10.1038/nature11505.

[162] G. A. Worth and G. W. Richting. Optimal control by computer. *Annu. Rep. Prog. Chem., Sect. C: Phys. Chem.*, 109:113, 2013. doi:10.1039/C3PC90003G.

[163] M. Holthaus and B. Just. Generalized π pulses. *Phys. Rev. A*, 49:1950–1960, 1994. doi:10.1103/PhysRevA.49.1950.

[164] U. Gaubatz, P. Rudecki, M. Becker, S. Schiemann, M. Külz, and K. Bergmann. Population switching between vibrational levels in molecular beams. *Chem. Phys. Lett.*, 149:463–468, 1988. doi:10.1016/0009-2614(88)80364-6.

[165] U. Gaubatz, P. Rudecki, S. Schiemann, and K. Bergmann. Population transfer between molecular vibrational levels by stimulated Raman scattering with partially overlapping laser fields. A new concept and experimental results. *J. Chem. Phys.*, 92:5363, 1990. doi:10.1063/1.458514.

[166] R. Kosloff, A. D. Hammerich, and D. J. Tannor. Excitation without demolition: Radiative excitation of ground-surface vibration by impulsive stimulated Raman scattering with damage control. *Phys. Rev. Lett.*, 69(15):2172–2175, 1992. doi:10.1103/PhysRevLett.69.2172.

[167] A. Bartana, R. Kosloff, and D. J. Tannor. Laser cooling of molecular internal degrees of freedom by a series of shaped pulses. *J. Chem. Phys.*, 99:196, 1993. doi:10.1063/1.465797.

[168] V. Engel, C. Meier, and D. J. Tannor. Local control theory: recent applications to energy and particle transfer processes in molecules. *Adv. Chem. Phys.*, 141:29–101, 2009. doi:10.1002/9780470431917.ch2.

[169] S. Gräfe, C. Meier, and V. Engel. Instantaneous dynamics and quantum control fields: Principle and numerical applications. *J. Chem. Phys.*, 122:184103, 2005. doi:10.1063/1.1891728.

[170] P. Marquetand and V. Engel. Predissociation and dissociation dynamics in quantum control fields. *Chem. Phys. Lett.*, 407(4–6):471–476, 2005. doi:10.1016/j.cplett.2005.03.136.

[171] T. Penfold, G. Worth, and C. Meier. Local control of multidimensional dynamics. *Phys. Chem. Chem. Phys.*, 12:15616–15627, 2010. doi:10.1039/C003768K.

[172] N. E. Henriksen and E. J. Heller. Gaussian wave packet dynamics and scattering in the interaction picture. *Chem. Phys. Lett.*, 148(6):567–571, 1988. doi:10.1016/0009-2614(88)80332-4.

[173] V. Engel and H. Metiu. The relative kinetic energy distribution of the hydrogen atoms formed by the dissociation of the electronically excited H_2 molecule. *J. Chem. Phys.*, 89:1986, 1988. doi:10.1063/1.455096.

[174] A. Z. Capri. *Nonrelativistic Quantum Mechanics*. World Scientific Publishing, edition edition, 2002.

[175] R. B. Vrijen, G. M. Lankhuijzen, and L. D. Noordam. Delayed Electron Emission in the Ionization of Rydberg Atoms with Half-Cycle THz Pulses. *Phys. Rev. Lett.*, 79, 1997. doi:10.1103/PhysRevLett.79.617.

[176] C. Wesdorp, F. Robicheaux, and L. D. Noordam. Displacing Rydberg Electrons: The Mono-Cycle Nature of Half-Cycle THz Pulses. *Phys. Rev. Lett.*, 87(8):083001, 2001. doi:10.1103/PhysRevLett.87.083001.

[177] D. Sugny, A. Keller, O. Atabek, D. Daems, S. Guérin, and H. R. Jauslin. Time-dependent unitary perturbation theory for intense laser-driven molecular orientation. *Phys. Rev. A*, 69:043407, 2004. doi:10.1103/PhysRevA.69.043407.

[178] C.-C. Shu, T. Rozgonyi, L. González, and N. E. Henriksen. A theoretical investigation of the feasibility of Tannor-Rice type control: Application to selective bond breakage in gas-phase dihalomethanes. *J. Chem. Phys.*, 136:174303, 2012. doi:10.1063/1.4706603.

[179] D. Sugny, S. Vranckx, M. Ndong, N. Vaeck, O. Atabek, and M. Desouter-Lecomte. Optimal control of molecular dynamics with zero-area fields: Application to molecular orientation and photofragmentation. *Phys. Rev. A (Submitted)*, 2014.

[180] D. Sugny, S. Vranckx, M. Ndong, O. Atabek, and M. Desouter-Lecomte. External constraints on optimal control strategies in molecular orientation and photofragmentation: role of zero-area fields. *J. Mod. Opt.*, 2013. doi:10.1080/09500340.2013.844281.

[181] L. S. Pontryagin. Classics of Soviet Mathematics – L. S. Pontryagin Selected Works in Four Volumes. In *The Mathematical Theory of Optimal Processes*, volume 4. CRC Press, 1987.

[182] A. E. Bryson. Optimal control – 1950 to 1985. *Control Systems, IEEE*, 16(3):26–33, 1996. doi:10.1109/37.506395.

[183] R. Kosloff, S. A. Rice, P. Gaspard, and S. Tersigni. Wavepacket dancing: Achieving chemical selectivity by shaping light pulses. *Chemical Physics*, 139(1):201, 1989. doi:10.1016/0301-0104(89)90012-8.

[184] W. Zhu, J. Botina, and H. Rabitz. Rapidly convergent iteration methods for optimal control population. *J. Chem. Phys.*, 108:1953, 1998. doi:10.1063/1.475576.

[185] D. Babikov. Accuracy of gates in a quantum computer based on vibrational eigenstates. *J. Chem. Phys.*, 121(16):7577, 2004. doi:10.1063/1.1791635.

[186] K. Sundermann and R. de Vivie-Riedle. Extensions to quantum optimal control algorithms and applications to special problems in state selective molecular dynamics. *J. Chem. Phys.*, 110:1896, 1999. doi:10.1063/1.477856.

[187] S. E. Sklarz and D. J. Tannor. Loading a Bose-Einstein condensate onto an optical lattice: An application of optimal control theory to the nonlinear Schrödinger equation. *Phys. Rev. A*, 66:053619, 2002. doi:10.1103/PhysRevA.66.053619.

[188] D. M. Reich, M. Ndong, and C. P. Koch. Monotonically convergent optimization in quantum control using Krotov's method. *J. Chem. Phys.*, 136:104103, 2012. doi:10.1063/1.3691827.

[189] J. P. Palao and R. Kosloff. Quantum Computing by an Optimal Control Algorithm for Unitary Transformations. *Phys. Rev. Lett.*, 89:188301, 2002. doi:10.1103/PhysRevLett.89.188301.

[190] C. M. Tesch and R. de Vivie-Riedle. Quantum Computation with Vibrationally Excited Molecules. *Phys. Rev. Lett.*, 89:157901, 2002. doi:10.1103/PhysRevLett.89.157901.

[191] C. M. Tesch and R. de Vivie-Riedle. Vibrational molecular quantum computing: Basis set independence and theoretical realization of the Deutsch-Jozsa algorithm. *J. Chem. Phys.*, 121:12158, 2004. doi:10.1063/1.1818131.

[192] J. P. Palao and R. Kosloff. Optimal control theory for unitary transformations. *Phys. Rev. A*, 68:062308, 2003. doi:10.1103/PhysRevA.68.062308.

[193] A. Jaouadi, E. Barrez, Y. Justum, and M. Desouter-Lecomte. Quantum gates in hyperfine levels of ultracold alkali dimers by revisiting constrained-phase optimal control design. *J. Chem. Phys.*, 139:041310, 2013. doi:10.1063/1.4812317.

[194] J. Werschnik and E. K. U. Gross. Tailoring laser pulses with spectral and fluence constraints using optimal control theory. *J. Opt. B*, 7(10):S300, 2005. doi:10.1088/1464-4266/7/10/014.

[195] J. Werschnik and E. K. U. Gross. Quantum optimal control theory. *J. Phys. B: At. Mol. Opt. Phys.*, 40(18):R175–R211, 2007. doi:doi:10.1088/0953-4075/40/18/R01.

[196] C. P. Koch, J. P. Palao, R. Kosloff, and F. Masnou-Seeuws. Stabilization of ultracold molecules using optimal control theory. *Phys. Rev. A*, 70:013402, 2004. doi:10.1103/PhysRevA.70.013402.

[197] V. S. Malinovsky, C. Meier, and D. J. Tannor. Optical paralysis in electronically congested systems: application to large-amplitude vibrational motion of ground state N_2. *Chem. Phys.*, 221:67–76, 1997. doi:10.1016/S0301-0104(97)00126-2.

[198] J. P. Palao, R. Kosloff, and C. P. Koch. Protecting coherence in optimal control theory: State-dependent constraint approach. *Phys. Rev. A*, 77:063412, 2008. doi:10.1103/PhysRevA.77.063412.

[199] C. Gollub, M. Kowalewski, and R. de Vivie-Riedle. Monotonic Convergent Optimal Control Theory with Strict Limitations on the Spectrum of Optimized Laser Fields. *Phys. Rev. Lett.*, 101:073002, 2008. doi:10.1103/PhysRevLett.101.073002.

[200] T. Hornung, M. Motzkus, and R. de Vivie-Riedle. Teaching optimal control theory to distill robust pulses even under experimental constraints. *Phys. Rev. A*, 65:021403(R), 2006. doi:10.1103/PhysRevA.65.021403.

[201] M. Le Bellac. *A Short Introduction to Quantum Information and Quantum Computation*. Cambridge University Press, 2006.

[202] R. Feynman. Simulating Physics with Computers. *International Journal of Theoretical Physics*, 21:467–488, 1982. doi:10.1007/BF02650179.

[203] G. Epstein, G. Frieder, and D. C. Rine. The development of multiple-valued logic as related to computer science. *Computer*, 7(9):20–32, 1974. doi:10.1109/MC.1974.6323304.

[204] R. Cleve, A. Ekert, C. Macchiavello, and M. Mosca. Quantum algorithms revisited. *Proc. R. Soc. Lond. A*, 454(1969):339, 1988. doi:10.1098/rspa.1998.0164.

[205] S. Ding and Z. Jin. Review on the study of entanglement in quantum computation speedup. *Chin. Sci. Bull.*, 52:2161–2166, 2007. doi:10.1007/s11434-007-0324-8.

[206] A. M. Nielsen and I. L. Chuang. *Quantum Computation and Quantum Information*. Cambridge University Press, 10th anniversary edition, 2010.

[207] J. Smith and M. Mosca. *Handbook of Natural Computing*, chapter Algorithms for Quantum Computers, page 1451. Springer Berlin Heidelberg, 2012. doi:10.1007/978-3-540-92910-9_43.

[208] D. Deutsch. Quantum Theory, the Church–Turing Principle and the Universal Quantum Computer. *Proc. R. Soc. Lond. A*, 400(1818):97, 1985. doi:10.1098/rspa.1985.0070.

[209] D. Deutsch and R. Jozsa. Rapid solutions of problems by quantum computation. *Proc. R. Soc. Lond. A*, 439(1907):553, 1992. doi:10.1098/rspa.1992.0167.

[210] P. W. Shor. Polynomial-Time Algorithms for Prime Factorization and Discrete Logarithms on a Quantum Computer. *SIAM J. Sci. Statist. Comput.*, 26:1484, 1997. doi:10.1137/S0097539795293172.

[211] R. L. Rivest, A. Shamir, and L. Adleman. A Method for Obtaining Digital Signatures and Public-Key Cryptosystems. *Communications of the ACM*, 21(2):120, 1978. doi:10.1145/359340.359342.

[212] S. Rich and B. Gellman. NSA seeks to build quantum computer that could crack most types of encryption. *The Washington Post*, Feb. 2014. URL: http://tinyurl.com/kgsktr8.

[213] D. R. Simon. On the Power of Quantum Computation. *Proc. 35th IEEE Symp. on Foundations of Computer Science*, 26(5):1474, 1994. doi:10.1109/SFCS.1994.365701.

[214] S. Hallgren. Polynomial-time quantum algorithms for Pell's equation and the principal ideal problem. *Proc. 34th ACM Symposium on Theory of Computing*, 54(1):653–658, 2002. doi:10.1145/509907.510001.

[215] G. Brassard, P. Hoyer, and A. Tapp. Quantum counting. In *Automata, Languages and Programming – 25th International Colloquium, ICALP'98 Aalborg, Denmark, July 13Ű17, 1998 Proceedings*, volume 1443 of *Lecture Notes in Computer Science*, pages 820–831. Springer Berlin Heidelberg, 1998. doi:10.1007/BFb0055105.

[216] S. Jordan. Quantum Algorithm Zoo, March 2014. URL: http://math.nist.gov/quantum/zoo/.

[217] A. M. Childs and W. van Dam. Quantum algorithms for algebraic problems. *Rev. Mod. Phys.*, 82(1):1, 2010. doi:10.1103/RevModPhys.82.1.

[218] L. K. Grover. Quantum Mechanics Helps in Searching for a Needle in a Haystack. *Phys. Rev. Lett.*, 79:325, 1997. doi:10.1103/PhysRevLett.79.325.

[219] C. Zalka. Grover's quantum searching algorithm is optimal. *Phys. Rev. A*, 60(4):2746–2751, 1999. doi:10.1103/PhysRevA.60.2746.

[220] C. P. Williams. *Explorations in Quantum Computing*. Springer London, 2011. doi:10.1007/978-1-84628-887-6.

[221] M. Boyer, G. Brassard, P. Hoyer, and A. Tapp. Tight bounds on quantum searching. *Fortsch. Phys.*, 46(4-5):493–506, 1998. doi:10.1002/(SICI)1521-3978(199806)46:4/5<493::AID-PROP493>3.0.CO;2-P.

[222] P. W. Shor. Scheme for reducing decoherence in quantum computer memory. *Phys. Rev. A*, 52(4):R2493–R2496, 1995. doi:10.1103/PhysRevA.52.R2493.

[223] J. Preskill. Reliable quantum computers. *Proc. R. Soc. Lond. A*, 454(1969):385–410, 1998. doi:10.1098/rspa.1998.0167.

[224] R. Raussendorf. Key ideas in quantum error correction. *Phil. Trans. R. Soc. A*, 370(28):4541–4565, 2012. doi:10.1098/rsta.2011.0494.

[225] S. J. Devitt, W. J. Munro, and K. Nemoto. Quantum error correction for beginners. *Rep. Prog. Phys.*, 76:076001, 2013. doi:10.1088/0034-4885/76/7/076001.

[226] D. D. Bhaktavatsala Rao and K. Molmer. Effect of qubit losses on Grover's quantum search algorithm. *Phys. Rev. A*, 86(4):042321, 2012. doi:10.1103/PhysRevA.86.042321.

[227] G. Brassard, P. Hoyer, and A. Tapp. Quantum cryptanalysis of hash and claw-free functions. In *Lecture Notes in Computer Science – Third Latin American Symposium Campinas, Brazil, April 20Ű24, 1998 Proceedings*, volume 1380 of *Lecture Notes in Computer Science*, pages 163–169. Springer Berlin Heidelberg, 1998. doi:10.1007/BFb0054319.

[228] N. J. Cerf, L. K. Grover, and C. P. Williams. Nested quantum search and structured problems. *Phys. Rev. A*, 61(3):032303, 2000. doi:10.1103/PhysRevA.61.032303.

[229] H. Buhrman, C. Durr, M. Heiligman, P. Hoyer, F. Magniez, M. Santha, and R. de Wolf. Quantum algorithms for element distinctness. *Computational Complexity, 16th Annual IEEE Conference*, pages 131–137, 2001. doi:10.1109/CCC.2001.933880.

[230] L.-Y. Hsu. Quantum secret-sharing protocol based on Grover's algorithm. *Phys. Rev. A*, 68(2):022306, 2003. doi:10.1103/PhysRevA.68.022306.

[231] A. Berzina, A. Dubrovsky, R. Freivalds, L. Lace, and O. Scegulnaja. Quantum Query Complexity for Some Graph Problems. In *SOFSEM 2004: Theory and Practice of Computer Science – 30th Conference on Current Trends in Theory and Practice of Computer Science*, volume 2932 of *Lecture Notes in Computer Science*, pages 140–150. Springer Berlin Heidelberg, 2004. doi:10.1007/978-3-540-24618-3_11.

[232] A. Ambainis and R. Spalek. Quantum Algorithms for Matching and Network Flows. In Springer Berlin Heidelberg, editor, *STACS 2006 – 23rd Annual Symposium on Theoretical Aspects of Computer Science*, volume 3884 of *Lecture Notes in Computer Science*, pages 172–183. Springer Berlin Heidelberg, 2006. doi:10.1007/11672142_13.

[233] M. Udrescu, L. Prodan, and M. Vladutiu. Implementing quantum genetic algorithms: a solution based on Grover's algorithm. *CF '06 – Proceedings of the 3rd conference on Computing frontiers*, pages 71–72, 2006. doi:10.1145/1128022.1128034.

[234] I. L. Chuang, N. Gershenfeld, and M. Kubinec. Experimental Implementation of Fast Quantum Searching. *Phys. Rev. Lett.*, 80(15):3408, 1998. doi:10.1103/PhysRevLett.80.3408.

[235] L. M. K. Vandersypen, M. Steffen, M. H. Sherwood, C. S. Yannoni, G. Breyta, and I. L. Chuang. Implementation of a three-quantum-bit search algorithm. *Appl. Phys. Lett.*, 76(5):646–648, 2000. doi:10.1063/1.125846.

[236] R. Das, T. S. Mahesh, and A. Kumar. Experimental implementation of Grover's search algorithm using efficient quantum state tomography. *Chem. Phys. Lett.*, 369(1–2):8–15, 2003. doi:10.1016/S0009-2614(02)01895-X.

[237] K.-A. Brickman, P. C. Haljan, P. J. Lee, M. Acton, L. Deslauriers, and C. Monroe. Implementation of Grover's quantum search algorithm in a scalable system. *Phys. Rev. A*, 72(5):050306(R), 2005. doi:10.1103/PhysRevA.72.050306.

[238] P. Walther, K. J. Resch, T. Rudolph, E. Schenck, H. Weinfurter, V. Vedral, M. Aspelmeyer, and A. Zeilinger. Experimental one-way quantum computing. *Nature*, 434:169–176, 2005. doi:10.1038/nature03347.

[239] L. DiCarlo, J. M. Chow, J. M. Gambetta, L. S. Bishop, B. R. Johnson, D. I. Schuster, J. Majer, A. Blais, S. M. Girvin, and R. J. Schoelkopf. Demonstration of two-qubit algorithms with a superconducting quantum processor. *Nature*, 460:240, 2009. doi:10.1038/nature08121.

[240] G. L. Long and L. Xiao. Experimental realization of a fetching algorithm in a 7-qubit NMR spin Liouville space computer. *J. Chem. Phys.*, 119(16):8473, 2003. doi:10.1063/1.1611177.

[241] D. P. DiVincenzo. The Physical Implementation of Quantum Computation. *Fortsch. Phys.*, 48:771–784, 2000. doi:10.1002/1521-3978(200009)48:9/11<771::AID-PROP771>3.0.CO;2-E.

[242] D. S. Abrams and S. Lloyd. Quantum Algorithm Providing Exponential Speed Increase for Finding Eigenvalues and Eigenvectors. *Phys. Rev. Lett.*, 83(24):5162, 1999. doi:10.1103/PhysRevLett.83.5162.

[243] A. Aspuru-Guzik, A. D. Dutoi, P. J. Love, and M. Head-Gordon. Simulated Quantum Computation of Molecular Energies. *Science*, 309(5741):1704–1707, 2005. doi:10.1126/science.1113479.

[244] B. P. Lanyon, J. D. Whitfield, G. G. Gillett, M. E. Goggin, M. P. Almeida, I. Kassal, J. D. Biamonte, M. Mohseni, B. J. Powell, M. Barbieri, A. Aspuru-Guzik, and A. G. White. Towards quantum chemistry on a quantum computer. *Nature Chemistry*, 2:106, 2009. doi:10.1038/nchem.483.

[245] J. A. Smolin, G. Smith, and A. Vargo. Oversimplifying quantum factoring. *Nature*, 499:163, 2013. doi:10.1038/nature12290.

[246] W. S. Warren. The Usefulness of NMR Quantum Computing. *Science*, 277:1688–1690, 1997. doi:10.1126/science.277.5332.1688.

[247] S. L. Braunstein, C. M. Caves, R. Jozsa, N. Linden, S. Popescu, and R. Schack. Separability of Very Noisy Mixed States and Implications for NMR Quantum Computing. *Phys. Rev. Lett.*, 83(5):1054–1057, 1999. doi:10.1103/PhysRevLett.83.1054.

[248] N. C. Menicucci and C. M. Caves. Local Realistic Model for the Dynamics of Bulk-Ensemble NMR Information Processing. *Phys. Rev. Lett.*, 88(16):167901, 2002. doi:10.1103/PhysRevLett.88.167901.

[249] A. Shnirman, G. Schön, and Z. Hermon. Quantum Manipulations of Small Josephson Junctions. *Phys. Rev. Lett.*, 79(12):2371–2374, 1997. doi:10.1103/PhysRevLett.79.2371.

[250] J. Clarke and F. K. Wilhelm. Superconducting quantum bits. *Nature*, 453:1031–1042, 2008. doi:10.1038/nature07128.

[251] J. L. O'Brien. Optical Quantum Computing. *Science*, 318(2):1567–1570, 2007. doi:10.1126/science.1142892.

[252] C. Adami and N. Cerf. Quantum Computation with Linear Optics. *Quantum Computing and Quantum Communications*, 1509:391, 1999. doi:10.1007/3-540-49208-9_36.

[253] E. Knill, R. Laflamme, and G. J. Milburn. A scheme for efficient quantum computation with linear optics. *Nature*, 409:46–52, 2001. doi:10.1038/35051009.

[254] J. I. Cirac and P. Zoller. Quantum Computations with Cold Trapped Ions. *Phys. Rev. Lett.*, 74(20):4091–4094, 1995. doi:10.1103/PhysRevLett.74.4091.

[255] T. Monz, P. Schindler, J. T. Barreiro, M. Chwalla, D. Nigg, W. A. Coish, M. Harlander, W. Hänsel, M. Hennrich, and R. Blatt. 14-Qubit Entanglement: Creation and Coherence. *Phys. Rev. Lett.*, 106:130506, 2011. doi:10.1103/PhysRevLett.106.130506.

[256] H. Häffner, C. F. Roos, and R. Blatt. Quantum computing with trapped ions. *Phys. Rep.*, 469(4):155–203, 2008. doi:10.1016/j.physrep.2008.09.003.

[257] D. Kielpinski, C. Monroe, and D. J. Wineland. Architecture for a large-scale ion-trap quantum computer. *Nature*, 417:709–711, 2002. doi:10.1038/nature00784.

[258] J. Chiaverini, J. Britton, D. Leibfried, E. Knill, M. D. Barret, R. . Blakestad, W. M. Itano, J. D. Jost, C. Langer, R. Ozeri, T. Schaetz, and J. D. Wineland. Implementation of the Semiclassical Quantum Fourier Transform in a Scalable System. *Science*, 308(5724):997–1000, 2005. doi:10.1126/science.1110335.

[259] D. Leibfried, E. Knill, S. Seidelin, J. Britton, R. B. Blakestad, J. Chiaverini, D. B. Hume, W. M. Itano, J. D. Jost, C. Langer, R. Ozeri, R. Reichle, and D. J. Wineland. Creation of a six-atom “Schrödinger cat" state. *Nature*, 438:639–642, 2005. doi:10.1038/nature04251.

[260] M. Anderlini, P. J. Lee, B. L. Brown, J. Sebby-Strabley, W. D. Phillips, and J. V. Porto. Controlled exchange interaction between pairs of neutral atoms in an optical lattice. *Nature*, 448:452–456, 2007. doi:10.1038/nature06011.

[261] C. Monroe and K. Jim. Scaling the Ion Trap Quantum Processor. *Science*, 339(6124):1164–1169, 2013. doi:10.1126/science.1231298.

[262] C. Monroe, R. Raussendorf, A. Ruthven, K. R. Brown, P. Maunz, L.-M. Duan, and J. Kim. Large-scale modular quantum-computer architecture with atomic memory and photonic interconnects. *Phys. Rev. A*, 89:022317, 2014. doi:10.1103/PhysRevA.89.022317.

[263] J. Roland and N. J. Cerf. Quantum search by local adiabatic evolution. *Phys. Rev. A*, 65(4):042308, 2002. doi:10.1103/PhysRevA.65.042308.

[264] R. Raussendorf and H. J. Briegel. A One-Way Quantum Computer. *Phys. Rev. Lett.*, 86(22):5188–5191, 2001. doi:10.1103/PhysRevLett.86.5188.

[265] R. W. Ogburn and J. Preskill. Topological Quantum Computation. *Lecture Notes in Computer Science*, 1509:341–356, 1999. doi:10.1007/3-540-49208-9_31.

[266] D–Wave, The Quantum Computing Company™, official website. URL: http://www.dwavesys.com/en/products-services.html.

[267] S. Aaronson. *Shtetl-Optimized*, the blog of Scott Aaronson, results of a search for all article concerning D-Wave. URL: http://www.scottaaronson.com/blog/?s=d-wave.

[268] T. F. Ronnow, Z. Wang, J. Job, S. Boixo, S. V. Isakov, D. Wecker, J. M. Martinis, D. A. Lidar, and M. Troyer. Defining and detecting quantum speedup. *arXiv:1401.3629*, 2014. URL: http://arxiv.org/abs/1401.2910.

[269] S. Aaronson. *Shtetl-Optimized*, the blog of Scott Aaronson, *My response to M. I. Dyakonov*. URL: http://www.scottaaronson.com/blog/?p=1211.

[270] M. I. Dyakonov. Prospects for quantum computing: extremely doubtful. *arXiv:1401.3629*, 2014. URL: http://arxiv-web3.library.cornell.edu/abs/1401.3629.

[271] C. M. Tesch, L. Kurtz, and R. de Vivie-Riedle. Applying optimal control theory for elements of quantum computation in molecular systems. *Chem. Phys. Lett.*, 343:633–641, 2001. doi:10.1016/S0009-2614(01)00748-5.

[272] E. A. Shapiro, I. Khavkine, M. Spanner, and M. Y. Ivanov. Strong-field molecular alignment for quantum logic and quantum control. *Phys. Rev. A*, 67(1):013406, 2003. doi:10.1103/PhysRevA.67.013406.

[273] M. Ndong, L. Bomble, D. Sugny, Y. Justum, and M. Desouter-Lecomte. NOT gate in a cis-trans photoisomerization model. *Phys. Rev. A.*, 76:043424, 2007. doi:10.1103/PhysRevA.76.043424.

[274] K. Mishima, K. Tokumo, and K. Yamashita. Quantum computing using molecular electronic and vibrational states. *Chemical Physics*, 343:61–75, 2008. doi:10.1016/j.chemphys.2007.10.027.

[275] Y. Ohtsuki. Simulating quantum search algorithm using vibronic states of I_2 manipulated by optimally designed gate pulses. *New J. Phys.*, 12:045002, 2010. doi:10.1088/1367-2630/12/4/045002.

[276] B. M. R. Korff, U. Troppmann, K. L. Kompa, and R. de Vivie-Riedle. Manganese pentacarbonyl bromide as candidate for a molecular qubit system operated in the infrared regime. *J. Chem. Phys.*, 123:244509, 2005. doi:10.1063/1.2141615.

[277] Y. Ohtsuki. Simulating the Deutsch-Jozsa algorithm using vibrational states of I_2 excited by optimally designed gate pulses. *Chem. Phys. Lett.*, 404(1–3):126–131, 2005. doi:10.1016/j.cplett.2005.01.080.

[278] S. Suzuki, K. Mishima, and K. Yamashita. *Ab initio* study of optimal control of ammonia molecular vibrational wavepackets : Towards molecular quantum computing. *Chem. Phys. Lett.*, 410(4–6):358–364, 2005. doi:10.1016/j.cplett.2005.05.090.

[279] Y. Teranishi, Y. Ohtsuki, K. Hosaka, H. Chiba, H. Katsuki, and K. Ohmori. Implementation of quantum gate operations in molecules with weak laser fields. *J. Chem. Phys.*, 124:114110, 2006. doi:10.1063/1.2172605.

[280] C. Gollub, U. Troppmann, and R. de Vivie-Riedle. The role of anharmonicity and coupling in quantum computing based on vibrational qubits. *New J. Phys.*, 8(4):48, 2006. doi:10.1088/1367-2630/8/4/048.

[281] K. Shioya, K. Mishima, and K. Yamashita. Quantum computing using molecular vibrational and rotational modes. *Mol. Phys.*, 105(9):1283, 2007. doi:10.1016/j.chemphys.2009.11.007.

[282] D. Weidinger and M. Gruebele. Quantum computation with vibrationally excited polyatomic molecules: effects of rotation, level structure and field gradients. *Mol. Phys.*, 105:1999–2008, 2007. doi:10.1080/00268970701504335.

[283] D. Weidinger and M. Gruebele. Simulations of quantum computation with a molecular ion. *Chemical Physics*, 350:139–144, 2008. doi:10.1016/j.chemphys.2008.01.059.

[284] D. Sugny, L. Bomble, T. Ribeyre, O. Dulieu, and M. Desouter-Lecomte. Rovibrational controlled-NOT gates using optimized stimulated Raman adiabatic passage techniques and optimal control theory. *Phys. Rev. A.*, 80:042325, 2009. doi:10.1103/PhysRevA.80.042325.

[285] K. Mishima and K. Yamashita. Quantum computing using molecular vibrational and rotational modes of the open-shell $^{14}N^{16}O$ molecule. *Chemical Physics*, 367:63–74, 2010. doi:10.1016/j.chemphys.2009.11.007.

[286] R. R. Zaari and A. Brown. Effect of diatomic molecular properties on binary laser pulse optimizations of quantum gate operations. *J. Chem. Phys.*, 135:044317, 2011. doi:10.1063/1.3617248.

[287] E. Berrios, M. Gruebele, D. Shyshlov, L. Wang, and D. Babikov. High Fidelity Quantum Gates with Vibrational Qubits. *J. Phys. Chem. A*, 116:11347–11354, 2012. doi:10.1021/jp3055729.

[288] E. Kuznetsova, M. Gacesa, S. F. Yelin, and R. Côté. Phase gate and readout with an atom-molecule hybrid platform. *Phys. Rev. A*, 81:030301(R), 2010. doi:10.1103/PhysRevA.81.030301.

[289] P. Rabl, D. DeMille, J. M. Doyle, M. D. Lukin, R. J. Schoelkopf, and P. Zoller. Hybrid Quantum Processors: Molecular Ensembles as Quantum Memory for Solid State Circuits. *Phys. Rev. Lett.*, 97(3):033003, 2006. doi:10.1103/PhysRevLett.97.033003.

[290] S. Lloyd. Obituary: Rolf Landauer (1927-99). *Nature*, 400:720, 1999. doi:10.1038/23376.

[291] E. Kuznetsova, R. Côté, K. Kirby, and S. F. Yelin. Analysis of experimental feasibility of polar-molecule-based phase gates. *Phys. Rev. A*, 78(1):012313, 2008. doi:10.1103/PhysRevA.78.012313.

[292] W. C. Stwalley and H. Wang. Photoassociation of Ultracold Atoms: A New Spectroscopic Technique. *J. Mol. Spectrosc.*, 195(2):194–228, 1999. doi:10.1006/jmsp.1999.7838.

[293] A. J. Kerman, J. M. Sage, S. Sainis, T. Bergeman, and D. DeMille. Production and State-Selective Detection of Ultracold RbCs Molecules. *Phys. Rev. Lett.*, 92(15):153001, 2004. doi:10.1103/PhysRevLett.92.153001.

[294] D. Wang, J. Qi, M. F. Stone, O. Nikolayeva, H. Wang, B. Hattaway, S. D. Gensemer, P. L. Gould, E. E. Eyler, and W. C. Stwalley. Photoassociative Production and Trapping of Ultracold KRb Molecules. *Phys. Rev. Lett.*, 93(24):243005, 2005. doi:10.1103/PhysRevLett.93.243005.

[295] C. A. Regal, C. Ticknor, J. L. Bohn, and D. S. Jin. Creation of ultracold molecules from a Fermi gas of atoms. *Nature*, 424:47–50, 2003. doi:10.1038/nature01738.

[296] C. A. Stan, M. W. Zwierlein, C. H. Schunck, S. M. F. Raupach, and W. Ketterle. Observation of Feshbach Resonances between Two Different Atomic Species. *Phys. Rev. Lett.*, 93(14):143001, 2004. doi:10.1103/PhysRevLett.93.143001.

[297] K. M. Jones, E. Tiesinga, P. D. Lett, and P. S. Julienne. Ultracold photoassociation spectroscopy: Long-range molecules and atomic scattering. *Rev. Mod. Phys.*, 78(2):483–535, 2006. doi:10.1103/RevModPhys.78.483.

[298] T. Köhler, K. Góral, and P. S. Julienne. Production of cold molecules via magnetically tunable Feshbach resonances. *Rev. Mod. Phys.*, 78(4):1311–1361, 2006. doi:10.1103/RevModPhys.78.1311.

[299] P. Pellegrini, S. Vranckx, and M. Desouter-Lecomte. Implementing quantum algorithms in hyperfine levels of ultracold polar molecules by optimal control. *Physical Chemistry Chemical Physics*, 13:18864–18871, 2011. doi:10.1039/C1CP21184F.

[300] L. D. Carr, D. DeMille, R. V. Krems, and J. Ye. Cold and ultracold molecules: science, technology and applications. *New J. Phys.*, 11:055049, 2009. doi:10.1088/1367-2630/11/5/055049.

[301] G. Quéméner and P. S. Julienne. Ultracold Molecules under Control! *Chem. Rev.*, 112(9):4949, 2012. doi:10.1021/cr300092g.

[302] T. Takekoshi, B. M. Patterson, and R. J. Knize. Observation of Optically Trapped Cold Cesium Molecules. *Phys. Rev. Lett.*, 81(23):5105–5108, 1998. doi:10.1103/PhysRevLett.81.5105.

[303] D. L. Bryce and R. E. Wasylishen. Microwave Spectroscopy and Nuclear Magnetic Resonance Spectroscopy – What Is the Connection? *Acc. Chem. Res.*, 36:327–334, 2003. doi:10.1021/ar020271+.

[304] J. Aldegunde, B. A. Rivington, P. S. Zuchowski, and J. M. Hutson. Hyperfine energy levels of alkali-metal dimers: Ground-state polar molecules in electric and magnetic fields. *Phys. Rev. A*, 78(3):033434, 2008. doi:10.1103/PhysRevA.78.033434.

[305] J. R. Eshbach and M. W. P. Strandberg. Rotational Magnetic Moments of $^1\Sigma$ Molecules. *Phys. Rev.*, 85:24–34, 1952. doi:10.1103/PhysRev.85.24.

[306] S. P. A. Sauer. A relation between the rotational g-factor and the electric dipole moment of a diatomic molecule. *Chem. Phys. Lett.*, 297:475–483, 1998. doi:10.1016/S0009-2614(98)01157-9.

[307] M. L. Wall and L. D. Carr. Dipole-dipole interactions in optical lattices do not follow an inverse cube power law. *New J. Phys.*, 15:123005, 2013. doi:10.1088/1367-2630/15/12/123005.

[308] J. Deiglmayr, M. Aymar, R. Wester, M. Weidemüller, and O. Dulieu. Calculations of static dipole polarizabilities of alkali dimers: Prospects for alignment of ultracold molecules. *J. Chem. Phys.*, 129:064309, 2008. doi:10.1063/1.2960624.

[309] C. Cohen-Tannoudji, B. Diu, and F. Laloë. *Mécanique Quantique*. Hermann, 1997.

[310] W. H. Press, S. A. Teukolsky, W. T. Vetterling, and B. P. Flannery. *Numerical Recipes in Fortran 77, second edition*. Cambridge University Press, 1996.

[311] M. Zhao and Dmitri Babikov. Phase control in the vibrational qubit. *J. Chem. Phys.*, 125:024105, 2006. doi:10.1063/1.2220039.

[312] J. Aldegunde, H. Ran, and J. M. Hutson. Manipulating ultracold polar molecules with microwave radiation: The influence of hyperfine structure. *Phys. Rev. A*, 80(4):043410, 2009. doi:10.1103/PhysRevA.80.043410.

[313] H. Ran, J. Aldegunde, and J. M. Hutson. Hyperfine structure in the microwave spectra of ultracold polar molecules. *New J. Phys.*, 12(4):043015, 2010. doi:10.1088/1367-2630/12/4/043015.

[314] D. J. Griffiths. *Introduction to Electrodynamics*. Prentice Hall, 1999.